MEASUREMENT OF NEUTRINO OSCILLATION PARAMETERS AND INVESTIGATION OF URANIUM AND THORIUM ABUNDANCES IN THE EARTH USING ANTI-NEUTRINOS

A DISSERTATION
SUBMITTED TO THE DEPARTMENT OF PHYSICS
AND THE COMMITTEE ON GRADUATE STUDIES
OF STANFORD UNIVERSITY
IN PARTIAL FULFILLMENT OF THE REQUIREMENTS
FOR THE DEGREE OF
DOCTOR OF PHILOSOPHY

Kazumi Tolich
March 2008

I certify that I have read this dissertation and that, in my opinion, it is fully adequate in scope and quality as a dissertation for the degree of Doctor of Philosophy.

(Giorgio Gratta) Principal Adviser

I certify that I have read this dissertation and that, in my opinion, it is fully adequate in scope and quality as a dissertation for the degree of Doctor of Philosophy.

(Martin Breidenbach)

I certify that I have read this dissertation and that, in my opinion, it is fully adequate in scope and quality as a dissertation for the degree of Doctor of Philosophy.

(Tsuneyoshi Kamae)

Approved for the University Committee on Graduate Studies.

Abstract

The Kamioka Liquid scintillator Anti-Neutrino Detector (KamLAND) was designed to detect electron anti-neutrinos from commercial nuclear reactors, $\bar{\nu}_{\mathrm{reactor}}$s, and the Earth, $\bar{\nu}_{\mathrm{geo}}$s, via inverse β-decay. The analysis presented in this thesis measures the mass-squared difference, Δm^2_{21}, and the mixing angle, θ_{12}, involved in neutrino oscillation, using $\bar{\nu}_{\mathrm{reactor}}$s while simultaneously measuring the $\bar{\nu}_{\mathrm{geo}}$ flux. Δm^2_{21} and θ_{12} are two of the fundamental constants of nature, whose values are not currently predicted by the Standard Model of particle physics. The study of the Earth's interior by measuring the $\bar{\nu}_{\mathrm{geo}}$ flux is a new avenue in geophysics, opened by KamLAND. This analysis significantly increases the sensitivity to neutrino oscillation parameters compared to previous KamLAND results. The improvement is achieved by an almost three-fold increase of statistics, the lowering of the analysis energy range as far as allowed by the inverse β-decay threshold, a better overall control of systematics, and the simultaneous analysis of $\bar{\nu}_{\mathrm{reactor}}$s and $\bar{\nu}_{\mathrm{geo}}$s.

The null hypothesis of an undistorted $\bar{\nu}_{\mathrm{reactor}}$ energy spectrum expected in the absence of neutrino oscillation is definitively rejected at the 99.98 % confidence level. Instead, the measured energy distribution is consistent with the expectation from two-flavor neutrino oscillation with $\sin^2 2\theta_{12} = 0.935^{+0.061}_{-0.065}$ and $\Delta m^2_{21} = 7.44^{+0.19}_{-0.18} \times 10^{-5}\,\mathrm{eV}^2$. This Δm^2_{21} figure is a threefold improvement on the previous KamLAND result. The so-called "LMA0" and "LMA2" regions, previously disfavored over the "LMA1" region at the 97.5 % and 98.0 % confidence levels, respectively, are now disfavored at the 99.95 % and 99.9991 % confidence levels. Assuming CPT-invariance, the $\sin^2 2\theta_{12}$ estimate is further improved by combining this measurement with the results from other experiments that measure the flux of neutrinos from the sun, yielding

$\sin^2 2\theta_{12} = 0.901^{+0.028}_{-0.032}$ and $\Delta m^2_{21} = 7.46^{+0.19}_{-0.18} \times 10^{-5}\,\mathrm{eV}^2$.

The effective $\bar{\nu}_{\mathrm{geo}}$ detection rate, defined as the rate of interactions with protons in the detector in the absence of detection inefficiency and neutrino oscillation, is measured to be 122^{+36}_{-35} $(10^{32}\,\mathrm{proton} \cdot \mathrm{year})^{-1}$. The detection of $\bar{\nu}_{\mathrm{geo}}$s is confirmed for the first time at the 99.995 % confidence level.

Acknowledgements

The KamLAND experiment is supported by the Japanese Ministry of Education, Culture, Sports, Science and Technology, and under the United States Department of Energy Office grant DEFG03-00ER41138. The reactor data are provided by courtesy of the following associations in Japan: Hokkaido, Tohoku, Tokyo, Hokuriku, Chubu, Kansai, Chugoku, Shikoku and Kyushu Electric Power Companies, Japan Atomic Power Co. and Japan Nuclear Cycle Development Institute. The Kamioka Mining and Smelting Company has provided service for activities in the mine.

I would like to thank the entire KamLAND collaboration, my colleagues, friends, and family members who have supported me while I worked on my research. I am truly grateful for Masayuki Koga and Kengo Nakamura who supported me in Mozumi. I enjoyed the friendship of Greg Keefer, Tim Classen, Tommy O'Donnel, and Christopher Mauger, who made our collaboration meetings like no other. Brian Fujikawa taught me how honest physics is done, and I very much enjoyed his friendship. I would like to thank Lauren Hsu and Glenn Horton-Smith for developing and helping me with the simulation tools that I use in my analysis, Patrick Decowski for helping me with computing issues, Bruce Berger for helping me with electronics, and Lindley Winslow for developing the energy finding algorithm without which I could not have done my analysis. I would also like to thank Mikhail Batygov and Kouichi Ichimura for discussions on various issues with the "simultaneous analysis." I really appreciate the friendship of Sanshiro Enomoto, who also helped me in a variety of subjects, from trigger electronics related issues to geoneutrino analysis. A huge thank-you goes to Dan Dwyer for discussions on many aspects of this analysis and giving me many good ideas. He also made my analysis much easier by developing an analysis tool on

which I based mine. My advisor, Giorgio Gratta, has given me advice, guidance, and creative ideas for me to explore. He showed me what it takes to be a well-rounded physicist by example. I enjoyed working with Matt Green, Russell Neilson, Naoko Kurahashi, Jesse Wodin, Francisco Leport, Andrea Pocar, Sam Waldman, and the rest of current and previous Gratta group members, who made my study at Stanford so much fun. I am sincerely indebted to Jason Detwiler for teaching me how to properly conduct analyses, numerous discussions, and his friendship. My husband, best friend, and mentor, Nikolai Tolich, deserves my deepest appreciation. He trained me to be the trigger electronics expert for KamLAND. I learned how physics should be done from the countless discussions I have had with him over the years. He provided me support, advice, suggestions, and love when I needed. I will be forever indebted to my mother, Asa Ishii, and sisters, Chiaki and Hiromi Ishii, and rest of my family for their constant support. I appreciate the encouragement my late father, Hiroaki Ishii, had given me; his last words to me, "I am looking forward to seeing you succeed in graduate school," still echo in my heart.

Contents

List of Tables

List of Figures

Chapter 1

Introduction

1.1 History of Neutrinos

Neutrinos were first postulated by Pauli in 1930 [1, 2], based on the observation that electrons emitted in nuclear β-decay have a continuous energy spectrum up to the monochromatic energy value expected from two-body decays. Pauli postulated that an undetected particle could be carrying away the missing energy. He deduced that this new particle must have no electric charge and spin of one half to conserve electric charge and angular momentum, respectively. In 1933, Fermi presented a theory of β-decay, incorporating Pauli's particle, which he called the "neutrino"[1] [3]. From the electron energy spectral shape near the end-point in β-decay, he concluded that the mass of the neutrino must be zero or very small in comparison with the electron mass. Reines and Cowan made the first experimental observation of neutrinos in 1956 by detecting electron anti-neutrinos, $\bar{\nu}_\mathrm{e}$s, anti-particles of electron neutrino, ν_e, via inverse β-decay [4, 5]. Davis' Homestake experiment detected ν_es from the sun for the first time in 1968 [6]. A second (anti)neutrino flavor, called the μ-(anti)neutrino, ν_μ ($\bar{\nu}_\mu$), was first detected in 1962 [7]. When τ leptons were discovered in 1975 [8], existence of a third (anti)neutrino flavor, called the τ-(anti)neutrino, ν_τ ($\bar{\nu}_\tau$), was speculated, and later detected in 2000 [9]. In the 1970's, the "Standard Model" of

---

[1] Pauli called his new particle the "neutron", but by 1933, neutrons as we know today had claimed the name "neutron."

fundamental particles and interactions, which describes the physics of strong, weak, and electromagnetic interactions, was formulated based on the experimental evidence available then. This model assumes that neutrinos and anti-neutrinos only participate in the weak interaction, have three distinctive flavors, e, μ, and τ, and do not have masses.

The Homestake experiment [6] found a deficit in the solar ν_e flux compared to the flux expected based on the "Standard Solar Model" spearheaded by Bahcall [10]. Initially, it was speculated that the deficit may arise from overlooked systematic errors in the Homestake experiment, or from deficiencies in the "Standard Solar Model." Other experiments, such as SAGE [11], GALLEX [12], Kamiokande II [13], and Super-Kamiokande [14] later also observed a deficit in the solar ν_e flux. Similarly, the flux ratio of ν_e ($\bar{\nu}_e$) to ν_μ ($\bar{\nu}_\mu$) created from pion decays in the upper atmosphere and measured by various experiments, such as IMB [15] and Kamiokande [16], differed from the ratio of ~1:2 predicted by the Standard Model. These anomalous neutrino flux measurements could all be described by supposing that neutrinos "oscillate," a phenomenon that requires neutrinos to have masses[2]. In 2002, the SNO experiment demonstrated that the total flux of all three flavors of neutrinos from the sun agrees with the Standard Solar Model calculations, while only a fraction of that flux was observed in the form of ν_es, as expected for "neutrino oscillation" [18].

1.2 Neutrino Oscillation

In neutrino oscillation, a neutrino, created in one of the three flavor eigenstates, $|\nu_e\rangle$, $|\nu_\mu\rangle$, and $|\nu_\tau\rangle$, can be detected as another flavor eigenstate after traveling some distance. A neutrino flavor eigenstate, $|\nu_l\rangle$, can be expressed as a superposition of definite-mass eigenstates, $|\nu_i\rangle$,

$$|\nu_l\rangle = \sum_i U_{li}\,|\nu_i\rangle, \tag{1.1}$$

---

[2] Maki *et al.* first proposed this phenomenon in 1962 [17].

where U_{li} is a unitary mixing matrix that can be parameterized with three mixing angles, θ_{12}, θ_{23}, and θ_{13}, a CP violating phase, δ, and two Majorana phases, α_1 and α_2:

$$\begin{pmatrix} U_{e1} & U_{e2} & U_{e3} \\ U_{\mu 1} & U_{\mu 2} & U_{\mu 3} \\ U_{\tau 1} & U_{\tau 2} & U_{\tau 3} \end{pmatrix} = \begin{pmatrix} 1 & 0 & 0 \\ 0 & \cos\theta_{23} & \sin\theta_{23} \\ 0 & -\sin\theta_{23} & \cos\theta_{23} \end{pmatrix} \times \begin{pmatrix} \cos\theta_{13} & 0 & \sin\theta_{13}\, e^{-i\delta} \\ 0 & 1 & 0 \\ -\sin\theta_{13}\, e^{i\delta} & 0 & \cos\theta_{13} \end{pmatrix} \times \begin{pmatrix} \cos\theta_{12} & \sin\theta_{12} & 0 \\ -\sin\theta_{12} & \cos\theta_{12} & 0 \\ 0 & 0 & 1 \end{pmatrix} \times \begin{pmatrix} e^{i\,\alpha_1/2} & 0 & 0 \\ 0 & e^{i\,\alpha_2/2} & 0 \\ 0 & 0 & 1 \end{pmatrix}. \tag{1.2}$$

In the ultra relativistic limit, the probability of a neutrino created in flavor eigenstate $|\nu_l\rangle$ to be detected in flavor eigenstate $|\nu_{l'}\rangle$ after traveling a distance L through vacuum is given by

$$P_{\nu_l \to \nu_{l'}}(E_\nu,\, L) = \sum_i |U_{li}U^*_{l'i}|^2 + \Re\left(\sum_i \sum_{j\neq i} U_{li}U^*_{l'i}U^*_{lj}U_{l'j}e^{i\frac{\Delta m^2_{ji}L}{2E_\nu}}\right), \tag{1.3}$$

where $\Delta m^2_{ji} = |m^2_j - m^2_i|$ denotes the magnitude of the difference between the squares of masses of mass eigenstates $|\nu_i\rangle$ and $|\nu_j\rangle$, and E_ν denotes the neutrino energy. Using the experimental results indicating that $\Delta m^2_{21} \gg \Delta m^2_{32}$ [19, 20], the ν_e survival probability for a case where L is much larger than $E_\nu/\Delta m^2_{32}$ can be approximated by

$$P_{\nu_e \to \nu_e}(E_\nu, L) \approx \sin^4\theta_{13} + \cos^4\theta_{13}\left[1 - \sin^2 2\theta_{12}\sin^2\left(\frac{1.27\Delta m^2_{21}\,[\mathrm{eV}^2]L\,[\mathrm{m}]}{E_\nu\,[\mathrm{MeV}]}\right)\right]. \tag{1.4}$$

Since θ_{13} is measured to be small [21], Equation 1.4 can be further simplified by the approximation $\theta_{13} \ll 1$, which yields to zeroth order,

$$P_{\nu_e \to \nu_e}(E_\nu, L) \approx 1 - \sin^2 2\theta_{12} \sin^2 \left(\frac{1.27 \Delta m^2_{21}\,[\mathrm{eV}^2] L\,[\mathrm{m}]}{E_\nu\,[\mathrm{MeV}]} \right). \tag{1.5}$$

As one can see in Equation 1.5, neutrino oscillation can occur only if Δm^2_{21} is non-zero, i.e., at least one of the mass eigenstates must have a finite mass. Equation 1.5 can also be applied to the $\bar{\nu}_e$ survival probability assuming CPT invariance. For more details on the neutrino oscillation formalism, see [22].

1.3 Anti-Neutrino Sources

The two important $\bar{\nu}_e$ sources used in this thesis are nuclear reactors emitting $\bar{\nu}_e$s ($\bar{\nu}_{\mathrm{reactor}}$s) from β-decays following nuclear fission and radioactive decays inside the Earth emitting $\bar{\nu}_e$s ($\bar{\nu}_{\mathrm{geo}}$s) from some β-decays in the uranium and thorium decay chains. The production mechanism of $\bar{\nu}_{\mathrm{reactor}}$s and $\bar{\nu}_{\mathrm{geo}}$s are explained in the following sections.

1.3.1 Anti-Neutrinos from Nuclear Reactors

Nuclear reactors generate heat mostly from nuclear fission. Additional heat is generated as the resulting fission fragments undergo a series of nuclear decays until they become stable. Along with heat, the β-decays of the fragments also produce $\bar{\nu}_e$s. More than 99.9 % of $\bar{\nu}_{\mathrm{reactor}}$s are produced from the β-decay following fission of only four nuclei: ^{235}U, ^{238}U, ^{239}Pu, and ^{241}Pu [26].

Although slightly different for each of these four isotopes, each fission and its subsequent decays release approximately 200 MeV and 6 $\bar{\nu}_e$s on average. The exact proportionality of the thermal energy production to the total number of $\bar{\nu}_e$s emitted by the reactor depends on the fuel composition in the reactor at a given time. This proportionality combined with the measured thermal power generated in the nuclear reactor can therefore provide an estimate of the $\bar{\nu}_{\mathrm{reactor}}$ production rates.

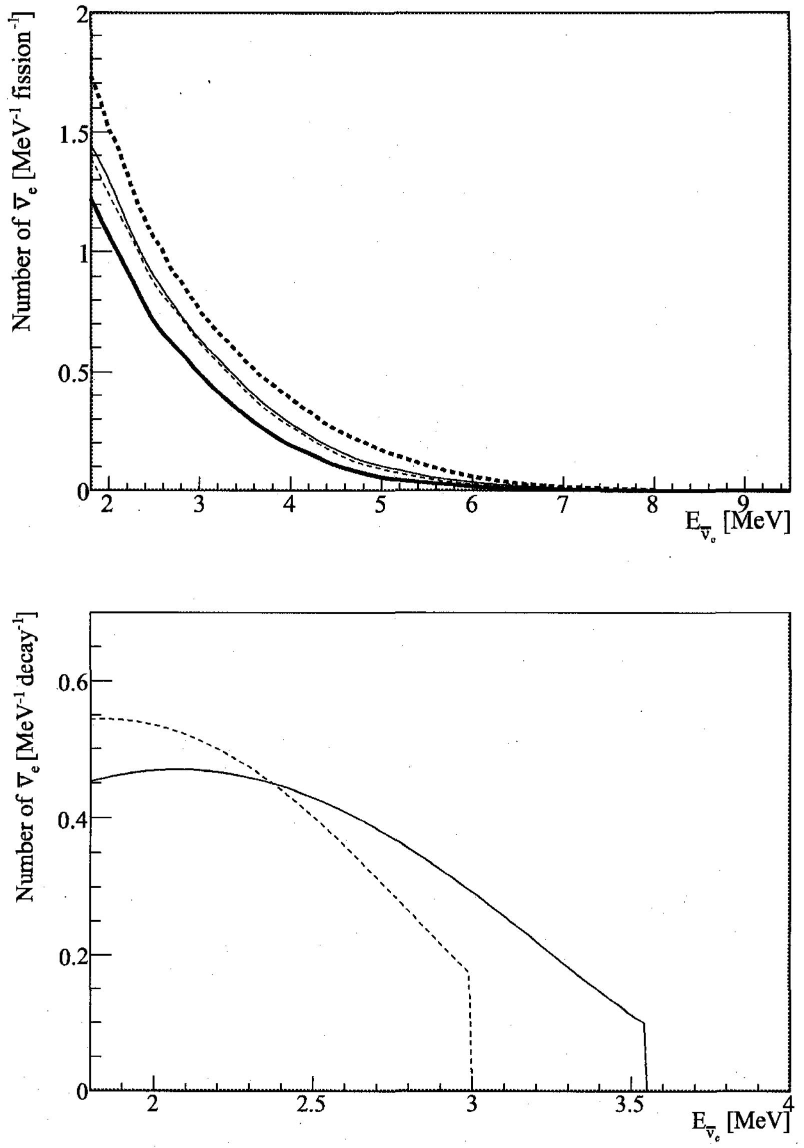

Figure 1.1: Top plot: energy spectra of $\bar{\nu}_e$s from β-decays following ^{235}U (thin solid line) [23], ^{238}U (thick dotted line) [24], ^{239}Pu (thick solid line), and ^{241}Pu (thin dotted line) [25] fission. Bottom plot: energy spectra of $\bar{\nu}_e$s from ^{106}Rh (solid line) and ^{144}Pr (dotted line) β-decays.

The top plot in Figure 1.1 shows the slight differences in the energy spectra of $\bar{\nu}_{\mathrm{e}}$s from ^{235}U, ^{238}U, ^{239}Pu, and ^{241}Pu. The energy spectra of $\bar{\nu}_{\mathrm{e}}$s from ^{235}U [23], ^{239}Pu, and ^{241}Pu [25] are extracted from measurements of the β-decay energy spectra of the fission fragments after exposing each isotope to a thermal neutron flux for approximately 12 hours. The $\bar{\nu}_{\mathrm{e}}$ energy spectrum for a single β-decay branch is calculated using the relation that the $\bar{\nu}_{\mathrm{e}}$ energy plus β energy equals the endpoint β energy of that branch. However, neither the actual number of branches nor the amplitudes and endpoint energies in the measured energy spectra of β-decays following ^{235}U, ^{239}Pu, and ^{241}Pu fission are known. Therefore, each of the measured β energy spectra from these isotopes is approximated by a combination of spectra from thirty hypothetical β-decay branches with some amplitude and endpoint energy. The $\bar{\nu}_{\mathrm{e}}$ spectra from all thirty hypothetical β-decay branches are then added. On the other hand, the energy spectrum of $\bar{\nu}_{\mathrm{e}}$s from ^{238}U is calculated theoretically up to 8 MeV[3] [24]. The theoretically calculated energy spectra of $\bar{\nu}_{\mathrm{e}}$s from ^{235}U, ^{239}Pu, and ^{241}Pu agree with the measured spectra within $\sim$10 %. Therefore a 10 % uncertainty is assumed for the calculated energy spectrum of $\bar{\nu}_{\mathrm{e}}$s from ^{238}U. To calculate the total $\bar{\nu}_{\mathrm{reactor}}$ energy spectrum from a nuclear reactor, the spectra from these isotopes need to be added together and weighted according to the fuel composition of the reactor. The average $\bar{\nu}_{\mathrm{reactor}}$ flux uncertainty above the inverse β-decay energy threshold (see Section 1.4) from the spectral shape uncertainty is estimated to be 2.5 %.

Since the β-decay energy spectra, from which the ^{235}U, ^{239}Pu, ^{241}Pu $\bar{\nu}_{\mathrm{e}}$ spectra are extracted, were measured after $\sim$12 hours of exposure to a thermal neutron flux, fragments with half-lives greater then a few hours had not yet reached equilibrium, and therefore were not included in these spectra. Contributions from such "long-lived" fragments are small, and mostly driven by ^{106}Ru and ^{144}Ce, with half-lives of 373.6 days and 284.9 days, respectively. Although the β-decays of ^{106}Ru and ^{144}Ce themselves do not produce $\bar{\nu}_{\mathrm{e}}$s with high enough energy to be observed via inverse β-decay, the β-decays of their daughters, ^{106}Rh and ^{144}Pr, do. The bottom plot in Figure 1.1 shows the energy spectra of $\bar{\nu}_{\mathrm{e}}$s produced in these decays.

---

[3] The contribution from the "missing" ^{238}U $\bar{\nu}_{\mathrm{e}}$ energy spectrum above 8 MeV to the total $\bar{\nu}_{\mathrm{reactor}}$ spectrum above 8 MeV is small since the fractional contribution of ^{238}U fission in the reactor is typically less than 10 %.

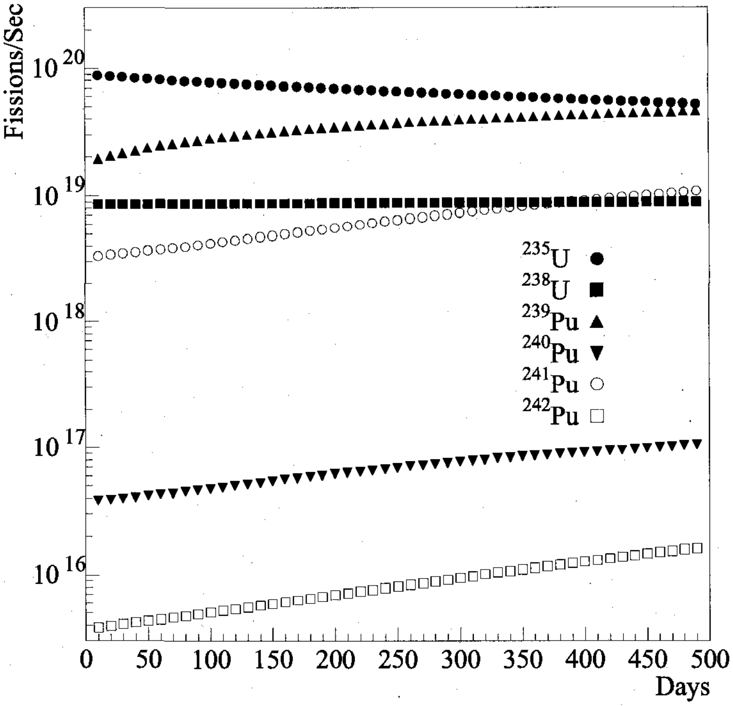

Figure 1.2: Simulated time evolution of fission rate for one of the Palo Verde reactors [26].

The fuel composition of a reactor changes during operation. While the fission of ^{235}U, ^{238}U, ^{239}Pu, and ^{241}Pu breaks up these isotopes, plutonium nuclei are bred through two other reactions: neutron capture on ^{238}U followed by two subsequent β-decays producing ^{239}Pu, and two neutron captures on ^{239}Pu creating ^{241}Pu. Overall, the numbers of ^{235}U and ^{238}U nuclei keep decreasing while the numbers of ^{239}Pu and ^{241}Pu nuclei keep increasing. Figure 1.2 shows a simulated time evolution of fission rates from various isotopes for one of the Palo Verde reactors as an example [26].

In order to sustain the reactor operation, when the fraction of ^{235}U in the core becomes too low, the reactor is powered down, and one third or one quarter of the fuel is replaced. Typically this occurs every year or two. The spent fuel is stored near the reactor for long periods of time after refueling to cool down while awaiting log-term storage. The spent fuel contains ^{106}Ru and ^{144}Ce that keep driving the long-lived isotope contribution of $\bar{\nu}_{\mathrm{reactor}}$s. The $\bar{\nu}_{\mathrm{reactor}}$ contributions driven by the "long-lived"

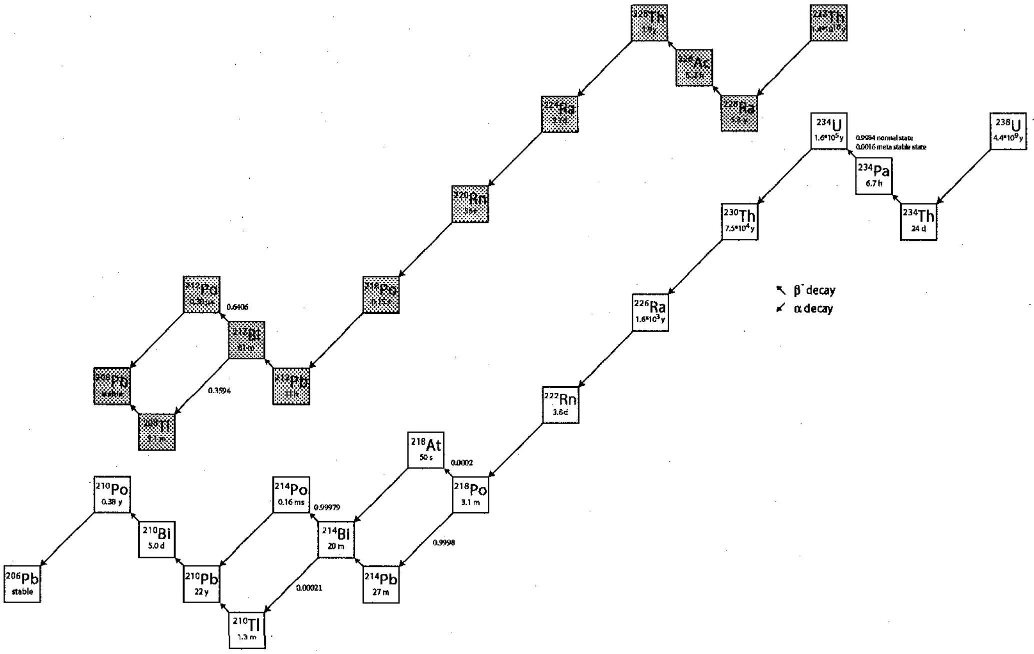

Figure 1.3: Decay chains of ^{238}U and ^{232}Th.

isotopes in the reactor core and spent fuel combined amount to ~1% of the total $\bar{\nu}_{\text{reactor}}$ flux.

The thermal power output, time evolution of the fuel composition, fuel cycles, and the spent fuel contribution need to be considered in calculating the total $\bar{\nu}_{\text{reactor}}$ energy spectrum from a nuclear reactor. The details on the $\bar{\nu}_{\text{reactor}}$ energy spectrum used in this thesis is discussed in Section 6.1.

1.3.2 Anti-Neutrinos from Radioactive Decays in the Earth

The radioactive decay chains of ^{238}U and ^{232}Th, shown in Figure 1.3, are thought to produce heat inside the Earth, driving mantle convection, plate tectonics, and, ultimately, earthquakes. Each β^--decay emits a $\bar{\nu}_e$, and the total energy spectra of $\bar{\nu}_{\text{geo}}$s produced in the ^{238}U and ^{232}Th decay chains, shown in Figure 1.4, are obtained by adding the spectra from all the β^--decay branches in Figure 1.3.

The $\bar{\nu}_{\text{geo}}$ flux at a particular point on the surface of the Earth depends on the concentration distributions of ^{238}U and ^{232}Th. $\bar{\nu}_{\text{geo}}$s, which travel mostly undisturbed

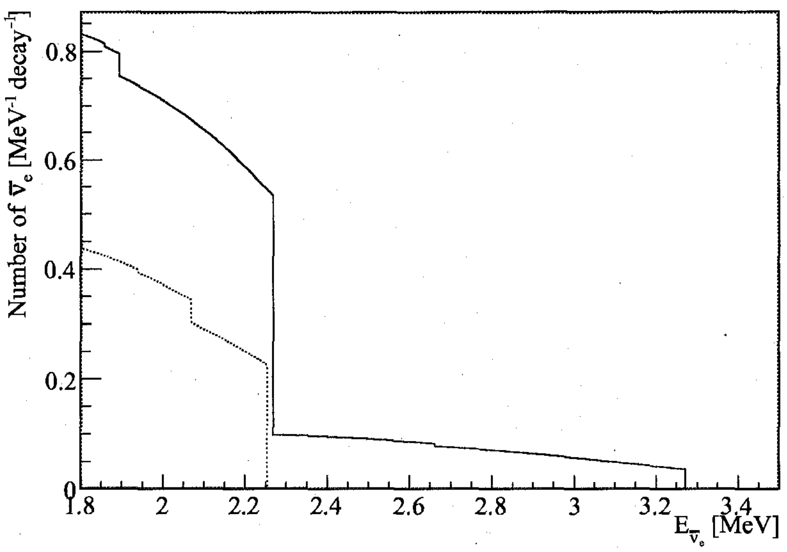

Figure 1.4: Energy spectra of $\bar{\nu}_{\text{geo}}$s from β-decays in the ^{238}U (solid line) and ^{232}Th (dotted line) decay chains (modified from [27]).

through the Earth, come directly from where the β^--decays occur inside the planet; therefore a measurement of their flux directly yields the composition of the Earth. To date, models of the Earth's structure and concentrations of these isotopes ([28] and [29], for example) have been constructed mostly using seismic data and chemical analysis of special kinds of meteorites and rocks. Although seismic data directly yields the mechanical properties of the inner Earth, it does not yield chemical composition of each layer. The current understanding of chemical compositions of the Earth relies on extrapolation from meteorites and rocks. The uncertainties in these methods are largely unknown. Therefore the direct measurement of the $\bar{\nu}_{\text{geo}}$ flux can become an important new tool for understanding radiogenic heat generation in the Earth, the source of energy that powers terrestrial dynamics.

Seismic data indicates that the Earth consists of the following major concentric regions (approximate radial thickness): crust (6 to 30 km), several layers of mantle (2900 km), outer core (2300 km), and inner core (1200 km) [30]. The density profile of these regions is shown in Figure 1.5. There are two distinctive types of crusts: oceanic

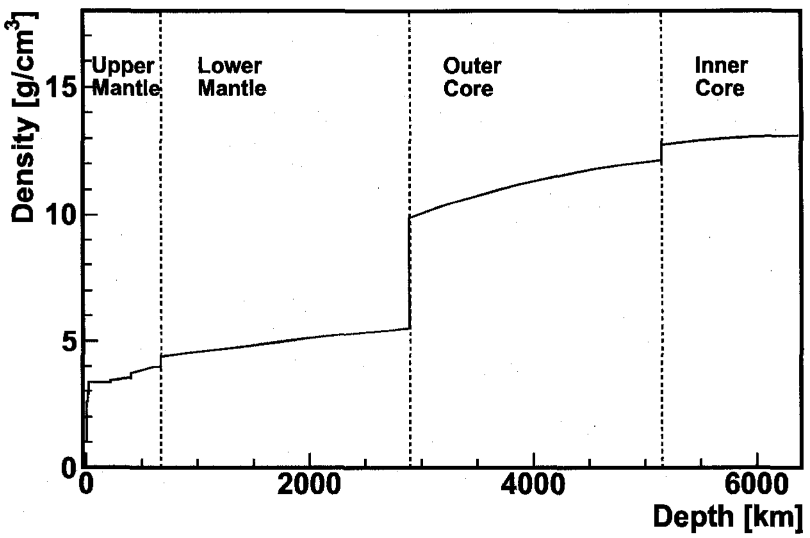

Figure 1.5: Density of the Earth as a function of the depth from the surface [28].

crusts, which are relatively young (~80 million years old) since they are constantly renewed at the mid-ocean ridges and recycled back into the inner Earth at subduction zones, and continental crusts, which are ~2 billion years old on average. Continental crusts are thicker than oceanic crusts, and further subdivided into upper, middle, and lower crusts. Sediment consisting of eroded continental crust and volcanic and biological materials covers the surface of both the continental and oceanic crusts. The composition of the sediment covering the continental crust is assumed to be the same as that of the continental crust.

The chemical composition in each region has been studied with various methods. Direct sampling of crusts is obtained from bore-holes. However, the deepest bore-hole reaches only 12 km into the crust [31], approximately 0.2 %, of the Earth's radius. "Xenoliths," rock fragments brought up from the mantle to the surface in lava flows without melting, give an indication of the chemical compositions of the upper mantle. However, xenoliths are rare, and may not be a good representation of the average mantle. These bore-hole and xenolith samples suggest that the crusts and mantle are composed mainly of silica, and the crusts, especially the continental crusts, contain high amounts of ^{238}U and ^{232}Th. A type of meteorite, type I carbonaceous chondrite [32], is assumed to have the same composition of chemical elements as the Earth did in its early formation stage, referred to as the "Bulk Silicate Earth (BSE) [33]," in which the mantle and the crust had not yet been differentiated. The ^{238}U and ^{232}Th contents of the mantle is estimated by subtracting these contributions from the crusts and sediment from the BSE. The core is believe to consist of mostly iron, in which ^{238}U and ^{232}Th are insoluble[4]. Hence the concentrations of these elements in the core are assumed to be negligible. Table 1.1 shows the estimated concentrations of ^{238}U and ^{232}Th in each region based on the above studies [28]. The mass ratio of ^{232}Th to ^{238}U, which chemical analyses of rocks and meteorites indicate, lies between 3.7 and 4.1, more reliably estimated than the absolute concentrations in each region [34].

Table 1.1: Estimated concentrations of ^{238}U and ^{232}Th in the major Earth regions [28].

Region	^{238}U [ppm]	^{232}Th [ppm]
Oceanic sediment	1.68	6.91
Oceanic crust	0.10	0.22
Upper continental crust	2.8	10.7
Middle continental crust	1.6	6.1
Lower continental crust	0.2	1.2
Mantle	0.012	0.048
Core	0	0
BSE	0.02	0.08

Based on the model, summarized in Table 1.1, the radiogenic power generation from the decay chains of ^{238}U and ^{232}Th is estimated to be 16 TW. All the other radioactive sources, mostly ^{40}K, contribute an additional ~3 TW. On the other hand, the total power dissipated from the Earth is estimated to be significantly higher than the estimated radiogenic power generation. The total power dissipation of the Earth is estimated to be 44.2 ± 1.0 TW by summing the heat flow measurements made

---

[4] Being lithophile elements with filled outer electron shells, ^{238}U and ^{232}Th form ionic bonds mainly with oxygen in silicates and oxides while metallic iron tends to bond with other transition metals.

in bore-holes and calculations based on empirical estimators derived from the observations for unsurveyed areas and areas with hydrothermal effects[5] [35]. A more controversial approach, using only the heat flow measurements made in bore-holes without the estimators that corrects for the hydrothermal circulation effects, yields $31 \pm 1\,\mathrm{TW}$ [36]. Although the exact mechanism is not known, the mantle is widely believed to convect. Models of mantle convection suggest that the radiogenic heat production rate should be the majority of the contribution to the Earth's heat dissipation rate [37, 38, 39]. Therefore if these models are correct, there is a discrepancy between the total power dissipation estimation ($44.2 \pm 1.0\,\mathrm{TW}$ or $31 \pm 1\,\mathrm{TW}$) and the radiogenic power production estimation ($\sim$19 TW). A measurement of the $\bar{\nu}_{\mathrm{geo}}$ flux can serve as an essential cross-check of the radiogenic power production estimation.

1.4 Anti-Neutrino Detection with KamLAND

KamLAND (Kamioka Liquid Scintillator Anti-Neutrino Detector) is a mineral-oil-based liquid scintillator detector which detects $\bar{\nu}_{\mathrm{e}}$s via inverse β-decay:

$$\bar{\nu}_{\mathrm{e}} + \mathrm{p} \rightarrow \mathrm{e}^{+} + \mathrm{n}. \tag{1.6}$$

A $\bar{\nu}_{\mathrm{e}}$ interacts with a proton, p, creating a positron, e^{+}, and a neutron, n. The e^{+} quickly loses its kinetic energy in the scintillator by ionizing molecules and then annihilates with an electron, emitting two 0.511 MeV γs[6]. Meanwhile, the n produced in inverse β-decay quickly thermalizes and is later captured by another p, creating a 2.2 MeV γ and a deuteron. The mean neutron capture time is $\sim 200\,\mu\mathrm{s}$, and the

---

[5] The heat flow measurements from many ocean floor areas are known to be biased too low due to the ocean water circulation removing the measurable heat [35].

[6] The e^{+} sometimes combines with an electron forming positronium (Ps) either in the para-Ps or ortho-Ps state [40]. The para-Ps state decays by emitting two 0.511 MeV γs with a lifetime of 125 ps. In vacuum, the ortho-Ps state decays by emitting three γs sharing total energy of 1.022 MeV with a lifetime of 140 ns. However, in matter, the majority of ortho-Ps interact with surrounding electrons and decay by emitting two 0.511 MeV γs with a lifetime of a few ns. The three-γ decays of the ortho-Ps state produce slightly different amount of light in the detector from two-γ decays, which have the same total energy (see Section 3.4). This small effect is ignored, and e^{+} is always assumed to emit two 0.511 MeV γs upon annihilation in this thesis.

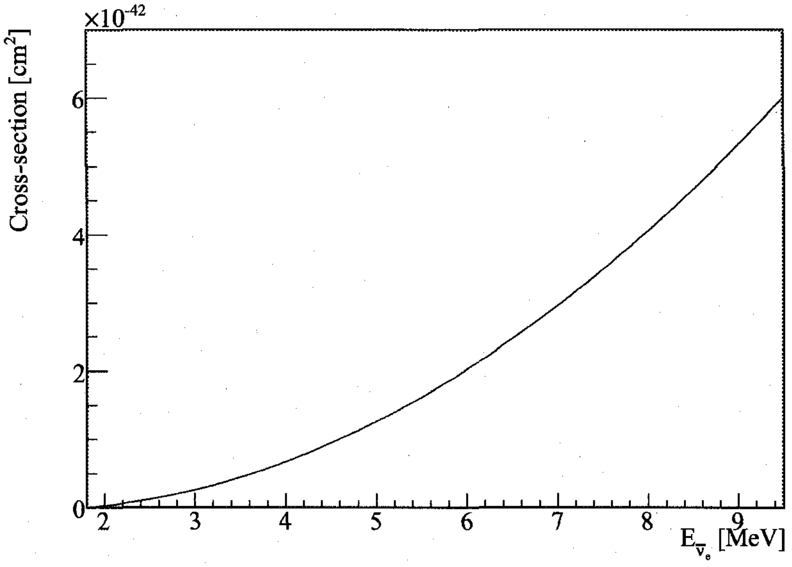

Figure 1.6: Inverse β-decay cross-section.

neutron-capture γ is generated typically within a few centimeters from the $\bar{\nu}_{\rm e}$ interaction vertex. In liquid scintillator, this sequence of events produces two temporally and spatially correlated flashes of light: the first flash (the "prompt" event) arises from the combination of the $\rm e^+$ ionization, the annihilation γs, and the thermalization of the n, and the second flash (the "delayed" event) results from the neutron-capture γ as it Compton-scatters through the scintillator.

To zeroth order in all terms of the form $1/M$ with $E_{\bar{\nu}_{\rm e}}/M$ being dominant among them, where M and $E_{\bar{\nu}_{\rm e}}$ denote the nucleon mass and $\bar{\nu}_{\rm e}$ energy, respectively, the total $\rm e^+$ energy, $E_{\rm e^+}$, and $E_{\bar{\nu}_{\rm e}}$ are related by [41]

$$E_{\bar{\nu}_{\rm e}} = E^{(0)}_{\rm e+} + \Delta m_{\rm n-p}, \tag{1.7}$$

where $\Delta m_{\rm n-p}$ denotes the n mass minus the p mass. Inverse β-decay is allowed only for $E_{\bar{\nu}_{\rm e}}$ greater than ~1.8 MeV, approximately corresponding to $\Delta m_{\rm n-p}$ plus mass of the $\rm e^+$. Figure 1.6 shows the inverse β-decay cross-section calculated to first order in all terms of the form $1/M$ [41] and including radiative corrections [42]. The total error in this cross-section is estimated to be 0.2 %. In order to calculate the observable

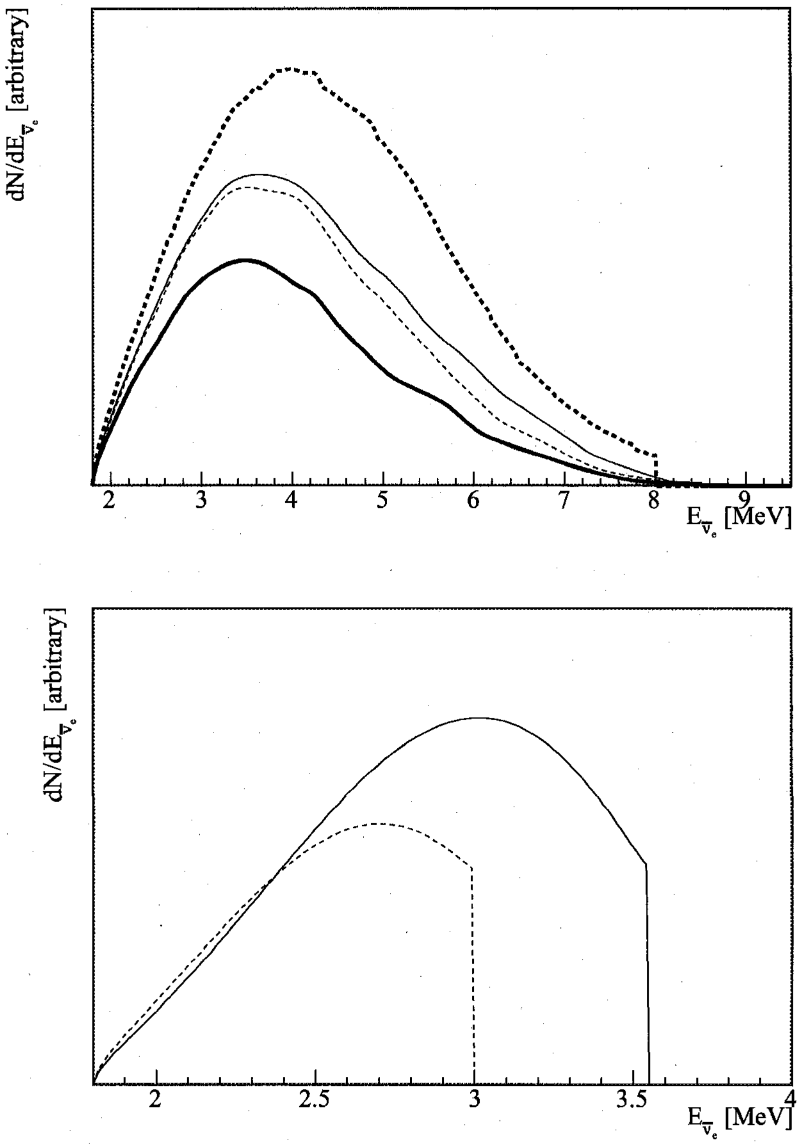

Figure 1.7: Top plot: Observable energy spectra of $\bar{\nu}_e$s from β-decays following ^{235}U (thin solid line), ^{238}U (thick dotted line), ^{239}Pu (thick solid line), and ^{241}Pu (thin dotted line) fission. Each spectrum is arbitrarily normalized to assume the equal fission rate. Bottom plot: Observable energy spectra of $\bar{\nu}_e$s from the β-decay of ^{106}Rh (solid line) and ^{144}Pr (dotted line). The spectra in both plots are obtained by multiplying the spectra in Figure 1.1 by the inverse β-decay cross-section. Neutrino oscillation effect is not included.

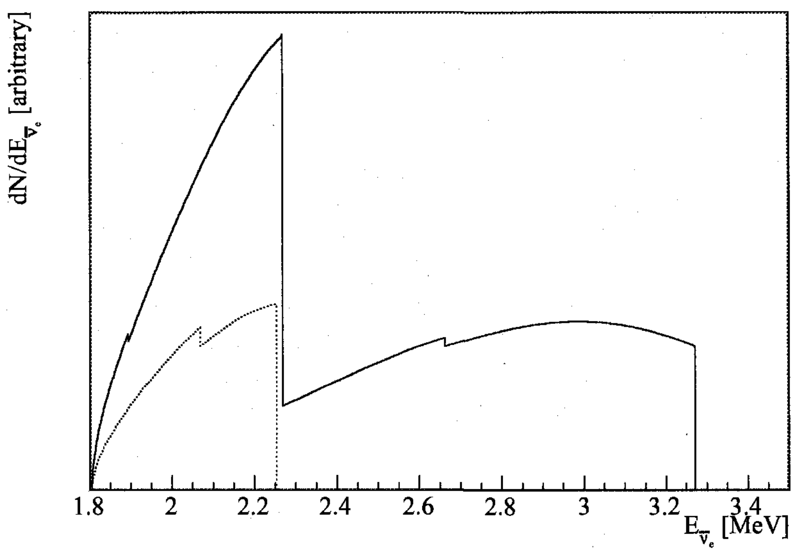

Figure 1.8: Observable energy spectra of $\bar{\nu}_{\rm geo}$s from β-decays in the ^{238}U (solid line) and ^{232}Th (dotted line) decay chains. This is obtained by multiplying Figure 1.4 by the inverse β-decay cross-section.

$E_{\bar{\nu}_e}$ spectrum, this cross-section needs to be multiplied by the $E_{\bar{\nu}_e}$ spectrum of the incident $\bar{\nu}_e$s. The raw energy spectra of $\bar{\nu}_e$s produced in a nuclear reactor, shown in Figure 1.1, and the Earth, shown in Figure 1.4, multiplied by the cross-section result in the spectra shown in Figures 1.7 and 1.8, respectively.

1.5 Previous Measurements with KamLAND

The KamLAND collaboration published results on measurements of the neutrino oscillation parameters, Δm^2_{21} and $\sin^2 2\theta_{12}$, in 2003 [43] and 2005 [44], based on the observation of $\bar{\nu}_{\rm reactor}$s from Japanese nuclear reactors. KamLAND separately conducted a study of $\bar{\nu}_{\rm geo}$ in 2005 [45]; this was the first time $\bar{\nu}_e$s were used as a tool for geophysics.

These analyses were conducted using the "real energy[7]" spectra of prompt events, $E^{\rm real}_{\rm prompt}$, which consists of the kinetic energy of e$^+$, two annihilation γs, and neutron

---

[7] For details of real energy, see Section 3.4.

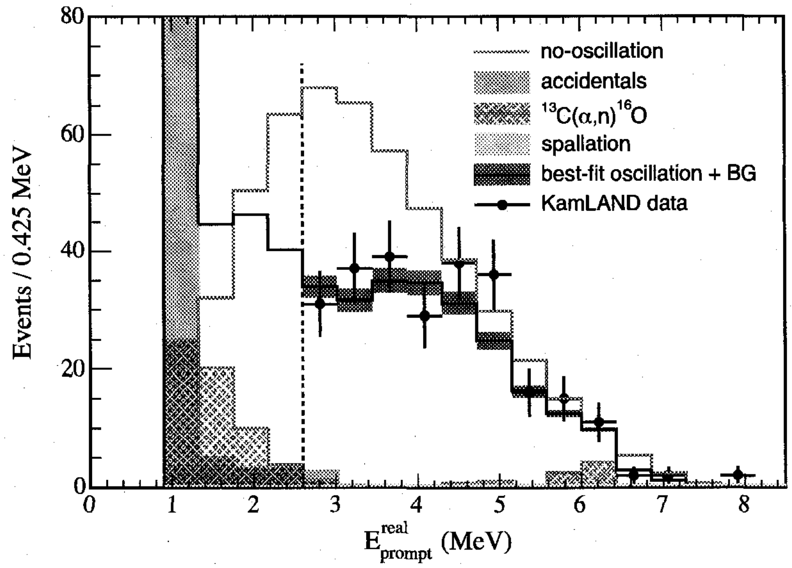

Figure 1.9: $E_{\text{prompt}}^{\text{real}}$ spectrum from the previous KamLAND result (colors modified from [44]). The vertical dotted line indicates the analysis energy threshold of 2.6 MeV. The dark shaded bands around the best fit spectrum indicate the systematic error above 2.6 MeV.

thermalization. $E_{\bar{\nu}_e}$ can be approximated by adding 0.8 MeV to $E_{\text{prompt}}^{\text{real}}$.

1.5.1 Oscillation Parameter Measurement

The $\bar{\nu}_{\text{reactor}}$s undergo oscillation as they travel from their respective nuclear reactor to KamLAND. Neutrino oscillation reduces the $\bar{\nu}_{\text{reactor}}$ flux and distorts the $\bar{\nu}_{\text{reactor}}$ energy spectrum according to Equation 1.5, where L denotes the distances to the nuclear reactors[8]. Although the $E_{\text{prompt}}^{\text{real}}$ spectrum of $\bar{\nu}_{\text{reactor}}$ extends down to the inverse β-decay threshold of ~1 MeV, the previous analyses on the neutrino oscillation parameters used an $E_{\text{prompt}}^{\text{real}}$ analysis threshold of 2.6 MeV to avoid backgrounds from random coincidences, $^{13}\text{C}(\alpha, \text{n})$, and $\bar{\nu}_{\text{geo}}$s, whose flux was not well-known.

In the second neutrino oscillation parameter measurement result [44], KamLAND observed 258 inverse β-decay candidates. In the absence of neutrino oscillation, 365.2

---

[8] Details of the expected $\bar{\nu}_{\text{reactor}}$ flux and energy spectrum calculations based on various values of neutrino oscillation parameters are discussed in Section 6.1.

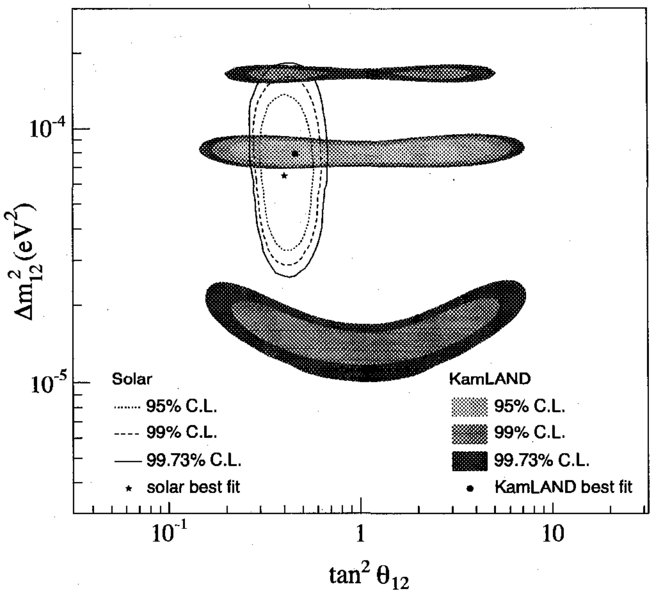

Figure 1.10: Neutrino oscillation parameter inclusion contours at different confidence levels from the previous KamLAND result (colors modified from [44]). The filled contours are from an analysis using only KamLAND data. The solid, dashed, and dotted lines are from solar ν_e experiments.

± 23.7 event-pairs, which included 17.8 ± 7.3 background event-pairs, were expected. This discrepancy between the observed and expected numbers of event-pairs confirmed the disappearance of $\bar{\nu}_{\mathrm{reactor}}$ at a confidence level of 99.998%. Disregarding the normalization, the observed $E^{\mathrm{real}}_{\mathrm{prompt}}$ spectrum disagreed with the shape of the expected $E^{\mathrm{real}}_{\mathrm{prompt}}$ spectrum in the absence of neutrino oscillation at a confidence level of 99.6%. Figure 1.9 shows the $E^{\mathrm{real}}_{\mathrm{prompt}}$ distribution. The KamLAND data exhibits a dip around 3 MeV relative to the no-oscillation expected spectrum. The neutrino oscillation parameters were estimated from the normalization and distortion of the $E^{\mathrm{real}}_{\mathrm{prompt}}$ spectrum, both of which depend on the absolute time due to the temporal variation in the nuclear reactor operation.

Figure 1.10 shows the inclusion contour in the neutrino oscillation parameter space, Δm^2_{21} and $\tan^2\theta_{12}$. The three regions allowed at the 99.73 % confidence level in the KamLAND-only analysis have been named as LMA0, LMA1, and LMA2 from bottom to top, where LMA stands for Large Mixing Angle[9]. KamLAND data preferred the LMA1 region, and the LMA0 and LMA2 regions were disfavored over the LMA1 region at confidence levels of 97.5 % and 98.0 %, respectively. When combined with neutrino oscillation results of solar ν_{e} experiments under the assumption of CPT invariance, this analysis gave $\Delta m^2_{21} = 7.9^{+0.6}_{-0.5} \times 10^{-5}\mathrm{eV}^2$ (KamLAND alone), and $\tan^2\theta_{12} = 0.40^{+0.10}_{-0.07}$.

1.5.2 $\bar{\nu}_{\mathrm{geo}}$ Investigation

The absolute number of $\bar{\nu}_{\mathrm{geo}}$s detected by KamLAND was estimated by fitting the $E^{\mathrm{real}}_{\mathrm{prompt}}$ spectrum in the low energy region, $0.9\,\mathrm{MeV} < E^{\mathrm{real}}_{\mathrm{prompt}} < 2.6\,\mathrm{MeV}$, using the energy spectral shapes of the expected $\bar{\nu}_{\mathrm{geo}}$s from ^{238}U and ^{232}Th decay chains (see Figure 1.8). The $\bar{\nu}_{\mathrm{geo}}$s undergo neutrino oscillation as they travel to KamLAND from where they are produced inside the Earth. Since the production points of $\bar{\nu}_{\mathrm{geo}}$s are spread out within the Earth, the $\sin^2\left(\frac{1.27\Delta m^2_{21}[\mathrm{eV}^2]\mathrm{L}[\mathrm{m}]}{E_\nu[\mathrm{MeV}]}\right)$ term in Equation 1.5 averages out to 0.5, and hence the $\bar{\nu}_{\mathrm{geo}}$ flux is reduced by $1 - 0.5\sin^2 2\theta_{12}$. The $\bar{\nu}_{\mathrm{geo}}$ energy spectral shapes do not change appreciably due to neutrino oscillation. Figure 1.11 shows the expected spectra of $\bar{\nu}_{\mathrm{geo}}$s as well as backgrounds. The fitted numbers of $\bar{\nu}_{\mathrm{geo}}$s from ^{238}U and ^{232}Th decay chains are 3 and 18, respectively.

In Figure 1.12, panel **a)** shows the confidence intervals of the $\bar{\nu}_{\mathrm{geo}}$ parameters, the sum of the number of $\bar{\nu}_{\mathrm{geo}}$s from the ^{238}U and ^{232}Th decay chains, and the normalized difference. Assuming a ^{232}Th to ^{238}U mass concentration ratio of 3.9, the 90 % confidence interval for total number of $\bar{\nu}_{\mathrm{geo}}$s detected ranges from 4.5 to 54.2 (see Figure 1.12 panel **b)**). A non-zero $\bar{\nu}_{\mathrm{geo}}$ signal was observed at the confidence level of ~95 %.

1.6 Motivation for a Simultaneous Analysis

The previous neutrino oscillation parameter results (see Section 1.5.1) were based on analyses using the $E^{\mathrm{real}}_{\mathrm{prompt}}$ threshold of 2.6 MeV to avoid mainly the $\bar{\nu}_{\mathrm{geo}}$s, as well as

---

[9] Before the KamLAND and SNO experiments made their clear observations of neutrino oscillations, several parameter regions were allowed by solar ν experiments, LMA being one of them.

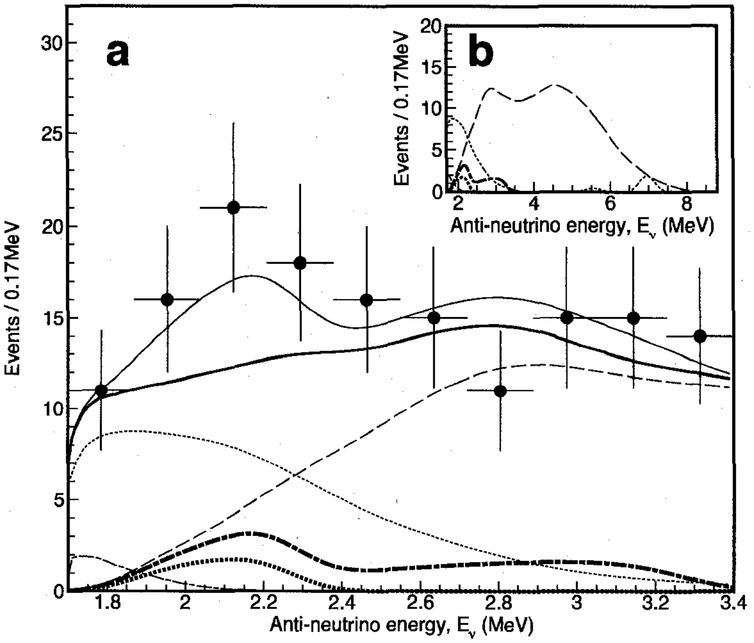

Figure 1.11: The expected energy spectra of $\bar{\nu}_{\rm geo}$s from ^{238}U (thick dot-dashed line) and ^{232}Th (thick dotted line) from the previous KamLAND result (colors modified from [45]) are based on the Earth model described in [28]. Expected spectra of $\bar{\nu}_{\rm reactor}$ (long dashed line), ^{13}C$(\alpha, {\rm n})$ (thin dotted line), random coincidence (thin dot-dashed line), the total background (thick solid line), and the total events (thin solid line) are also shown. Panel **a**) shows the $\bar{\nu}_{\rm geo}$ candidate data (markers with error bars). In panel **b**), the expected spectra are extended to show the higher energy region.

backgrounds from random coincidences and ^{13}C$(\alpha, {\rm n})$. The separate $\bar{\nu}_{\rm geo}$ study (see Section 1.5.2), conducted with $E^{\rm real}_{\rm prompt}$ between 0.9 MeV and 2.6 MeV, treats $\bar{\nu}_{\rm reactor}$s as background, and fixed the $\bar{\nu}_{\rm reactor}$ $E^{\rm real}_{\rm prompt}$ spectral shape based on the neutrino oscillation parameters obtained previously.

Instead of studying the neutrino oscillation parameters and $\bar{\nu}_{\rm geo}$s separately, these studies can be conducted simultaneously. Observing the full energy spectrum of $\bar{\nu}_{\rm reactor}$ should increase the sensitivity of the neutrino oscillation parameter measurement. By determining the $\bar{\nu}_{\rm reactor}$ spectrum more accurately, the $\bar{\nu}_{\rm geo}$ measurement should also improve since $\bar{\nu}_{\rm reactor}$s are the largest background to the $\bar{\nu}_{\rm geo}$ measurement. Finally, a joint analysis will properly take into account for correlations between the

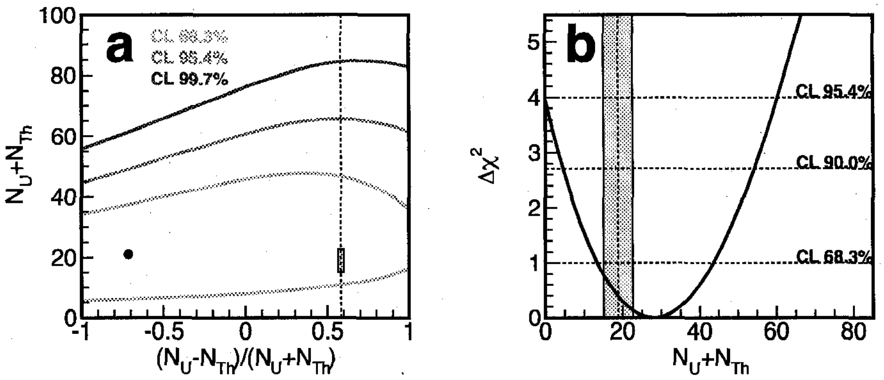

Figure 1.12: $\bar{\nu}_{\text{geo}}$ parameter results from the previous KamLAND study (colors modified from [45]). Panel **a**) shows the confidence level contours in the $\bar{\nu}_{\text{geo}}$ parameter space floating the ratio of $\bar{\nu}_{\text{geo}}$ contributions from ^{238}U and ^{232}Th. Panel **b**) shows the $\Delta\chi^2$ of the total number of $\bar{\nu}_{\text{geo}}$s observed with a fixed ^{232}Th to ^{238}U mass ratio of 3.9, estimated from other geophysical and planetary considerations. The gray boxes in both panel **a**) and **b**) indicate the expected $\bar{\nu}_{\text{geo}}$s based on the Earth model described in [28].

fitted neutrino oscillation and $\bar{\nu}_{\text{geo}}$ parameters. This thesis pursues such a joint analysis.

The analyses described in Section 1.5 were conducted using different $\bar{\nu}_{\text{e}}$ candidate selection cuts. The candidate selection cuts for the $\bar{\nu}_{\text{geo}}$ study were much tighter because of a large contribution from the random coincidence background at lower energy. Combining these analyses and performing the fit simultaneously involves consolidating the different candidate selection cuts.

The quantity $E^{\text{real}}_{\text{prompt}}$ used in the previous analyses is a rather unnatural unit since it assumes that e^+s cause the prompt events. However, prompt events from background signals are not necessarily caused by e^+s. These events and e^+s would have the same $E^{\text{real}}_{\text{prompt}}$ when they produce the same amount of light in the detector. A e^+ with no kinetic energy would yield the minimum allowed $E^{\text{real}}_{\text{prompt}}$ of ~1 MeV. Therefore the $E^{\text{real}}_{\text{prompt}}$ of a background event that produces less light in the detector does not correspond to any physical event involving e^+s, and so is not well-defined. To avoid these problems, the analysis presented in this thesis is conducted in terms of the observable energy based on light yield.

Chapter 2

Detector

KamLAND (Kamioka Liquid scintillator Anti-Neutrino Detector) is located in a rock cavern in the Kamioka mine, ~1000 m below the summit of Mt. Ikenoyama in Gifu, Japan. Mt. Ikenoyama shields the detector from cosmic rays. Figure 2.1 shows a schematic of the detector, which consists of two major sections, the inner detector (ID) and the outer detector (OD), separated by a spherical stainless steel vessel of 9 m radius. The ID section is designed for detection of $\bar{\nu}_e$s, and the OD section acts as a cosmic ray active veto while also attenuating γ radiation from the surrounding rock. Light produced in the ID and OD is detected by photo multiplier tubes (PMTs), which convert photons that hit their photo-cathodes into an electrical signal. Waveforms from the PMTs, readout as voltage as a function of time, are recorded and later used to reconstruct the energies and positions of events[1]. To test the performance of the algorithms in finding the energy and position, radioactive calibration sources with known energies are deployed at known positions.

2.1 Inner Detector

An approximately spherical balloon of 6.5 m radius is suspended inside the stainless steel vessel and filled with $1171 \pm 25\,\mathrm{m}^3$ of liquid scintillator (LS)[2]. Charged particles

---

[1] See Sections 3.2 and 3.3 for details of these algorithms.

[2] The total volume of the LS was measured during detector filling.

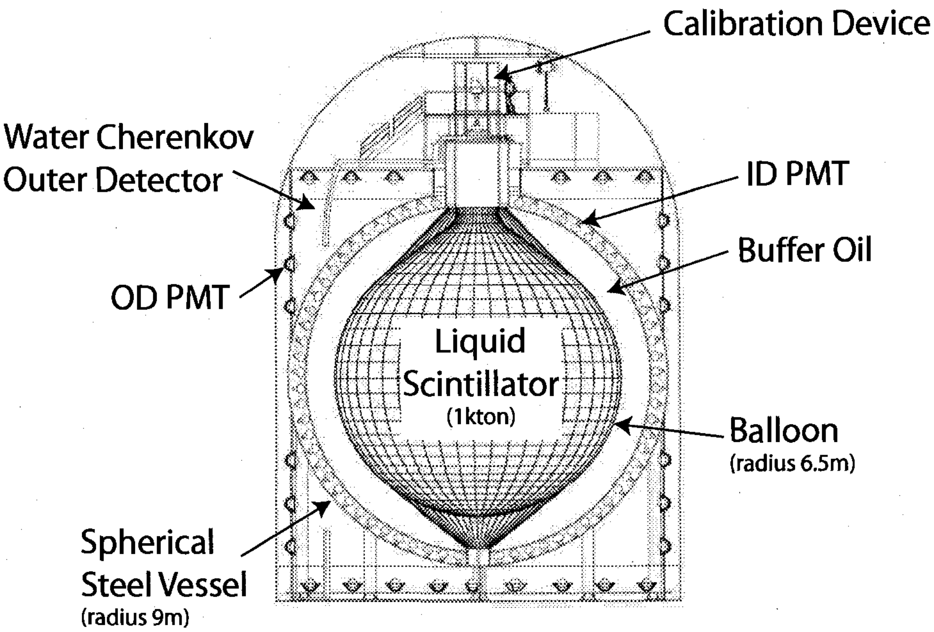

Figure 2.1: Schematic diagram of the KamLAND detector.

traversing the LS produce light, which is detected by PMTs mounted inside the stainless steel vessel. The transparent balloon, which is suspended by a netting of Kevlar ropes from the top of the detector, is only 135 μm thick and made of three layers; two layers of EVOH (ethylene vinyl alcohol) copolymer composite films sandwich a layer of nylon. Approximately 1800 m^3 of non-scintillating mineral oil (buffer oil) fills the space between the balloon and the steel vessel surrounding the PMTs. The buffer oil acts as a shield for external radiation such as γs from ^{208}Tl decays in the rock and ^{40}K decays in the PMT glass. A 3.3 mm thick acrylic sphere of 8.3 m radius in front of PMTs prevents radioactive radon produced in the PMTs from entering the LS.

The LS consists of 80 % dodecane ($H_{26}C_{12}$) and 20 % pseudocumene (1,2,4 - trimethylbenzene, $H_{12}C_9$) by volume, with 1.36 ± 0.03 g/L of PPO (2,5 - diphenyloxazole, $H_{11}C_{15}NO$) as a fluor. Various optical properties of the LS were measured on a test bench; the light attenuation length is 10 m for photons at a wavelength of 400 nm, the light yield is 57 % that of anthracene, and the refractive index is 1.45 for photons at a wavelength of 410 nm. The hydrogen-to-carbon ratio of the scintillator is calculated to be 1.97, which was verified by elemental analysis with 2 % precision.

The LS density was measured to be 0.778 g/m^3 at 11.5 °C with 0.01 % precision and varies by 0.1 % due to variation of temperature within the detector. The LS density is only 0.04 % higher than that of the buffer oil (dodecane and isoparaffin) outside the balloon, making the tension in the ropes and the balloon which enclose the scintillator manageable. The liquid levels of the LS and the buffer oil are carefully monitored to keep enough pressure inside the balloon to maintain the appropriate shape. To reduce background radiation in both the LS and the buffer oil, commercially available pure mineral oil and LS were purified with water extraction and nitrogen stripping [46], achieving uranium, thorium, and potassium concentrations of 3.5×10^{-18}g/g, 5.2×10^{-17}g/g, and less than 2.7×10^{-16}g/g, respectively. For more details on the LS, see [47].

An array of 1325 Hamamatsu RS7250 17-inch-diameter PMTs[3] and 554 Hamamatsu R3600 20-inch-diameter PMTs, is mounted inside the stainless steel vessel facing the center of the ID. The Hamamatsu RS7250 PMTs have better timing performance than the Hamamatsu R3600 PMTs. Also, 6 PMTs with 5-inch-diameter look down to the ID from the top of the detector. In this analysis, only the data collected with the Hamamatsu RS7250 PMTs are used for the ID signal giving a total photo-cathode coverage of approximately 22 %. These PMTs have a time resolution of approximately 3 ns, and the quantum efficiency of the PMTs is approximately 20 % for photons with wavelengths between 340 and 400 nm. The observed number of photo-electrons per MeV per PMT is approximately 0.2, therefore many PMTs observe no photo-electrons for typical events in a few MeV range. For proper operation of PMTs, a set of compensation coils encompassing the entire detector are used to reduce the terrestrial magnetic field.

Three thermometers were initially attached at the top, center, and bottom of a vertical line running slightly off the central axis of the detector. Radioactivity in the line and especially the three thermometers produced background events; therefore the line and thermometers were removed on April 19th, 2004. The periods before and after this date are defined as "period I" and "period II," respectively.

---

[3] The diameter of these PMTs is actually 20 inches, but the photo-cathodes are masked down to 17-inch diameter to improve their transit-time spread.

2.2 Outer Detector

The OD is a cylindrical water-Cherenkov cosmic ray veto detector, which surrounds the stainless steel vessel and contains approximately 3000 m^3 of pure water. Hamamatsu R3600 PMTs detect Cherenkov light produced by muons going through the OD. The OD also acts as an attenuator for neutrons and γs by reducing the number of these particles entering the ID from outside the detector. The water in the OD is circulated constantly to remove excess heat produced by PMTs in the ID and OD.

The OD has four sections: top, upper, lower, and bottom. The stainless steel containment sphere separates the top and upper sections from the lower and bottom sections. The PMTs in the top and bottom sections are attached on the ceiling and the floor of the OD, facing downward and upward, respectively. The PMTs in the upper and the lower sections are attached on the wall of the OD facing towards the cylindrical axis of the detector. The top, upper, lower, and bottom sections contain 50, 60, 60, and 55 PMTs, respectively. Tyvek®[4] plastic sheets optically separate each section of the OD. These sheets are highly reflective and line all inner surfaces of the OD to optimize light collection by the PMTs in each section.

2.3 Electronics and Data Acquisition

The system to record PMT data consists of three major components: the KamFEE (KamLAND Front-End Electronics) system, which includes 200 KamFEE boards[5], the trigger system, and the DAQ (Data AcQuisition) system. The main purpose of these components are that the KamFEE system acquires and digitizes PMT waveforms, the trigger system decides whether to record the data, and the DAQ system records the data. These three components communicate with each other as shown in Figure 2.2. The DAQ system sends various commands to the trigger system, such as run start and stop. The DAQ system also separately sends both the trigger system

---

[4] DuPont Tyvek® is a lightweight and durable material.

[5] Another set of redundant front-end electronics, called MACRO electronics, also record waveforms. However, the waveforms recorded with the MACRO electronics are not analyzed in this thesis.

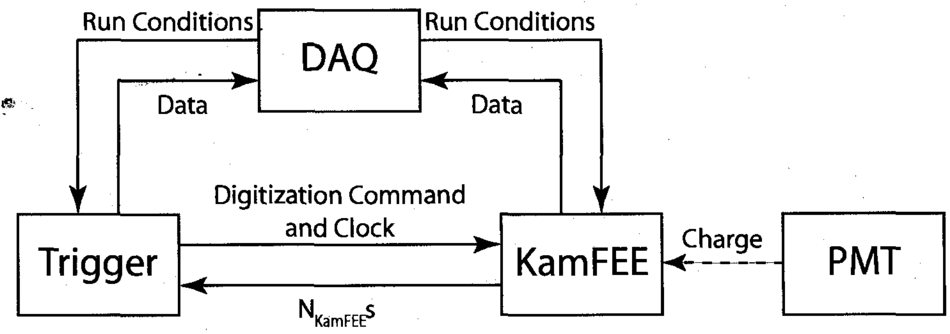

Figure 2.2: Schematic diagram of the communications among the electronics and the DAQ system.

and the KamFEE system run conditions which determine the behavior of these components during a run. The trigger board, a main part of the trigger system, has an internal 40 MHz clock signal, which is distributed to all the KamFEE boards to keep them synchronized with the trigger board. On each clock tick, each KamFEE board sends the trigger board the number of PMTs connected to it that had a positive signal in the last 125 ns, N_{KamFEE}. If the trigger board decides to record the data permanently, it generates a trigger record, and depending on which set of conditions are met, sends a waveform digitization command to the KamFEE boards. The DAQ system asynchronously reads out the trigger record and the waveform data.

2.3.1 KamLAND Front-End Electronics System

The KamFEE system consists of 10 VME crates, each of which holds twenty 9U VME KamFEE boards. Each KamFEE board processes input signals from 12 PMTs. Major components of a KamFEE board are amplifiers with three different gains, high ($\times 20$), medium ($\times 4$), and low ($\times 0.5$), providing the ability to measure a wide range in the number of photo-electrons (PEs), and ATWDs (Analog Transient Waveform Digitizers) to acquire and digitize waveforms.

Two ATWDs acquire waveforms from one PMT; when one ATWD is busy, the other can acquire a waveform, reducing dead-time. ATWDs start acquiring 128-sample-long waveforms when the waveform voltage exceeds a discriminator threshold. The DAQ system can adjust both the discriminator threshold and the sampling frequency. The sampling frequency for a normal run is typically set to approximately 0.65 GHz, making the length of a waveform approximately 200 ns. Each ATWD has 4 inputs and can simultaneously acquire 4 independent waveforms. The three waveforms from one PMT, after three different amplifications, use three of the four available ATWD inputs. A sinusoidal waveform derived from the 40 MHz clock signal feeds the remaining ATWD input and is used to calibrate the sampling time.

After completing the acquisition of waveforms, the ATWDs hold them for a predetermined duration of time, which is set to be 175 ns during a normal run. By the end of this time, if the KamFEE boards have not received the digitization command from the trigger board, the acquired waveforms are erased within approximately 1 μs, making the ATWDs available to acquire more waveforms. Alternatively, if the KamFEE boards receive a digitization command, they digitize the acquired waveforms with a 10-bit ADC, which takes approximately 30 μs. Waveforms in all three gains are recorded for high energy interactions such as muons going through the detector since the amplitudes of the high and medium gain waveforms for such events typically saturate the 10-bit ADC. On the other hand, only the waveforms in the high gain ATWD channels are recorded for events with energy in the MeV range, which provides less than a few photons per PMT. Each waveform is associated with a timestamp of when the KamFEE board received the digitization command from the trigger board, where timestamp is the number of clock ticks since the beginning of the run. The timestamp is used later to associate all the different waveforms and the trigger record from the same event. Each waveform also has an associated launch offset value, which is the number of clock ticks between when the ATWD started acquiring a waveform and when it received the digitization command from the trigger board.

2.3.2 Trigger Electronics System

The main components of the trigger system are a custom-built trigger processor board (trigger board) and a variety of ancillary components housed in a VME crate (trigger VME crate). The trigger board communicates with the DAQ system through modules in the trigger VME crate. The trigger command and clock signal are distributed to the KamFEE boards through other modules also in the trigger VME crate. In case the main DAQ system becomes overwhelmed due to high data rates, caused by a supernova explosion[6] for example, the trigger record is duplicated and independently recorded by the trigger backup DAQ system. For more information on the trigger backup DAQ system and the trigger system VME modules, see Appendix A. The trigger board also communicates with the absolute-time acquisition system (see Appendix C). This would be important in order to compare observations by KamLAND with those of other experiments in case of a global event, such as a supernova explosion.

The trigger board decides whether the data should be recorded. The conditions on which this decision is made are referred to as the "trigger type." For details on the various trigger types, see [27] and Appendix B. This decision is based on the enabled trigger types and thresholds, and the sum of all the N_{KamFEE}s in each section of the detector[7]: in the ID (N_{ID})[8], OD top (N_{ODtop}), OD upper (N_{ODupper}), OD lower (N_{ODlower}), OD bottom (N_{ODbottom}), and the chimney ($N_{5''}$). When the trigger board decides to record the data, it produces a trigger record consisting of the timestamp, the trigger type, and the values of N_{ID}, N_{ODtop}, N_{ODupper}, N_{ODlower}, N_{ODbottom}, and $N_{5''}$.

During normal data taking, the trigger board sends a digitization command to the KamFEE boards most often via a "prompt" trigger, defined to occur when N_{ID} goes above a threshold, set to 200 or 180, before and after April 13th, 2004, respectively. Similarly, the trigger board sends a digitization command to the KamFEE boards for each section of the OD when N_{ODtop}, N_{ODupper}, N_{ODlower}, or N_{ODbottom} goes over their respective thresholds. The trigger board sends the digitization commands back to KamFEE boards within ~400 ns from the time KamFEE boards calculate N_{KamFEE}s, on which the trigger board based its decision. This timing specification ensures the digitization commands to reach the KamFEE boards before they erase the acquired

---

[6] A typical supernova explosion is expected to produce a burst of neutrino events lasting for a few seconds.

[7] Although most of the decisions to record data are based on N_{KamFEE}s, some are strictly based on timing, such as the 1pps trigger and GPS trigger. For more details on trigger types, see [27] and Appendix B.

[8] N_{ID} does not include the number of Hamamatsu R3600 PMTs with a photon-hit in the ID.

waveforms. Some trigger types do not send a digitization command to KamFEE boards. The trigger board issues a "history" trigger, for instance, when N_{ID} goes above a history trigger threshold, usually set to 120, and while it remains above threshold for up to 8 consecutive clock ticks to keep track of the time evolution of N_{ID}. There are similar "OD history" triggers for each section of the OD. More detailed information on the trigger electronics system is available in [27], and Appendix A.

2.3.3 DAQ System

The main tasks of the DAQ system are to set run conditions for the trigger system and the KamFEE system, to readout the data from these systems, to record them on the data storage disk, and to provide the user interface for run control and configuration. The DAQ software used for the KamLAND experiment is called KiNOKO (KiNOKO is Network distributed Object oriented KamLAND Online system). KiNOKO is a networked parallel processing system installed on 15 front-end computers, which asynchronously read data from 15 VME crates (10 for reading out all KamFEE boards, 1 for the trigger system, and 4 for the MACRO electronics[9]). The data is then transfered to a back-end computer which is also controlled by KiNOKO. In this back-end computer, KiNOKO performs a simple online analysis on the readout data. The data flow rate from each VME crate, for example, is calculated at this stage. Another important quantity that KiNOKO calculates is $N_{\mathrm{Max\,ID}}$, defined to be the maximum N_{ID} in the consecutive trigger records obtained via history triggers in an event. Similarly, KiNOKO also calculates the maximum N_{ODtop}, N_{ODupper}, N_{ODlower} and N_{ODbottom} using history triggers for the corresponding OD section. After calculations of these and other quantities, KiNOKO displays them in histograms and graphs, which can be used to monitor data taking realtime. A detector operator can start or stop a run through KiNOKO, where a run is a period of continuous data taking typically lasting 24 hours. During a run start procedure, the electronics devices are configured through KiNOKO. For more details on KiNOKO, see [28].

---

[9] Another set of redundant front-end electronics that are not used in this thesis.

2.4 Detector Calibration

Radioactive sources with known energies are deployed into the ID through a small opening in the ID chimney. Before December 2005, all deployments were performed along the central vertical axis (z-axis) of the detector, and the positions of the radioactive sources along this axis were known within a few mm. In December 2005, a so-called "4-π" system was commissioned, which can deploy radioactive sources at positions away from the vertical axis. The 4-π system deploys pole segments connected to form a straight shaft. The number of pole segments and the angle at which the pole is deployed can be adjusted. Each pole segment is equipped to hold a radioactive source. Although the absolute position of the poles, and therefore the sources, are not precisely known, the distances between the sources in the pole segments are known to within a few mm.

The energies and types of radioactive sources which have been deployed in the ID are listed below:

- ^{203}Hg produces 0.279 MeV γs.
- ^{68}Ge produces e^+s, each of which annihilates with an e^- inside the source containment capsule producing two 0.511 MeV γs.
- ^{65}Zn produces 1.116 MeV γs.
- ^{60}Co produces two γs at 1.173 MeV and 1.332 MeV in very short temporal coincidence.
- ^{60}Co^{68}Ge is a composite source that contains ^{60}Co and ^{68}Ge in the same capsule. To reduce the detector dead-time and the risk of introducing radioactive impurity in the detector due to calibration runs, these sources are combined and deployed together.
- ^{241}Am^{9}Be produces mainly three types of events [48]:
    - Neutrons with kinetic energies between ~5.5 and ~11 MeV.

- Pairs of a 4.439 MeV γ and a neutron with kinetic energy between ~1.5 and ~6.5 MeV, emitted simultaneously.
- A 4.439 MeV γ, a 3.215 MeV γ, and a neutron with kinetic energy below ~3 MeV, emitted simultaneously.

The neutrons produced from the ^{241}Am^{9}Be source in the LS lose their kinetic energy primarily via elastic scattering with protons. The scattered protons produce scintillation light in the LS, that is quenched because of the high ionization density (see Section 3.4). If the neutrons have enough energy, they can also lose energy via inelastic scattering on ^{12}C in the LS, which produces 4.439 MeV γs. The free neutrons eventually capture on protons or ^{12}C, producing 2.223 MeV and 4.945 MeV γs, respectively.

Chapter 3

Event Reconstruction

The light produced in the ID by scintillation and Cherenkov radiation from ionizing particles and muons is viewed by the PMTs. The energies and positions of point-like events or muon tracks must be calculated from these PMT signals. The first step in reconstructing events is to associate all of the asynchronously read-out waveforms and the trigger record with the same timestamp as an event. This is performed offline in software. After all the information from each event is grouped, the pulses in the waveforms are identified, and their times and charges are calculated. These times and charges are then used by the position, energy, and muon track finding algorithms. These algorithms are tested using various methods, typically based on deployed radioactive sources or naturally occurring radioactivity in the detector.

3.1 Pulse Time and Charge

The arrival time and charge of pulses are extracted from each waveform in an event using two different methods; the Small Pulse Analyzer (SPA), ideal for waveforms containing small pulses from low energy events, and the Large Pulse Analyzer (LPA), ideal for waveforms containing large pulses from muons.

At the beginning of a run, 50 waveforms from all ATWDs are recorded at a fixed frequency, rather than based on N_{ID}, and are therefore unlikely to contain any pulses. From these "empty" waveforms, fixed fluctuations characteristic to each

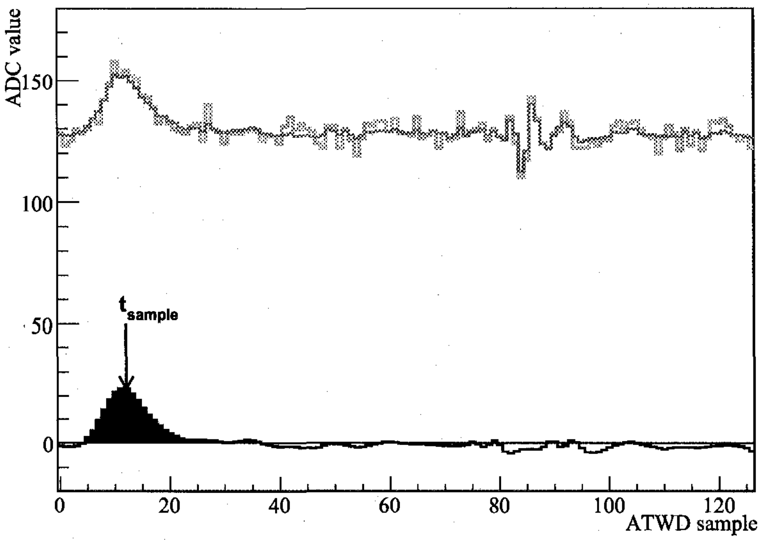

Figure 3.1: An example of a raw waveform (light thick gray line), ATWD-fluctuation-subtracted waveform (dark gray line), and fully corrected waveform (black line) containing one small pulse. The filled area represents the charge of the pulse, and t_{sample} indicates the pulse time calculated by the SPA, which is defined to be the time when the waveform reaches its maximum height for a small pulse.

ATWD sample are obtained. These ATWD fluctuations are then subtracted from the raw waveforms in the remainder of the run. Figure 3.1 shows an example of a waveform. The light thick gray line indicates the raw waveform, and the dark gray line indicates the waveform after subtracting the ATWD fluctuation.

Each waveform is offset from zero ADC value even when there is no photon signal. This ADC offset varies for each waveform and needs to be properly subtracted to accurately estimate the charge of the pulse in the waveform. The SPA calculates the ADC offset by iteratively calculating the mean ADC value and removing extreme samples until the difference between the mean and the highest remaining ADC value equals the difference between the mean and the lowest remaining ADC value within an accuracy of 2.5 %. The ADC offset of the waveform is the mean ADC value of the remaining samples. This method fails for waveforms containing a larger pulse whose height does not return to zero by the end of the ~200 ns waveform window. For this reason, the LPA calculates the ADC offset by taking the mean of the first 10 ATWD samples, which are unlikely to contain a pulse. For both the SPA and the LPA, after the ADC offset is subtracted from the ATWD-fluctuation-subtracted waveform, it is smoothed using a Savitzky-Golay filter [49], which removes high frequency components while tending to preserve the maxima, the minima, and the width. The black line in Figure 3.1 shows an example waveform after all of these corrections are applied.

Next, "pulses" are defined, and their charges and times are extracted. The SPA defines each contiguous area above zero as a pulse as long as that area is greater than 15 % of the waveform's total area above zero. The 15 % cut is chosen to reduce misidentification of noise as pulses. The LPA defines the entire waveform to be one pulse.

The area of each pulse gives a measure of its charge, in units of ADC value × ATWD samples. To avoid underestimating the charge of a pulse by using a waveform with a truncated amplitude, the charge of a pulse is calculated using the corrected waveform from the lowest gain recorded for a particular signal. To calculate the number of PEs, the charge is divided by the $1\,PE$ equivalent charge (q_0) of each ATWD obtained from calibration runs with the ^{60}Co source deployed at the center of the detector. The q_0s are updated every few weeks.

The total PEs in an event is defined as $N_{PE\,\mathrm{ID}}$, and the RMS of PMT-to-PMT PE variation, $RMS_{PE\,\mathrm{ID}}$, is given by

$$RMS_{PE\,\mathrm{ID}} = \sqrt{\sum_{i}^{N} \frac{(PE_i - \langle PE \rangle)^2}{N}}, \tag{3.1}$$

where N denotes the number of PMTs with at least one pulse, PE_{i} denotes the PE of the ith PMT, and $\langle PE \rangle$ denotes the average PE for all PMTs with at least one pulse in the event. These two variables, $N_{PE\,\mathrm{ID}}$ and $RMS_{PE\,\mathrm{ID}}$, are used to classify event types, particularly muons (see Section 3.6).

The times of pulses are always calculated from the waveforms from the high gain since this provides consistency across the wide range of signal amplitudes. The SPA defines the time of a pulse, t_{sample}, in units of number of ATWD samples from the start of the waveform, to be the peak of the second-order polynomial fit to the corrected waveform from the lowest gain recorded for a particular signal. On the other hand, the LPA defines the time of a pulse to be the time when the corrected waveform from the high gain crosses 50 ADC value. Since each waveform in an event can be recorded at different time, the pulse time needs to be given with respect to the arrival of the trigger command, which should be the same for all ATWDs. The sampling durations differ slightly among all the ATWDs, so actual duration between the beginning of the waveform and the time of a particular sample differ depending on the ATWDs. The relative timing of each pulse with respect to the time of the trigger command is given by

$$t_{\mathrm{relative}}\,[\mathrm{ns}] = t_{\mathrm{sample}} \times p_{\mathrm{sample}}\,[\mathrm{ns/sample}] - N_{\mathrm{launch}} \times 25\,\mathrm{ns} + t_0\,[\mathrm{ns}], \tag{3.2}$$

where p_{sample} denotes the duration of one ATWD sample in ns, N_{launch} denotes the launch offset (see Section 2.3.1), and t_0 denotes the timing correction for each ATWD due to the signal travel time differences caused by slight differences in each cable length or behavior in each KamFEE channel. p_{sample} is calibrated for each ATWD at the start of each run using the 40 MHz clock signal feed into the fourth ATWD input as described in Section 2.3.1. t_0 for each ATWD is measured with the ^{60}Co source deployed at the center of the detector and updated every few weeks.

3.2 Position Reconstruction

The event position is reconstructed in two major steps; a rough estimation is made using the PE distribution among the PMTs, then fine tuning is done using the times that the photons take to travel in a straight line from the event position to the PMTs. The times and PEs of the pulses used in these steps are estimated with the SPA.

In the first step, the rough estimation of the event position is calculated from the average of all the PMT positions weighted by the PEs, and the estimated position vector from the center of the detector is multiplied by the empirical correction factor of 1.62. The factor 1.62 is chosen by comparing the estimated positions with the actual positions of the ^{60}Co source deployed along the vertical central axis of the detector. Due to this factor, events at large radius are sometimes estimated to be outside of the ID by this first step. If the estimated radius exceeds 8.5 m, the estimated position is forced to the radius of 8.5 m in the same direction with respect to the center of the ID.

During the second step, the event position is fine-tuned in multiple iterations. The event position is adjusted using

$$\delta t = t_{\text{arrival}} - t_{\text{travel}}, \tag{3.3}$$

the difference between the actual photon arrival time, t_{arrival}, and the estimated photon travel time t_{travel}, for the current estimated event position. t_{travel} is calculated using the effective speeds of light in the LS and buffer oil of 196.1 mm/ns and 220 mm/ns, respectively. These effective speeds of light are empirically adjusted to minimize the reconstructed position bias for radioactive sources deployed along the central vertical axis. The index of refraction measured to be 1.45 as described in Section 2.1 corresponds to a phase velocity of 207 mm/ns. However, PMTs detect individual photons that propagate at the wave-packet group velocity, approximately 195 mm/ns. This group velocity is close to the adjusted effective speed of light in the LS. The accuracy of the reconstructed positions is much more sensitive to the effective speed of light in the LS than that in the buffer oil. The difference between the measured and the adjusted effective speed of light in the buffer oil might be due to the inaccuracy in the model used in the position reconstruction algorithm, such as ignoring refraction at the boundary between the LS and the buffer oil.

The algorithm uses photons most of which reach the PMTs directly, i.e., without absorption and re-emission, by selecting pulses in a 15 ns window around the peak of δt distribution, as shown in Figure 3.2. During each iteration, the estimated event position is pushed by a distance in a direction that reduces the width of the δt distribution in this 15 ns peak window. The event position reconstruction algorithm has seven possible exit statuses for each event, "valid" for a successful fit, and six other statuses for a fit that failed for various reasons, such as too few pulses in the

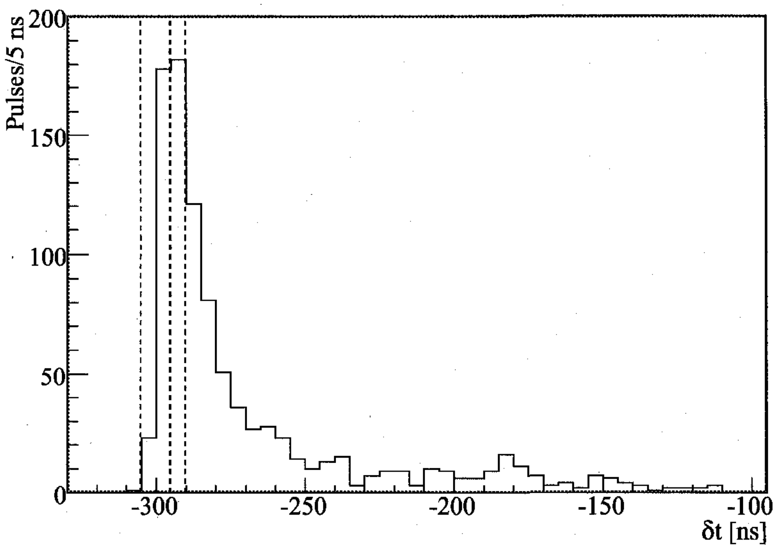

Figure 3.2: An example of the δt distribution for an event. The position finding algorithm uses the pulses between the thin vertical dotted lines. The thick vertical dotted line indicates the mean δt of these pulses.

event. Most of the events with a failed position reconstruction are caused by very low energy point-like events which do not produce enough photons or noise caused by muons, such as after-pulses in the PMTs and multiple signal reflections in the PMT cables. For more details on the position reconstruction algorithm, see Appendix D.

The performance of the event position finding algorithm is evaluated with radioactive sources, with energies in the range of ~1 MeV to ~5 MeV, deployed at various known positions from -5.5 m to 6 m along the central vertical axis. Figure 3.3 shows the biases and RMS's of the reconstructed positions in the vertical direction for ^{68}Ge, ^{65}Zn, ^{60}Co, and ^{241}Am^{9}Be. The biases for these sources within a 5.5 m radius along the vertical axis are less than 5 cm, and the RMS's are within 30 cm.

The data from various source deployments off the vertical axis using the 4-π system confirm that the reconstructed position biases at various radii and angles from the center of the detector are all less than ~5 cm within the fiducial volume radius of 5.5 m (see Section 5.3.3). For more details on the 4-π calibration results, see [50].

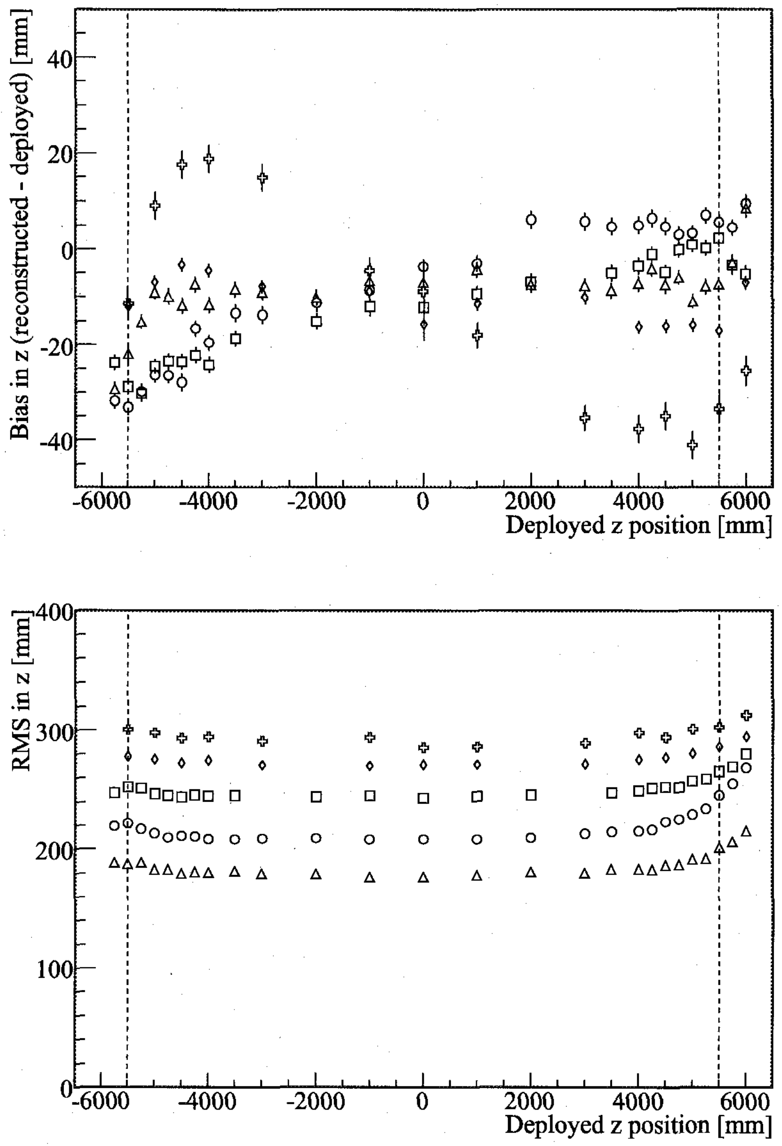

Figure 3.3: Reconstructed position biases (top plot) and *RMS*'s (bottom plot) for events from various radioactive calibration sources deployed along the vertical central axis. The biases are taken from the differences between the mean of the reconstructed positions and the source deployment positions in the z-direction. The dotted vertical lines indicate the fiducial volume radius of 5.5 m (see Section 5.3.3). The sources displayed here are ^{68}Ge (circle), ^{65}Zn (square), ^{60}Co (triangle), ^{241}Am^{9}Be 2.223 MeV γ (diamond), and ^{241}Am^{9}Be 4.439 MeV and 4.945 MeV γ (cross).

3.3 Visible Energy Reconstruction

The visible energy, E_{vis}, is based on the number of photons produced in an event. Given the observed PEs and the event position, E_{vis} is determined by considering the following effects:

- The higher the E_{vis} of an event, the more photons are produced, and the more PEs each PMT produces on average.
- The PMTs closer to the event produce more PEs because their photo-cathodes have a larger solid-angle with respect to the event position.
- The PMTs far from the event position produce less PEs due to light attenuation in the LS and the buffer oil. This attenuation is modeled as an exponential decay in the number of PEs as a function of the distance between the event and the PMT positions. The attenuation length is tuned based on calibrations using radioactive sources at varying distances from the PMTs.
- There is a probability distribution of observed number of PEs from a particular PMT, for a given expected number of PEs in the same PMT.
- There is a small probability that each PMT observes background photons.
- If the event of interest occurs soon after another event, there is a finite probability that some ATWDs are not available to record the PMT signal since they are busy recording the previous event.

E_{vis} is estimated by maximizing the likelihood for observing the observed PE distribution. The E_{vis} reconstruction process returns one of three possible statuses: "valid" for a successful fit, "unknown" for an event having too few PMT signals, and "not valid" for a failed fit.

The performance of the event E_{vis} finding algorithm is evaluated using radioactive sources with energies in the range of ~1 MeV to ~5 MeV, deployed at various known positions from -5.5 m to 6 m along the vertical central axis. Figure 3.4 shows the reconstructed E_{vis} deviations with respect to that at the center for ^{68}Ge, ^{65}Zn, ^{60}Co,

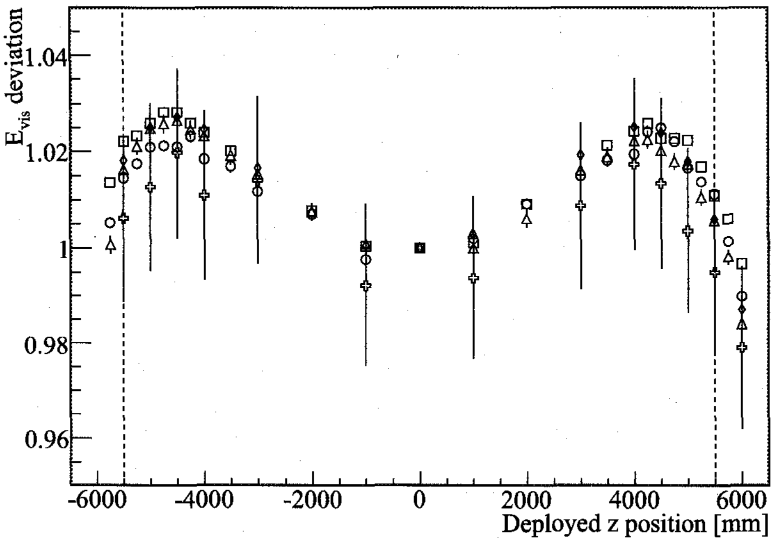

Figure 3.4: Reconstructed $E_{\rm vis}$ deviations for events from various radioactive calibration sources deployed along the vertical central axis. The deviation is the ratio of the reconstructed $E_{\rm vis}$ compared to the reconstructed $E_{\rm vis}$ at the center. The dotted vertical lines indicate the fiducial volume radius of 5.5 m (see Section 5.3.3). The sources displayed here are ^{68}Ge (circle), ^{65}Zn (square), ^{60}Co (triangle), ^{241}Am^{9}Be 2.223 MeV γ (diamond), and ^{241}Am^{9}Be 4.945 MeV γ (cross). The long error bars are from the ^{241}Am^{9}Be 4.945 MeV γ events. All the other error bars are comparable to or smaller than the size of the markers.

and ^{241}Am^{9}Be source events along the vertical axis. The deviation shown an "M"-shaped structure as a function of the z positions, which is less than ~3 % within the ±5.5 m range.

The data from various source deployments off the vertical axis using the 4-π system confirm that the $E_{\rm vis}$ deviations at various radii and angles from the center of the detector are all less than ~3 % [50].

3.3.1 Visible Energy Reconstruction Bias after Muons

The reconstructed $E_{\rm vis}$ is slightly shifted after muons since muons deposit large amount of charge in the PMTs, shifting the baseline of the electronics for a while. The mean reconstructed $E_{\rm vis}$ of the ^{60}Co events between 0.8 ms and 1.2 ms after muons is

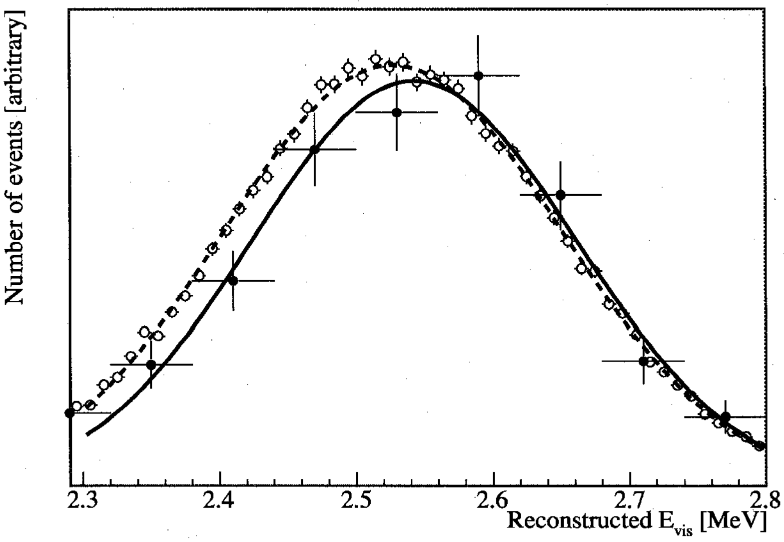

Figure 3.5: Reconstructed E_{vis} distribution for ^{60}Co events chosen from 0.8 ms to 1.2 ms after muons (filled marker) and from 100 ms and 1 s after muons (open marker). A Gaussian is fitted to each of the distributions. The fit to the distribution with the filled markers (solid curve) yields a mean and sigma of 2.5427 ± 0.0064 MeV and 1.1866 ± 0.0063 MeV, respectively, and a $\chi^2/n.d.f.$ of 3.5/5. The fit to the histogram with the open markers (dotted curve) yields a mean and sigma of 2.52713 ± 0.00055 MeV and 0.12341 ± 0.00052 MeV, respectively, and a $\chi^2/n.d.f.$ of 41.9/47.

2.5427 ± 0.0064 MeV while that of events more than 100 ms after muons is 2.52713 ± 0.00055 MeV, as shown in Figures 3.5, corresponding to a bias of 0.62 ± 0.25 %. The reconstructed E_{vis} is more biased if the events that follow muons in shorter times are included. The mean reconstructed E_{vis} of the ^{60}Co events between 0.2 ms and 1.2 ms after muons is 2.5452 ± 0.0042 MeV, corresponding to a bias of 0.72 ± 0.17 %

3.4 Real Energy and Visible Energy

The real energy, E_{real}, of a particle is defined to be the total kinetic energy of the particle. For a positron, E_{real} is its kinetic energy plus 1.022 MeV from the two γs produced in its annihilation with an electron. The light output from an event with a given E_{real} varies due to the effects of light quenching and Cherenkov radiation.

The visible energy, E_{vis}, incorporates these effects and is calculated based on the number of photons produced in an event. A model to convert E_{real} to E_{vis} for each particle type, γ, α, p, and e^+, is developed by using Monte Carlo simulations and by incorporating light quenching and Cherenkov radiation effects [51]. This model is used to convert expected E_{real} spectra of positrons produced in inverse β-decays from $\bar{\nu}_{\text{reactor}}$s and $\bar{\nu}_{\text{geo}}$s, as well as theoretically calculated E_{real} spectra of other background events, into expected E_{vis} spectra.

Light quenching occurs when a highly ionizing particle saturates the scintillation photon production. Birks' law [52], $\frac{dE_{\text{vis}}}{dx}$, empirically describes the amount of E_{vis} deposited in distance dx and is given by

$$\frac{dE_{\text{vis}}}{dx} = \frac{\frac{dE_{\text{real}}}{dx}}{1 + k_b \frac{dE_{\text{real}}}{dx}}, \tag{3.4}$$

where $\frac{dE_{\text{real}}}{dx}$ denotes the stopping power, and k_b denotes Birks' constant, which is assumed to be energy and particle independent. For a particle with a large stopping power, $\frac{dE_{\text{vis}}}{dx}$ saturates at $1/k_b$. The fractional-E_{vis} loss due to quenching of scintillation light as a function of E_{real}, $\delta_q(E_{\text{real}})$, is obtained from a Monte Carlo simulation for each particle type. α particles are ideal for determining k_b since they do not produce Cherenkov light and have a large stopping-power, making E_{vis} sensitive to k_b.

Cherenkov light is produced when a charged particle is traveling in a dielectric medium faster than the speed of light in that medium. The amount of Cherenkov light produced is proportional to the velocity of the charged particle. The Cherenkov radiation contribution to E_{vis} is modeled with $k_C \delta_C (E_{\text{real}})$, where k_C denotes a scaling factor for the Cherenkov radiation contribution which does not depend on E_{real} or particle type, while $\delta_C(E_{\text{real}})$, which is obtained from a Monte Carlo simulation for each particle type, depends on E_{real}.

The relationship between E_{real} and E_{vis} is modeled by

$$\frac{E_{\text{vis}}}{E_{\text{real}}} = a_0 \left[1 - \delta_q(E_{\text{real}}) + k_0 \delta_0 (E_{\text{real}}) + k_C \delta_C (E_{\text{real}})\right], \tag{3.5}$$

where a_0 denotes an overall scaling, $\delta_0(E_{\text{real}})$ denotes the amount of E_{vis} lost during

Table 3.1: Energy calibration points. The central values are measurements at the center of the ID, and the errors include temporal and spatial variations. ^{68}Ge and ^{60}Co produce two γs in an event, so the E_{real} and the E_{vis} for these events are divided by two. Unlike other calibration sources, ^{12}C(n,γ)^{13}C, ^{214}Po(0,^{4}He)^{210}Pb, and ^{212}Po(0,^{4}He)^{208}Pb are distributed throughout the ID, and the central values are estimated by selecting only the events reconstructed near the center of the ID. The details of each calibration point measurement are described in Appendix E.

Calibration	E_{real} [MeV]	Reconstructed E_{vis} [MeV]
^{203}Hg	0.2791967	0.2400 ± 0.0055
^{68}Ge	$(1.022006)/2$	$(0.923 \pm 0.013)/2$
^{65}Zn	1.115539	1.1031 ± 0.0082
^{1}H(n,γ)^{2}H (from ^{241}Am^{9}Be)	2.22457	2.333 ± 0.025
^{60}Co	$(2.50572)/2$	$(2.5057 \pm 0.0093)/2$
^{12}C(n,γ)^{13}C	4.946431	5.407 ± 0.064
^{214}Po(0,^{4}He)^{210}Pb	7.68682	0.6201 ± 0.0097
^{212}Po(0,^{4}He)^{208}Pb	8.78486	0.814 ± 0.014

Table 3.2: Fitted energy parameters.

Parameter	Best-fit value
a_0	1.061 ± 0.024
k_b	$0.00971 \pm 0.00027 \mathrm{g\,cm^{-2}\,MeV^{-1}}$
k_0	0.84 ± 0.14
k_C	0.43 ± 0.11

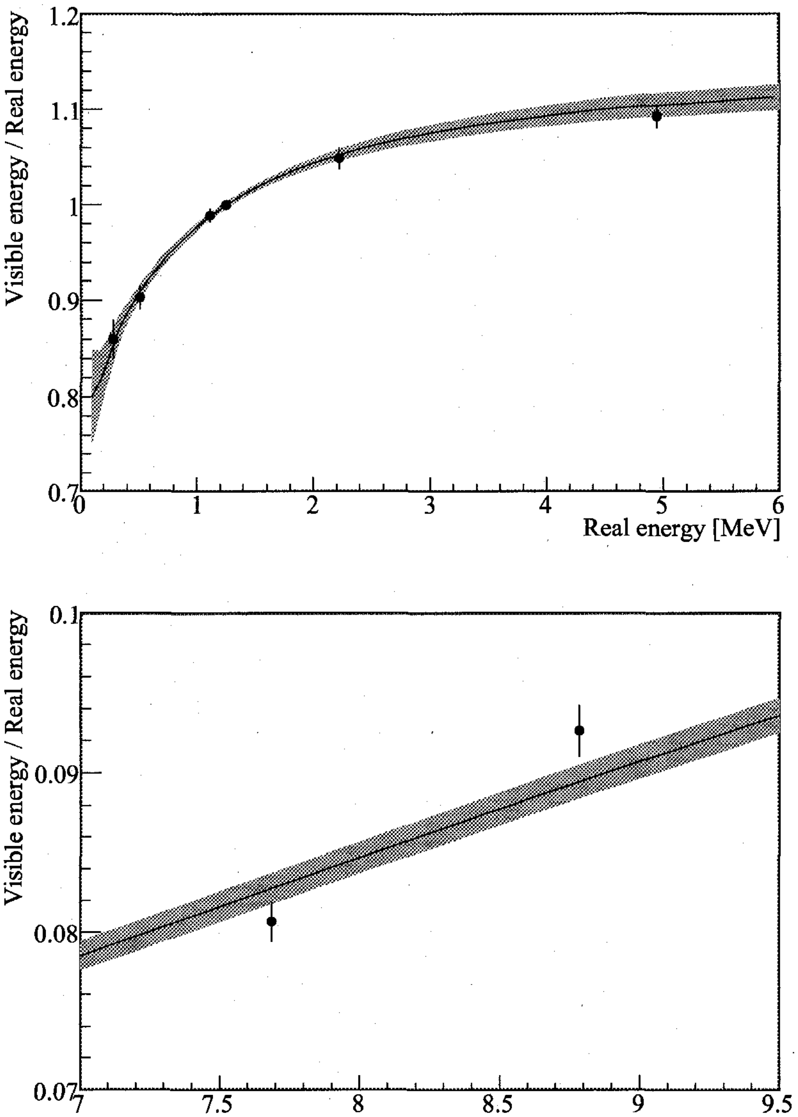

Figure 3.6: $E_{\mathrm{vis}}/E_{\mathrm{real}}$ for γs (top plot) and α particles (bottom plot). A simultaneous fit produces the best-fit $E_{\mathrm{vis}}/E_{\mathrm{real}}$ relations shown in the line. The gray bands represent the values allowed by the $1\,\sigma$ errors in k_b, k_{O}, and k_C. The $\chi^2/n.d.f.$ of this fit is 7.1/4.

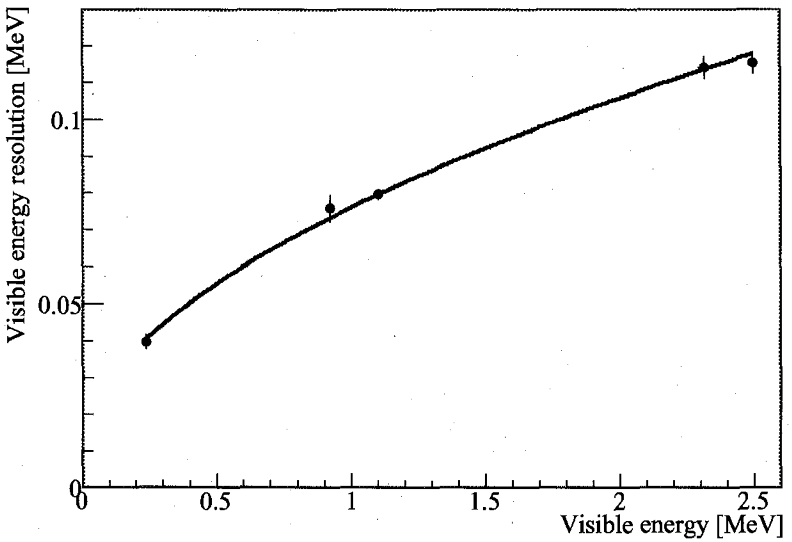

Figure 3.7: E_{vis} reconstruction resolutions for γ energy calibration points. The data points are ^{203}Hg, ^{68}Ge, ^{65}Zn, ^{1}H(n,γ)^{2}H, and ^{60}Co from left to right. Equation 3.6 is fitted to the data points. The fitted σ_0 and σ_1 are 0.0176 ± 0.0053 MeV and 0.0736 ± 0.0014 MeV, respectively. The $\chi^2/n.d.f.$ of this fit is 1.3/3.

the calculation of the quenching correction due to the finite particle tracking threshold in the Monte Carlo simulation, and k_0 denotes an energy and particle-type independent parameter that recovers the lost energy in the Monte Carlo. E_{vis} is defined and calibrated to have the same value as E_{real} at (2.501/2) MeV, the average of two γ energies from the ^{60}Co calibration source. The four "energy parameters," a_0, k_b k_0, and k_C, are obtained by fitting Equation 3.5 to the reconstructed E_{vis} values of various event types with known E_{real} values, summarized in Table 3.1. The best-fit energy parameter values are given in Table 3.2, and Figure 3.6 shows the best-fit $E_{\text{vis}}/E_{\text{real}}$ curves for γ and α particles.

To account for the reconstruction resolution, a Gaussian smearing is applied to the E_{vis} obtained with Equation 3.5. The width of the Gaussian, $\sigma_{E_{\text{vis}}}$, is modeled by

$$\sigma_{E_{\text{vis}}}^2 = \sigma_0^2 + \sigma_1^2 \frac{E_{\text{vis}}}{1\,\text{MeV}}, \tag{3.6}$$

where σ_0 accounts for the background photons, and σ_1 accounts for the statistical fluctuations in the number of photons observed from the event of interest. σ_0 and σ_1 are estimated using the E_{vis} reconstruction resolutions for γ energy calibration points from ^{203}Hg, ^{68}Ge, ^{65}Zn, ^{1}H(n,γ)^{2}H, and ^{60}Co, as shown in Figure 3.7. The fitted σ_0 and σ_1 are 0.0176 ± 0.0053 MeV and 0.0736 ± 0.0014 MeV, respectively.

3.5 Muon Track Reconstruction

Muons going through the detector produce a large amount of light by scintillation in the LS and Cherenkov radiation in both the LS and the buffer oil. The muon track reconstruction algorithm uses the arrival time distribution of the first photons that hit each PMT. This algorithm uses the times of the pulses estimated by the LPA.

Cherenkov light is emitted at a constant angle, θ, with respect to the muon track, forming the shape of a forward opening cone. Assuming that muons pass through the detector at the same speed as that of light in vacuum, θ is given by [53],

$$\cos\theta = \frac{1}{n}, \tag{3.7}$$

where n denotes the index of refraction in the LS and the buffer oil; although the LS and the buffer oil have slightly different values of n's, for simplicity, a single value of 1.45 is used for both. Although the scintillation light is emitted isotropically, the first scintillation photons to reach each PMT from a muon track are emitted at the same angle as the Cherenkov light.

For a given muon track, the arrival time of the first photon, t_{first}, that travels directly from the track is estimated for each PMT. The probability for ith PMT to have $\delta t_{\mathrm{first}\,i}$, the difference between t_{first} and the actual first photon arrival time, $P\left(\delta t_{\mathrm{first}\,i}\right)$, is modeled with a Gaussian function with an exponential tail and a 1 % contribution from uncorrelated pulses. The Gaussian function accounts for the jitter in the direct light arrival times, and the exponential tail accounts for the indirect light arrival times from the muon. The track is fitted by maximizing the likelihood (L_μ) for the observed t_{first} distribution. The muon track is rejected if the final $\chi^2 = -2\log L_\mu$

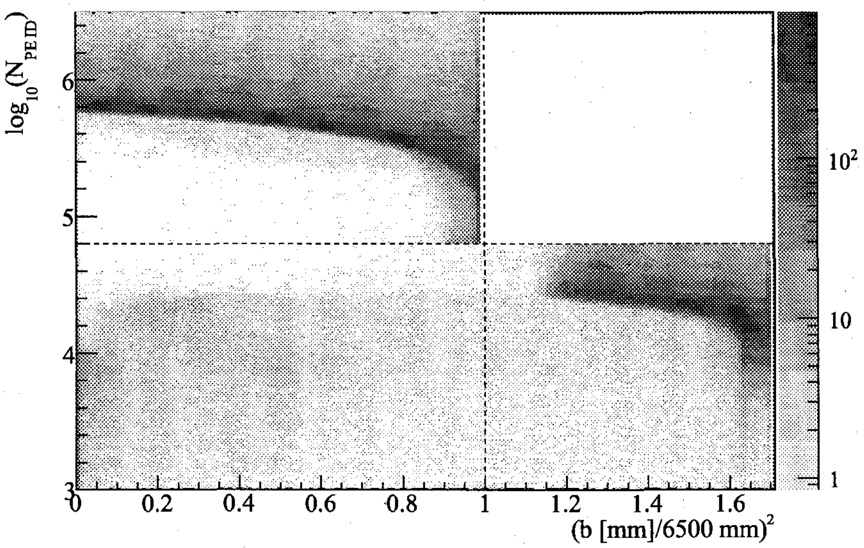

Figure 3.8: Distribution of reconstructed muon track impact parameter, b, versus $N_{PE\,\mathrm{ID}}$. The vertical dotted line indicates the radius of the balloon, assumed to be spherical. The horizontal dotted line indicates the $N_{PE\,\mathrm{ID}}$ threshold for LS muon event tag (see Section 3.6).

is poor. The algorithm converges in finding ~99 % of muon tracks with reasonable χ^2.

Figure 3.8 shows the distribution of $N_{PE\,\mathrm{ID}}$ and reconstructed muon track impact parameter, b, defined to be the shortest distance between the muon track and the center of the ID. Muons with $b < 6.5\,\mathrm{m}$ go through the LS producing both scintillation and Cherenkov light, resulting in much larger $N_{PE\,\mathrm{ID}}$ than muons with $b > 6.5\,\mathrm{m}$ which produce only Cherenkov light.

3.6 Event Tag and Multiplets

After events are reconstructed, each event is tagged according to the event type selection cuts using variables, such as $N_{\mathrm{Max\,ID}}$, $N_{\mathrm{Max\,OD}}$ (the sum of maximum N_{ODtop}, N_{ODupper}, N_{ODlower} and N_{ODbottom}, see Section 2.3.3), $N_{PE\,\mathrm{ID}}$, and $RMS_{PE\,\mathrm{ID}}$ (see Section 3.1). An event can be tagged as multiple event types if it satisfies all the conditions for these event types (see Table 3.3). Then all events are organized into multiplets, grouping events in temporal coincidences. All events within 1.5 ms of another event are recorded into a multiplet. An event is added to the same multiplet if the time since the last event in the multiple is less than 1.5 ms. Alternately, if an event and its preceding event are more than 1.5 ms apart, then a new multiplet is created with the event as the first entry in the multiplet.

Table 3.3: Some of the important event tags used in this analysis.

Tag	Conditions
Flasher	$N_{PE\,\mathrm{ID}} > 10^3$
	$RMS^2_{PE\,\mathrm{ID}}/N_{PE\,\mathrm{ID}} > 2$
OD Muon	$N_{\mathrm{Max\,OD}} \geq 10$
$N_{\mathrm{Max\,ID}}$ Muon	$N_{\mathrm{Max\,ID}} \geq 1250$
Oil Muon	Not tagged as a LS Muon or Flasher
	$N_{PE\,\mathrm{ID}} > 10^3$
	$RMS^2_{PE\,\mathrm{ID}}/N_{PE\,\mathrm{ID}} > 0.015$
LS Muon	$N_{PE\,\mathrm{ID}} > 10^{4.8}$
	OR[a]
	$N_{PE\,\mathrm{ID}} = 0$
	OD-to-ID trigger type (see [27])
	Tagged as a $N_{\mathrm{Max\,ID}}$ Muon
Shower Muon	$N_{PE\,\mathrm{ID}} > 7 \times 10^5$
ID Muon	Tagged as a LS Muon or Oil Muon
Muon	Tagged as an ID Muon or OD Muon
Post Muon Noise	Less than 50 μs since last LS Muon
	$N_{PE\,\mathrm{ID}}$ is less than that of the last LS Muon
High $N_{PE\,\mathrm{ID}}$	$N_{PE\,\mathrm{ID}} \geq 5000$
	Not tagged as ID Muon
Gap	Longer than 100 ms since the previous trigger record

---

[a] The following cuts are only applied for all the runs before run 1313, the period when the OD-to-ID triggers (see [27]) did not properly send a waveform digitization command to KamFEE.

Chapter 4

Cosmogenic Spallation Products

Pions created by cosmic rays in the upper atmosphere decay into muons, which can reach KamLAND. These muons, having very high energies, can activate the detector material producing unstable nuclei by spallation processes while going through the detector. These "spallation products" can represent important background events to inverse β-decay detection, but can also be useful to estimate various systematic errors in this analysis due to their uniform distributions in the ID. If half-lives are short, they are easily identifiable since they are produced in coincidence with muons. The detector response for high energy events is studied using ^{12}B β-decays, which have a relatively high endpoint energy. Spallation neutrons yield the mean neutron capture time and the detector response at the neutron capture energy, both of which are important since neutrons represent the tag for the inverse β-decay. In terms of background events, both high energy neutrons produced outside the detector entering the LS and ^{9}Li β-decays produce spatially and temporally correlated events that mimic inverse β-decays and its subsequent neutron capture.

4.1 ^{12}B

Cosmic muons going through the detector produce radioactive ^{12}B through reactions with ^{12}C in the LS [54]. ^{12}B β-decays into the stable ^{12}C with a half-life of 20.20 $\pm$ 0.02 ms and an endpoint energy of 13.4 MeV. These ^{12}B β-decays can serve as an

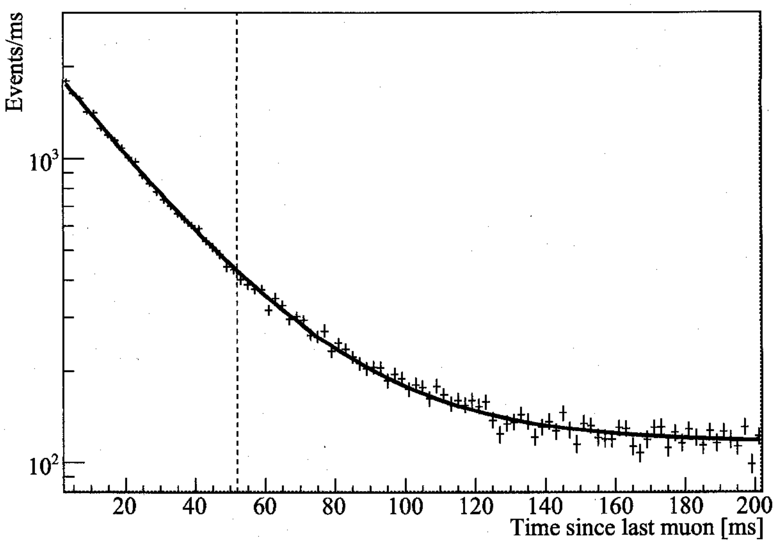

Figure 4.1: The ^{12}B β-decay decay time distribution. An exponential function plus a constant (solid line) is fitted to the data, which yields a ^{12}B half-life of 20.59 ± 0.18 ms with a $\chi^2/n.d.f.$ of 97.5/97. The left and right side of the dotted vertical line is the window from which ^{12}B β-decay candidates and background events are selected, respectively.

analysis tool, particularly to assess the E_{vis} and position reconstruction algorithm performances. ^{12}B β-decay candidates are selected based on this half-life and the expected E_{vis} spectrum[1].

Figure 4.1 shows the distribution of the time difference between a ^{12}B β-decay candidate and the previous muon. This distribution yields a half-life of 20.59 ± 0.18 ms, which is compatible with the nominal ^{12}B half-life of 20.20 ± 0.02 ms. The tail of the distribution is due to background events, which are uncorrelated with muons.

Figure 4.2 shows the background-subtracted E_{vis} distribution of ^{12}B β-decay candidates, where the ^{12}B signal and the background events are taken from time windows, 2 ms to 52 ms and 52 ms to 202 ms after associated muons, respectively. Figure 4.2 also shows the overlaid expected E_{vis} spectrum, normalized to the number of entries.

---

[1] For details on other ^{12}B β-decay identification cuts, see Appendix F.1.

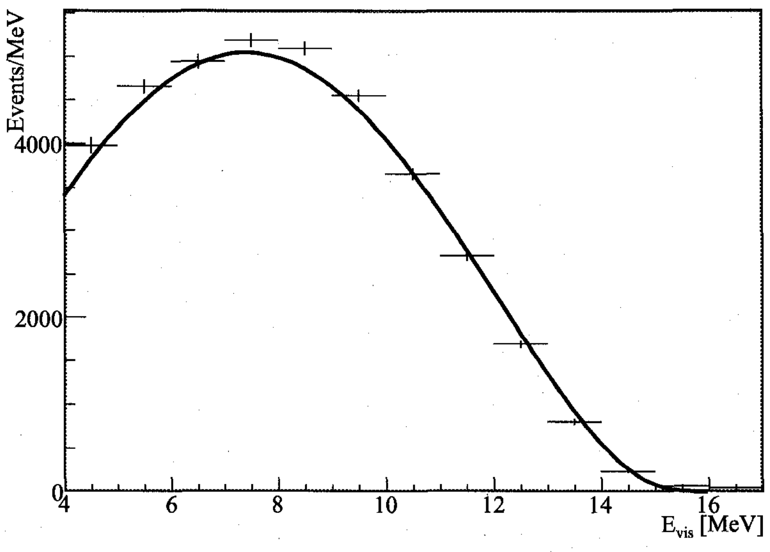

Figure 4.2: The background-subtracted ^{12}B β E_{vis} distribution. The solid line indicates the expected E_{vis} spectrum, normalized to the number of entries in the data histogram.

The expected E_{vis} spectrum is obtained by converting the theoretical β-spectrum into E_{vis} spectrum as described in Section 3.4. The data and the expected spectrum are in a good agreement.

Figure 4.3 shows the background-subtracted radial distribution of the ^{12}B β-decay events with E_{vis} between 4 MeV and 10 MeV. Although the ^{12}B E_{vis} spectrum spans below 4 MeV and beyond 10 MeV, only events within these E_{vis} limits are selected since other radioactivity backgrounds in the detector overwhelm the ^{12}B candidates at lower E_{vis}, and 10 MeV corresponds to the upper end of the $\bar{\nu}_{\text{reactor}}$ E_{vis} spectrum. Uniformly distributed events in volume without reconstruction resolution should appear flat as shown as the filled box in Figure 4.3. There is an excess in the number of events reconstructed outside the balloon while the number of events reconstructed inside the balloon decreases at higher radius. This indicates a position reconstruction bias particularly at large radius for events in the E_{vis} range between 4 MeV and 10 MeV.

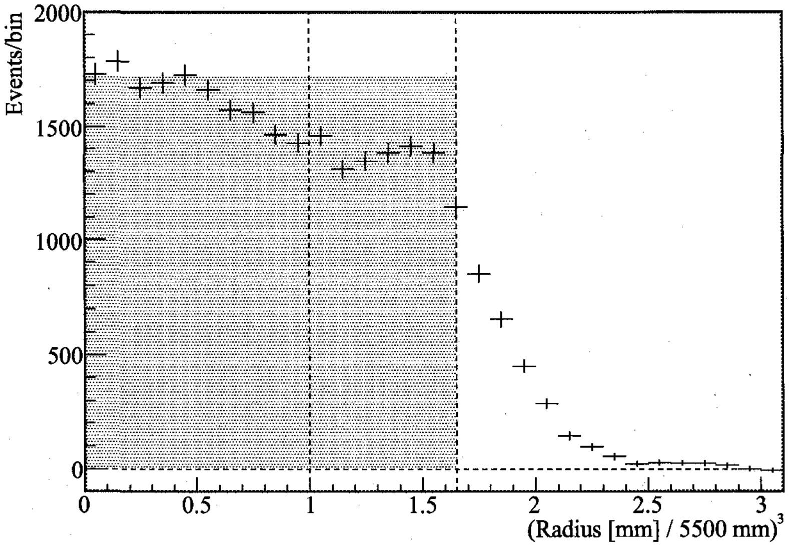

Figure 4.3: The radial distribution of the background-subtracted ^{12}B β-decay candidate events with E_{vis} between 4 and 10 MeV. The two vertical lines from left to right indicate the 5.5 m fiducial volume cut (see Section 5.3) and the balloon radius at 6.5 m. The filled box represents the uniform distribution in volume without reconstruction resolution, normalized to the number of entries.

4.2 Neutrons

Muons going through some material can interact with nuclei in the matter and produce neutrons. While high energy neutrons produced outside the detector can sometimes enter the LS becoming background events for inverse β-decay detection[2], spallation neutrons produced uniformly in the LS are useful for estimating some of the important systematic errors and understanding the detector response to neutrons. The neutrons produced in the LS are captured on protons with a mean capture time of $\sim$200 μs, producing a γ with E_{real} of 2.2 MeV, corresponding to E_{vis} of $\sim$2.4 MeV. The expected capture time and E_{vis} are used to select neutron capture events for the following studies on the mean neutron capture time ($\tau_{\text{capture, spall}}$), the reconstructed E_{vis} distribution, and the reconstructed radial distribution.

---

[2] See Section 6.6 for details on neutrons as background events.

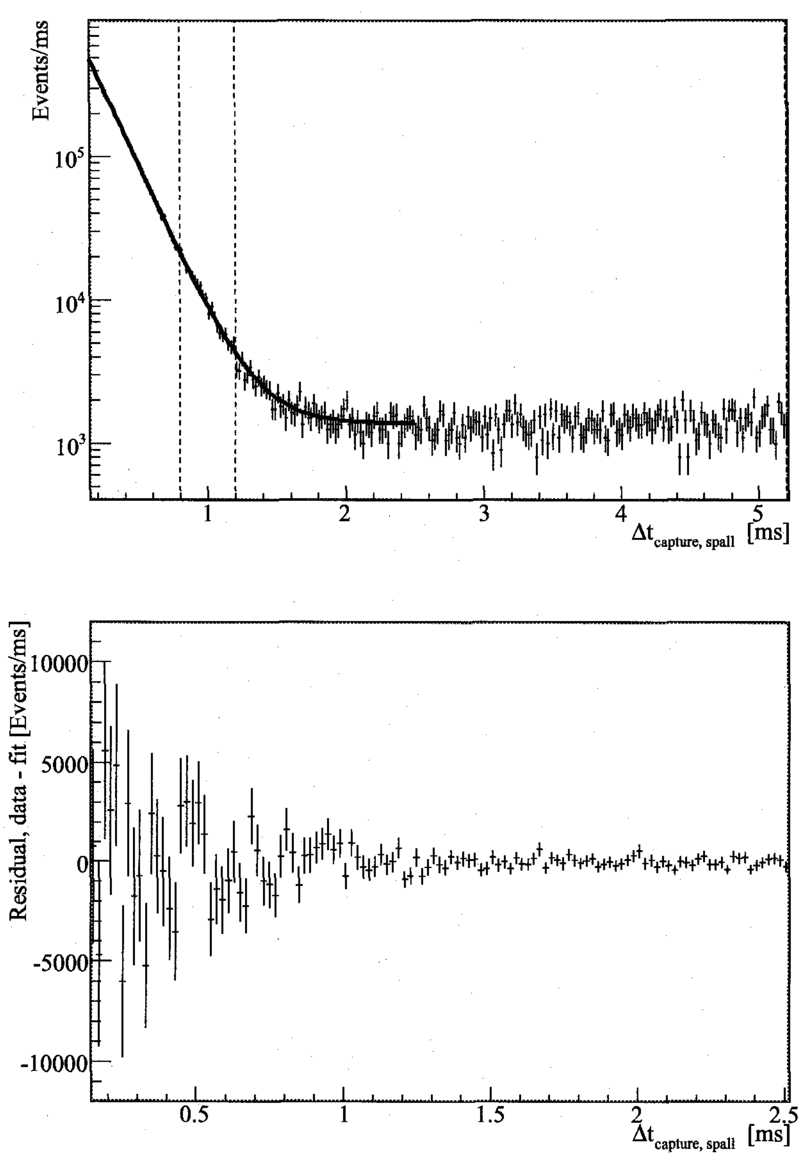

Figure 4.4: $\Delta t_{\text{capture, spall}}$ distribution (top plot) and residual (bottom plot). An exponential function plus a constant (solid line) is fitted to the data in the range of $150\,\mu\text{s} < \Delta t_{\text{capture, spall}} < 2.5\,\text{ms}$, which yields $\tau_{\text{capture, spall}} = 206.53 \pm 0.11\,\mu\text{s}$ with a $\chi^2/n.d.f.$ of 105.8/114. The dotted vertical lines indicate the $\Delta t_{\text{capture, spall}}$ windows for signals and the background events to be subtracted for Figure 4.5 and Figure 4.6; neutron candidates and background events are selected by $0.8\,\text{ms} < \Delta t_{\text{capture, spall}} < 1.2\,\text{ms}$ and $1.2\,\text{ms} < \Delta t_{\text{capture, spall}} < 5.2\,\text{ms}$, respectively.

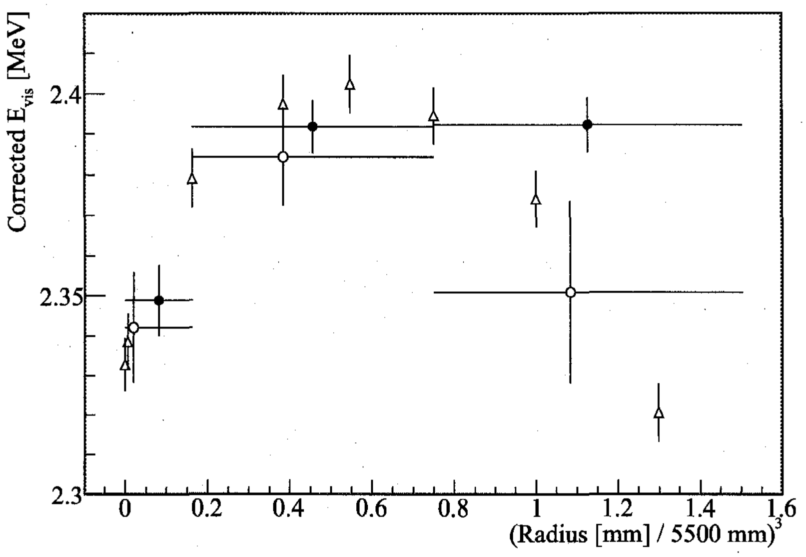

Figure 4.5: The corrected E_{vis} for spallation neutrons and ^{241}Am^{9}Be neutrons. Each of the spallation neutron E_{vis} points is background-subtracted, and then corrected for the reconstructed E_{vis} bias after muon, described in Section 3.3.1. Each of the ^{241}Am^{9}Be neutron E_{vis} points is corrected for the source capsule shadowing, described in Appendix E.4.1. The black dots refer to the spallation neutrons with reconstructed positions in concentric spherical shells. The open circles refer to the spallation neutrons with reconstructed positions in 2 m-radius-cylinders along the vertical central axis of the detector. The open triangles refer to ^{241}Am^{9}Be neutrons along the vertical central axis.

Figure 4.4 shows the distribution of the time difference between a spallation neutron candidate event[3] and its previous muon, $\Delta t_{\text{capture, spall}}$. An exponential function plus a constant are fitted to the data in the range of $150\,\mu\text{s} < \Delta t_{\text{capture, spall}} < 2.5\,\text{ms}$. The lower fit limit of $\Delta t_{\text{capture, spall}} = 150\,\mu\text{s}$ is chosen to reduce the effect of reconstruction inefficiency and bias caused by large charge deposits of muons that affect the detector for a while. This fit yields $\tau_{\text{capture, spall}} = 206.53 \pm 0.11\,\mu\text{s}$. The constant tail in the distribution is produced by background events that are uncorrelated with muons.

The reconstructed neutron capture E_{vis} varies slightly depending on the position

---

[3] The details of the cuts to select spallaion neutrons for this study are discussed in Appendix F.2.1.

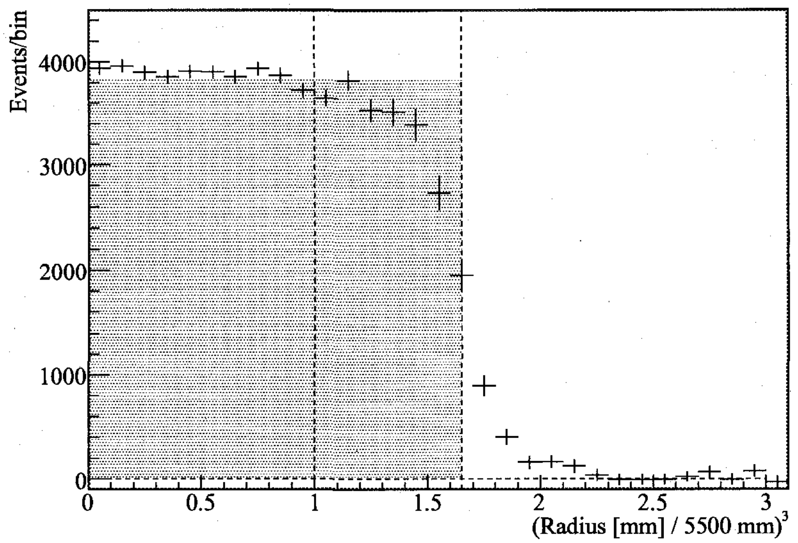

Figure 4.6: The background-subtracted spallation neutron capture event radial distribution. The two vertical lines from left to right indicate the 5.5 m fiducial volume cut (see Section 5.3) and the balloon radius at 6.5 m. The filled box represents the uniform distribution in volume without reconstruction resolution, normalized to the number of entries.

inside the LS due to the reconstruction bias of the E_{vis} estimator as shown in Section 3.3. Figure 4.5 shows the background-subtracted E_{vis} for spallation neutrons at various positions, where the neutron signal and the background events, respectively, are taken from time windows, 0.8 ms to 1.2 ms and 1.2 s to 5.2 s after associated muons[4]. The events with small $\Delta t_{\text{capture, spall}}$ are avoided to reduce possible effects from the E_{vis} bias due to the electronics baseline shift after muons. Figure 4.5 also shows E_{vis} for ^{241}Am^{9}Be neutrons at various positions, indicating that the E_{vis} for the spallation neutron captures along the vertical central axis agree with those for ^{241}Am^{9}Be neutrons. The E_{vis} for the spallation neutrons in the concentric spherical shells at high radius deviates from that around the central vertical axis.

Figure 4.6 shows the background-subtracted radial distribution of the neutron capture events[5]. The reconstructed neutron capture event distribution is relatively

---

[4] The details of the cuts to select spallaion neutrons for this study are discussed in Appendix F.2.2.

[5] The details of the cuts to select spallaion neutrons for this study are discussed in Appendix F.2.3.

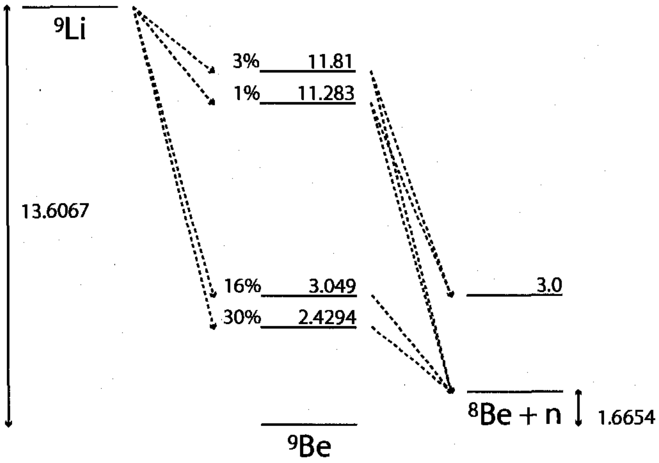

Figure 4.7: Decay schematic of ^{9}Li [55].

flat within the 5.5 m radius from the center of the ID, and drops sharply at the balloon radius of 6.5 m, indicating that the position reconstruction bias is small at neutron capture E_{vis} ~2.4 MeV.

4.3 ^{9}Li

Cosmic muons going through the detector produce radioactive ^{9}Li through reactions with ^{12}C in the LS [54]. ^{9}Li β-decays with a half-life of 178.3 ± 0.4 ms, sometimes decaying to one of several excited states of ^{9}Be, which then decays by neutron emission as shown in Figure 4.7 [55]. The initial β-decay and later neutron capture of the emitted neutron produce two temporally and spatially correlated events, which can mimic inverse β-decay and its subsequent neutron capture. However, ^{9}Li β-decay is easily identified by correlation with muons, forming triple coincidence events[6]: muons, ^{9}Li β-decays, and neutron captures. An estimate of the expected number of background event-pairs due to ^{9}Li for $\bar{\nu}_e$ detection in this analysis is described in Section 6.5. The E_{vis} spectrum of the ^{9}Li candidates can also be used to assess the E_{vis} reconstruction performance.

---

[6] The ^{9}Li candidates are selected by applying the Candidate Selection Cuts described in Section 5.3, except reversing the Shower/Misreconstructed Muon Cut and the Muon Cylinder Cut.

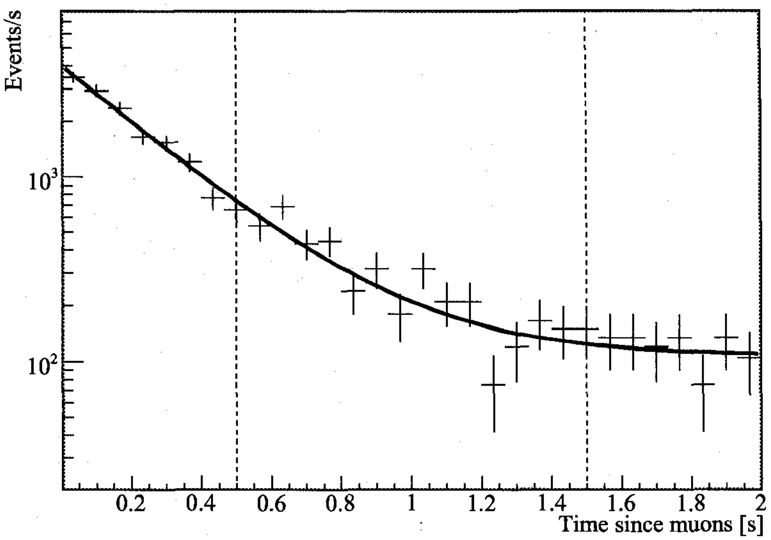

Figure 4.8: Time between events tagged as Shower Muons (see Section 3.6) and spallation ^{9}Li β-decay events. The thick line indicates the fit to an exponential function plus a constant, which yields the half-life of 190.2 ± 9.5 ms with a $\chi^2/n.d.f.$ of 25/27. The vertical dotted vertical lines indicate the time-since-muon windows for signals and the background events to be subtracted for Figure 4.9; ^{9}Li β-decay candidates and background events are selected from 2 ms to 0.5 s and 0.5 s to 1.5 s after associated muons, respectively.

Figure 4.8 shows the time difference between ^{9}Li β-decay candidates and events tagged as Shower Muons[7], muons which have a high light yield in the LS. Shower Muons, compared to all the other categories of muons, produce most of ^{9}Li in the LS. The fitted half-life, 190.2 ± 9.5 ms is just outside of the 1 σ error from the nominal ^{9}Li half-life of 178.3 ± 0.4 ms. Figure 4.9 shows the background-subtracted $E_{\rm vis}$ spectrum of the ^{9}Li β-decay candidates, where the ^{9}Li β-decay signal and the background events are taken from time windows, 2 ms to 0.5 s and 0.5 s to 1.5 s after associated muons, respectively. This distribution is overlaid with the expected $E_{\rm vis}$ spectrum, normalized to the number of entries. The expected $E_{\rm vis}$ spectrum is obtained by converting the theoretical β-spectrum into $E_{\rm vis}$ spectrum as described in Section 3.4. The data and the expected spectrum are in reasonable agreement.

---

[7] See Section 3.6 for the definition of Shower Muon.

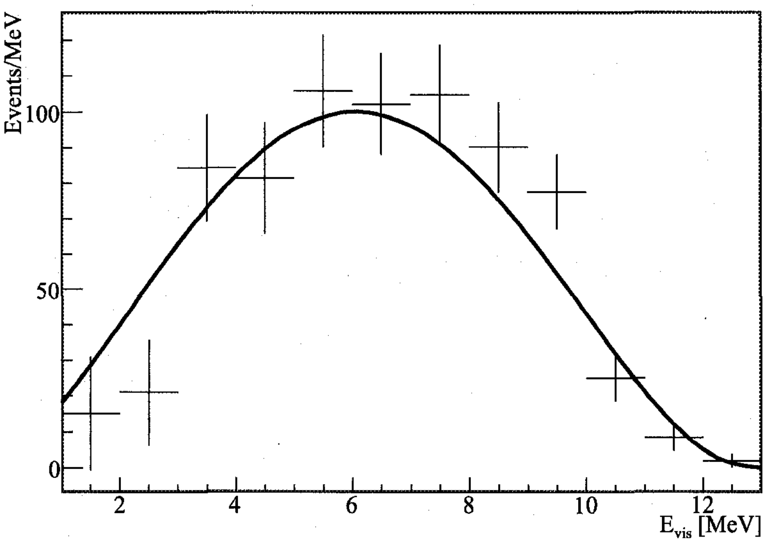

Figure 4.9: Background-subtracted E_{vis} spectrum of ^{9}Li β-decay events. The thick line indicates the expected spectrum normalized to the number of events in the histogram.

Chapter 5

Candidate Selection

The present analysis is based on data collected between April 2002 and April 2007. After removing the calibration runs and the problematic run periods, the livetime is calculated to be 1432.090 ± 0.072 days (see Section 5.1). This analysis is based on a spherical "fiducial volume" of radius 5.5 m in order to eliminate the outermost part of the ID where backgrounds are higher, and event reconstruction algorithms are not well-calibrated. The number of target protons within the fiducial volume is estimated to be $(4.59 \pm 0.18) \times 10^{31}$ (see Section 5.2).

The $\bar{\nu}_e$ detection signature, prompt-delayed event-pairs produced by inverse β-decays and their subsequent neutron captures, is selected by applying a set of cuts, described in Section 5.3, to reject backgrounds. The efficiencies of these cuts in selecting inverse β-decay are calculated in Sections 5.5 through 5.10.

5.1 Livetime

Extreme care has been taken to maximize the detector livetime[1]; the detector operates around the clock taking data, except during the daily run change for a few minutes, and occasional maintenance work, both of which add up to less than ~5 % of the time. However, the detector sometimes operates under conditions not optimized for $\bar{\nu}_e$

---

[1] Maximizing the detector livetime is important to increase the probability of detecting unpredictable events, such as a supernova explosion.

detection, such as during the detector calibration every few weeks. Also, the detector sometimes operates with known problems, such as when a significant number of PMTs do not have high voltage applied and when there is a continuous electronics noise. Therefore good runs are selected by removing these calibration runs and problematic periods.

During normal runs, the trigger board produces trigger records at well over 100 Hz unless it disables the data acquisition due to overwhelming data flow. The trigger board disable periods are identified by gaps in the trigger records longer than 0.1 s. Due to the sufficiently high trigger rate, less than 0.005 % of livetime is mistakenly excluded based on gaps longer than 0.1 s that are not caused by the trigger board disabling the data acquisition.

The total livetime is calculated by summing the good run periods excluding the gaps using the timestamps in the trigger record. Taking a conservative error of 0.005 %, the livetimes for periods I and II are calculated to be $(4.62740 \pm 0.00023) \times 10^7$ s and $(7.74585 \pm 0.00039) \times 10^7$ s, respectively, totaling 1432.090 ± 0.072 days.

5.2 Number of Target Protons

The number of target protons in the fiducial volume, within 5.5 m from the center of the ID, is calculated from

$$N_{\mathrm{p}} = \rho_{\mathrm{p}} V_{\mathrm{LS}} f_{\mathrm{FV}}, \tag{5.1}$$

where ρ_{p} is the proton number density of the LS, V_{LS} is the total volume of the LS (see Section 2.1), and f_{FV} is the ratio of the fiducial volume to the total LS volume. Using the measured density of the LS, ρ_{LS}, and hydrogen-to-carbon ratio, $N_{\mathrm{H/C}}$ (see Section 2.1), ρ_{p} is calculated to be $(6.6121 \pm 0.0066) \times 10^{22}$ protons cm^{-3} from

$$\rho_{\mathrm{p}} = \frac{\rho_{\mathrm{LS}}\, \mathrm{N_A}}{m_{\mathrm{H}} + \frac{m_{\mathrm{C}}}{N_{\mathrm{H/C}}}}, \tag{5.2}$$

where $\mathrm{N_A}$ is Avogadro's number, and m_{H} and m_{C} are the molar masses of hydrogen and carbon, respectively.

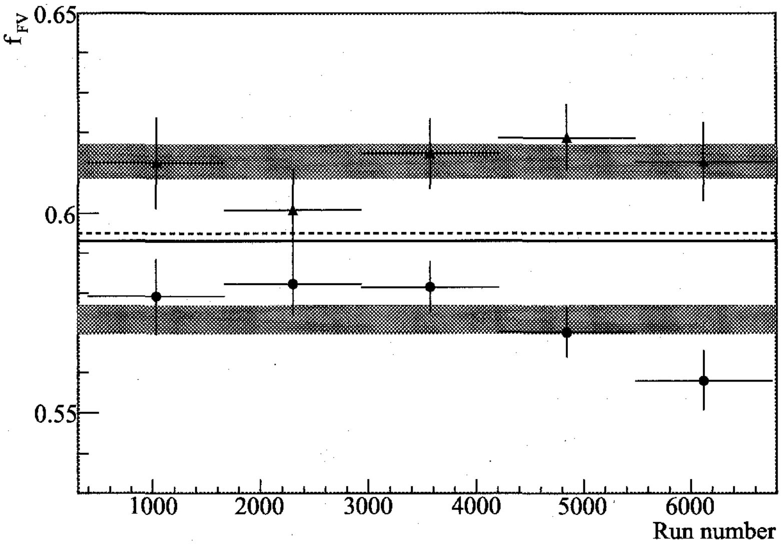

Figure 5.1: f_{FV} as a function of run number. The values represented by the circular and triangular markers are calculated with spallation ^{12}B β-decay and spallation neutron capture events, respectively. The gray bands indicate the statistical 1 σ error range for f_{FV}s calculated from neutrons (top) and ^{12}B (bottom). The thick solid horizontal line indicates the estimated central f_{FV} value. The thick dotted horizontal line indicates the nominal f_{FV} value if the fiducial radius is exactly 5500 mm without a reconstruction bias, and $V_{LS} = 1171\,\mathrm{m}^3$ (see Section 2.1).

f_{FV} is estimated using cosmogenic spallation ^{12}B β-decays and neutrons captures, which are assumed to be uniformly produced in the LS by muons going through the detector. f_{FV} is given by the number of events whose reconstructed radius is within 5500 mm compared to the total number of events. The estimated f_{FV} using ^{12}B β-decays with $4\,\mathrm{MeV} < E_{vis} < 10\,\mathrm{MeV}$ is 0.5735 ± 0.0035, and the estimated f_{FV} using neutron captures is 0.6129 ± 0.0043. Figure 5.1 shows the f_{FV} estimated with ^{12}B and neutrons as a function of run number.

The difference between f_{FV} calculated with ^{12}B β-decays and neutron captures is not completely understood. It is possible that such difference is due to the dependence of the position reconstruction algorithm on E_{vis}. Figure 5.2 shows f_{FV} as a function of ^{12}B β E_{vis}, which is relatively stable between 4 MeV and 10 MeV. However, it appears that the position reconstruction performance changes between ~2 MeV and ~5 MeV

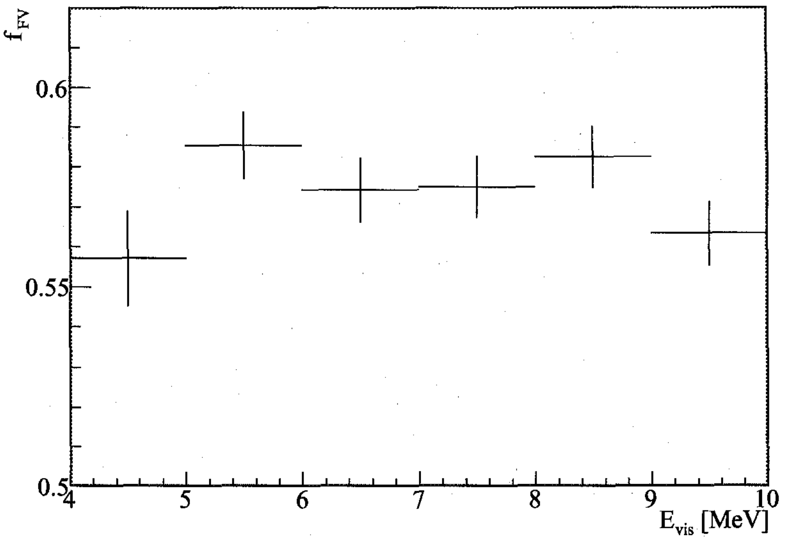

Figure 5.2: f_{FV} as a function of E_{vis} for ^{12}B β-decays.

as shown in Figure 3.3; the biases of the reconstructed positions of the ^{241}Am^{9}Be neutron captures, indicated by the diamond markers, are much smaller than those of ^{241}Am^{9}Be γs around 5 MeV, indicated by the cross markers. Also, the reconstructed position distribution of spallation neutrons (see Figure 4.6) is much flatter within the fiducial volume, and drops more sharply at the balloon boundary than that of spallation ^{12}B, chosen with E_{vis} between 4 and 10 MeV (see Figures 4.3).

Overall f_{FV} is estimated as the average of f_{FV} estimated using the ^{12}B and neutrons, and its error the full envelope resulting from the two techniques. This results in $f_{\mathrm{FV}} = 0.593 \pm 0.020$. Therefore, the number of target protons, N_{p} is calculated to be $(4.59 \pm 0.18) \times 10^{31}$ using Equation 5.1.

5.3 Candidate Selection Cuts

The Candidate Selection Cuts are chosen to select pairs of events from inverse β-decays and their subsequent neutron captures with high efficiency while rejecting background events. Many event selection cuts rely on the event tags, described in

Section 3.6.

5.3.1 Basic Good Event Cuts

The following cuts are applied to ensure good data quality within the selected runs.

- $N_{\mathrm{Max\,ID}}$ Cut: Only events with $N_{\mathrm{Max\,ID}}$ greater than or equal to 200 for period I and 180 for period II[2] are considered to avoid events with lower $N_{\mathrm{Max\,ID}}$ that are occasionally acquired during normal runs with special trigger types and unknown triggering efficiencies. The $N_{\mathrm{Max\,ID}}$ threshold efficiency is calculated in Section 5.5.

- Multiplet Cut: If a multiplet, described in Section 3.6, has more than 9 events, all the events in the multiplet are removed to eliminate a noisy period. Since the average event rate is a few tens of Hz, this process removes negligible number of good events.

- Reconstruction Status Cut: Events must have valid position and E_{vis} reconstruction statuses. The reconstruction efficiency is estimated in Section 5.6.

5.3.2 Cosmogenic Spallation Cuts

The following cuts are applied to avoid muons and their spallation products that can mimic inverse β-decays and their subsequent neutron captures, such as short-lived neutrons (see Section 4.2) and long-lived ^{9}Li, produced along the paths of muons (see Section 4.3). The efficiency due to these cuts is estimated in Section 5.7.

- Shower/Misreconstructed Muon Cut: The full detector volume is vetoed for 2 s after an event tagged as a Shower Muon or an ID Muon on which the muon track reconstruction algorithm failed since such an event can produce various long-lived spallation products, such as ^{9}Li.

---

[2] These periods are defined by when the thermometers were removed (see Section 2.1). However, this period boundary is only 6 days after the N_{ID} trigger threshold was lowered from 200 to 180.

- Muon Cut: The full detector volume is vetoed for 2 ms after an event tagged as a Muon to avoid noise caused by the electronics and PMTs after muons and short-lived spallation products, such as neutrons.

- Muon Cylinder Cut: The volume in a cylinder of radius 3 m from the muon track is vetoed for 2 s after an ID Muon with a valid reconstructed muon track to avoid long-lived spallation products such as ^{9}Li along the muon track. This cut is applied only to the prompt candidate events described in Section 5.3.3.

- High $N_{PE\,\mathrm{ID}}$ Event Cut: The full detector volume is vetoed for 2 ms after an event tagged as a High $N_{PE\,\mathrm{ID}}$. Undetected muons outside the detector can produce high energy neutrons that reach the LS, and the thermalization of these high energy neutrons in the LS can cause High $N_{PE\,\mathrm{ID}}$ events. Such high energy neutrons can also create secondary neutrons, and the captures of these neutrons can mimic inverse β-decays and their subsequent neutron captures. The High $N_{PE\,\mathrm{ID}}$ Event Cut is designed to reduce these background events. See Section 6.6 for more details on spallation neutrons as background events.

- Gap Cut: Muons could have passed through the detector producing long-lived spallation products while the trigger board was disabled. Therefore the full detector volume is vetoed for 2 s after an event tagged as a Gap, which identifies periods when the trigger board was disabled.

5.3.3 Coincidence Selection Cuts

The following cuts are applied to select inverse β-decays and their subsequent neutron captures with high efficiency, using their temporal and spatial coincidence signals, and the narrow E_{vis} distribution of the neutron capture γ.

- ΔR Cut: $\Delta R < 1600\,\mathrm{mm}$, where ΔR denotes the distance between the prompt and delayed events. Section 5.8 discusses the efficiency of this cut.

- Δt Cut: $0.5\,\mu\mathrm{s} < \Delta t < 1000\,\mu\mathrm{s}$, where Δt denotes the time between the prompt and delayed events. Section 5.9 discusses the efficiency of this cut.

- $E_{\rm p}$ Cut: $0.9\,\mathrm{MeV} < E_{\rm p} < 15\,\mathrm{MeV}$ for period I and $0.8\,\mathrm{MeV} < E_{\rm p} < 15\,\mathrm{MeV}$ for period II, where $E_{\rm p}$ denotes the $E_{\rm vis}$ of the prompt events. The detector $N_{\rm ID}$ threshold was lowered in period II enabling the analysis $E_{\rm vis}$ threshold to be lowered in order to increase the efficiency. Although the expected $E_{\rm vis}$ spectrum for $\bar{\nu}_{\rm reactor}$s spans only up to ∼10 MeV, events with $E_{\rm vis}$ up to 15 MeV are included to gain a better constraint on high energy background events (see Sections 6.6 and 6.7). The efficiency of this cut is calculated during the fit (see Chapter 7) since the energy parameters (see Section 3.4) are simultaneously fitted, which changes the expected $E_{\rm p}$ spectral shape.

- $E_{\rm d}$ Cut: $2.04\,\mathrm{MeV} < E_{\rm d} < 2.76\,\mathrm{MeV}$, where $E_{\rm d}$ denotes the $E_{\rm vis}$ of the delayed events. Most of the neutrons produced in inverse β-decay are captured by protons in the LS creating 2.2 MeV γs, which corresponds to $E_{\rm vis}$ of ∼2.4 MeV. Section 5.10 discusses the efficiency of this cut.

- $R_{\rm average}$ Cut: To avoid the sections of the detector where the position reconstruction bias is large, and to avoid the large number of background events that are produced at the balloon surface near 6.5 m, the fiducial volume is defined to be within the 5.5 m from the center of the ID. This cut is applied on the average radius of the prompt-delayed event-pair, $R_{\rm average}$.

- High Candidate Multiplet Cut: The prompt and delayed candidate event-pair is isolated from other pairs. For example, if three events form two or three pairs, all of them are thrown away. The probability of two events from an inverse β-decay and its subsequent neutron capture being coincident with another event is negligible, and such multiple coincidence events are likely caused by thermalization and captures of high energy spallation neutrons and those of secondary neutrons that they produce (see Sections 6.6).

5.4 Simulated Delayed Event Distribution

The fiducial volume cut, $R_{\rm average} < 5.5\,\mathrm{m}$, is applied to the radius of the average positions of the prompt and delayed event-pairs to ensure constant detection efficiency

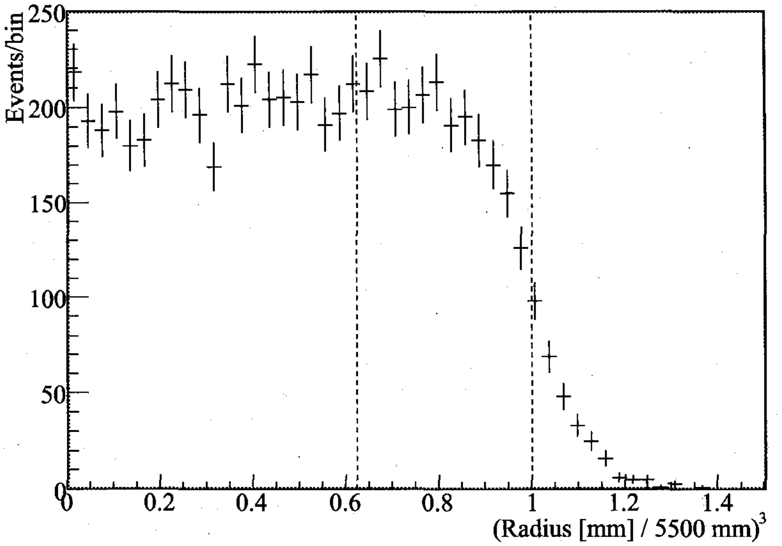

Figure 5.3: Delayed event distribution for inverse β-decays simulated with various initial $\bar{\nu}_e$ energies. The dotted vertical lines, from left to right, correspond to radii of 4700 mm and 5500 mm.

for $\bar{\nu}_e$s within the fiducial volume. Applying this cut, combined with the ΔR Cut, results in the radial distribution of either prompt or delayed events starting to decrease at 4.7 m radius and becoming zero at 6.3 m. This radial event distribution is used to weight-average quantities that have a radial bias, such as detection inefficiency due to the $N_{\mathrm{Max\,ID}}$ threshold (see Section 5.5) and E_{vis} distribution of neutron capture γs (see Section 5.10), over the fiducial volume.

To obtain this radial distribution, equal numbers of inverse β-decays with various initial $\bar{\nu}_e$ energies (2 MeV, 4 MeV, 6 MeV, 8 MeV, and 10 MeV) are simulated uniformly in the ID within a 8 m radius using KLG4sim[3]. These simulated events are then reconstructed using the default event reconstruction algorithms, and the Candidate Selection Cuts (see Section 5.3) are applied. Figure 5.3 shows the delayed

---

[3] KLG4sim is a simulation package specifically developed for the KamLAND detector, which can produce individual PMT pulses based on the energy, position, and types of the events simulated. The simulated data can be reconstructed by the same algorithms used on the real data. KLG4sim is based on the Geant4 simulation package.

event distribution from all the simulated inverse β-decays with various initial $\bar{\nu}_e$ energies. The fractions of number of delayed events are calculated in three concentric radial regions, $0\,\mathrm{m} < r < 4.7\,\mathrm{m}$, $4.7\,\mathrm{m} < r < 5.5\,\mathrm{m}$, and $5.5\,\mathrm{m} < r < 6.3\,\mathrm{m}$, to be 0.603 ± 0.014, 0.349 ± 0.013, and 0.0474 ± 0.0059, respectively.

5.5 $N_{\mathrm{Max\,ID}}$ Threshold Efficiency

$N_{\mathrm{Max\,ID}}$, roughly defined as the number of PMTs that receive at least one photon in an event, is related to E_{vis}, and the correlation between $N_{\mathrm{Max\,ID}}$ and E_{vis} depends on the event position. The $N_{\mathrm{Max\,ID}}$ threshold efficiency as a function of E_{vis}, $\varepsilon_{N_{\mathrm{Max\,ID}}}(E_{\mathrm{vis}})$, is defined as

$$\varepsilon_{N_{\mathrm{Max\,ID}}}(E_{\mathrm{vis}}) = \frac{N_{N_{\mathrm{Max\,ID}}\,\mathrm{threshold}}(E_{\mathrm{vis}})}{N_{\mathrm{total}}(E_{\mathrm{vis}})}, \tag{5.3}$$

where, at a given E_{vis}, $N_{N_{\mathrm{Max\,ID}}\,\mathrm{threshold}}(E_{\mathrm{vis}})$ denotes the number of events with $N_{\mathrm{Max\,ID}}$ greater than the $N_{\mathrm{Max\,ID}}$ threshold (200 for period I and 180 for period II), and $N_{\mathrm{total}}(E_{\mathrm{vis}})$ denotes the total number of events. Because the correlation between $N_{\mathrm{Max\,ID}}$ and E_{vis} depends on the event position, $\varepsilon_{N_{\mathrm{Max\,ID}}}(E_{\mathrm{vis}})$ is estimated separately in three concentric radial regions, $r < 4.7\,\mathrm{m}$, $4.7\,\mathrm{m} < r < 5.5\,\mathrm{m}$, and $5.5\,\mathrm{m} < r < 6.3\,\mathrm{m}$. Figure 5.4 shows $\varepsilon_{N_{\mathrm{Max\,ID}}}(E_{\mathrm{vis}})$ distribution obtained from a special low N_{ID} threshold run and an error function fit for each region and period. Since the fitted means, $\mu_{N_{\mathrm{Max\,ID}}}$, and sigmas, $\sigma_{N_{\mathrm{Max\,ID}}}$, are estimated using just one run, their time variations are estimated using the variations of mean and RMS of E_{vis}, respectively, for all the events whose $N_{\mathrm{Max\,ID}}$ is equal to the $N_{\mathrm{Max\,ID}}$ threshold from all the good runs in period I and II.

Using the fitted $\mu_{N_{\mathrm{Max\,ID}}}$ and $\sigma_{N_{\mathrm{Max\,ID}}}$ in each region and period, including the time variation systematic errors, $\varepsilon_{N_{\mathrm{Max\,ID}}}$ in each region and period is calculated from

$$\varepsilon_{N_{\mathrm{Max\,ID}}} = \frac{\int_{E_{\mathrm{p}}\,\mathrm{threshold}}^{15\,\mathrm{MeV}} \varepsilon_{N_{\mathrm{Max\,ID}}}(E_{\mathrm{vis}})\,\frac{dP}{dE_{\mathrm{vis}}}(E_{\mathrm{vis}})\,dE_{\mathrm{vis}}}{\int_{E_{\mathrm{p}}\,\mathrm{threshold}}^{15\,\mathrm{MeV}} \frac{dP}{dE_{\mathrm{vis}}}(E_{\mathrm{vis}})\,dE_{\mathrm{vis}}} \tag{5.4}$$

where $\frac{dP}{dE_{\mathrm{vis}}}(E_{\mathrm{vis}})$ is the expected E_{p} distribution for $\bar{\nu}_{\mathrm{reactor}}$ or $\bar{\nu}_{\mathrm{geo}}$. Here, the "unoscillated" $\frac{dP}{dE_{\mathrm{vis}}}(E_{\mathrm{vis}})$ for $\bar{\nu}_{\mathrm{reactor}}$ is used for simplicity. However, it has been shown

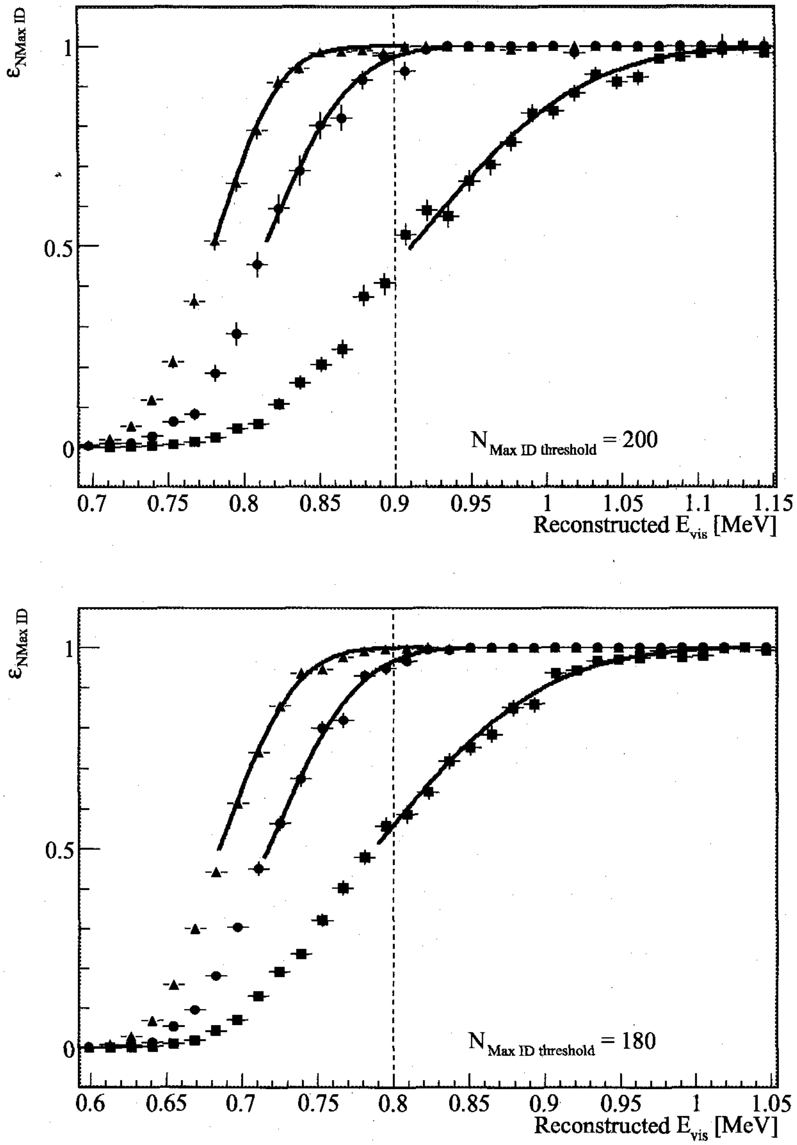

Figure 5.4: $\varepsilon_{N_{\mathrm{Max\,ID}}}(E_{\mathrm{vis}})$ in three concentric radial regions in the detector from run 3888, which has a low N_{ID} threshold of 35. The top and bottom plots are for $N_{\mathrm{Max\,ID}}$ thresholds of 200 and 180, respectively. The triangle, circle, and square markers are for data obtained from $r < 4.7\,\mathrm{m}$, $4.7\,\mathrm{m} < r < 5.5\,\mathrm{m}$, and $5.5\,\mathrm{m} < r < 6.3\,\mathrm{m}$, respectively. The solid curves are the fits to error functions. The dotted vertical line indicates the analysis E_{vis} threshold of 0.9 MeV for period I and 0.8 MeV for period II.

that the use of the spectrum including neutrino oscillation provides virtually identical results.

Table 5.1: $\varepsilon_{N_{\mathrm{Max\,ID}}}$ for $\bar{\nu}_{\mathrm{reactor}}$s and $\bar{\nu}_{\mathrm{geo}}$s. The errors are given in parenthesis.

Event type	$\varepsilon_{N_{\mathrm{Max\,ID}}}$ period I	$\varepsilon_{N_{\mathrm{Max\,ID}}}$ period II
$\bar{\nu}_{\mathrm{reactor}}$	0.999954(54)	0.9999934(30)
^{238}U $\bar{\nu}_{\mathrm{geo}}$	0.99941(70)	0.999914(38)
^{232}Th $\bar{\nu}_{\mathrm{geo}}$	0.9984(18)	0.99978(10)

In both periods I and II, $\varepsilon_{N_{\mathrm{Max\,ID}}}$ from three radial regions are then weight-averaged according to the event fraction in each region estimated in Section 5.4. This yields overall $\varepsilon_{N_{\mathrm{Max\,ID}}}$ for both of $\bar{\nu}_{\mathrm{reactor}}$ and $\bar{\nu}_{\mathrm{geo}}$ event types to be basically 1 within small errors for both periods as shown in Table 5.1. Appendix G describes more details on the $\varepsilon_{N_{\mathrm{Max\,ID}}}$ calculation.

5.6 Reconstruction Efficiency

The position and E_{vis} reconstruction algorithms occasionally fail and estimate the position or E_{vis} of an event well outside the normal distribution for a given true position or energy, possibly due to unknown effects that are not considered in these algorithms. Such failures are accounted for by a "reconstruction efficiency," $\varepsilon_{\mathrm{recon}}$, estimated using the ^{60}Co^{68}Ge and ^{241}Am^{9}Be sources with known energies and deployed positions, and the events acquired during normal runs. The reconstruction efficiency obtained from calibration source runs, $\varepsilon_{\mathrm{recon,\,source}}$, is reasonably constant across various positions as shown in Figure 5.5. $\varepsilon_{\mathrm{recon,\,source}}$ for ^{60}Co^{68}Ge and ^{241}Am^{9}Be events are estimated by fitting a constant to $\varepsilon_{\mathrm{recon,\,source}}$ at various positions, resulting in 0.99986 ± 0.00020 and 0.99747 ± 0.00012, respectively. The average of the fitted $\varepsilon_{\mathrm{recon,\,source}}$ is 0.998665 ± 0.00012.

The time variation of $\varepsilon_{\mathrm{recon}}$ is estimated from the time variation of the fraction of events with valid exit statuses from reconstruction algorithms, using events acquired

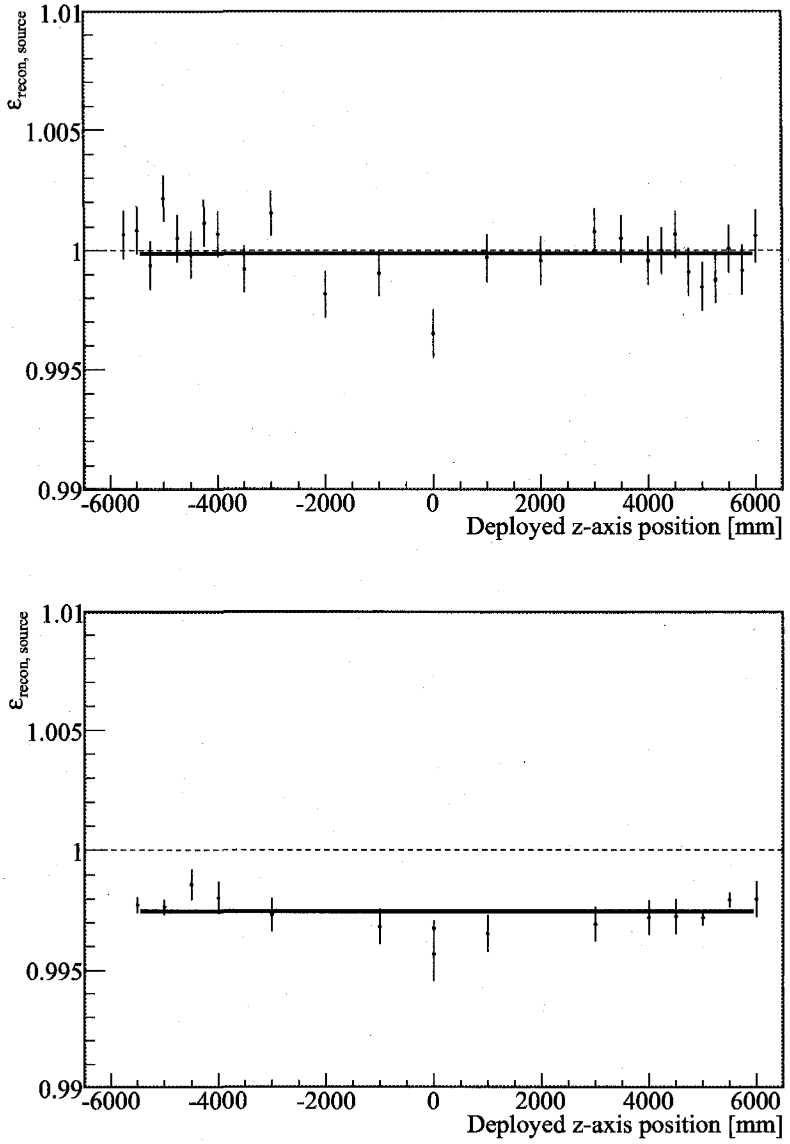

Figure 5.5: $\varepsilon_{\text{recon, source}}$ of ^{60}Co^{68}Ge (top plot) and ^{241}Am^{9}Be (bottom plot) source events at various positions along the central vertical axis. The fitted constant (thick line) to the ^{60}Co^{68}Ge data is 0.99986 ± 0.00020, and the $\chi^2/n.d.f.$ is 35.0/24. The fitted constant (thick line) to the ^{241}Am^{9}Be data is 0.99747 ± 0.00012, and the $\chi^2/n.d.f.$ is 18.6/14.

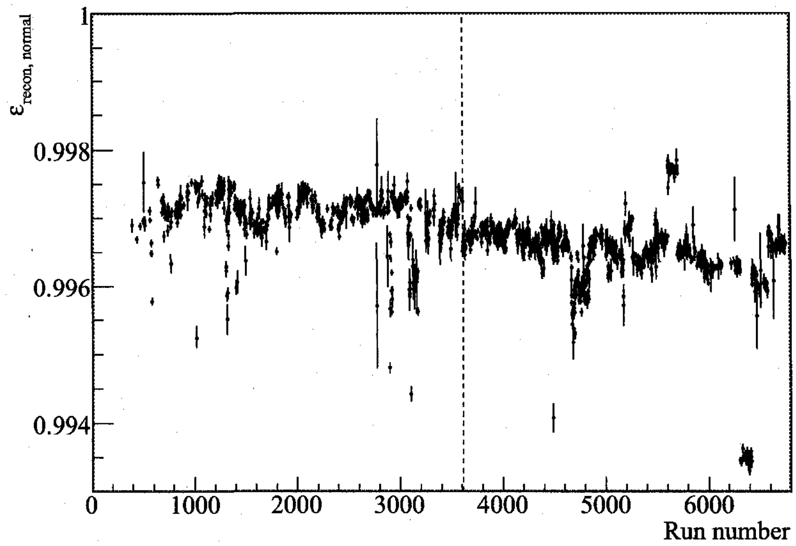

Figure 5.6: Time variation of $\varepsilon_{\text{recon, normal}}$ from normal runs. The dotted vertical line separates periods I and II.

during normal runs, $\varepsilon_{\text{recon, normal}}$, shown in Figure 5.6. Slight differences in the calibration conditions for the pulse time and charge finding algorithm (see Section 3.1) cause the occasional jumps in $\varepsilon_{\text{recon, normal}}$. The maximum deviation of $\varepsilon_{\text{recon, normal}}$ from $\varepsilon_{\text{recon, source}}$ is 0.0022, which is taken as the error of $\varepsilon_{\text{recon}}$, resulting in an estimated $\varepsilon_{\text{recon}}$ of 0.9987 ± 0.0022. More details on the $\varepsilon_{\text{recon}}$ calculation is described in Appendix H.

5.7 Cosmogenic Spallation Cut Efficiency

Cosmogenic Spallation Cuts, described in Section 5.3.2, are designed to reduce the spallation-product background caused by muons, by applying, for short periods of time, a veto of either the entire detector volume or cylindrical regions of the detector along the muon trajectory. The Cosmogenic Spallation Cut efficiency, $\varepsilon_{\text{spall}}$, is hard to calculate analytically since the efficiency of the Muon Cylinder Cut depends on the trajectories of the muons with respect to the detector. Therefore, $\varepsilon_{\text{spall}}$ is estimated

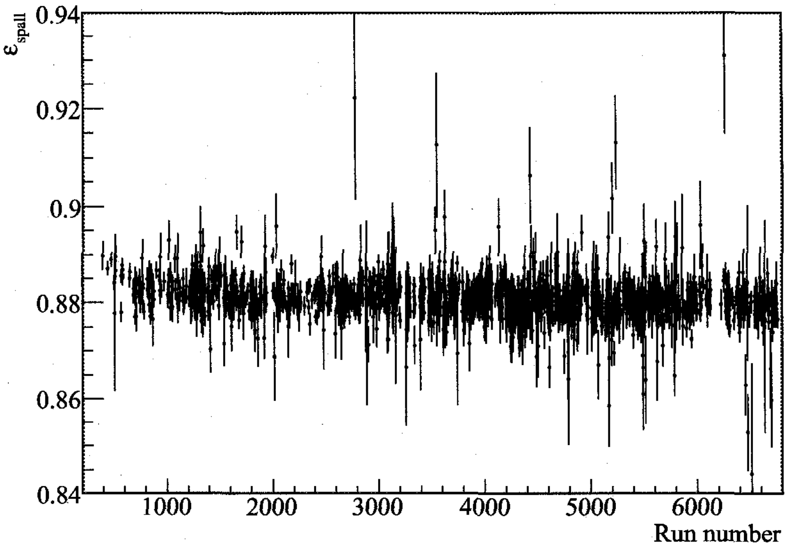

Figure 5.7: Time variation of $\varepsilon_{\text{spall}}$.

with a Monte Carlo simulation instead. Point-like events are simulated uniformly in time and in the fiducial volume for each good normal run, and the Cosmogenic Spallation Cuts are then applied to these simulated events using the actual events in the data on which these cuts are based, i.e., muons, High $N_{PE\,\text{ID}}$ events, and Gaps.

$\varepsilon_{\text{spall}} = 0.880880 \pm 0.000037$ is calculated from the fraction of the simulated events that pass the Cosmogenic Spallation Cuts. Figure 5.7 shows $\varepsilon_{\text{spall}}$ calculated for each run. Only two cuts, the Shower/Misreconstructted Muon Cut and the Muon Cylinder Cut, contribute significantly to the total efficiency loss, and each contributes approximately equally.

5.8 ΔR Cut Efficiency

The neutrons produced in inverse β-decays are captured by protons in the LS within a few centimeters from where they are created. The ΔR Cut ($\Delta R < 1.6\,\text{m}$) is designed to select spatially correlated prompt and delayed event-pairs. The ΔR Cut efficiency, $\varepsilon_{\Delta R}$, is estimated by simulating an equal number of inverse β-decays uniformly within

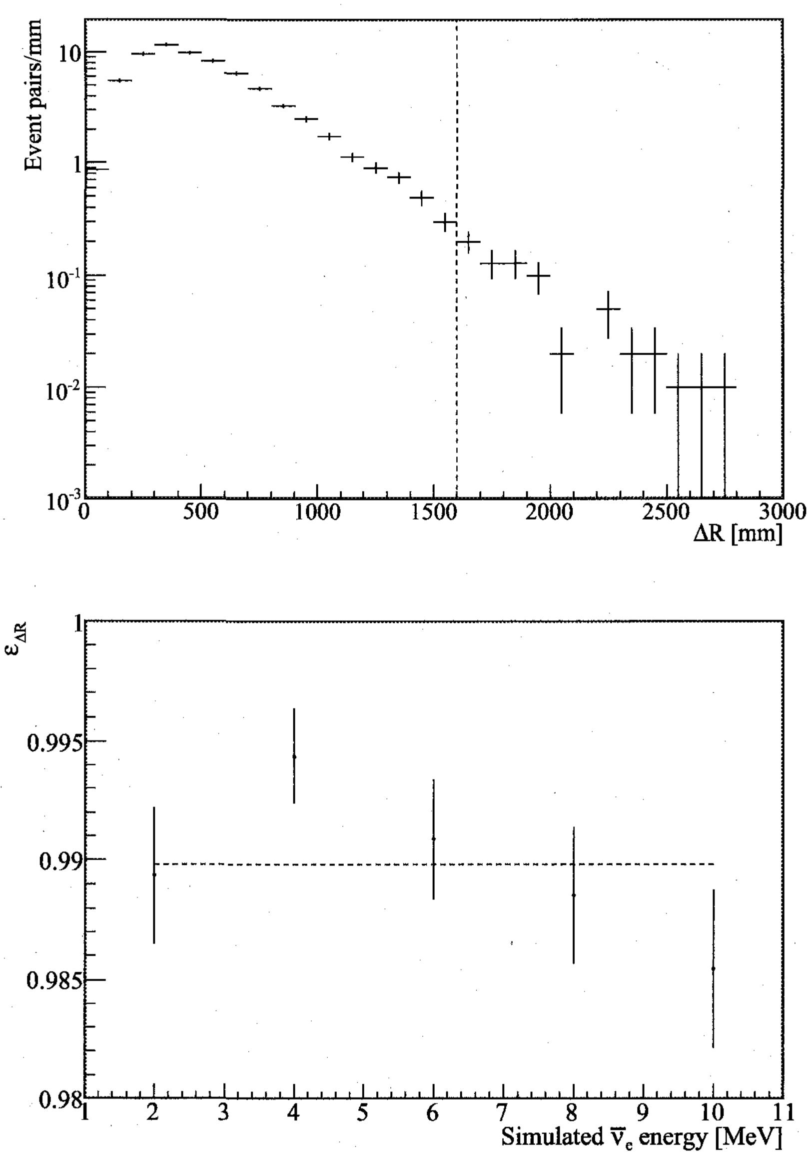

Figure 5.8: ΔR distribution (top plot) and $\varepsilon_{\Delta R}$ (bottom plot) for simulated inverse β-decays. The dotted vertical line in the top plot indicates the ΔR Cut of 1.6 m. The dotted horizontal line in the bottom plot shows the $\varepsilon_{\Delta R}$ estimated by combining all the simulated data.

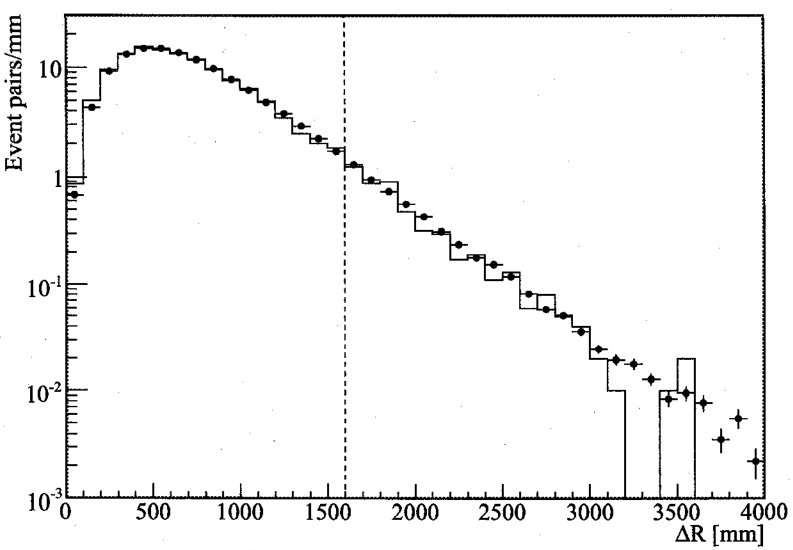

Figure 5.9: ΔR distributions of actual (dots with error bars) and simulated (solid line) ^{241}Am^{9}Be source events. The distribution from actual data is normalized to the number of entries for the simulated data. The dotted vertical line indicates the ΔR Cut of 1.6 m.

the ID from $\bar{\nu}_e$s with energies at 2 MeV, 4 MeV, 6 MeV, 8 MeV, and 10 MeV using KLG4sim. The simulated data are processed using the default event reconstruction algorithms, and ΔR is calculated from the simulated prompt-delayed event-pairs that pass the Candidate Selection Cuts except the ΔR Cut (see Section 5.3.3).

The top plot in Figure 5.8 shows the resulting ΔR distribution; 98.87 % of the pairs in this distribution pass the ΔR Cut. This efficiency, $\varepsilon_{\Delta R}$, depends slightly on the energy of the simulated $\bar{\nu}_e$s, as shown in the bottom plot in Figure 5.8. The maximum dispersion of 0.0057, shown in this figure, is taken as the error on $\varepsilon_{\Delta R}$.

Possible differences between the simulation and real data are addressed by comparing the ΔR distribution from ^{241}Am^{9}Be data simulated by KLG4sim to that from actual ^{241}Am^{9}Be calibration data. The ^{241}Am^{9}Be source produces coincidence events where the first events are either the thermalization of the neutrons alone or that together with a γ, and the second events are the neutron captures on protons in the LS. The ΔR distributions from actual and simulated ^{241}Am^{9}Be data are shown in Figure 5.9. The comparison yields that $\varepsilon_{\Delta R}$ for the actual $^{241}\mathrm{Am}^{9}\mathrm{Be}$ data, 0.95820 ± 0.00026, is $0.27 \pm 0.18\,\%$ lower than $\varepsilon_{\Delta R}$ for simulated $^{241}\mathrm{Am}^{9}\mathrm{Be}$ events, 0.9607 ± 0.0017. Therefore the estimated $\varepsilon_{\Delta R}$ from simulated inverse β-decays is shifted, and the error is increased accordingly, yielding $\varepsilon_{\Delta R}$ of 0.9861 ± 0.0060.

5.9 Δt Cut Efficiency

The neutron emitted in an inverse β-decay quickly loses its kinetic energy, and begins a thermal motion. Once the neutron is thermalized, the probability of a neutron capture occurring in any given instant is constant. Therefore the capture time distribution is an exponential function with a mean capture time in the LS, τ.

For a given τ, the efficiency of the Δt Cut ($0.5\,\mu\mathrm{s} < \Delta t < 1000\,\mu\mathrm{s}$), $\varepsilon_{\Delta t}$, is given by

$$\varepsilon_{\Delta t} = \int\limits_{0.5\,\mu\mathrm{s}}^{1000\,\mu\mathrm{s}} \frac{1}{\tau} \exp\left(-\frac{t}{\tau}\right) dt, \tag{5.5}$$

and the error on $\varepsilon_{\Delta t}$ due to uncertainty in τ is given by

$$\begin{aligned} d\varepsilon_{\Delta t} &= \left|\frac{\partial \varepsilon}{\partial \tau}\right| d\tau \\ &= \left| \left[\frac{t}{\tau^2} \exp\left(-\frac{t}{\tau}\right) \right]_{t=0.5\,\mu\mathrm{s}}^{1000\,\mu\mathrm{s}} \right| d\tau. \end{aligned} \tag{5.6}$$

τ is estimated using captures of neutrons from the $^{241}\mathrm{Am}^{9}\mathrm{Be}$ calibration source. The $^{241}\mathrm{Am}^{9}\mathrm{Be}$ source produces coincidence events where the first events are either the thermalization of the neutrons alone or that together with a γ, and the second events are the neutron captures on protons in the LS. To reduce background mainly due to radioactivity in the detector for this estimate, the second events are selected with a E_{vis} window of $\pm 0.4\,\mathrm{MeV}$ around the mean neutron capture E_{vis}, calculated for each deployed position, and the first and second events are reconstructed both within 50 cm from the deployed source positions. Figure 5.10 shows the distribution of the time differences between all the selected event-pairs from the $^{241}\mathrm{Am}^{9}\mathrm{Be}$ source,

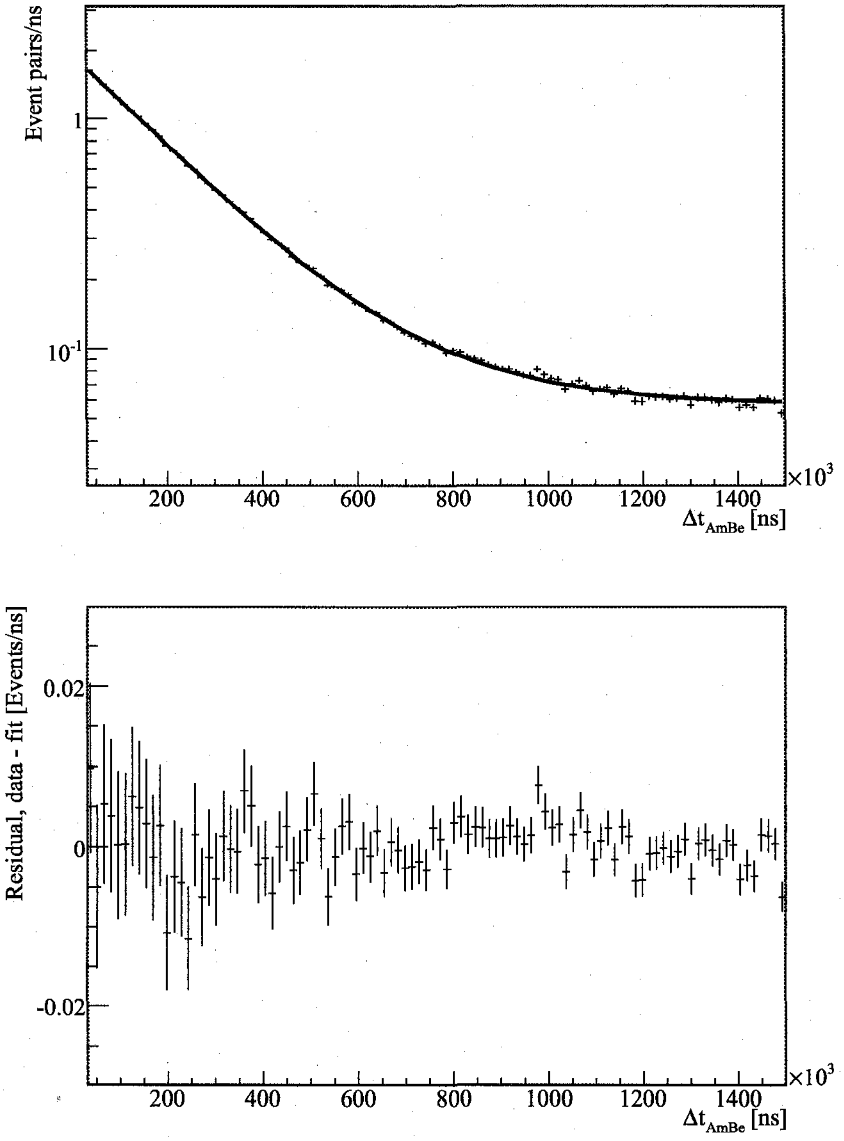

Figure 5.10: Δt_{AmBe} distribution (top plot) and residual distribution (bottom plot). The solid curve in the top plot is the fit to an exponential function plus a constant from Δt_{AmBe} of $30\,\mu$s to 1.5 ms. The fitted τ is $205.44 \pm 0.60\,\mu$s, and the $\chi^2/n.d.f.$ of this fit is 105.6/97.

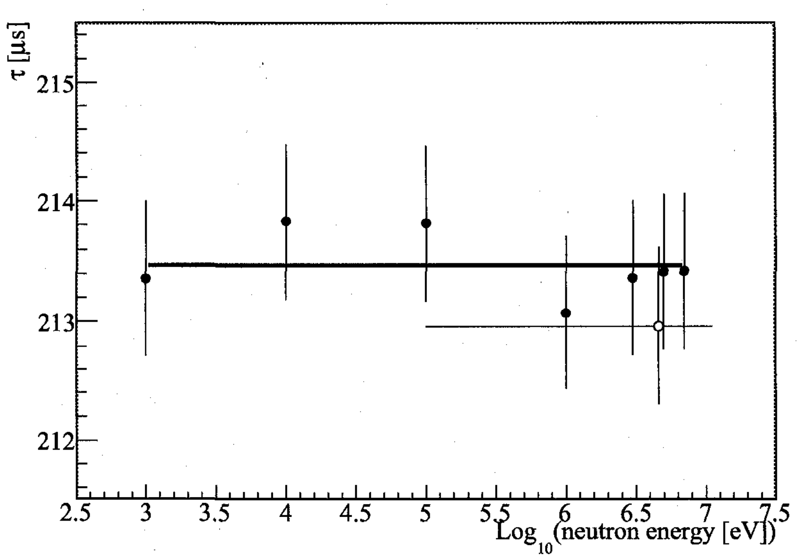

Figure 5.11: τ estimated from bare neutrons (filled markers) simulated at various initial neutron energies and simulated ^{241}Am^{9}Be neutrons (open marker). The horizontal error bar for the simulated ^{241}Am^{9}Be neutrons indicates their neutron energy range. The thick horizontal line is the weighted average of τ from the bare neutrons at various energies, 213.47 μs.

Δt_{AmBe}. An exponential function plus a constant is fitted to the Δt_{AmBe} distribution in the range of $30\,\mu\mathrm{s} < \Delta t_{\mathrm{AmBe}} < 1.5\,\mathrm{ms}$, where the lower limit is chosen to avoid the period when ATWDs are more likely to be busy recording the first events. The fit yields $\tau = 205.44 \pm 0.60\,\mu\mathrm{s}$.

τ obtained with neutrons produced by the ^{241}Am^{9}Be source may slightly differ from that obtained with isolated neutrons because of neutron captures in the materials composing the ^{241}Am^{9}Be source and its deployment equipment. This possible bias is assessed with KLG4sim by simulating monoenergetic "bare" neutrons at various energies (1 keV, 0.01 MeV, 0.1 MeV, 1 MeV, 3 MeV, 5 MeV, and 7 MeV) and ^{241}Am^{9}Be neutrons with the deployment equipment, and comparing the resulting neutron capture times. Although the neutrons from inverse β-decays have energies between ~1 keV and ~0.1 MeV, bare neutrons with higher energies are simulated to confirm that the capture time is consistent for higher neutron energies that are relevant for background events for inverse β-decay detection (see Chapter 6). Figure 5.11 shows the resulting τ for these simulated neutrons; the estimated τ for neutrons at various energies are consistent. A weighted average of τ is calculated to be 213.47 μs, and the maximum τ deviation of 0.39 μs from the weighted average is taken as its error.

The simulated ^{241}Am^{9}Be neutrons yield τ of $212.96 \pm 0.65\,\mu$s. This is slightly lower than $213.47 \pm 0.39\,\mu$s from simulated bare neutrons. Approximately 1 % of the simulated ^{241}Am^{9}Be neutrons are captured on the source containment capsule, which contains mostly iron. Iron has an approximately ten times larger cross-section for neutron capture than protons, so the ^{241}Am^{9}Be neutrons are expected to have a slightly shorter mean capture time than bare neutrons. τ estimated from simulated neutrons are significantly higher than τ estimated from the ^{241}Am^{9}Be data, probably because KLG4sim uses a slightly inaccurate neutron capture cross-section. Therefore the fractional difference, rather than absolute difference, of $0.24 \pm 0.35\,\%$ between the estimated τ from the simulated bare neutrons and ^{241}Am^{9}Be neutrons is applied to the τ estimated using the ^{241}Am^{9}Be neutron data, which yields $205.93 \pm 0.94\,\mu$s.

This is consistent with $\tau_{\text{capture, spall}}$ of $206.53 \pm 0.11\,\mu$s estimated using the spallation neutrons in Section 4.2. Note, however, that this comparison is only a cross-check; since spallation neutrons have much higher energies than the inverse β-decay neutrons, different processes in the thermalization may result in different τs. In addition, the muons that produce the spallation, with their high charge deposit, may minutely affect the detector conditions for periods immediately following them, possibly affecting τ.

Using the estimated τ of $205.93 \pm 0.94\,\mu$s in Equations 5.5 and 5.6, $\varepsilon_{\Delta t}$ is estimated to be 0.98979 ± 0.00093.

5.10 E_{d} Cut Efficiency

More than 99 % of the neutrons created in inverse β-decays are captured on protons, creating 2.2 MeV γs. E_{vis} of these monoenergetic γs corresponds to ~2.4 MeV, which is smeared due to detector and E_{vis} reconstruction resolutions. The E_{d} Cut, $2.04\,\mathrm{MeV} < E_{\mathrm{d}} < 2.76\,\mathrm{MeV}$, is designed to have high efficiency for these events. When neutrons are captured on other nuclei in the detector, they create γs at different energies. Including the E_{vis} reconstruction resolution, the fraction, $f_{E_{\mathrm{d}},i}$, of γs created by the neutron captures on a nuclei of type i that pass E_{d} Cut depends on the γ energy. Therefore, the E_{d} Cut efficiency, $\varepsilon_{E_{\mathrm{d}}}$, is calculated from

$$\varepsilon_{E_{\mathrm{d}}} = \frac{\sum_i R_i\,\sigma_i\,f_{E_{\mathrm{d}},i}}{\sum_i R_i\,\sigma_i}, \tag{5.7}$$

where R_i and σ_i denote the target fraction and the cross-section for nuclei of type i, respectively. The target fractions, cross-sections, and capture γ energies of nuclei in the KamLAND scintillator are given in Table 5.2. Since $R_i\,\sigma_i$ for ^{1}H is much larger than that for all the other target nuclei, and $f_{E_{\mathrm{d}},i}$ is negligible for all but ^{1}H, Equation 5.7 can be approximated with

$$\varepsilon_{E_{\mathrm{d}}} \approx \frac{R_{^1\mathrm{H}}\,\sigma_{^1\mathrm{H}}\,f_{\mathrm{E_d},^1\mathrm{H}}}{\sum_i R_i\,\sigma_i}. \tag{5.8}$$

Table 5.2: Neutron capture targets in the KamLAND scintillator and their cross-sections and capture γ energies [27]. The errors are indicated in parentheses.

Target nuclei	Target fraction	(n,γ) reaction cross-section [mb]	γ energy [MeV]
^{1}H	0.6626(66)	332.6(7)	2.22
^{2}H	$9.94(67) \times 10^{-5}$	0.519(7)	6.25
^{12}C	0.3334(33)	3.53(7)	4.95
^{13}C	$3.71(11) \times 10^{-3}$	1.37(4)	8.17
^{14}N	$1.365(14) \times 10^{-4}$	7.50(75)	10.83
^{16}O	$6.76(7) \times 10^{-5}$	0.190(19)	4.14

The distribution of E_{d}, from monoenergetic γ with detector and E_{vis} reconstruction resolutions, is modeled by a Gaussian function. For a given mean, $\mu_{E_{\mathrm{d}}}$, and width, σ_{E_d}, f_{E_d} is given by

$$f_{E_\mathrm{d}} = \int_{2.04\,\mathrm{MeV}}^{2.76\,\mathrm{MeV}} \frac{1}{\sqrt{2\pi}\sigma_{E_\mathrm{d}}} \exp\left(-\frac{(x-\mu_{E_\mathrm{d}})^2}{2\sigma_{E_\mathrm{d}}^2}\right) dx. \tag{5.9}$$

The error on f_{E_d} due to uncertainties in μ_{E_d} and σ_{E_d} is calculated from

$$df_{E_\mathrm{d}} = \sqrt{\left(\frac{\partial f_{E_\mathrm{d}}}{\partial \sigma_{E_\mathrm{d}}} d\sigma_{E_\mathrm{d}}\right)^2 + \left(\frac{\partial f_{E_\mathrm{d}}}{\partial \mu_{E_\mathrm{d}}} d\mu_{E_\mathrm{d}}\right)^2}, \tag{5.10}$$

where $d\sigma_{E_\mathrm{d}}$ and $d\mu_{E_\mathrm{d}}$ denote errors on σ_{E_d} and μ_{E_d}, respectively, and

$$\begin{aligned} \frac{\partial f_{E_\mathrm{d}}}{\partial \sigma_{E_\mathrm{d}}} &= \int_{2.04\,\mathrm{MeV}}^{2.76\,\mathrm{MeV}} \frac{(x-\mu_{E_\mathrm{d}})^2 - \sigma_{E_\mathrm{d}}^2}{\sqrt{2\pi}\sigma_{E_\mathrm{d}}^4} \exp\left(-\frac{(x-\mu_{E_\mathrm{d}})^2}{2\sigma_{E_\mathrm{d}}^2}\right) dx \\ &= -\left[\frac{(x-\mu_{E_\mathrm{d}})}{\sqrt{2\pi}\sigma_{E_\mathrm{d}}^2} \exp\left(-\frac{(x-\mu_{E_\mathrm{d}})^2}{2\sigma_{E_\mathrm{d}}^2}\right)\right]_{x=2.04\,\mathrm{MeV}}^{2.76\,\mathrm{MeV}}, \end{aligned} \tag{5.11}$$

and

$$\begin{aligned} \frac{\partial f_{E_\mathrm{d}}}{\partial \mu_{E_\mathrm{d}}} &= \int_{2.04\,\mathrm{MeV}}^{2.76\,\mathrm{MeV}} \frac{x-\mu_{E_\mathrm{d}}}{\sqrt{2\pi}\sigma_{E_\mathrm{d}}^3} \exp\left(-\frac{(x-\mu_{E_\mathrm{d}})^2}{2\sigma_{E_\mathrm{d}}^2}\right) dx \\ &= -\left[\frac{1}{\sqrt{2\pi}\sigma_{E_\mathrm{d}}} \exp\left(-\frac{(x-\mu_{E_\mathrm{d}})^2}{2\sigma_{E_\mathrm{d}}^2}\right)\right]_{x=2.04\,\mathrm{MeV}}^{2.76\,\mathrm{MeV}}. \end{aligned} \tag{5.12}$$

Table 5.3: Fitted μ_{E_d}, corrected μ_{E_d}, and fitted σ_{E_d} in three different radius ranges.

Radius [m]	Fitted μ_{E_d} [MeV]	Corrected μ_{E_d} [MeV]	Fitted σ_{E_d} [MeV]
$r < 4.5$	2.3962 ± 0.0026	2.3813 ± 0.0065	0.1187 ± 0.0020
$4.5 < r < 5.5$	2.4196 ± 0.0029	2.4046 ± 0.0067	0.1117 ± 0.0025
$5.5 < r < 6.3$	2.4017 ± 0.0040	2.3868 ± 0.0072	0.1211 ± 0.0042

μ_{E_d} and σ_{E_d} are estimated using the spallation neutron capture events, which are distributed throughout the LS. Due to the slight bias in reconstructed $E_{\rm vis}$ as a function of positions, if all the spallation neutron-captures within the ID are used to estimate $\mu_{E_{\rm d}}$ and $\sigma_{E_{\rm d}}$, they would be biased toward $\mu_{E_{\rm d}}$ and $\sigma_{E_{\rm d}}$ values at high radius. To avoid over-weighting the $E_{\rm d}$ distribution at large radius, $E_{\rm d}$ distributions in three radial volumes, $r < 4.7\,{\rm m}$, $4.7\,{\rm m} < r < 5.5\,{\rm m}$, and $5.5\,{\rm m} < r < 6.3\,{\rm m}$, are obtained, and each of them is corrected for the $E_{\rm vis}$ reconstruction bias after muons, described in Section 3.3.1. Table 5.3 summarizes the results. The $f_{E_{\rm d}}$ is evaluated for each radial region to be 0.99728 ± 0.00049 ($r < 4.7\,{\rm m}$), 0.99872 ± 0.00032 ($4.7\,{\rm m} < r < 5.5\,{\rm m}$), and 0.9969 ± 0.0010 ($5.5\,{\rm m} < r < 6.3\,{\rm m}$). The overall $f_{E_{\rm d}}$ is calculated to be 0.99776 ± 0.00032 by weight-averaging these values according to the expected event fractions in these regions described in Section 5.4. Using the target fractions and cross-sections, $\varepsilon_{E_{\rm d}}$ is calculated to be

$$\begin{aligned}\varepsilon_{E_{\rm d}} &= (0.99466 \pm 0.00013)\, f_{E_{\rm d}} \\ &= 0.99243 \pm 0.00035. \end{aligned} \tag{5.13}$$

5.11 Efficiency Summary

Table 5.4 summarizes the $\bar{\nu}_{\rm e}$ detection efficiencies due to the various Candidate Selection Cuts described in this chapter.

Table 5.4: $\bar{\nu}_{\rm e}$ detection efficiencies.

Type	Efficiency	Error	Reference section
$\varepsilon_{N_{\rm Max\,ID}}$ $(\bar{\nu}_{\rm reactor})^a$	> 0.999954	< 0.000054	5.5 and G
$\varepsilon_{N_{\rm Max\,ID}}$ $(\bar{\nu}_{\rm geo})^a$	> 0.9984	< 0.0018	5.5 and G
$\varepsilon_{\rm recon}$	0.9987	0.0022	5.6 and H
$\varepsilon_{\rm spall}$	0.880880	0.000037	5.7
$\varepsilon_{\Delta R}$	0.9861	0.0060	5.8
$\varepsilon_{\Delta t}$	0.98979	0.00093	5.9
$\varepsilon_{E_{\rm d}}$	0.99243	0.00035	5.10

---

[a] $\varepsilon_{N_{\rm Max\,ID}}$ depends on the event type and period.

Table 5.5: Detection efficiency classes. The errors are indicated in parentheses.

Class	Efficiency	Included Efficiencies	Additional Errors
$\varepsilon_{\mathrm{common}}$	0.860(35)	$\varepsilon_{\mathrm{recon}}$, $\varepsilon_{\mathrm{spall}}$, $\varepsilon_{\Delta t}$, and $\varepsilon_{E_{\mathrm{d}}}$	σ, N_{p}, and livetime
$\varepsilon_{\mathrm{reactor}}$	0.986(34)	$\varepsilon_{N_{\mathrm{Max\,ID}}}$ and $\varepsilon_{\Delta R}$	Reactor systematics
$\varepsilon_{\mathrm{geo}}$	0.986	$\varepsilon_{N_{\mathrm{Max\,ID}}}$ and $\varepsilon_{\Delta R}$	

The various types of detection efficiencies are grouped into three classes: $\varepsilon_{\mathrm{common}}$, $\varepsilon_{\mathrm{reactor}}$, and $\varepsilon_{\mathrm{geo}}$, as summarized in Table 5.5. $\varepsilon_{\mathrm{common}}$ is the multiplication of the efficiencies that are common to detection of both $\bar{\nu}_{\mathrm{reactor}}$s and $\bar{\nu}_{\mathrm{geo}}$s. The error for $\varepsilon_{\mathrm{common}}$ also includes the inverse β-decay cross-section uncertainty (see Section 1.4), livetime uncertainty (see Section 5.1), and N_{p} uncertainty (see Section 5.2). $\varepsilon_{\mathrm{reactor}}$ is the multiplication of the efficiencies that apply only to the $\bar{\nu}_{\mathrm{reactor}}$ detection[4]. The error for $\varepsilon_{\mathrm{reactor}}$ also includes the reactor systematic error described in Section 6.1. $\varepsilon_{\mathrm{geo}}$ is the multiplication of the efficiencies that apply only to the $\bar{\nu}_{\mathrm{geo}}$ detection.

---

[4] $\varepsilon_{\Delta R}$ is separated for $\bar{\nu}_{\mathrm{reactor}}$ and $\bar{\nu}_{\mathrm{geo}}$ detection although the same central value of $\varepsilon_{\Delta R}$ is used for both, since this has the most variation as a function of E_{vis}.

Chapter 6

Signals and Backgrounds

The Candidate Selection Cuts described in Section 5.3 select inverse β-decays and their subsequent neutron captures from $\bar{\nu}_{\mathrm{reactor}}$s and $\bar{\nu}_{\mathrm{geo}}$s. After applying these cuts, a number of background events are expected to remain in the candidate list. The various event types are discriminated from each other using four observable quantities, E_{p}, E_{d}, Δt, and t (absolute time). In this chapter, the expected rate and spectra, or Probability Density Functions (PDFs) if normalized to unity, as a function of these four variables for the signal and background event types are discussed.

6.1 Anti-Neutrinos from Nuclear Reactors

Most of the event-pairs that pass the Candidate Selection Cuts described in Section 5.3 are expected to be inverse β-decays and their subsequent neutron captures from $\bar{\nu}_{\mathrm{reactor}}$s. As described in Section 1.3.1, the majority of $\bar{\nu}_{\mathrm{reactor}}$s are produced from β-decays following fission of ^{235}U, ^{238}U, ^{239}Pu, and ^{241}Pu in the nuclear reactor and β-decays of ^{106}Rh and ^{144}Pr in the reactor and in the spent fuel. Approximately 50 nuclear reactor cores operate in Japan located between 87 km and 830 km from the KamLAND site, and the calculation of the expected $\bar{\nu}_{\mathrm{reactor}}$ energy spectrum at the KamLAND site requires the knowledge of $\bar{\nu}_{\mathrm{reactor}}$ contribution from each isotope in each reactor. The instantaneous $\bar{\nu}_{\mathrm{reactor}}$ energy spectrum expected at the KamLAND site including the neutrino oscillation effect is calculated from

$$\frac{dN}{dE_{\bar{\nu}_e}}(E_{\bar{\nu}_e},\, t\,|\, \sin^2 2\theta_{12},\, \Delta m^2_{21}) = \sum_i \left[\frac{\sum_j f_{i,j}(t) \frac{dN_j}{dE_{\bar{\nu}_e}}(E_{\bar{\nu}_e})}{4\pi L_i^2} P_{\bar{\nu}_e \to \bar{\nu}_e}(E_{\bar{\nu}_e},\, L_i \,|\, \sin^2 2\theta_{12},\, \Delta m^2_{21}) \right], \tag{6.1}$$

where i goes over each nuclear reactor site, j goes over each contributing isotope (^{235}U, ^{238}U, ^{239}Pu, and ^{241}Pu fission chains, and ^{106}Ru and ^{144}Ce long-lived isotopes), $f_{i,j}(t)$ denotes the instantaneous rate of β-decays following the fission of ^{235}U, ^{238}U, ^{239}Pu, and ^{241}Pu or the instantaneous β-decay rate for ^{106}Ru and ^{144}Ce for reactor i, $\frac{dN_j}{dE_{\bar{\nu}_e}}(E_{\bar{\nu}_e})$ denotes the energy spectrum of $\bar{\nu}_e$s from isotope j (see Figure 1.1), L_i denotes the distance between reactor site i and KamLAND, and $P_{\bar{\nu}_e \to \bar{\nu}_e}(E_{\bar{\nu}_e},\, L_i \,|\, \sin^2 2\theta_{12},\, \Delta m^2_{21})$ denotes the neutrino oscillation survival probability (see Equation 1.5).

Each Japanese nuclear reactor company provides Tohoku University, as a member of the KamLAND collaboration, the data on the thermal power and fuel cycle of each nuclear reactor core in Japan. They provide this data on a weekly basis during stable operation, and on an hourly basis when the reactor shuts down or powers up. Tokyo Electric Power Company, Inc. and Tohoku University calculate the fission rates of ^{235}U, ^{238}U, ^{239}Pu, and ^{241}Pu for each day using this data and their burn-up model[1]. The fuel composition is estimated with an accuracy of 1 %, and the thermal power output of the reactors is measured with an accuracy of 2 %.

As described in Section 1.3.1, β-decays of ^{106}Rh and ^{144}Pr in the reactor and the spent fuel also contribute a small yet not entirely ignorable flux, ~1 %, of $\bar{\nu}_{\text{reactor}}$s detectable with KamLAND. ^{106}Rh and ^{144}Pr are daughter nuclei in the decay chains of ^{106}Ru and ^{141}Ce, which have relatively long half-lives of 373.6 days and 284.9 days, respectively. The $\bar{\nu}_{\text{reactor}}$ contributions from ^{106}Rh and ^{144}Pr are estimated using the history of the fission rate of each fuel isotope for each reactor site, the known fission yields of ^{106}Ru and ^{141}Ce [56], and their half-lives. An approximation has to be made for the history of the fission rates before KamLAND operation began since the fuel

---

[1] The data is provided under a special agreement between the power company and Tohoku University. The reactor operators prohibit third parties accessing this model to calculate the fission rate of each isotope.

cycle data for this period are not available. Constant fission rates of ^{235}U, ^{238}U, ^{239}Pu, and ^{241}Pu, obtained by averaging their fission rates in the first 9 months of KamLAND operation, is assumed. The $\bar{\nu}_{\text{reactor}}$s from the spent fuel are assumed to traverse the same distance between the reactors, from which the fuel was removed, and KamLAND since spent fuel is typically stored near the reactor for approximately 10 years, much longer than the half-lives of ^{106}Ru and ^{141}Ce.

The $\bar{\nu}_{\text{reactor}}$ flux from nuclear reactors in Korea is estimated with a 10 % error from the electricity generation records assuming that the fuel composition of Korean reactors is the same as the average composition of the reactors in Japan. The $\bar{\nu}_{\text{reactor}}$s from the Korean reactors contribute approximately 3.4 % of the expected $\bar{\nu}_{\text{reactor}}$ flux at the KamLAND site assuming no neutrino oscillation. The $\bar{\nu}_{\text{reactor}}$ flux contribution from reactors outside of Japan and Korea are approximated with a 50 % error by placing one reactor for each country whose $\bar{\nu}_{\text{reactor}}$ flux is estimated from the reported electrical power produced in nuclear reactors. Together, all these reactors contribute approximately 1% of the expected $\bar{\nu}_{\text{reactor}}$ flux at the KamLAND site, assuming no neutrino oscillation.

The total systematic error on the expected $\bar{\nu}_{\text{reactor}}$ flux at the KamLAND site is 3.4 % obtained by combining the 1 % error from fuel composition uncertainty, the 2 % error from thermal power uncertainty, the 0.6 % error from the non-Japanese reactor contribution uncertainty, and the 2.5 % error from the $\frac{dN_j}{dE_{\bar{\nu}_e}}$ uncertainty (see Section 1.3.1). Note here that error on the $\bar{\nu}_{\text{reactor}}$ flux is important for the $\sin^2 2\theta_{12}$ measurement, and has less effect on Δm^2_{21} measurement since Δm^2_{21} is sensitive mostly to the E_{p} spectral distortion.

The expected E_{p} spectrum for $\bar{\nu}_{\text{reactor}}$s is obtained by multiplying the $\bar{\nu}_{\text{reactor}}$ energy spectrum from Equation 6.1 with the inverse β-decay cross-section (see Figure 1.6), and converting the product into a E_{vis} spectrum as discussed in Section 3.4. Figure 6.1 shows the expected $\bar{\nu}_{\text{reactor}}$ E_{p} spectra for various neutrino oscillation parameters, obtained by using the central energy parameter values (see Section 3.4) and a detection efficiency of 1, and separately integrating over period I and II.

The E_{d} and Δt PDFs are obtained from measurements of actual neutron captures since the delayed events of the $\bar{\nu}_{\text{reactor}}$ signal are captures of neutrons created in inverse

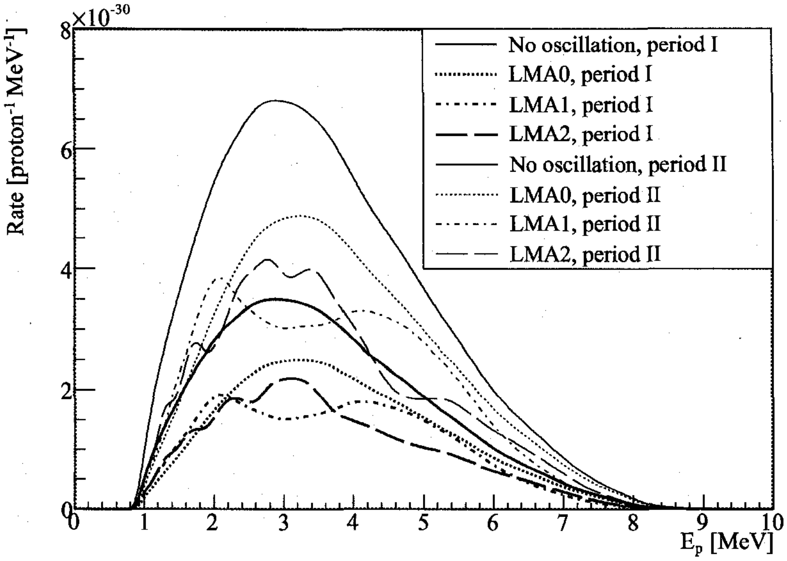

Figure 6.1: Expected $\bar{\nu}_{\text{reactor}}$ E_{p} spectra based on the estimated central values of the energy parameters in Section 3.4 for various neutrino oscillation parameters. The instantaneous spectra are integrated over period I and II. The expected $\bar{\nu}_{\text{reactor}}$ E_{p} spectra assuming no neutrino oscillation, and assuming oscillation with $\tan^2\theta_{12} = 0.45$ and $\Delta m^2_{21} = 1 \times 10^{-5}\text{eV}^2$ (LMA0), $8 \times 10^{-5}\text{eV}^2$ (LMA1), and $2 \times 10^{-4}\text{eV}^2$ (LMA2) are shown.

β-decays. The E_{d} PDF is well-modeled by a Gaussian function, and its mean and sigma are obtained from the spallation neutron capture E_{vis}. The E_{vis} distributions of the γs emitted from neutron captures on protons are calculated in three concentric regions, $r < 4.7\,\text{m}$, $4.7\,\text{m} < r < 5.5\,\text{m}$, and $5.5\,\text{m} < r < 6.3\,\text{m}$, as described in Section 5.10. These three distributions are weight-averaged according to the expected event fractions in these regions, described in Section 5.4, and corrected for the E_{vis} reconstruction bias after muons, described in Section 3.3.1. This yields a mean of $2.390 \pm 0.022\,\text{MeV}$ and a sigma of $0.1164 \pm 0.0018\,\text{MeV}$ for the Gaussian function, modeled for the E_{d} PDF. The Δt PDF is well-modeled by an exponential function, and its mean decay time is estimated to be $205.93 \pm 0.94\,\mu\text{s}$ using $^{241}\text{Am}^9\text{Be}$ source neutrons, as described in Section 5.9.

The expected $\bar{\nu}_{\text{reactor}}$ detection rate varies significantly as a function of time due to

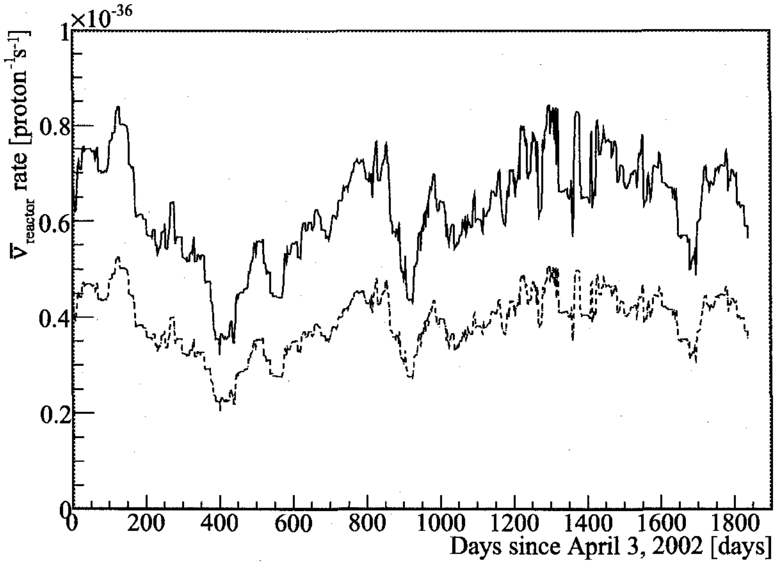

Figure 6.2: Expected $\bar{\nu}_{\rm reactor}$ detection rate as a function of time, integrated over $E_{\rm p}$, assuming a detection efficiency of 1. The solid and dotted lines indicate the $\bar{\nu}_{\rm reactor}$ detection rates assuming no neutrino oscillation and neutrino oscillation with $\sin^2 2\theta_{12} = 0.8$ and $\Delta m^2_{21} = 8 \times 10^{-5}\,{\rm eV}^2$, respectively.

the nuclear reactor operation variation, which can help discriminating $\bar{\nu}_{\rm reactor}$ signals from all the other event types. Figure 6.2 shows the time variation of the expected $\bar{\nu}_{\rm reactor}$ detection rate, integrated over $E_{\rm p}$, assuming no detection inefficiency.

6.2 Anti-Neutrinos from the Earth

Another type of signals is $\bar{\nu}_{\rm geo}$s produced inside the Earth by β-decays of isotopes in the ^{238}U and ^{232}Th decay chains. Based on any Earth model that describes the distribution and concentration of isotope i in the Earth, the expected detection rate of $\bar{\nu}_{\rm geo}$s with KamLAND is calculated per unit time per target proton by

$$\Phi_i = \varepsilon \iint A_i \, \frac{a_i(\mathbf{L})\,\rho(\mathbf{L})}{4\pi|\mathbf{L}|^2} \, P_{\bar{\nu}_{\rm e}\to\bar{\nu}_{\rm e}}(E_{\bar{\nu}_{\rm e}}, |\mathbf{L}|)\, \sigma(E_{\bar{\nu}_{\rm e}}) \, \frac{dN_i}{dE_{\bar{\nu}_{\rm e}}}(E_{\bar{\nu}_{\rm e}})\, d\mathbf{L}\, dE_{\bar{\nu}_{\rm e}}, \tag{6.2}$$

where $\varepsilon = \varepsilon_{\mathrm{common}}\, \varepsilon_{\mathrm{geo}}\, \varepsilon_{E_{\mathrm{p}}}{}^{2}$, A_i denotes the decay rate per unit mass ($A_{^{238}\mathrm{U}} = 1.24 \times 10^{7}\,\mathrm{s}^{-1}\mathrm{kg}^{-1}$ and $A_{^{232}\mathrm{Th}} = 0.41 \times 10^{7}\,\mathrm{s}^{-1}\mathrm{kg}^{-1}$), $\mathbf{L}$ denotes the position relative to the KamLAND site, $a_i(\mathbf{L})$ denotes the isotope mass concentration at position $\mathbf{L}$, $\rho(\mathbf{L})$ denotes the rock density, $P_{\bar{\nu}_{\mathrm{e}}\to\bar{\nu}_{\mathrm{e}}}(E_{\bar{\nu}_{\mathrm{e}}}, |\mathbf{L}|)$ denotes the survival probability due to neutrino oscillation (see Equation 1.5), $\sigma(E_{\bar{\nu}_{\mathrm{e}}})$ is the inverse β-decay cross-section (see Figure 1.6), and $\frac{dN_i}{dE_{\bar{\nu}_{\mathrm{e}}}}(E_{\bar{\nu}_{\mathrm{e}}})$ denotes the $\bar{\nu}_{\mathrm{geo}}$ energy spectrum (see Figure 1.4). The integral of $d\mathbf{L}$ is over the volume of the Earth, and the integral of $dE_{\bar{\nu}_{\mathrm{e}}}$ is over all energy. Since the production points of $\bar{\nu}_{\mathrm{geo}}$s are spread out within the Earth, the $\sin^2\left(\frac{1.27\Delta m^2_{21}[\mathrm{eV}^2]\mathrm{L}[\mathrm{m}]}{E_\nu[\mathrm{MeV}]}\right)$ term in $P_{\bar{\nu}_{\mathrm{e}}\to\bar{\nu}_{\mathrm{e}}}(E_{\bar{\nu}_{\mathrm{e}}}, |\mathbf{L}|)$ averages out to 0.5, and Equation 6.2 can be approximated with

$$\Phi_i \approx \varepsilon\,\left(1 - 0.5\sin^2 2\theta_{12}\right)\, I_i \int A_i\, \frac{a_i(\mathbf{L})\,\rho(\mathbf{L})}{4\pi|\mathbf{L}|^2}\, d\mathbf{L}, \tag{6.3}$$

where

$$\begin{aligned} I_i &\equiv \int \sigma(E_{\bar{\nu}_{\mathrm{e}}})\, \frac{dN_i}{dE_{\bar{\nu}_{\mathrm{e}}}}(E_{\bar{\nu}_{\mathrm{e}}})\, dE_{\bar{\nu}_{\mathrm{e}}} \\ &= 2.55 \times 10^{-44}\, \frac{\bar{\nu}_{\mathrm{geo}}\mathrm{s\ cm}^2}{^{238}\mathrm{U\ decay}} \\ &\text{or} \\ &= 5.16 \times 10^{-45}\, \frac{\bar{\nu}_{\mathrm{geo}}\mathrm{s\ cm}^2}{^{232}\mathrm{Th\ decay}}. \end{aligned} \tag{6.4}$$

Equation 6.3 can be rewritten as

$$\Phi_i = \varepsilon\,\left(1 - 0.5\sin^2 2\theta_{12}\right)\Phi_{\mathrm{effective},\,i}, \tag{6.5}$$

where

$$\Phi_{\mathrm{effective},\,i} \equiv I_i \int A_i\, \frac{a_i(\mathbf{L})\,\rho(\mathbf{L})}{4\pi|\mathbf{L}|^2}\, d\mathbf{L}. \tag{6.6}$$

$\Phi_{\mathrm{effective},\,i}$ denotes the effective $\bar{\nu}_{\mathrm{geo}}$ detection rate, independent of the detection efficiency and neutrino oscillation parameter, $\sin^2 2\theta_{12}$. $\Phi_{\mathrm{effective},\,i}$ only depends on the Earth model since the uncertainty on the inverse β-decay cross-section is included

---

[2] $\varepsilon_{E_{\mathrm{p}}}$ is applied during the fit. See Chapter 7 for more details.

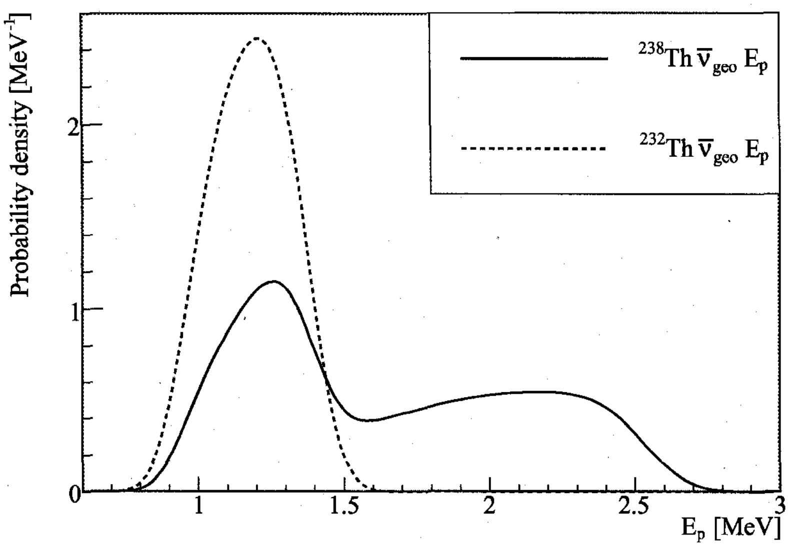

Figure 6.3: ^{238}U and ^{232}Th $\bar{\nu}_{\text{geo}}$ E_{p} PDFs based on the estimated central values of the energy parameters in Section 3.4.

in the detection efficiency, as described in Section 5.11. Based on $a_i(\mathbf{L})$ and $\rho(\mathbf{L})$ derived from the Earth model described in Section 1.3.2, the expected $\Phi_{\text{effective}, {}^{238}\text{U}}$ and $\Phi_{\text{effective}, {}^{232}\text{Th}}$ are 49 and 12 $(10^{32}\,\text{p} \cdot \text{yr})^{-1}$ (per 10^{32} target protons per year), respectively. If the Earth is "fully radiogenic," i.e., all the measured heat dissipation rate at the surface of the Earth, 44.2 TW, comes from power generated by the radioactivity in the Earth, $\Phi_{\text{effective}, {}^{238}\text{U}}$ and $\Phi_{\text{effective}, {}^{232}\text{Th}}$ can range from 79 to 114 and 19 to 28 $(10^{32}\,\text{p} \cdot \text{yr})^{-1}$, respectively. Here, the lower bounds are the case where all the excess radioactivity compared to the Earth model described in Section 1.3.2 is in the mantle, and the upper bounds are the case where the radioactivity is fractionally increased in the various sections of the Earth, while keeping the mass ratios among ^{232}Th, ^{238}U and other isotopes, mainly ^{40}K, constant in both cases. Note here that models with quite different $a_i(\mathbf{L})$ and $\rho(\mathbf{L})$ can be accommodated by the same data if the resulting $\Phi_{\text{effective}, i}$ are the same.

The expected E_{p} spectra for $\bar{\nu}_{\text{geo}}$ are obtained by converting the $\bar{\nu}_{\text{geo}}$ energy spectra given in Figure 1.8 into E_{vis} spectra as described in Section 3.4. Figure 6.3 shows the expected $\bar{\nu}_{\mathrm{geo}}$ E_{p} PDFs obtained by using the central values of the energy parameters (see Section 3.4).

The E_{d} and Δt PDFs for neutron captures following the inverse β-decays from $\bar{\nu}_{\mathrm{geo}}$s are the same as those from $\bar{\nu}_{\mathrm{reactor}}$s (see Section 6.1). Given that half-lives of ^{238}U and ^{232}Th are 4.47×10^9 and 14.0×10^9 years, respectively, and the timescale of changes in the Earth structure is large, the t PDF for $\bar{\nu}_{\mathrm{geo}}$ is assumed to be constant.

6.3 Random Coincidence Background

The largest background arises from random coincidences; two uncorrelated events from radioactivity in the LS that happened to be temporally and spatially nearby can pass the Candidate Selection Cuts, described in Section 5.3.

The expected number and PDFs of such random event-pairs, N_{random}, is estimated directly by using the data acquired in all the good runs:

$$N_{\mathrm{random}} = N_{\Delta t}\, P_{\mathrm{other}}, \tag{6.7}$$

where $N_{\Delta t}$ is the number of uncorrelated events that form timing coincidences, estimated using the events in all the good runs organized into multiplets (see Section 3.6). P_{other} is the probability of randomly paired events passing the Candidate Selection Cuts (see Section 5.3), except the Δt Cut, and is estimated from

$$P_{\mathrm{other}} = \frac{N_{\mathrm{other}}}{N_{\mathrm{paired}}}, \tag{6.8}$$

where N_{paired} denotes the number of randomly paired events, and N_{other} denotes the number of these randomly paired events that pass the Candidate Selection Cuts, except the Δt Cut.

Before events are randomly paired, a list of unpaired or "singles events" is generated for each good run. To keep the data volume manageable, events that fail the $N_{\mathrm{Max\,ID}}$ Cut or Reconstruction Status Cut (see Section 5.3.1), or events with E_{vis} less than 0.8 MeV or reconstructed radius greater than 6.5 m are discarded from this

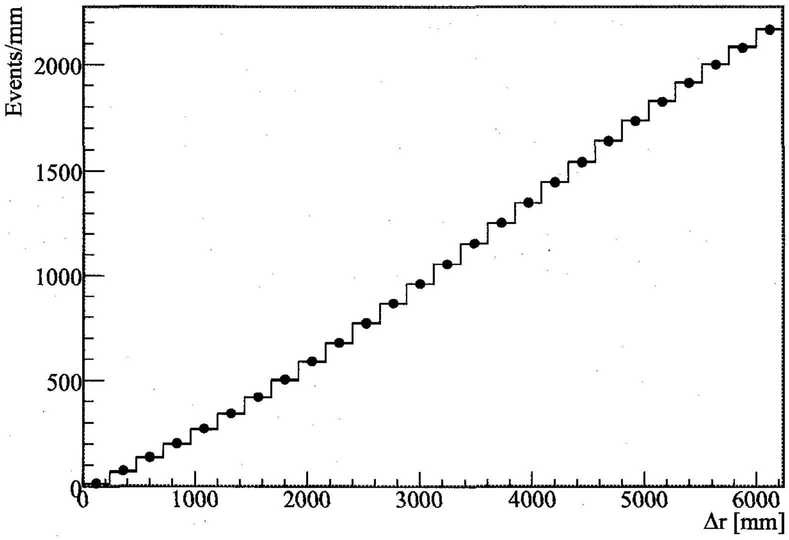

Figure 6.4: Δr distributions of event-pairs in timing coincidence used for the $N_{\Delta t}$ estimation (solid line), and a subset of randomly paired events counted for N_{paired} (dots with error bars). The distribution for the randomly paired events is normalized to the integral in the range of $1500\,\text{mm} < \Delta r < 6000\,\text{mm}$.

singles event list. To ensure that $N_{\Delta t}$ and P_{other} are calculated from the same initial event sets, these cuts also are applied to the events organized into multiplets, used for the $N_{\Delta t}$ estimation.

To avoid correlated events due to noisy periods or muons and their spallation products from being counted in the estimation of $N_{\Delta t}$, the Multiplet Cut (see Section 5.3.1) and the Cosmogenic Spallation Cuts (see Section 5.3.2) are applied to the events organized into multiplets. These cuts should also be applied to the singles events to ensure that correlated events do not alter P_{other}. However, the Multiplet Cut is difficult to apply to the singles events, so it is ignored. The consequence of ignoring this cut is negligible since the overwhelming majority of singles events that pass the Muon Cut, as a part of the Cosmogenic Spallation Cuts, would not form a multiplet with more than 10 entries. The Muon Cylinder Cut is not applied to the singles events at this stage since they do not have well-defined "prompt events," which are needed to apply this cut.

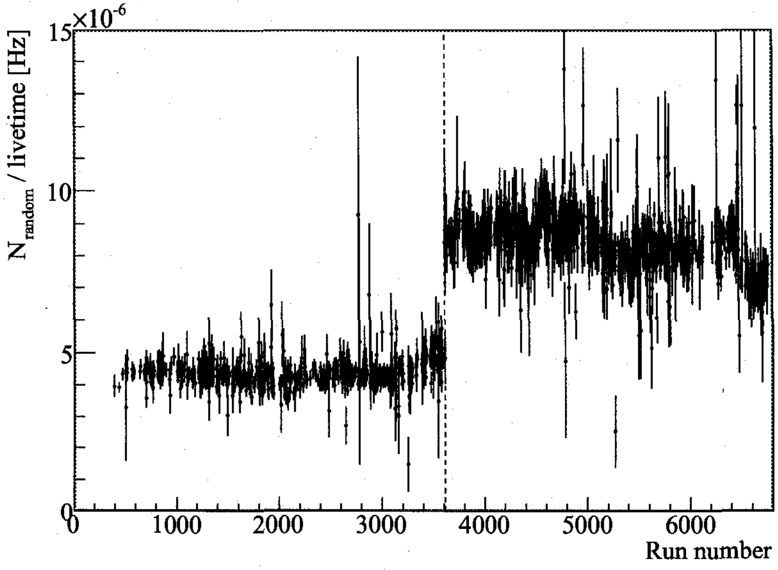

Figure 6.5: N_{random} per livetime for each good run. The vertical dotted line separates period I and II.

After the above cuts are applied to the singles events, N_{paired} for each good run is obtained by repeating the process of randomly associating two singles events, recorded anytime within a run, to form a "prompt-delayed" event-pair. If the prompt event of a pair fails the Muon Cylinder Cut, the pair is discarded and not counted towards N_{paired}. In order to avoid pairing the same events multiple times while generating sufficient number of event-pairs, random event-pairs are generated until N_{paired} is 20 times the number of singles events remaining after applying all the cuts described above, excluding the Muon Cylinder Cut, in each run.

$N_{\Delta t}$ is estimated from the number of event-pairs in the multiplets that pass the Δt Cut after the various cuts described above are applied to the multiplets. To assess the degree of correlated-event contamination in the selected event-pairs, the distribution of distance between these event-pairs, Δr, is compared to that for a subset of randomly paired events, which are counted for N_{paired}, as shown in Figure 6.4. This shows that these distributions are in good agreement, indicating no sign of spatial correlations between the pairs in timing coincidence. Therefore, the contamination of correlated event-pairs counted in the $N_{\Delta t}$ estimation is assumed negligible.

The total number of random coincidence background event-pairs estimated in period I and II are 202.30 ± 0.35 and 653.41 ± 0.74, respectively. The expected number in period II is larger since the livetime is larger, and the E_p and $N_{\mathrm{Max\,ID}}$ thresholds are lower for period II. Figure 6.5 shows N_random divided by the livetime of each good run. The time dependence is assumed negligible within each period since Figure 6.5 shows stability of N_random rate within each period. The expected E_p and E_d PDFs are obtained from the distributions of the events counted for N_other. Figure 6.6 shows the expected E_p spectra, normalized to the expected rates, and the E_d PDFs. Since the prompt-delayed event-pairs from this background type are not temporarily correlated by definition, the expected Δt spectrum is flat.

6.3.1 Random Coincidence Background Cross-Check

The method of calculating the expected number and E_p, E_d, and Δt spectra for the random coincidence background event-pairs is cross-checked using the Candidate Selection Cuts except $1\,\mathrm{ms} < \Delta t < 1.5\,\mathrm{ms}$, instead of $0.5\,\mu\mathrm{s} < \Delta t < 1\,\mathrm{ms}$. Since neutrons are captured with a mean capture time of $\sim 200\,\mu s$, most neutrons are captured before the start of this alternative Δt window. Therefore the event-pairs selected with the modified candidate selection cuts should select mostly random coincidence event-pairs. The expected random coincidence event-pairs in this Δt window in period I and II are 101.55 ± 0.18 and 328.25 ± 0.38 while 97 and 306 event-pairs pass the modified candidate selection cuts, respectively. Figure 6.7 shows the expected E_p, E_d, and Δt spectra and data for random coincidence event-pairs in the $1\,\mathrm{ms} < \Delta t < 1.5\,\mathrm{ms}$ window. Although the statistics are rather low, there is no indication of significant disagreement between the data and the expected number of event-pairs and spectra.

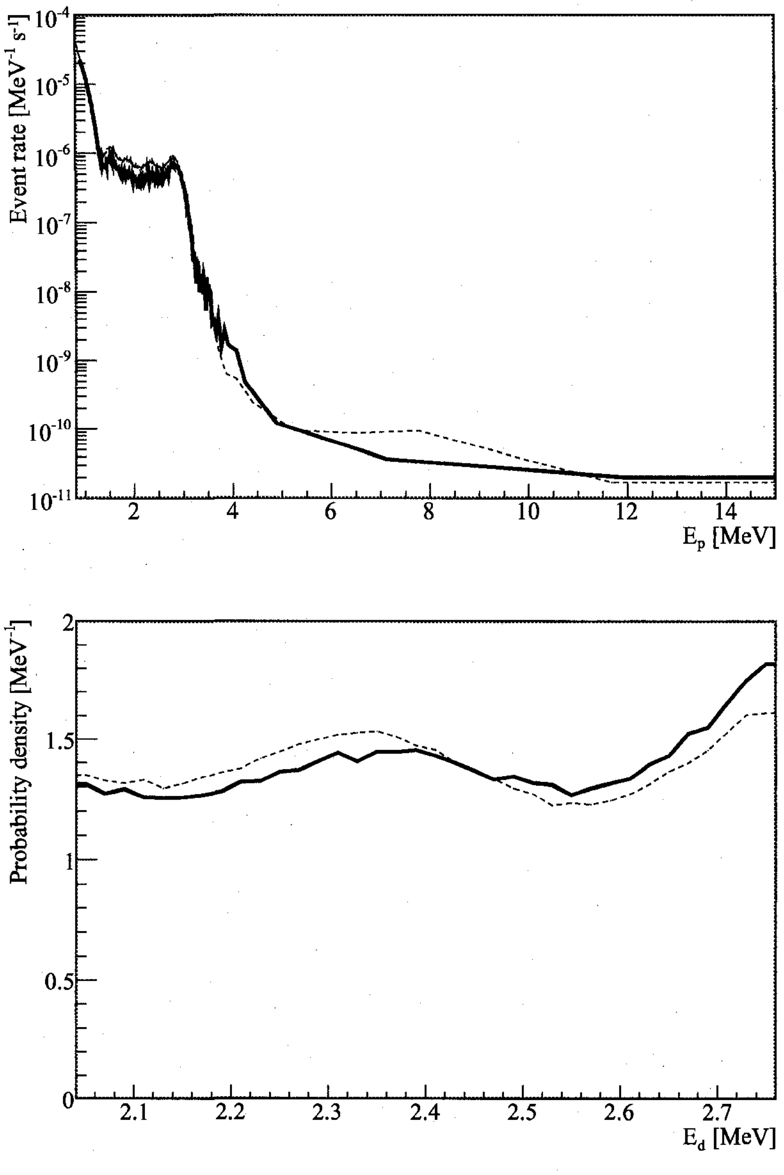

Figure 6.6: Random coincidence background E_p spectra normalized to the expected event rates (top plot) and E_d PDFs (bottom plot) for period I (solid thick line) and period II (dotted line).

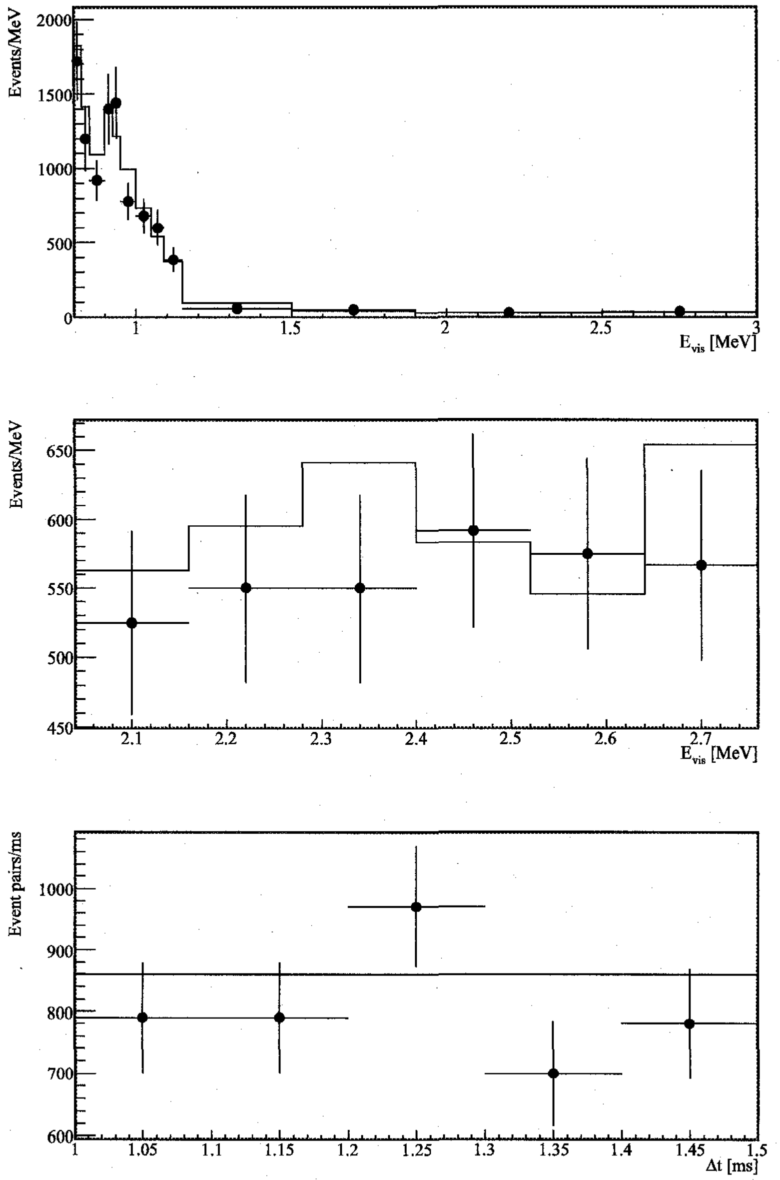

Figure 6.7: Random coincidence background spectra cross-check. The top, middle, and bottom plots show E_{p}, E_{d}, and Δt spectra, respectively. The data points are for the event-pairs which pass the Candidate Selection Cuts except that Δt is chosen from $1\,\mathrm{ms} < \Delta t < 1.5\,\mathrm{ms}$. The solid curves are the expected spectra for the random coincidence event-pairs in the $1\,\mathrm{ms} < \Delta t < 1.5\,\mathrm{ms}$ window.

6.4 ^{13}C(α, n) Background

Radioactivity in the detector causes another type of backgrounds, "^{13}C(α, n) background events." α particles can sometimes interact with naturally occurring ^{13}C in the LS, causing ^{13}C(α, n) reactions, which combined with the thermalization and capture of the produced neutron can mimic prompt-delayed event-pairs from inverse β-decays and their subsequent neutron captures.

The main source of α particles is ^{210}Po decays in the LS. ^{222}Rn, which was unintentionally introduced into the detector during the detector construction, has decayed into ^{210}Pb. This ^{210}Pb is distributed throughout the detector and decays into ^{210}Po with a half-life of 22.3 years[3]. With a half-life of 138 days, the ^{210}Po α-decays, producing α particles with a kinetic energy of 5.3 MeV, which is quenched to E_{vis} of ~0.3 MeV, well below the analysis E_{vis} threshold. However, when α particles interact with ^{13}C, they can cause events with high enough E_{vis} to be seen above the threshold.

With an initial α energy of 5.3 MeV, the ^{13}C(α, n) reaction can produce ^{16}O in the ground, first, or second excited state. When ^{16}O is created in the ground state, the neutron is emitted with energy between ~2.5 and ~7.5 MeV. Most of the neutrons thermalize via elastic scatterings with protons. However, some high energy neutrons can also lose energy via inelastic scattering with a ^{12}C, emitting a 4.439 MeV γ. When ^{16}O is created in the first excited state, the ^{16}O returns to the ground state by internal pair conversion, emitting an electron-positron pair with a total energy of 6.049 MeV. When ^{16}O is created in the second excited state, the ^{16}O returns to the ground state by emitting a 6.130 MeV γ. The neutrons created in the ^{13}C(α, n)^{16}O* reactions, which have very low energy, thermalize via elastic scatterings.

Event rate of ^{13}C(α, n) reactions depends on activity of the ^{210}Po α-decays, which can be estimated from a peak in the E_{vis} spectrum caused by the α particles. Since E_{vis} of the α particles is very low, ~0.3 MeV, the E_{vis} reconstruction algorithm may not have high enough reconstruction efficiency or accuracy for the ^{210}Po activity measurement. Instead, the activity of the ^{210}Po α-decays is estimated using the

---

[3] See Figure 1.3 for the decay chain of ^{222}Rn that eventually decays to ^{210}Po.

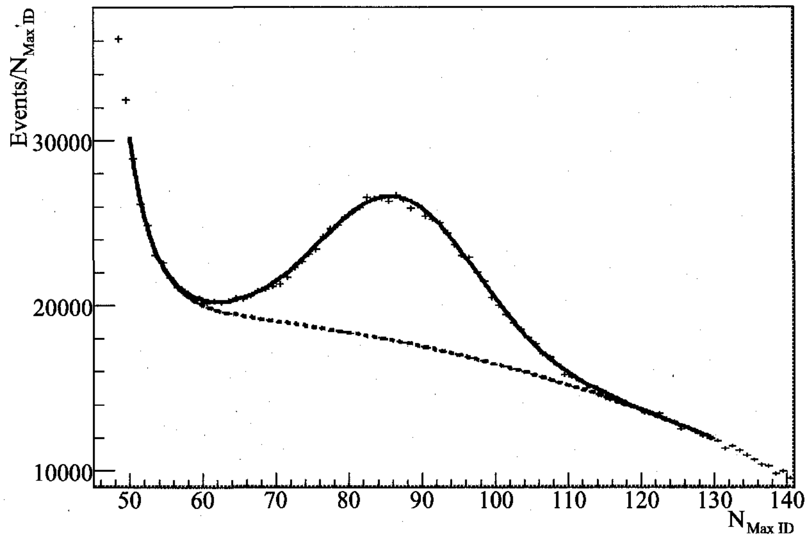

Figure 6.8: ^{210}Po α-decay peak in the $N_{\mathrm{Max\,ID}}$ distribution from run 3888, which has a special low N_{ID} threshold. The distribution is fitted from $N_{\mathrm{Max\,ID}}$ of 50 to 130 with an exponential plus a second order polynomial for background and a Gaussian for the ^{210}Po α events (solid line). The background functions are shown as a dotted line. The $\chi^2/n.d.f.$ of this fit is 82.5/72.

$N_{\mathrm{Max\,ID}}$ spectrum from special runs with low N_{ID} threshold since $N_{\mathrm{Max\,ID}}$ becomes a good indicator for E_{vis} without much position dependence at such a low E_{vis}. The Gaussian-shaped ^{210}Po peak in the $N_{\mathrm{Max\,ID}}$ distribution of all events recorded is visible above the spectrum of other background events, mainly ^{85}Kr β-decays, as shown in Figure 6.8. Since it is difficult to estimate the spectral shape of other background events, the $N_{\mathrm{Max\,ID}}$ spectral shape is modeled by a Gaussian function for the ^{210}Po peak, and a second order polynomial plus an exponential for the other background.

Estimation of the ^{210}Po α-decay activity inside the fiducial volume must rely on the position reconstruction, which has non-negligible reconstruction inefficiency and significant bias for such low E_{vis}. To reduce inefficiency for the ^{210}Po activity study, all "acceptably reconstructed events," which include events with somewhat degraded position reconstruction quality unless "Unknown", "Not valid," or "Bad" position reconstruction status is set (see Appendix D), are considered. A systematic

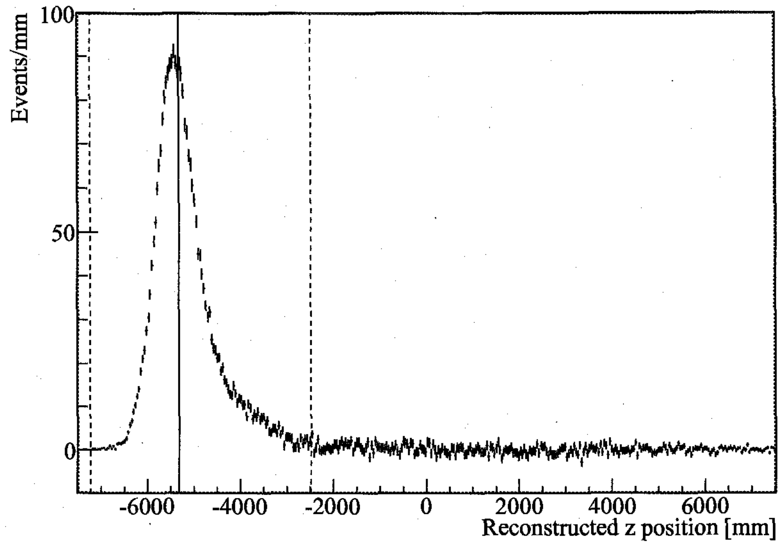

Figure 6.9: Reconstructed z-position distribution of events from the ^{203}Hg source deployed at -5.5 m. The dotted vertical lines indicate the range from which the median (solid vertical line) is calculated.

error on the estimated ^{210}Po activity due to reconstruction inefficiency is estimated by comparing the activities estimated from all events recorded and the "acceptably reconstructed events" without the fiducial volume cut. The position reconstruction bias at the fiducial volume boundary, 5.5 m, is estimated using the reconstructed position distribution of the events from the ^{203}Hg source deployed at ±5.5 m along the z-axis of the detector since its E_{vis}, ~0.24 MeV, is close to that of ^{210}Po α particles, ~0.3 MeV. Figure 6.9 shows the distribution of reconstructed z-positions for ^{203}Hg deployed at -5.5 m. The medians of the reconstructed positions of the events from the ^{203}Hg source deployed at -5.5 m and 5.5 m are -5.32 m and 5.25 m, respectively, the absolute values of which are used as upper and lower limits for the fiducial volume radius. The medians, as opposed to the means or modes, are appropriate here since the reconstructed position distributions of the events are not necessarily symmetrical about the means or modes. The average of the ^{210}Po activities within these fiducial volume limits is taken as the central value, and the difference divided by two is taken as its systematic error.

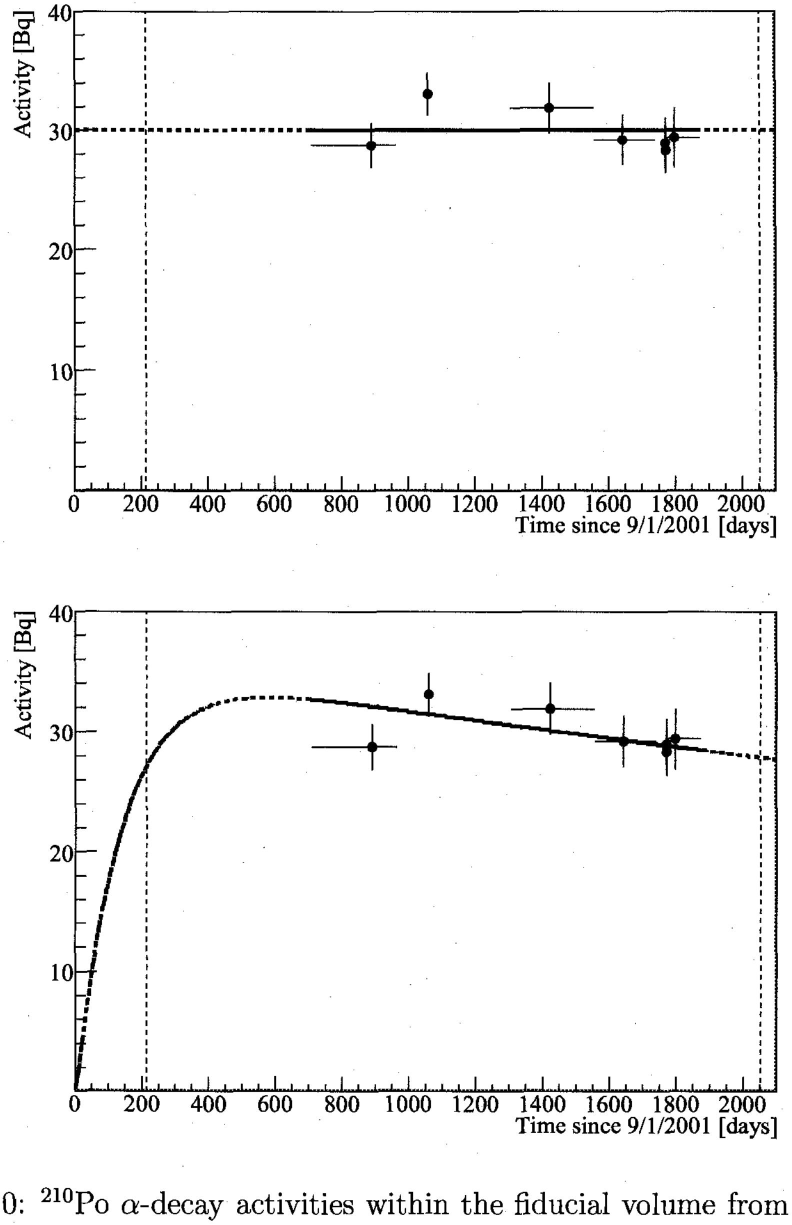

Figure 6.10: ^{210}Po α-decay activities within the fiducial volume from the periods in the seven sets of runs. A constant is fitted to the data in the top plot, yielding a constant activity of 30.03 ± 0.77 Bq with a $\chi^2/n.d.f.$ of 5.4/6. A model accounting for ^{210}Po build-up and decay, described by Equation 6.9, is used in the bottom plot yielding a normalization factor of 35.17 ± 0.91 Bq and a $\chi^2/n.d.f.$ of 5.4/6.

Table 6.1: Fitted ^{210}Po α-decay activities in seven sets of runs. The fitted numbers of ^{210}Po α-decays are divided by the livetimes. The values in the second column are from all events recorded, and those in the third column are from the "acceptably reconstructed events." The activities within the fiducial volume are estimated using the lower (4th column) and upper (5th column) limits for the fiducial volume radius corresponding to 5.5 m for ^{210}Po α-decays.

Run number	All [Bq]	Reconstructed [Bq]	$r < 5.25\,\mathrm{m}$ [Bq]	$r < 5.32\,\mathrm{m}$ [Bq]
2783 to 3615	83.6 ± 2.3	83.1 ± 2.3	28.2 ± 1.3	29.3 ± 1.3
3888	94.3 ± 2.1	94.1 ± 2.3	32.5 ± 1.2	33.7 ± 1.2
4493 to 5147	92.7 ± 2.6	90.9 ± 2.7	31.3 ± 1.4	32.5 ± 1.5
5152 to 5671	91.8 ± 2.5	89.7 ± 2.5	28.5 ± 1.3	29.9 ± 1.3
5757	88.6 ± 2.4	86.3 ± 2.4	28.3 ± 1.3	29.6 ± 1.4
5767	90.1 ± 2.3	88.2 ± 2.4	27.7 ± 1.2	28.9 ± 1.2
5778 to 6276	85.4 ± 3.2	82.7 ± 3.1	28.9 ± 1.9	29.8 ± 1.9

There are many low-N_{ID} threshold runs throughout the data-set analyzed in this thesis. These runs are divided into seven sets, by combining short runs to gain statistics while leaving three long runs by themselves. For each set, the activities of ^{210}Po α-decays are estimated as shown in Table 6.1. As a function of time since September 1st, 2001, Figure 6.10 shows the estimated ^{210}Po activities inside the fiducial volume, including the systematic errors due to the position reconstruction efficiency and bias calculated for each set of runs. The top plot shows a fit to a constant yielding an average ^{210}Po activity within the fiducial volume of 30.03 ± 0.77 Bq. The bottom plot in Figure 6.10 shows the fit to the model of the activity build-up and decay described by the function:

$$
\begin{aligned}
A\,\lambda_{\mathrm{Bi}}\,\lambda_{\mathrm{Po}} \quad \times \quad & \left[\frac{e^{-\lambda_{\mathrm{Pb}}\,t}}{(\lambda_{\mathrm{Bi}} - \lambda_{\mathrm{Pb}})\,(\lambda_{\mathrm{Po}} - \lambda_{\mathrm{Pb}})} \right. \\
+ \quad & \left. \frac{e^{-\lambda_{\mathrm{Bi}}\,t}}{(\lambda_{\mathrm{Pb}} - \lambda_{\mathrm{Bi}})\,(\lambda_{\mathrm{Po}} - \lambda_{\mathrm{Bi}})} + \frac{e^{-\lambda_{\mathrm{Po}}\,t}}{(\lambda_{\mathrm{Pb}} - \lambda_{\mathrm{Po}})\,(\lambda_{\mathrm{Bi}} - \lambda_{\mathrm{Po}})} \right], \qquad (6.9)
\end{aligned}
$$

where λ_{Bi}, λ_{Po}, and λ_{Pb} denote the decay constants for ^{210}Bi, ^{210}Po, and ^{210}Pb, respectively, and A denotes the normalization, which is the fitted parameter. Based

Table 6.2: Estimated total ^{210}Po α-decays for various background functions from run 3888, which has a special low N_{ID} threshold. The first column is the functions used to fit the background, where a_0, a_1, a_2, b, and c are fitted. The third column, Probability, is the probability based on the $\chi^2/n.d.f.$ of the fit.

Background function	$N_{\mathrm{Max\,ID}}$ limits	Probability	Fitted ^{210}Po decays
$a_0 + a_1\,x$	60 to 105	0.13	$(2.411 \pm 0.088) \times 10^5$
$a_0 + a_1\,x + a_2\,x^2$	60 to 120	0.11	$(2.34 \pm 0.13) \times 10^5$
$a_0 + a_1\,x + a_2\,x^2$	60 to 125	0.15	$(2.347 \pm 0.076) \times 10^5$
$a_0 + a_1\,x + a_2\,x^2$	60 to 130	0.14	$(2.249 \pm 0.049) \times 10^5$
$a_0 + a_1\,x + b\,e^{cx}$	50 to 105	0.12	$(2.50 \pm 0.10) \times 10^5$
$a_0 + a_1\,x + a_2\,x^2 + b\,e^{cx}$	50 to 125	0.21	$(2.405 \pm 0.080) \times 10^5$
$a_0 + a_1\,x + a_2\,x^2 + b\,e^{cx}$	50 to 130	0.19	$(2.308 \pm 0.056) \times 10^5$

on this fit, the average ^{210}Po decay activity within the fiducial volume in the analysis period is 31.33 ± 0.81 Bq. Therefore, the activities estimated using the constant fit and this model are consistent. The value from the constant fit is used in the analysis, and the difference between the two different fit functions is taken as a systematic error.

An additional systematic error comes from the assumption that the $N_{\mathrm{Max\,ID}}$ spectrum of the other background events is modeled simply by a second order polynomial plus an exponential. Various functions and fit limits are tried to estimate the variation in the number of ^{210}Po α-decay events estimated using all the events recorded in special run 3888, which has a N_{ID} threshold of 35. Only four functions give a reasonable fit that yields convergence, an accurate error matrix, and a fit probability greater than 0.1, based on the $\chi^2/n.d.f.$ Table 6.2 summarizes the fitted numbers of ^{210}Po α-decay events, and probabilities for various reasonable fit functions. The percentage difference between the maximum and minimum numbers of ^{210}Po α-decay events fitted is ~11 %, which is included in the error on the ^{210}Po activity, yielding 30.0 ± 3.5 Bq.

The number of neutrons produced per α particle, Y, is given by

$$Y = \rho \int_{0}^{E_\alpha} dE \, \frac{\sigma(E)}{\frac{dE}{dx}(E)} = (6.0 \pm 0.3) \times 10^{-8}, \tag{6.10}$$

where $\rho = 3.7 \times 10^{20}\,\mathrm{cm}^{-3}$ denotes the density of ^{13}C in the target, $\sigma(E)$ denotes the reaction cross-section [57], $\frac{dE}{dx}(E)$ denotes the α particle stopping power [58], and E_α denotes the maximum kinetic energy of the α particle. The error is estimated from comparison between a calculation using C targets with natural C isotope compositions and measurements [59]. Combining the estimated ^{210}Po activity, the number of neutrons produced per α particle (Y), and a detection efficiency, the expected $^{13}\mathrm{C}(\alpha, \mathrm{n})$ background rate is estimated to be $(1.53 \pm 0.20) \times 10^{-6}$ per second in the entire E_{vis} range. The detection efficiency here includes $\varepsilon_{N_{\mathrm{Max\,ID}}}$, $\varepsilon_{\mathrm{recon}}$, $\varepsilon_{\mathrm{spall}}$, $\varepsilon_{\Delta R}$, $\varepsilon_{\Delta t}$, and $\varepsilon_{E_{\mathrm{d}}}$[4], and is assumed to be constant in E_{p} even below the E_{p} analysis threshold; although the actual efficiency drops significantly below E_{p} threshold mostly due to the $N_{\mathrm{Max\,ID}}$ Cut, the difference between the assumed constant efficiency and actual efficiency below the E_{p} threshold becomes irrelevant once the E_{p} Cut is applied during the analysis fit, described in Section 7.2.

As described in the beginning of this section, ^{210}Po α particles can cause $^{13}\mathrm{C}(\alpha, \mathrm{n})$ reactions that result in thermalization of neutrons via elastic scatterings alone, or those combined with inelastic scattering with ^{12}C, or de-excitation of $^{16}\mathrm{O}^*$. The fraction of each reaction type is estimated by simulating 10^4 $^{13}\mathrm{C}(\alpha, \mathrm{n})$ reactions using the cross-sections for the $^{13}\mathrm{C}(\alpha, \mathrm{n})$ reactions, inelastic scattering of a neutron with a ^{12}C, and elastic scattering of a neutron with a proton and a ^{12}C. This simulation yields 88640 events with only neutron elastic scattering, 2105 events with a ^{12}C inelastic scattering, and 9256 events with $^{16}\mathrm{O}^*$ de-excitation. Using the number of events in each reaction type, the ratio of the number of the inelastic ^{12}C scattering events to the total is estimated to be 0.02105 ± 0.00045, where the error comes from the statistical error on the simulated number of events. The ratio of the number of $^{13}\mathrm{C}(\alpha, \mathrm{n})^{16}\mathrm{O}^*$ events to total is estimated to be 0.09 ± 0.09, where a 100 % error is assigned to this

---

[4] Since $\varepsilon_{E_{\mathrm{p}}}$ is calculated during the fit, it is not included in this estimate.

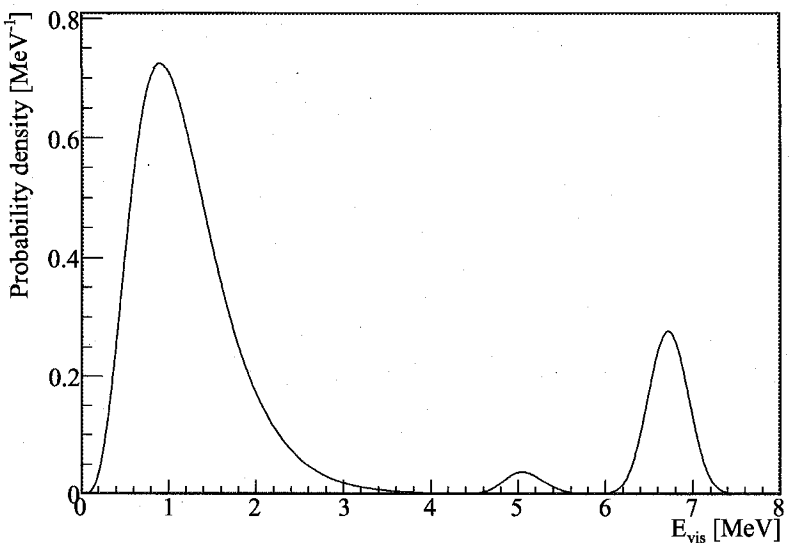

Figure 6.11: Expected ^{13}C(α, n) E_{p} PDF obtained using the central values of energy parameters (see Section 3.4).

ratio since the cross-section of ^{13}C$(\alpha, \mathrm{n})^{16}$O* reaction is not well-known.

The expected E_{p} spectral shape for the elastic scatterings of neutrons from the ^{13}C$(\alpha, \mathrm{n})^{16}$O reactions is calculated using a Monte Carlo [50]. This Monte Carlo simulates neutrons scattering elastically with protons and ^{12}C, and scattering inelastically with ^{12}C. The kinetic energy of each proton from elastic process is converted into E_{vis} using the model described in Section 3.4, and all the values of E_{vis} from one thermalizing neutron are added. The resulting E_{p} spectral shape for the neutrons that thermalize via elastic scattering is parameterized, and can be varied based on different energy parameters (see Section 3.4). The E_{vis} peak for neutrons that undergo inelastic scattering with ^{12}C is obtained by converting the E_{real} of a 4.439 MeV γ into E_{vis} according to the model, and adding the simulated spectral shape for the elastic scattering of these neutrons. The E_{vis} peak from the de-excitation of the first excited ^{16}O is obtained by converting the E_{real} of electron and positron, assuming the kinetic energy is shared equally, into E_{vis} spectrum. Similarly, the E_{vis} peak from the de-excitation of the second excited ^{16}O is obtained by converting the E_{real} of a

6.130 MeV γ into E_{vis}. The expected E_{p} PDF of the $^{13}\mathrm{C}(\alpha, \mathrm{n})$ background using the central values of energy parameters is shown in Figure 6.11.

The expected E_{d} and Δt PDFs for neutron captures following the $^{13}\mathrm{C}(\alpha, \mathrm{n})$ reactions are the same as those of neutron captures following the inverse β-decays from $\bar{\nu}_{\mathrm{reactor}}$s (see Section 6.1). The time dependence of $^{13}\mathrm{C}(\alpha, \mathrm{n})$ background events is assumed to be constant since the $^{210}\mathrm{Po}$ α-decay activity, shown in Figure 6.10, does not favor the model described with Equation 6.9 over a constant.

6.5 ^{9}Li Background

As described in Section 4.3, cosmic muons going through the detector can create $^{9}\mathrm{Li}$ whose decays can result in pairs of events that mimic the inverse β-decays and their subsequent neutron captures. The Shower/Misreconstructed Muon Cut and Muon Cylinder Cut (see Section 5.3.2) are designed to eliminate these $^{9}\mathrm{Li}$ β-decays by applying detector vetoes for 2 s: a full volume veto after events tagged as a Shower Muon or Misreconstructed Muon, and a three-meter-radius cylindrical volume veto around successfully reconstructed muons, respectively. However, $^{9}\mathrm{Li}$ β-decay events can become background events if they pass these cuts. The number of $^{9}\mathrm{Li}$ background events that remain after applying the Candidate Selection Cuts, described in Section 5.3, is extrapolated from the number of $^{9}\mathrm{Li}$ candidates that pass the Candidate Selection Cuts, except the Shower/Misreconstructed Muon Cut, and Muon Cylinder Cut.

The number of $^{9}\mathrm{Li}$ background events that pass the Shower/Misreconstructed Muon Cut is estimated from the normalization of an exponential function, fitted with a fixed half-life of $\tau_{^{9}\mathrm{Li}} = 178.3\,\mathrm{ms}$ to the distribution of the time difference between the events tagged as a Shower Muon or Misreconstructed Muon and $^{9}\mathrm{Li}$ candidates as shown in Figure 6.12. Using this normalization, 1186 ± 40, the exponential function is integrated from a time difference of 2 s to infinity, yielding 0.498 ± 0.017 events not removed by the Shower/Misreconstructed Muon Cut.

The number of $^{9}\mathrm{Li}$ background events that follow successfully reconstructed muons is estimated by first fitting an exponential function with a fixed half-life of $\tau_{^{9}\mathrm{Li}} = 178.3\,\mathrm{ms}$ to the distribution of time difference between the successfully reconstructed

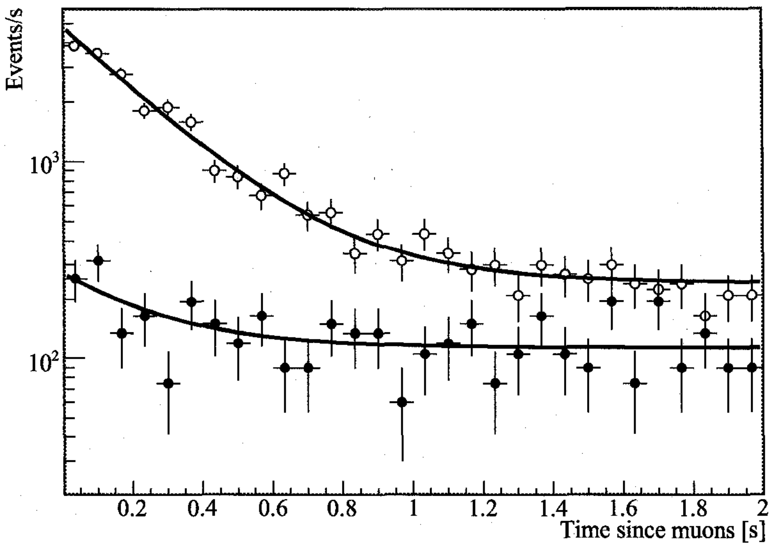

Figure 6.12: Time between muons and spallation ^{9}Li β-decay events. The filled circles are for ^{9}Li β-decay events obtained by reversing the Muon Cylinder Cut, and the open circles are for those after events tagged as Shower Muons or Misreconstructed Muons. The solid lines indicate fits to an exponential function plus a constant, using the nominal half-life of ^{9}Li β-decay, 178.3 ms. The fitted number of ^{9}Li decays and $\chi^2/n.d.f.$ for those obtained by reversing the Muon Cylinder Cut are 41 ± 11 and 29.4/28, respectively. The fitted numbers of ^{9}Li decays and $\chi^2/n.d.f.$ for those after events tagged as Shower Muons or Misreconstructed Muons are 1186±40 and 29.1/28, respectively.

muons and ^{9}Li candidates whose position is reconstructed within 3 m from the reconstructed muon track, as shown in Figure 6.12. Using the fitted normalization, 41 ± 12, the number of events outside the cylinder around the muon tracks is obtained from

$$N_{\text{cylinder}} = (41 \pm 12)\, R_{\text{out/in}} \frac{\ln 2}{\tau_{^9\text{Li}}} \int_{2\,\text{ms}}^{2\,\text{s}} \exp\left(-\frac{\ln 2}{\tau_{^9\text{Li}}} t\right) dt, \tag{6.11}$$

where $R_{\text{out/in}}$ is the ratio of ^{9}Li β-decay events expected to be outside to inside of the 3 m cylinder around the muons. $R_{\text{out/in}}$ is estimated from spallation neutrons produced by muons with successfully reconstructed tracks. Figure 6.13 shows the

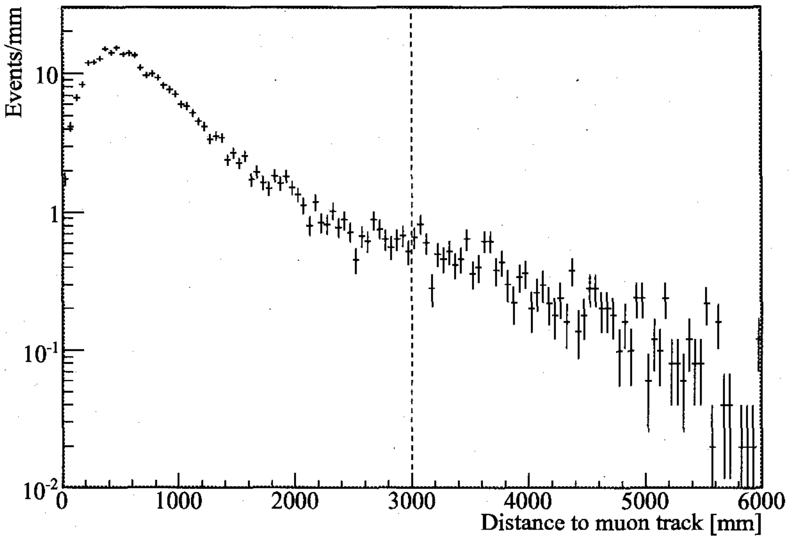

Figure 6.13: Distance between muon tracks and spallation neutron events. The dotted vertical line indicates the 3 m cylindrical cut along the muon track.

distribution of minimum distances between the tracks of muons and the associated spallation neutron event positions. The ratio of neutron events outside to inside of the 3 m cylinder along the muon track is 0.0615 ± 0.0023. This yields 2.49 ± 0.72 ^{9}Li background events that pass the Muon Cylinder Cut. The number of ^{9}Li background events that decay more than 2 s after a successfully reconstructed muon is negligible.

The total number of expected ^{9}Li background events that pass the Candidate Selection Cuts is estimated to be 2.98 ± 0.72. The expected E_p spectral shape of ^{9}Li background events using the central values of the energy parameters (see Section 3.4) is shown in Figure 4.9. The E_d and Δt PDFs for neutron captures following the ^{9}Li β-decays are the same as those for neutron captures following the inverse β-decays for $\bar{\nu}_{\mathrm{reactor}}$s (see Section 6.1). The ^{9}Li background events are assumed to have no time dependence.

6.6 Fast Neutron Background

Thermalization and subsequent captures of high energy neutrons produced by muons can mimic inverse β-decays and their subsequent neutron captures. These neutrons, "fast neutrons," sometimes produce secondary neutrons through spallation process, and the multiple-neutron capture-γs can also form coincidence event-pairs. Fast neutrons produced by muons passing through the detector are easily identified by coincidences with the detected muons. However, undetected muons that pass near KamLAND without being detected by the OD can still produce fast neutrons that reach the LS and produce correlated events.

The nature of the fast neutron background events is investigated with fast neutrons that are produced by muons entering only the OD. Such fast neutron candidates are selected by applying the Candidate Selection Cuts, described in Section 5.3, except reversing the 2 ms full-volume veto following an event tagged as an OD Muon, and the cuts specifically designed to eliminate fast neutrons, the High $N_{PE\,\mathrm{ID}}$ Event Cut, and the High Candidate Multiplicity Cut. These cuts select spatially and temporally correlated event-pairs that follow muons entering the OD without reaching the ID. The unfilled histogram from the top plot in Figure 6.14 shows the "prompt event" E_{vis} distribution for the resulting fast neutron candidates. The peak around E_{vis} $\sim$2.4 MeV is caused by two neutron captures forming a prompt-delayed event-pair. Removing events that follow thermalization of high energy fast neutrons by applying the High $N_{PE\,\mathrm{ID}}$ Event Cut eliminates most of the fast neutron candidates in the neutron-capture-pair peak, as shown in the gray filled histogram in Figure 6.14 (top plot). Furthermore, removing events that form multiple correlated event-pairs by applying the High Candidate Multiplicity Cut further reduces the neutron-capture-pair peak, and the resulting E_{vis} distribution is shown in the black filled histogram in Figure 6.14 (top plot). Although the statistics are rather low, this spectrum seems relatively flat. Therefore a flat E_{p} PDF is assumed for the fast neutron background events in the $\bar{\nu}_{\mathrm{e}}$ candidate list.

The bottom plot in Figure 6.14 shows the distribution of the average position for "prompt" and "delayed" events of fast neutron candidates following OD muons.

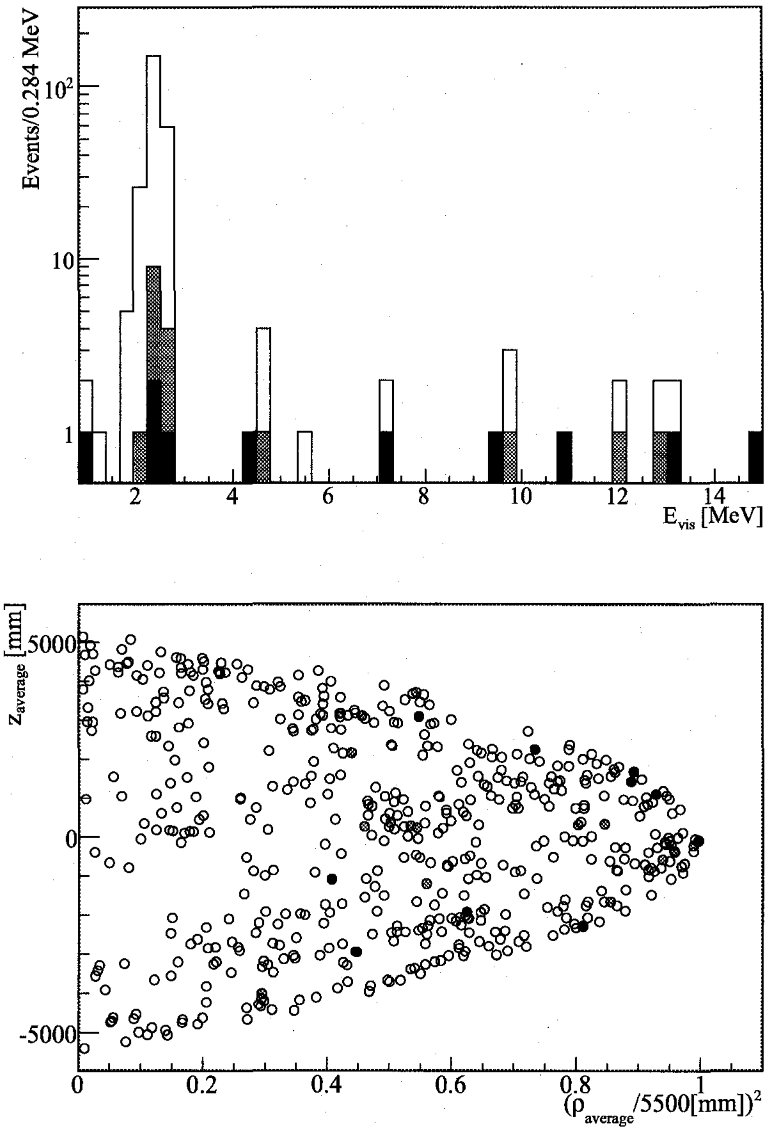

Figure 6.14: "Prompt event" E_{vis} spectra (top plot) and "prompt-delayed event" average position distributions (bottom plot) for fast neutrons. The unfilled histogram and markers are for the events obtained by applying the Candidate Selection Cuts described in Section 5.3, except the High $N_{PE\,\text{ID}}$ Event Cut, High Candidate Multiplicity Cut, and reversing the veto after an OD Muon. The gray histogram and markers are for the remaining events after applying the High $N_{PE\,\text{ID}}$ Event Cut to the above events. The black histogram and markers are for the events obtained by additionally applying the High Candidate Multiplicity Cut.

The unfilled markers indicate the average positions of the fast neutron candidates including those following high energy fast neutrons. These reach deep into the LS although they are slightly more concentrated around the fiducial volume boundary. Removing events following high energy fast neutrons eliminates many of the events that reach the center of the ID, as shown in the gray filled markers in the bottom plot in Figure 6.14, because high energy fast neutrons have a longer attenuation length. Removing events that form multiple correlated event-pairs results in the black filled markers in Figure 6.14 (bottom plot). These events may be somewhat concentrated around the equator, where the OD is the thinest, and therefore the buffer between the surrounding rock and the ID is thinest, making it easier for fast neutrons to penetrate into the LS. Since the OD is the least efficient in detecting muons going near the thinnest part of the OD, there may be quite a few fast neutrons that are not associated with detected muons. Since the efficiency of detecting such muons is not well understood, the expected number of fast neutrons that pass the Candidate Selection Cuts is not estimated directly. Instead, the PDF normalization is allowed to freely float to match the selected $\bar{\nu}_{\mathrm{e}}$ candidate distribution, as described in Section 7.2.

The E_{d} and Δt PDFs for neutron captures following the thermalization of fast neutrons or other captures of neutrons produced from the same muons are the same as those for neutron captures following the inverse β-decays from $\bar{\nu}_{\mathrm{reactor}}$s (see Section 6.1). The fast neutron background events are assumed to have no time dependence.

6.7 Atmospheric ν Background

A possible source of background is from quasi-elastic neutral current interaction of atmospheric νs with neutrons in ^{12}C nuclei. The recoil neutron produces a prompt event, and its capture produces the delayed event. The atmospheric ν background events are studied using a KLG4sim simulation [60]. For simplicity, this simulation assumes that atmospheric νs interact with free neutrons, neglecting nuclear effects of ^{12}C. Therefore the result of this simulation is treated as a very rough estimation. The cross-section for interactions between a ν and a neutron is obtained by modifying the

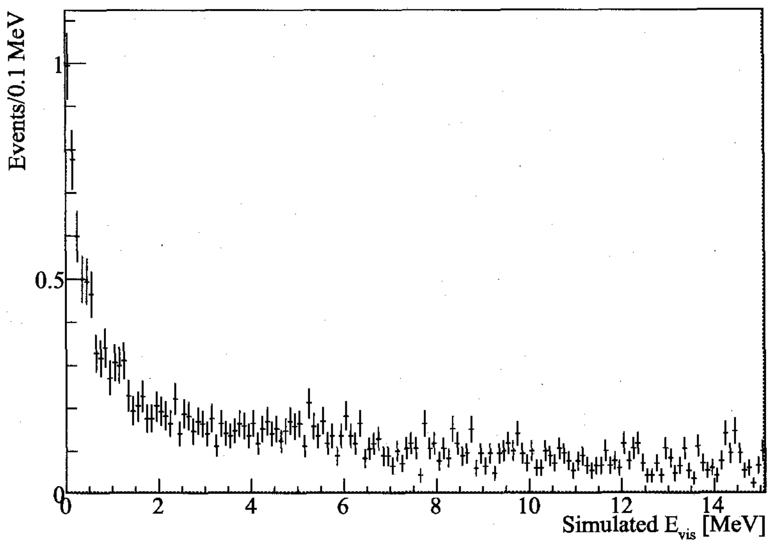

Figure 6.15: E_{vis} distribution of simulated atmospheric νs [60].

cross-section for interaction between a ν and a proton [61]. The atmospheric ν energy spectrum and flux are taken from the calculation by Honda *et al.* [62]. Figure 6.15 shows the E_{vis} distribution of the prompt events from the simulated atmospheric ν background, the shape of which is used as the expected E_{p} PDF.

According to this simulation, the number of background event-pairs from atmospheric νs is expected to be less than ~10. However, this value is not used as a constraint since this is a very crude estimate. Instead, the PDF normalization is allowed to freely float to match the selected $\bar{\nu}_{\text{e}}$ candidate distribution, as described in Section 7.2.

The E_{d} and Δt PDFs for neutron captures following atmospheric ν interactions are the same as those for neutron captures following inverse β-decays from $\bar{\nu}_{\text{reactor}}$s (see Section 6.1). The atmospheric ν background is assumed to have no time dependence.

Chapter 7

Likelihood Analysis and Results

This analysis simultaneously estimates the neutrino oscillation parameters, $\sin^2 2\theta_{12}$ and Δm^2_{21}, assuming 2-flavor neutrino oscillation, and $\bar{\nu}_{\rm geo}$ parameters, $\Phi_{\rm geo\,sum}$ and $\Phi_{\rm geo\,diff}$, defined in Section 7.2. The expected numbers of event-pairs and spectra of various event types, discussed in Chapter 6, for given parameters, are fitted to the selected $\bar{\nu}_{\rm e}$ candidate event-pairs by maximizing the likelihood function. The analysis is conducted in three different modes defined by "Mode-I analysis," "Mode-II analysis," and "Mode-III analysis." Mode-I analysis uses the expected number of events and the spectral shapes in $E_{\rm p}$, $E_{\rm d}$, and Δt. Under Mode-I analysis, the existence of neutrinos oscillation is studied by fitting the data assuming two-flavor neutrino oscillation and no oscillation, and examining their goodness-of-fit. Mode-II analysis uses the expected number of events and spectral shapes in $E_{\rm p}$, $E_{\rm d}$, Δt, and t. By adding expectation in t, Mode-II analysis improves over Mode-I in discriminating $\bar{\nu}_{\rm reactor}$s from other event types since $\bar{\nu}_{\rm reactor}$s have significant time dependence based on the nuclear reactor operation variation, as discussed in Section 6.1. Mode-III analysis combines Mode-II analysis with the results from solar neutrino experiments [63]. The $\sin^2 2\theta_{12}$ measurement in Mode-III is improved over Mode-I and II due to the better sensitivity in $\sin^2 2\theta_{12}$ attained by the solar ν measurements. Having a tighter constraint on $\sin^2 2\theta_{12}$ also improves the $\bar{\nu}_{\rm geo}$ measurement.

7.1 $\bar{\nu}_{\mathrm{e}}$ Candidates

The Candidate Selection Cuts described in Section 5.3 selects 1966 candidate event-pairs in the entire data-set. Figure 7.1 shows the distributions of R_{average}, ΔR, Δt, and E_{d} of the event-pairs that pass the Candidate Selection Cuts except the cuts based on the variables displayed in the plots. Plot a) shows the spatial distribution of average positions of the selected event-pairs. Within the fiducial volume, indicated by the dotted line, the event-pair distribution is relatively flat. The event-pairs outside of the fiducial volume are from radioactivity on the surface of the balloon. Plot b) shows the ΔR distribution of the selected event-pairs. Correlated event-pairs appear in the peak around ~400 mm, and the random coincidence event-pairs cause the increasing slope at high ΔR. Plot c) shows the Δt distribution of the selected event-pairs. The exponential shape due to neutron capture time distribution is clearly seen. The flat tail is due to the random coincidence event-pairs. Plot d) shows the E_{d} distribution of the selected event-pairs. The peak around ~2.4 MeV is due to neutron captures on protons, and the events around ~5.5 MeV are due to neutron captures on ^{12}C. The large peak at low E_{d} is mostly due to random coincidence event-pairs.

7.2 Likelihood Analysis and Parameters

This analysis estimates various parameters by performing a multi-dimensional unbinned maximum log-likelihood fit. When the number of candidate event-pairs is small, an unbinned fit has an advantage over a binned fit, which loses information in the process of binning. Particularly, since this is a multi-dimensional fit, the number of bins in each dimension would have to be very small in order to have sufficient number of entries in each bin if a binned analysis were conducted. The log-likelihood function is given by

$$\begin{aligned}\log L\left(\vec{x}\,|\,\vec{\theta}\right) &= \sum_i \left\{ -\bar{N}_i(\vec{\theta}) + \sum_j^{N_i} \log\left[\sum_k \bar{N}_{i,k}(\vec{\theta})\, P_{i,k}\left(\vec{x}_j\,|\,\vec{\theta}\right)\right]\right\} \\ &- \frac{1}{2}\chi_p^2(\vec{\theta}). \end{aligned} \tag{7.1}$$

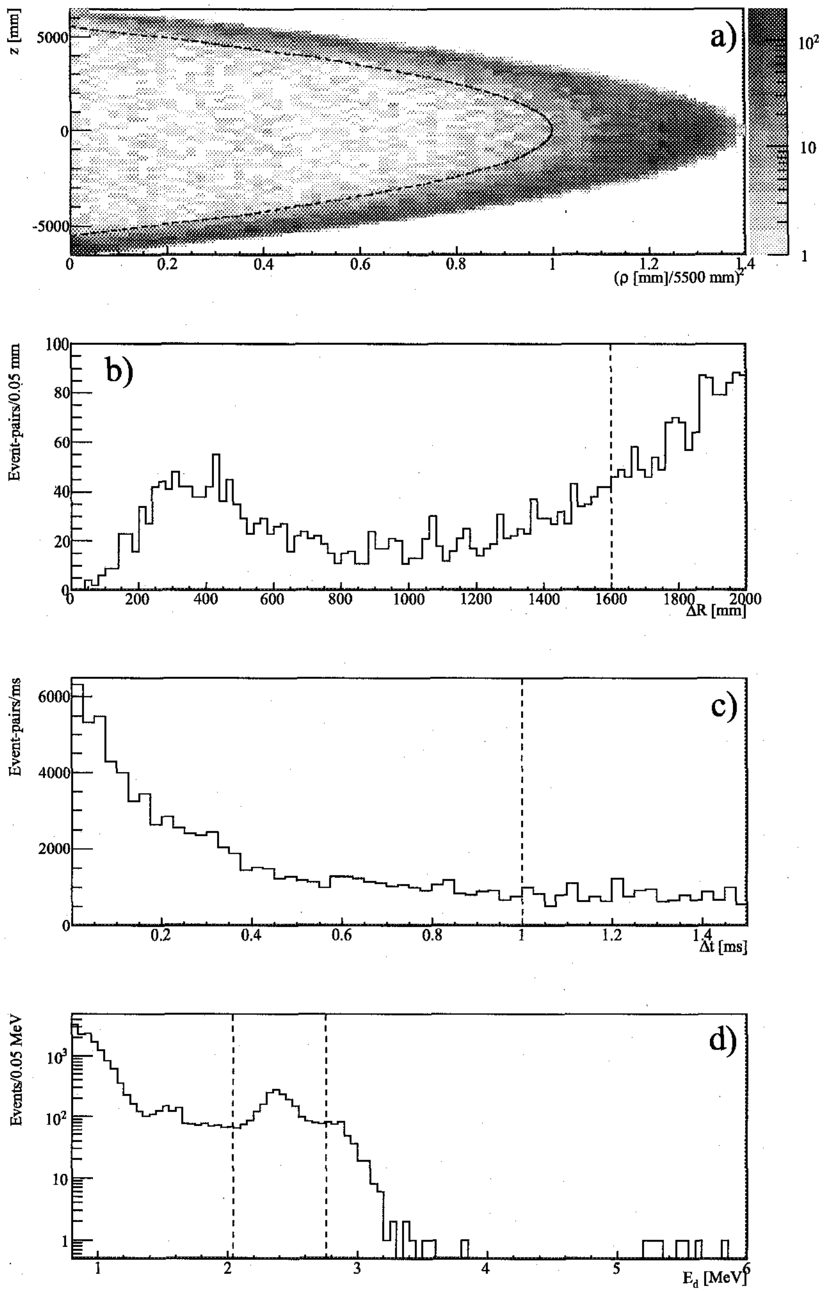

Figure 7.1: $\bar{\nu}_e$ candidate distributions. Plots a), b), c), and d) show the distribution of the event-pairs that pass the Candidate Selection Cuts except the cut based on the variable displayed in each plot, R_{average}, ΔR, Δt, and E_d, respectively. The cuts are indicated by the dotted lines.

The index i runs over data-periods I and II. $\bar{N}_i(\vec{\theta})$ denotes the number of candidate event-pairs expected in period i for a given set of model parameter values, $\vec{\theta}$. The index j runs over all the candidate event-pairs observed in period i, N_i. The index k runs over all the different event types. $\bar{N}_{i,k}(\vec{\theta})$ denotes the expected number of event-pairs of type k in period i. $P_{i,k}\left(\vec{x}_j \,|\, \vec{\theta}\right)$ denotes the probability of observing a set of variables measured for jth event-pair, $\vec{x}_j$, for an event type k in period i. Finally, χ_p^2 is a penalty term given by

$$\chi_p^2(\vec{\theta}) = \sum_l \left(\frac{\theta_{l,\,\mathrm{estimated}} - \theta_{l,\,\mathrm{fitted}}}{\Delta\theta_{l,\mathrm{estimated}}} \right)^2 , \tag{7.2}$$

where the index l runs over all the "nuisance" parameters whose errors are estimated before the fit. $\theta_{l,\,\mathrm{estimated}}$, $\theta_{l,\,\mathrm{fitted}}$, and $\Delta\theta_{l,\,\mathrm{estimated}}$ denote the estimated value, the fitted value, and the error on the estimated value of the lth nuisance parameter, respectively. $\chi_p^2(\vec{\theta})$ becomes large when the fitted nuisance parameter value deviates from the estimated value, making $\log L$ small. By varying $\vec{\theta}$, the best-fit is calculated by maximizing Equation 7.1.

The $\Delta\chi^2$, the difference in χ^2s between the best-fit and a fit with one or more parameter(s) fixed, is calculated from

$$\Delta\chi^2 = -2\left(\log L_{\mathrm{max}} - \log L\left(\theta_i\right)\right), \tag{7.3}$$

where L_{max} is the likelihood at the best-fit. $L\left(\theta_i\right)$ is the likelihood obtained with parameter(s) θ_i fixed, and all other parameters allowed to vary until the likelihood is maximized. The confidence interval for θ_i is based on the $\Delta\chi^2$; intervals of one parameter at 68.27 % (1 σ), 95.45 % (2 σ), 99.73 % (3 σ), and 99.9937 % (4 σ) confidence levels are given by the range between the parameter values where $\Delta\chi^2$ is less than 1.00, 4.00, 9.00, and 16.00, respectively, and contours of two parameters at these confidence levels are given by the region enclosed by the parameter values where $\Delta\chi^2$ is less than 2.30, 6.18, 11.83, and 19.33, respectively.

7.2.1 Mode-I Analysis

Mode-I analysis uses the expected spectra in E_p, E_d, and Δt for all the expected event types, i.e., $P_{i,k}\left(\vec{x}_j\,|\,\vec{\theta}\right)$ in Equation 7.1 is given by

$$\begin{aligned} P_{i,k}\left(\vec{x}_j\,|\,\vec{\theta}\right) &= \frac{dP_{i,k}}{dE_\mathrm{p}\,dE_\mathrm{d}\,d\Delta t}\left(\vec{x}_j\,|\,\vec{\theta}\right) \\ &= \frac{dP_{i,k}}{dE_\mathrm{p}}\left(\vec{x}_j\,|\,\vec{\theta}\right)\frac{dP_{i,k}}{dE_\mathrm{d}}\left(\vec{x}_j\right)\frac{dP_{i,k}}{d\Delta t}\left(\vec{x}_j\right). \end{aligned} \tag{7.4}$$

7.2.2 Mode-II Analysis

As well as E_p, E_d, and Δt, Mode-II analysis uses the expected spectra in t, in order to help discriminating the $\bar{\nu}_\mathrm{reactor}$ signals from all the other event types. $P_{i,k}\left(\vec{x}_j\,|\,\vec{\theta}\right)$ in Equation 7.1 for Mode-II analysis is given by

$$P_{i,k}\left(\vec{x}_j\,|\,\vec{\theta}\right) = \frac{dP_{i,k}}{dE_\mathrm{p}\,dE_\mathrm{d}\,d\Delta t\,dt}\left(\vec{x}_j\,|\,\vec{\theta}\right). \tag{7.5}$$

For $\bar{\nu}_\mathrm{reactor}$s, this is given by

$$\begin{aligned} &\frac{dP_{i,\mathrm{reactor}}}{dE_\mathrm{p}\,dE_\mathrm{d}\,d\Delta t\,dt}\left(\vec{x}_j\,|\,\vec{\theta}\right) = \\ &\quad\frac{dP_{i,\mathrm{reactor}}}{dE_\mathrm{p}\,dt}\left(\vec{x}_j\,|\,\vec{\theta}\right)\frac{dP_{i,\mathrm{reactor}}}{dE_\mathrm{d}}\left(\vec{x}_j\right)\frac{dP_{i,\mathrm{reactor}}}{d\Delta t}\left(\vec{x}_j\right), \end{aligned} \tag{7.6}$$

while for all other event types it is given by

$$\frac{dP_{i,k}}{dE_\mathrm{p}\,dE_\mathrm{d}\,d\Delta t\,dt}\left(\vec{x}_j\,|\,\vec{\theta}\right) = \frac{1}{T_i}\frac{dP_{i,k}}{dE_\mathrm{p}}\left(\vec{x}_j\,|\,\vec{\theta}\right)\frac{dP_{i,k}}{dE_\mathrm{d}}\left(\vec{x}_j\right)\frac{dP_{i,k}}{d\Delta t}\left(\vec{x}_j\right), \tag{7.7}$$

where T_i is the total livetime in period i.

7.2.3 Mode-III Analysis

Assuming CPT-invariance, which implies that the $\bar{\nu}_\mathrm{e}$ survival probability is the same as that of ν_e for the same energy and baseline, Mode-III analysis combines Mode-II analysis with the flux measurements of the νs from the sun (solar νs), performed by

SNO [64], Super-Kamiokande [65], Homestake [66], SAGE [67], and Gallex/GNO [68]. This analysis uses the measurements of solar νs from three reactions in the sun: νs from the pp chain, electron captures by ^{7}Be, and β^+-decays of ^{8}B [10]. Assuming neutrino oscillation parameters are in the LMA region, the solar ν flux suppression factors due to oscillation can be approximated by $\sim 1 - 0.5 \sin^2\theta_{12}$ for νs from the pp chain and ^{7}Be, which have relatively low energies, and by $\sim \sin^2\theta_{12}$ for νs from ^{8}B, which have relatively high energies [69]. Therefore penalty terms are constructed from the difference between the reported solar ν fluxes measured by each experiment and the expected solar ν fluxes based on the neutrino oscillation parameters and the Solar Standard Model [70], constrained by the solar irradiance[1] [71].

The log-likelihood equation for Mode-III is given by

$$\log L_{\mathrm{Mode-III}}\left(\vec{x}\,|\,\vec{\theta}\right) = \log L_{\mathrm{Mode-II}}\left(\vec{x}\,|\,\vec{\theta}\right) + \log L_{\mathrm{solar}}(\vec{\theta}), \tag{7.8}$$

where $\log L_{\mathrm{Mode-II}}\left(\vec{x}\,|\,\vec{\theta}\right)$ is given by Equation 7.1 combined with Equation 7.5, and $\log L_{\mathrm{solar}}(\vec{\theta})$ is the likelihood contribution from the solar ν experiment results.

7.2.4 Model Parameters

Table 7.1 lists the free-floating model parameters, i.e., with no associated χ^2_p term. The first four parameters are the neutrino oscillation parameters and $\bar{\nu}_{\mathrm{geo}}$ parameters that this analysis is designed to measure. $\sin^2 2\theta_{12}$ and Δm^2_{21} are strongly correlated with the $\bar{\nu}_{\mathrm{reactor}}$ E_{p} spectrum, as shown in Figure 6.1. $\Phi_{\mathrm{geo\,sum}}$ and $\Phi_{\mathrm{geo\,diff}}$ are defined by

$$\Phi_{\mathrm{geo\,sum}} \equiv \Phi_{\mathrm{effective},\,^{238}\mathrm{U}} + \Phi_{\mathrm{effective},\,^{232}\mathrm{Th}} \tag{7.9}$$

and

$$\Phi_{\mathrm{geo\,diff}} \equiv \frac{\Phi_{\mathrm{effective},\,^{238}\mathrm{U}} - \Phi_{\mathrm{effective},\,^{232}\mathrm{Th}}}{\Phi_{\mathrm{effective},\,^{238}\mathrm{U}} + \Phi_{\mathrm{effective},\,^{232}\mathrm{Th}}}. \tag{7.10}$$

where $\Phi_{\mathrm{effective},\,^{238}\mathrm{U}}$ and $\Phi_{\mathrm{effective},\,^{232}\mathrm{Th}}$ are defined in Equation 6.5. These parameter combinations are used in the fit because KamLAND is primarily sensitive to the sum

---

[1] Solar irradiance is the average rate of solar radiation that the Earth receives per unit area.

Table 7.1: Free-floating model parameters.

Parameter	Description
$\sin^2 2\theta_{12}$	Neutrino oscillation mixing angle
Δm^2_{21}	Neutrino oscillation mass-squared difference
$\Phi_{\mathrm{geo\,sum}}$	$\bar{\nu}_{\mathrm{geo}}$ effective event rate
$\Phi_{\mathrm{geo\,diff}}$	^{238}U-^{232}Th $\bar{\nu}_{\mathrm{geo}}$ effective event rate normalized difference
$R_{\mathrm{fast\,n}}$	Rate of fast neutron background
$R_{\mathrm{atm}\,\nu}$	Rate of atmospheric ν background

Table 7.2: Nuisance model parameters. The errors on the estimated parameter values are indicated in parentheses.

Parameter	Estimate	Description
a_0	1.061(24)	Energy parameter for normalization
$k_b\,[\mathrm{mg\,cm^{-2}\,MeV^{-1}}]$	9.71(27)	Energy parameter for Birk's law
k_0	0.84(14)	Energy parameter for Monte Carlo
k_C	0.43(11)	Energy parameter for Cherenkov radiation
$\varepsilon_{\mathrm{common}}$	0.875(35)	$\bar{\nu}_{\mathrm{reactor}}$ and $\bar{\nu}_{\mathrm{geo}}$ common efficiency
$\varepsilon_{\mathrm{reactor}}$	0.986(34)	$\bar{\nu}_{\mathrm{reactor}}$ only detection efficiency
$N_{\mathrm{random\,I}}$	202.30(35)	# of random coincidence in period I
$N_{\mathrm{random\,II}}$	653.41(74)	# of random coincidence in period II
$R_{^{13}\mathrm{C}(\alpha,\mathrm{n})}\,[10^{-6}\,\mathrm{s^{-1}}]$	1.53(20)	Detection rate of ^{13}C(α, n)
$F_{^{13}\mathrm{C}(\alpha,\mathrm{n}),\,\mathrm{C}}$	0.02105(45)	Fraction of ^{12}C scattering ^{13}C(α, n)
$F_{^{13}\mathrm{C}(\alpha,\mathrm{n})^{16}\mathrm{O}^*}$	0.09(9)	Fraction of ^{13}C(α, n)^{16}O*
$N_{^9\mathrm{Li}}$	2.98(72)	Number of ^{9}Li
$\phi_1\,[10^{10}\,\mathrm{cm^{-2}\,s^{-1}}]$	5.94(6)	pp solar ν flux [63] (for Mode-III)
$\phi_7\,[10^{9}\,\mathrm{cm^{-2}\,s^{-1}}]$	4.9(6)	^{7}Be solar ν flux [63] (for Mode-III)
$\phi_8\,[10^{6}\,\mathrm{cm^{-2}\,s^{-1}}]$	6(1)	^{8}B solar ν flux [63] (for Mode-III)

of the ^{238}U and ^{232}Th $\bar{\nu}_{\rm geo}$ fluxes, rather than their difference, for which the geochemical measurements of meteorites and rocks have better sensitivity (see Section 1.3.2). The reference Earth model described in Section 1.3.2, predicts the central values of $\Phi_{\rm geo\,sum}$ and $\Phi_{\rm geo\,diff}$ to be 61 $(10^{32}\,{\rm p}\cdot{\rm yr})^{-1}$ and 0.6, respectively. If the Earth is "fully radiogenic," as described in Section 6.2, $\Phi_{\rm geo\,sum}$ can take a range between 98 and 142 $(10^{32}\,{\rm p}\cdot{\rm yr})^{-1}$.

The rate of fast neutron and atmospheric ν backgrounds, $R_{\rm fast\,n}$ and $R_{{\rm atm}\,\nu}$ in Table 7.1, respectively, are difficult to estimate, and hence they are freely floated in this analysis. The $\bar{\nu}_{\rm e}$ candidate prompt events at high $E_{\rm p}$ can discriminate these backgrounds from other types of events since no other event types are expected above $\sim$10 MeV except the ^{9}Li backgrounds, whose expected number of event-pairs in the data-set is estimated fairly accurately.

Table 7.2 lists the model nuisance parameters. The four energy parameters discussed in Section 3.4 modify the expected $E_{\rm p}$ PDF shapes for $\bar{\nu}_{\rm reactor}$ and $\bar{\nu}_{\rm geo}$ signals and ^{13}C$(\alpha,{\rm n})$ and ^{9}Li backgrounds. Since the error on $\varepsilon_{\rm geo}$ is negligible compared to the statistical error on the $\Phi_{\rm geo\,sum}$, $\varepsilon_{\rm geo}$ is not fitted. Based on the spectral shape, $\varepsilon_{\rm E_p}$ for these event types are calculated during the fit. ϕ_1, ϕ_7, and ϕ_8 are the expected solar flux at the surface of the Earth in the absence of neutrino oscillation, described in Section 7.2.3.

7.3 Best-Fits

The unbinned maximum log-likelihood fits from Mode-I, II, and III analyses determine the best-fit model parameter values as summarized in Table 7.3. This shows that none of the best-fit nuisance model parameters deviates from the estimated values. Figures 7.2 and 7.3, for Mode-I and II analyses, respectively, show the best-fit $E_{\rm p}$ spectra of various event types as well as the distributions of the candidates after subtracting the best-fit random coincidence background. The random coincidence background $E_{\rm p}$ spectrum is easily subtracted since it is directly measured, unlike many of the other spectra which are calculated based on the theoretical $E_{\rm real}$ and energy parameters. The top plots show the entire $E_{\rm p}$ region analyzed, and the middle and bottom plots

Table 7.3: Best-fit parameter values. The first six parameters are floated without penalty, and the rest are nuisance parameters with expected values and penalties. The errors on the estimated parameter values are given in parentheses.

Parameter	Expected	Mode-I	Mode-II	Mode-III
$\sin^2 2\theta_{12}$[a]	N/A	$0.917^{+0.062}_{-0.066}$	$0.935^{+0.061}_{-0.065}$	$0.901^{+0.028}_{-0.032}$
Δm^2_{21}[a] $[10^{-5}\,\mathrm{eV}^2]$	N/A	$7.54^{+0.21}_{-0.21}$	$7.44^{+0.19}_{-0.18}$	$7.46^{+0.19}_{-0.18}$
$\Phi_{\mathrm{geo\,sum}}$[b] $[(10^{32}\,\mathrm{p}\cdot\mathrm{yr})^{-1}]$	N/A	110^{+41}_{-38}	131^{+41}_{-38}	122^{+36}_{-35}
$\Phi_{\mathrm{geo\,diff}}$[b]	N/A	$0.22^{+0.63}_{-0.92}$	$0.60^{+0.40}_{-0.62}$	$0.51^{+0.49}_{-0.64}$
$R_{\mathrm{fast\,n}}$ $[\mathrm{yr}^{-1}\,\mathrm{MeV}^{-1}]$	N/A[c]	0.2	0.2	0.2
$R_{\mathrm{atm}\,\nu}$ $[\mathrm{yr}^{-1}]$	N/A[d]	0	0	0
a_0	1.061(24)	1.064	1.061	1.062
k_b $[\mathrm{mg\,cm^{-2}\,MeV^{-1}}]$	9.71(24)	9.75	9.72	9.72
k_0	0.84(14)	0.84	0.85	0.85
k_C	0.43(11)	0.40	0.42	0.42
$\varepsilon_{\mathrm{common}}$	0.875(35)	0.870	0.867	0.860
$\varepsilon_{\mathrm{reactor}}$	0.986(34)	0.991	0.989	0.983
$N_{\mathrm{random\,I}}$	202.30(35)	202.31	202.31	202.31
$N_{\mathrm{random\,II}}$	653.41(74)	653.39	653.39	653.39
$R_{^{13}\mathrm{C}(\alpha,\mathrm{n})}$ $[10^{-6}\,\mathrm{s}^{-1}]$	1.53(20)	1.53	1.54	1.54
$F_{^{13}\mathrm{C}(\alpha,\mathrm{n}),\mathrm{C}}$	0.02105(45)	0.02106	0.02106	0.02106
$F_{^{13}\mathrm{C}(\alpha,\mathrm{n})^{16}\mathrm{O}^*}$	0.09(9)	0.09	0.10	0.10
$N_{^9\mathrm{Li}}$	2.98(72)	3.04	3.05	3.04
ϕ_1 $[10^{10}\,\mathrm{cm^{-2}\,s^{-1}}]$	5.96(6) [63]	N/A	N/A	6.00
ϕ_7 $[10^{9}\,\mathrm{cm^{-2}\,s^{-1}}]$	4.9(6) [63]	N/A	N/A	5.4
ϕ_8 $[10^{6}\,\mathrm{cm^{-2}\,s^{-1}}]$	6(1) [63]	N/A	N/A	5

---

[a] The calculation of the errors are described in Section 7.5.

[b] The calculation of the errors are described in Section 7.6.

[c] If the OD efficiency is assumed to detect ~50 % of muons that produce fast neutron background, $R_{\mathrm{fast\,n}}$ should be ~$0.2\,\mathrm{yr}^{-1}\,\mathrm{MeV}^{-1}$. See Section 6.6 for details.

[d] According to a crude estimation based on a simple simulation, $R_{\mathrm{atm}\,\nu}$ should be less than ~$3\,\mathrm{yr}^{-1}$. See Section 6.7 for details.

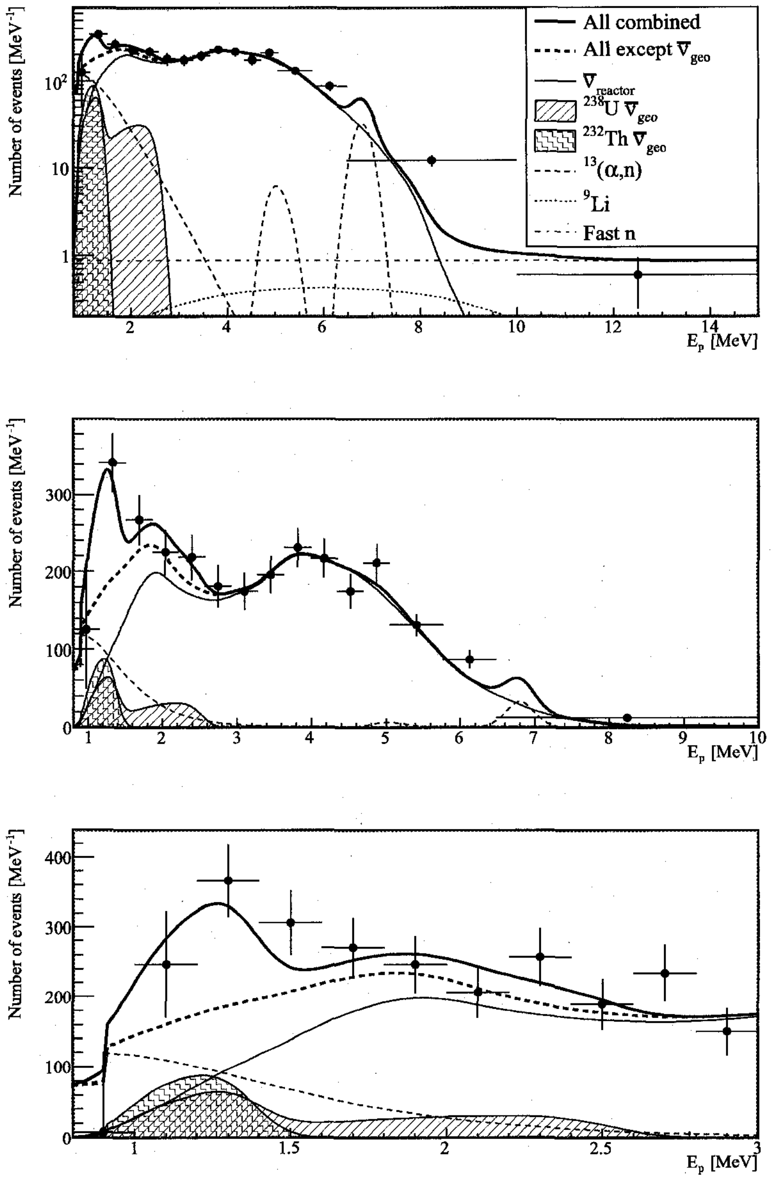

Figure 7.2: Mode-I analysis best-fit E_p spectra. The dots with error bars are candidate event distribution minus best-fit random coincidence background spectrum. The spectra shown are all combined, all combined except $\bar{\nu}_\mathrm{geo}$, $\bar{\nu}_\mathrm{reactor}$, ^{238}U $\bar{\nu}_\mathrm{geo}$, ^{232}Th $\bar{\nu}_\mathrm{geo}$, ^{13}C(α, n), ^{9}Li, and fast neutrons; see the legend in the top plot.

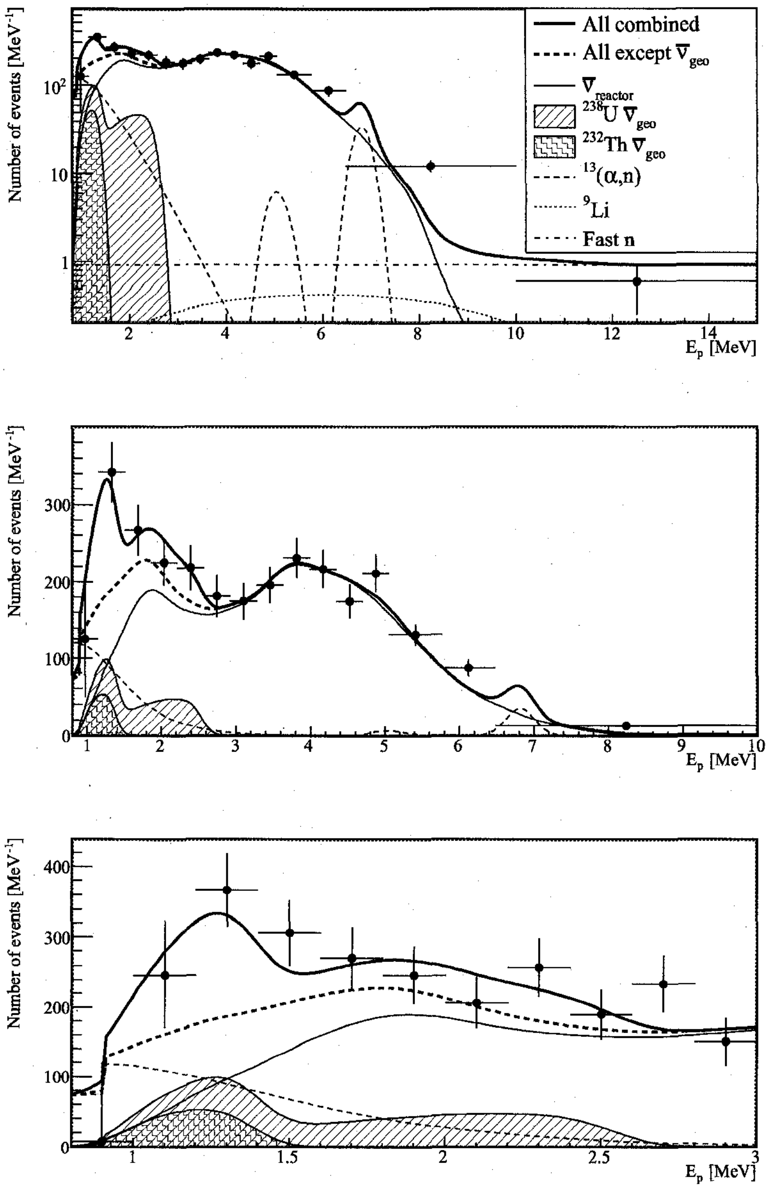

Figure 7.3: Mode-II analysis best-fit E_{p} spectra. The dots with error bars are candidate event distribution minus best-fit random coincidence background spectrum. The spectra shown are all combined, all combined except $\bar{\nu}_{\mathrm{geo}}$, $\bar{\nu}_{\mathrm{reactor}}$, ^{238}U $\bar{\nu}_{\mathrm{geo}}$, ^{232}Th $\bar{\nu}_{\mathrm{geo}}$, $^{13}\mathrm{C}(\alpha, \mathrm{n})$, ^{9}Li, and fast neutrons; see the legend in the top plot.

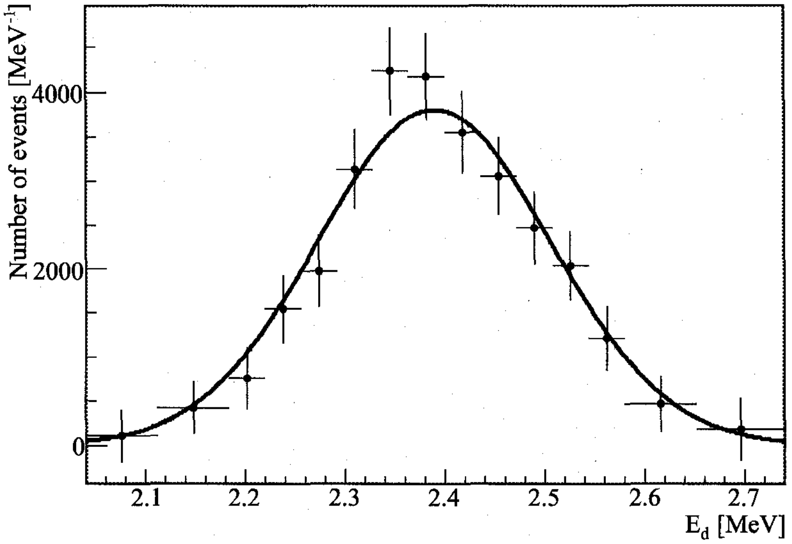

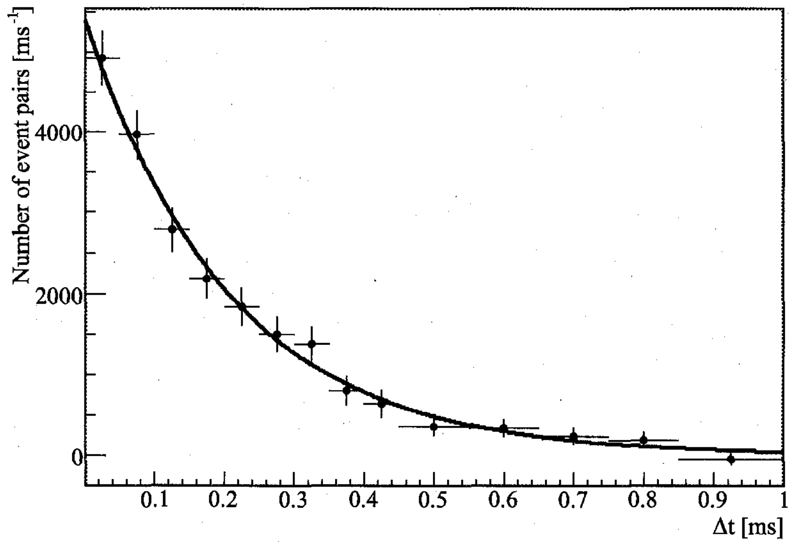

Figure 7.4: Mode-II analysis best-fit E_{d} (top plot) and Δt (bottom plot) spectra of neutron capture events. The dots with error bars are candidate event distribution minus best-fit random coincidence background spectrum. The solid lines indicate the PDFs for E_{d} and Δt scaled by the sum of the neutron capture events from the best-fit.

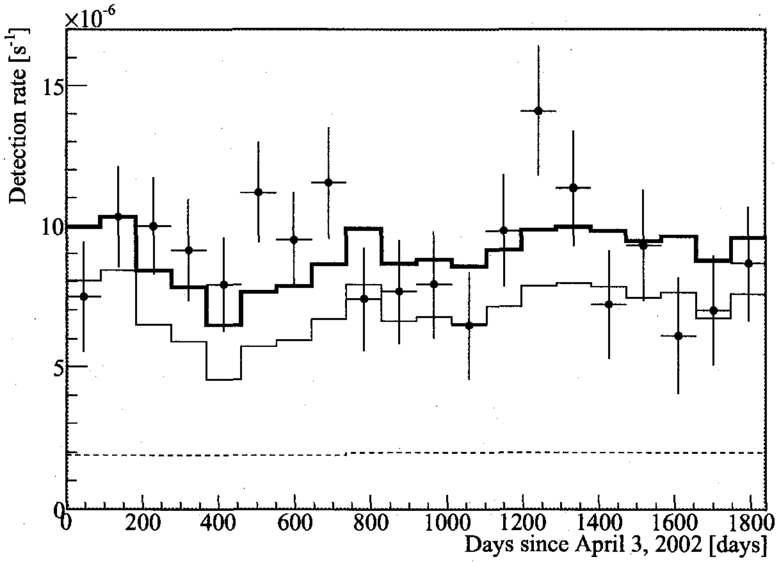

Figure 7.5: Mode-II analysis best-fit time spectra. The dots with error bars are candidate event-pair distribution minus best-fit random coincidence background spectrum. The thin solid line indicates the best-fit $\bar{\nu}_{\rm reactor}$ spectrum. The dotted line indicates the sum of the best-fit spectra for $\bar{\nu}_{\rm geo}$ signal and ^{13}C$(\alpha, \rm n)$, ^{9}Li, fast neutron, and atmospheric ν backgrounds. The thick solid line is the sum of the spectra indicated by the dotted and thin solid lines.

focus on the $\bar{\nu}_{\text{reactor}}$ and $\bar{\nu}_{\text{geo}}$ E_{p} regions, respectively. The main differences between the best-fit E_{p} spectra from Mode-I and II analyses are the normalizations of ^{238}U and ^{232}Th $\bar{\nu}_{\text{geo}}$s. The top and bottom plots in Figure 7.4 and Figure 7.5 show the best-fit E_{d}, Δt, and t spectra from Mode-II analysis, respectively, all obtained by combining the best-fit spectra of all the event types, except random coincidence backgrounds. These plots also show the distributions of the candidate event-pairs after subtracting the best-fit random coincidence backgrounds spectra. The best-fit E_{d} and Δt spectra from Mode-I are not appreciably different from those from Mode-II analysis. The correlation coefficient matrices for Mode-I, II, and III analysis best-fits are given in Tables I.1, I.2, and I.3, respectively, in Appendix I.

7.4 Goodness-of-Fit

Based on how well a particular model fits the data, "goodness-of-fit," the model can be accepted or rejected. Although the unbinned maximum likelihood fit effectively determines the best-fit parameter values, $\chi^2 = -2\log L$ at its maximum does not yield the goodness of the fit to the data [72]. Instead, the goodness-of-fit for Mode-I analysis is estimated using a Monte Carlo simulation from the following procedures. First, 1000 Monte Carlo data-sets are created using the best-fit E_{p}, E_{d} and Δt spectra of all event types from Mode-I analysis. The number of each event type to be simulated in each Monte Carlo data-set is obtained from a Poisson distribution with a mean from the best-fit number of events of the actual candidate data-set. Using the exact same method as the real data-set, all the parameters are fitted for each Monte Carlo data-set. Using the resulting best-fit spectra, equal-probability-binning histograms are prepared for the E_{p}, E_{d} and Δt distributions, and the Pearson χ^2 for each variable is calculated for each data-set. As an example, the top plot in Figure 7.6 shows the E_{p} distribution of the actual candidate data-set in 50 equal-probablity binning, used to calculate the Pearson χ^2. For a given number of bins, the Pearson χ^2 of the candidate data-set is compared to those of the Monte Carlo data-sets. The goodness-of-fit p-value is the fraction of Monte Carlo data-sets that have a Pearson χ^2 larger than that of the candidate data-set. As examples, Figure 7.7 shows the Pearson χ^2 distributions

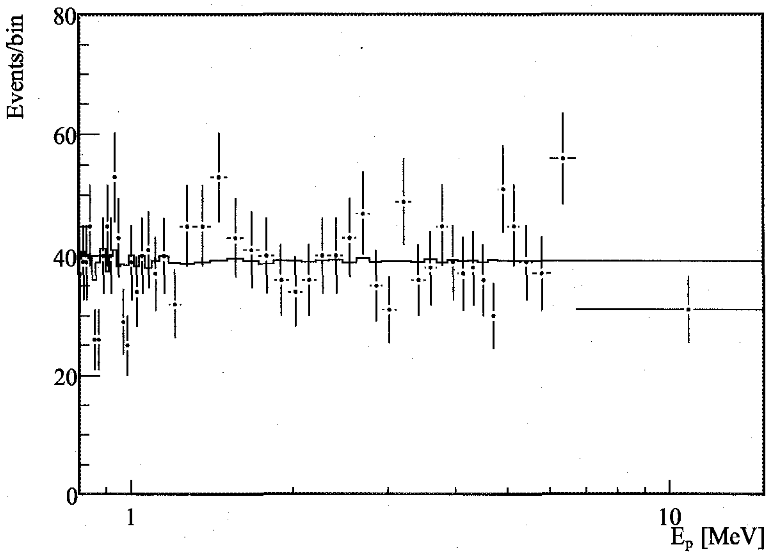

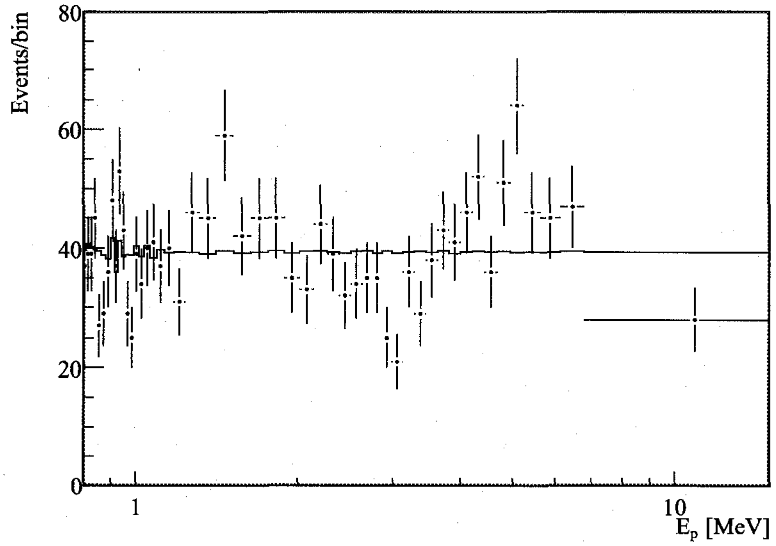

Figure 7.6: E_p distributions of candidates (markers with error bars) in 50 equal-probablity bins, prepared from the best-fit E_p spectra (solid lines). Top plot is for the best-fit obtained assuming two-flavor neutrino oscillation. The bottom plot is for the best-fit obtained assuming no neutrino oscillation and floating $\varepsilon_\mathrm{reactor}$ without a penalty, as described in Section 7.4.1.

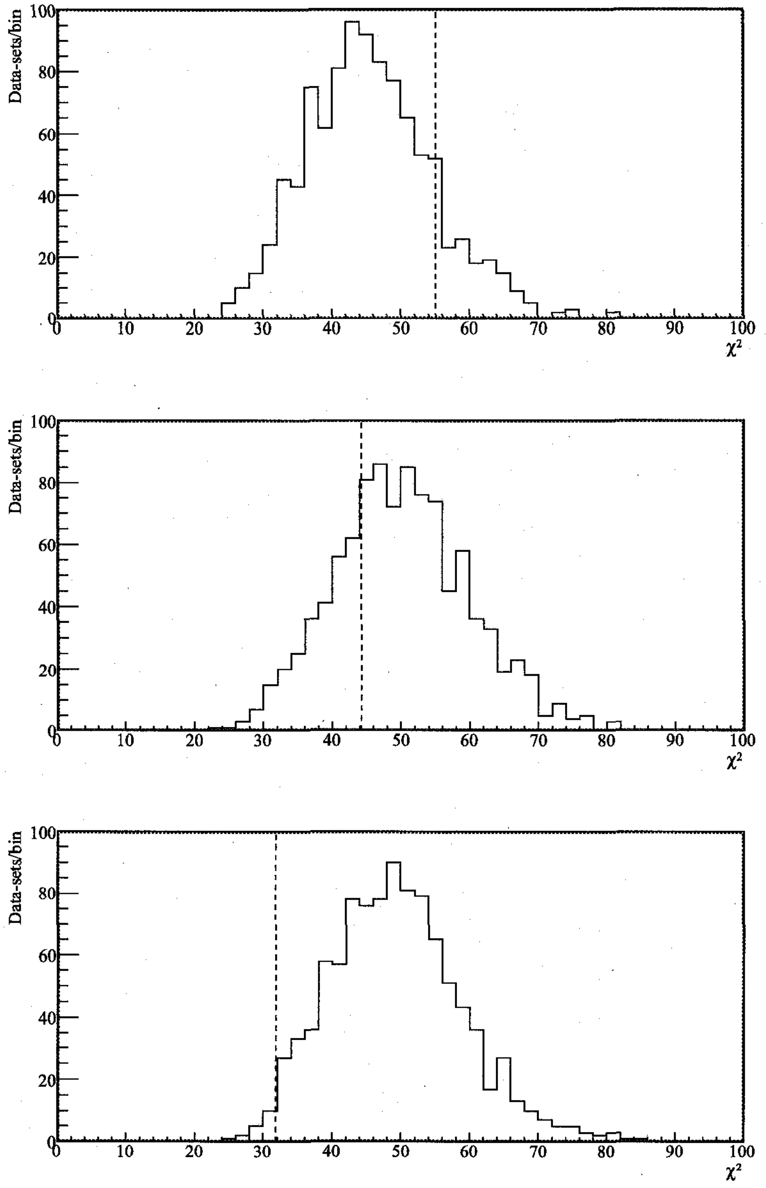

Figure 7.7: Pearson χ^2 distributions for 50 equal-probablity binnings of the Monte Carlo E_{p} (top plot), E_{d} (middle plot), and Δt (bottom plot) distributions. The vertical dotted lines indicate the Pearson χ^2 for the candidate data-set.

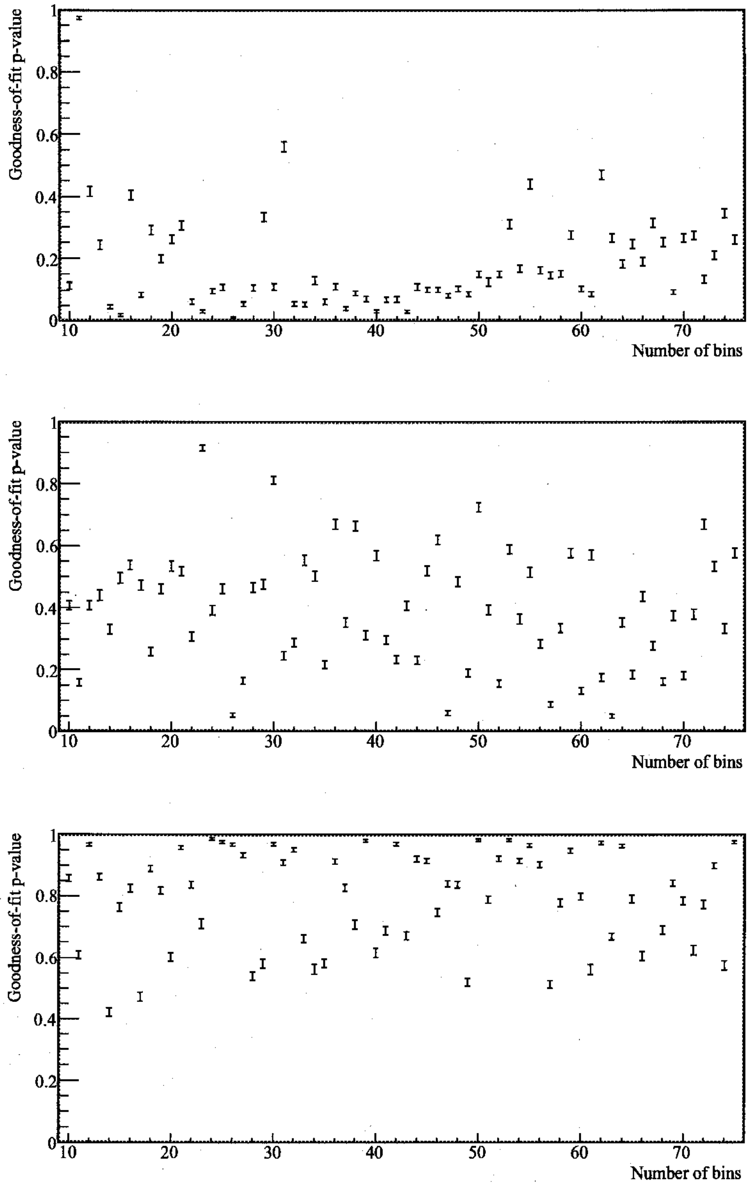

Figure 7.8: E_{p} (top plot), E_{d} (middle plot), Δt (bottom plot) spectra goodness-of-fit p-value vs. number of equal-probablity bins. The uncertainties in the goodness-of-fit p-value due to the statistical errors of the Monte Carlo simulation are shown as the error bars.

for the E_p, E_d, and Δt spectra for 50 equal-probablity binnings. This binning was chosen *a priori* since it is approximately the center of the optimal range based on the number of the candidate event-pairs [72]. For this number of bins, the goodness-of-fit p-values are 15 %, 73 %, and 98 % for E_p, E_d, and Δt spectra, respectively; the statistical errors from the Monte Carlo simulation are ignored. The goodness-of-fit for E_d and Δt spectra are better than that for E_p spectrum, probably because the E_d and Δt PDFs are directly measured while all the E_p PDFs, except that of random coincidence and fast neutron backgrounds, are theoretically calculated. The goodness-of-fit p-value, however, depends on the number of bins used as shown in Figure 7.8. Although most of the goodness-of-fit p-values obtained with other numbers of bins are slightly lower than those obtained with 50 bins, there is no sign of a problem in any of the goodness-of-fit.

7.4.1 $\bar{\nu}_\mathrm{reactor}$ E_p Spectral Distortion

The significance of $\bar{\nu}_\mathrm{reactor}$ E_p spectral distortion is explored by fixing $\sin^2 2\theta_{12} = 0$, which is equivalent to assuming that there is no neutrino oscillation, and allowing $\varepsilon_\mathrm{reactor}$ to freely float during the fit. The top plot in Figure 7.9 shows the best-fit E_p spectra for the various event types in this case. The disagreement between the best-fit spectrum and the data, after subtracting the best-fit random coincidence background spectrum, is apparent. The bottom plot in Figure 7.6 shows the E_p distribution of the candidates in 50 equal-probablity binning, prepared from its best-fit E_p spectrum in this case. The E_p distribution of the candidates clearly favors the best-fit spectrum obtained assuming two-flavor neutrino oscillation, shown in the top plot in Figure 7.6. Goodness-of-fit in this case is calculated using a similar method to that described in Section 7.4 by obtaining the Pearson χ^2 distribution for 1000 Monte Carlo data-set. The technique of using the fraction of Monte Carlo data-sets with a larger Pearson χ^2 fails in this case since all Monte Carlo data-sets have smaller Pearson χ^2 than the candidate data-set. Instead, the number of degree of freedom (*ndf*) is estimated from the Pearson χ^2 distribution of the Monte Carlo data-sets, and goodness-of-fit p-value of the candidate data-set is obtained from $1 - \Gamma(0.5\,ndf,\, 0.5\,\chi^2)$, where Γ is the upper

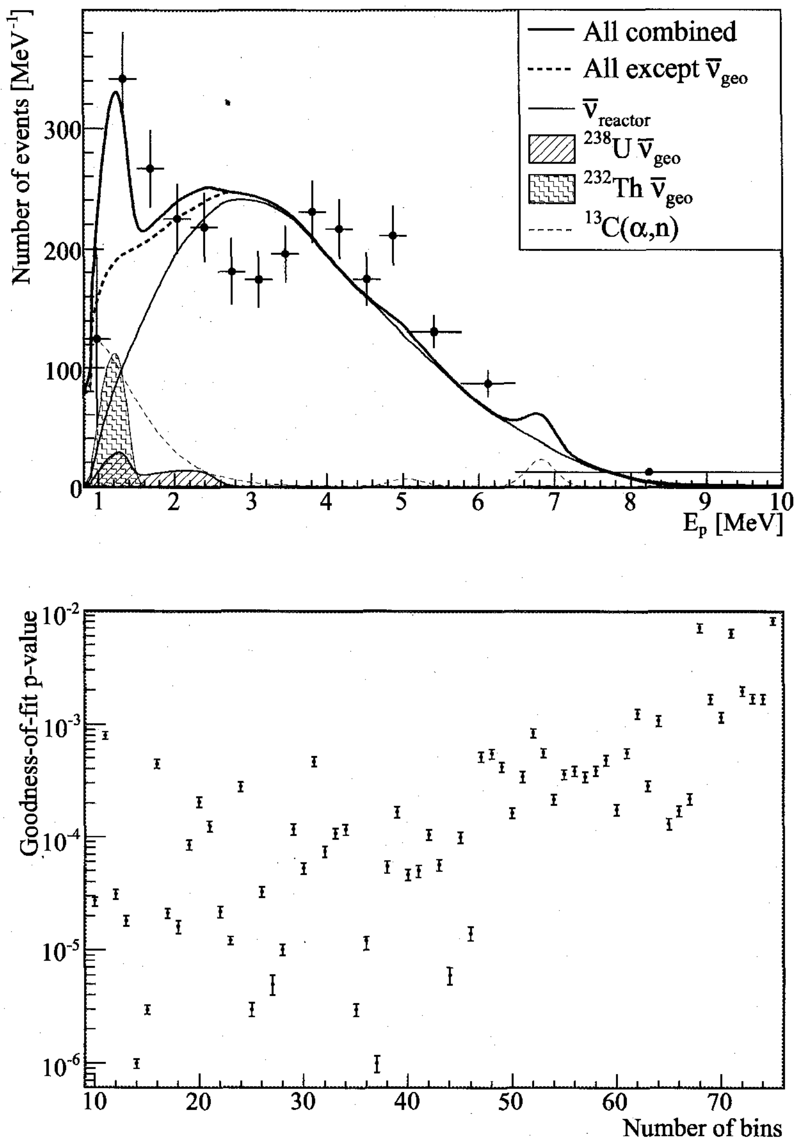

Figure 7.9: Best-fit E_p spectra (top plot) and goodness-of-fit p-values (bottom plot) obtained using unoscillated $\bar{\nu}_\mathrm{reactor}$ spectrum with unconstrained normalization. Top plot: the best-fit random coincidence events are subtracted from the data (markers with error bars). The best-fit E_p spectra of fast neutron, ^{9}Li, and atmospheric ν backgrounds are too small to be seen. Bottom plot: the goodness-of-fit p-value depends on the number of equal-probablity bins. The uncertainties in the goodness-of-fit p-value due to the statistical errors of the Monte Carlo simulation are shown as the error bars.

incomplete gamma function. The bottom plot in Figure 7.9 shows the goodness-of-fit p-value versus number of equal-probability bins used. Although the goodness-of-fit p-value varies depending on the number of bins selected, any of them is much worse than the goodness-of-fit p-values obtained by assuming two-flavor neutrino oscillation shown in the top plot in Figure 7.8. For 50 equal-probability binning, for example, the null hypothesis of an undistorted $\bar{\nu}_{\text{reactor}}$ energy spectrum is definitively rejected at the 99.98 % confidence level.

7.5 Neutrino Oscillation Parameter Results

Mode-I, II, and III analyses yield best-fit neutrino oscillation parameters and their $1\,\sigma$ confidence intervals of $\sin^2 2\theta_{12} = 0.917^{+0.062}_{-0.066}$ and $\Delta m^2_{21} = 7.54^{+0.21}_{-0.21} \times 10^{-5}\,\text{eV}^2$, $\sin^2 2\theta_{12} = 0.935^{+0.061}_{-0.065}$ and $\Delta m^2_{21} = 7.44^{+0.19}_{-0.18} \times 10^{-5}\,\text{eV}^2$, and $\sin^2 2\theta_{12} = 0.901^{+0.028}_{-0.032}$ and $\Delta m^2_{21} = 7.46^{+0.19}_{-0.18} \times 10^{-5}\,\text{eV}^2$, respectively. The $1\,\sigma$ confidence intervals around the best-fit values are obtained from the one dimensional $\Delta\chi^2$ scans, as shown in Figures 7.10. The solar ν measurements used in Mode-III analysis put a tighter constraint on $\sin^2 2\theta_{12}$, but has little effect on Δm^2_{21}, which can be clearly seen by comparing the two dimensional confidence contours for Δm^2_{21} verses $\sin^2 2\theta_{12}$ for Mode-I, II, and III analyses in Figures 7.11. Only the LMA1 region is shown since the LMA0 and LMA2 regions are disfavored over the LMA1 region at confidence levels of 99.96 % and 99.997 % for mode-I analysis, and 99.95 % and 99.9991 % for Mode-II analysis, respectively.

7.6 $\bar{\nu}_{\text{geo}}$ Parameter Results and $\bar{\nu}_{\text{geo}}$ Observation

Mode-I, II, and III analyses yield best-fit $\bar{\nu}_{\text{geo}}$ parameters and their $1\,\sigma$ confidence intervals of $\Phi_{\text{geo sum}} = 110^{+41}_{-38}$ $(10^{32}\,\text{p} \cdot \text{yr})^{-1}$ and $\Phi_{\text{geo diff}} = 0.22^{+0.63}_{-0.92}$, $\Phi_{\text{geo sum}} = 131^{+41}_{-38}$ $(10^{32}\ \text{p} \cdot \text{yr})^{-1}$ and $\Phi_{\text{geo diff}} = 0.60^{+0.40}_{-0.62}$, and $\Phi_{\text{geo sum}} = 122^{+36}_{-35}$ $(10^{32}\,\text{p} \cdot \text{yr})^{-1}$ and $\Phi_{\text{geo diff}} = 0.51^{+0.49}_{-0.64}$, respectively. The $1\,\sigma$ confidence intervals around the best-fit values are obtained from the one dimensional $\Delta\chi^2$ scans, shown in Figure 7.12, except the upper errors of $\Phi_{\text{geo diff}}$ for Mode-II and III analyses are set by the physically

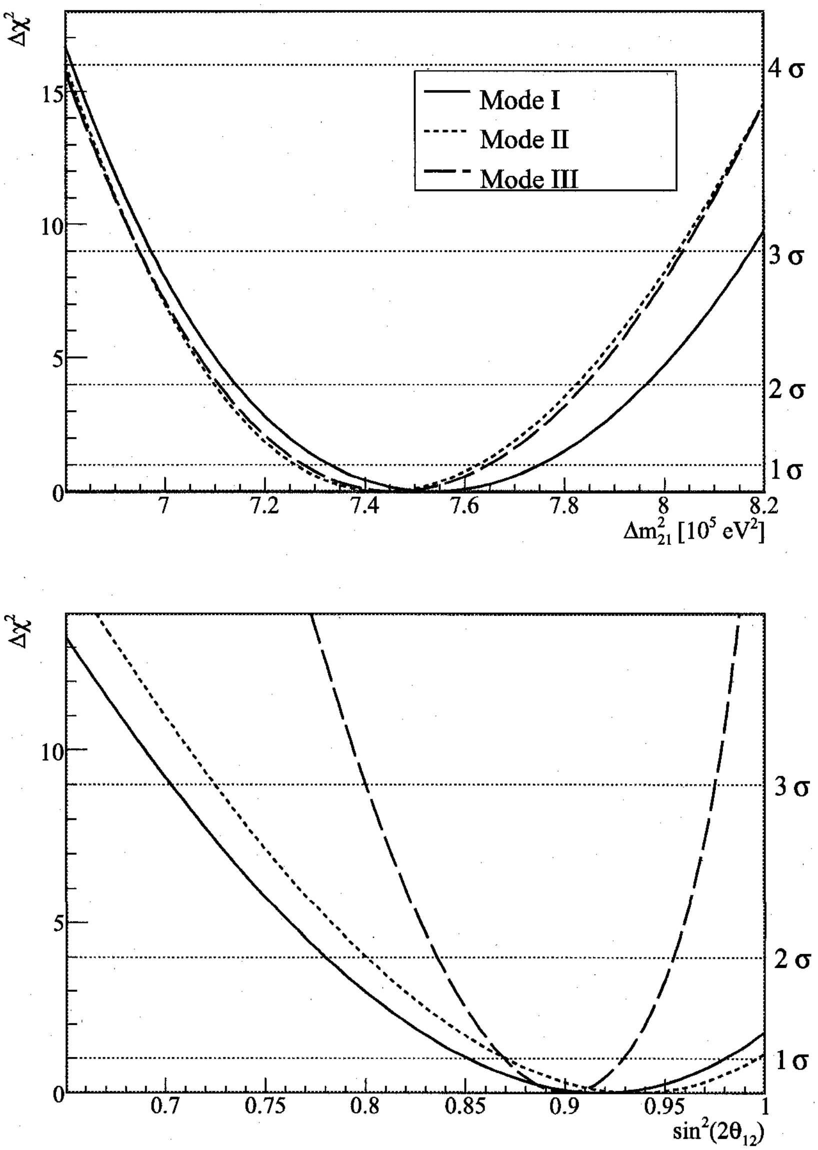

Figure 7.10: Comparison of the one dimensional $\Delta\chi^2$ scans for Δm^2_{21} (top plot) and $\sin^2 2\theta_{12}$ (bottom plot) from Mode-I, II, and III analyses. The thin dotted horizontal lines indicate the $\Delta\chi^2$ values used to calculate the confidence levels.

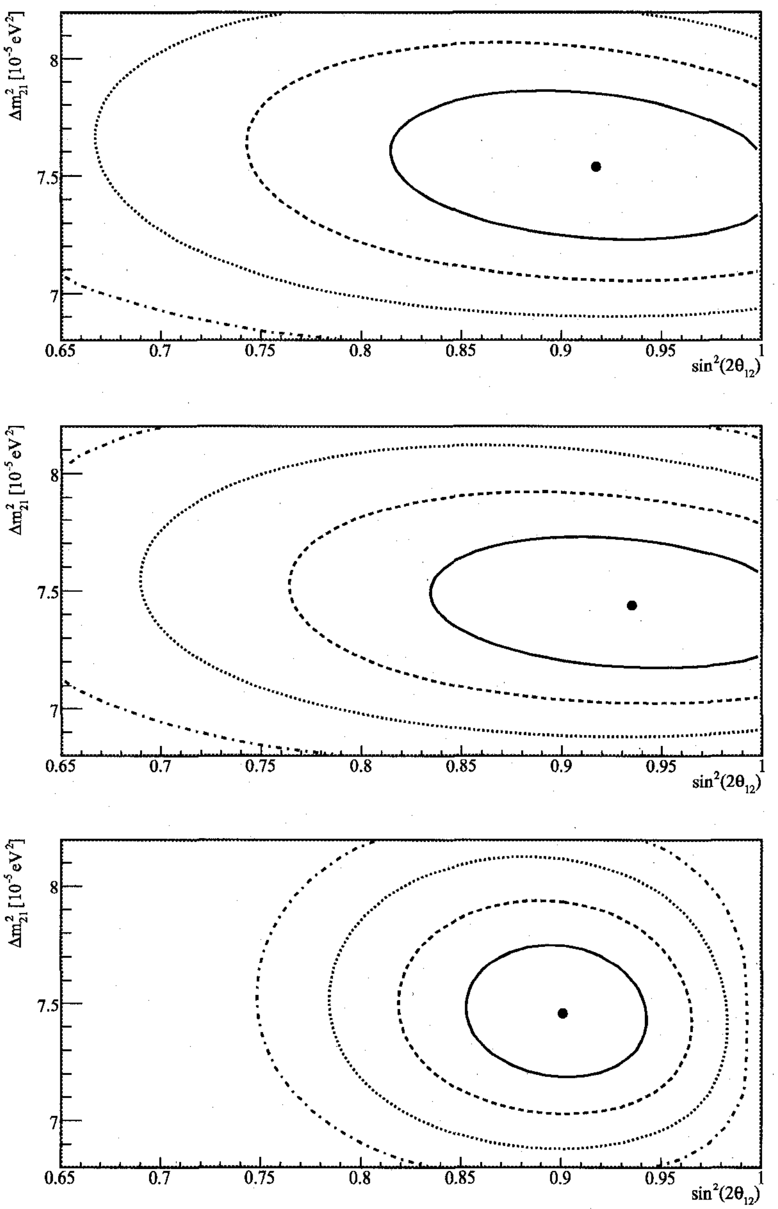

Figure 7.11: Neutrino oscillation parameter confidence contours for Mode-I (top plot), II (middle plot), and III (bottom plot) analyses. The confidence levels are $1\,\sigma$ (solid), $2\,\sigma$ (dashed), $3\,\sigma$ (dotted), and $4\,\sigma$ (dot-dashed). The dots indicate the best-fit values.

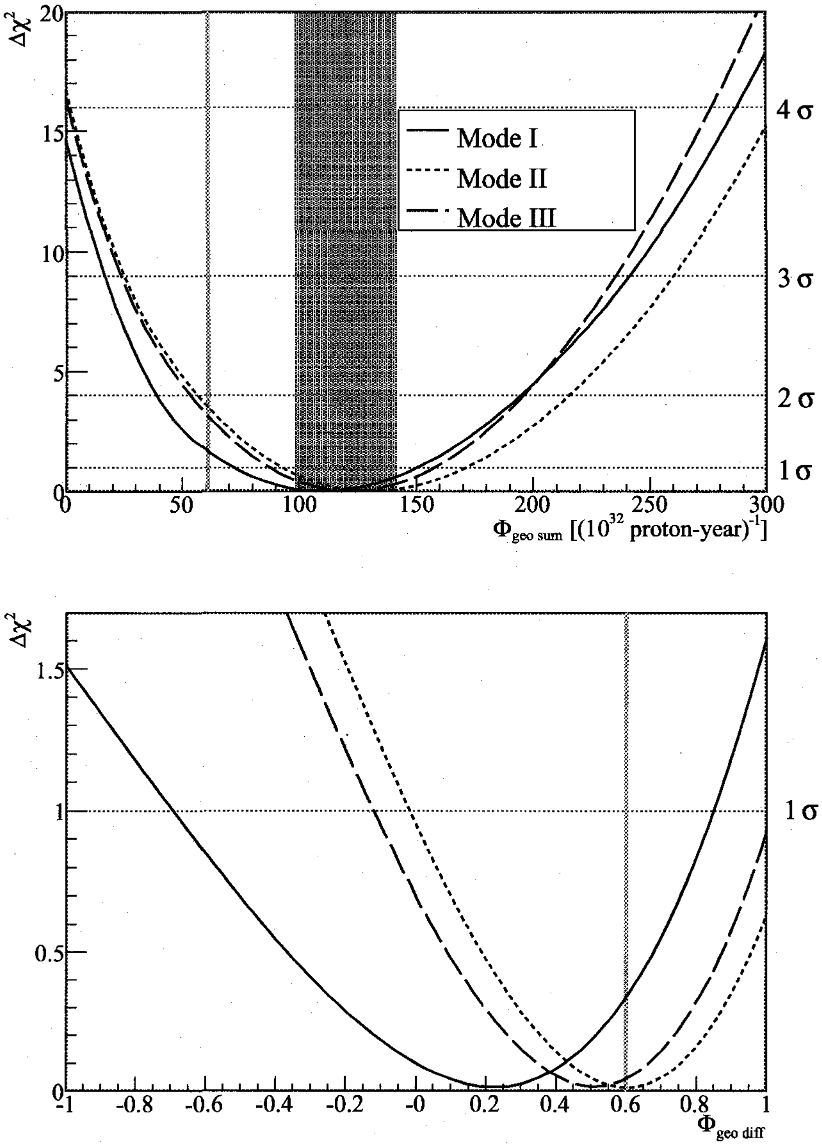

Figure 7.12: Comparison of the one dimensional $\Delta\chi^2$ scans for $\Phi_{\mathrm{geo\,sum}}$ (top plot) and $\Phi_{\mathrm{geo\,diff}}$ (bottom plot) from Mode-I, II, and III analyses. The dotted horizontal lines indicate the $\Delta\chi^2$ values used to calculate the confidence levels. The thick gray vertical lines are the central expected values based on the reference Earth model described in Section 1.3.2. The filled box in the top plot represents the range of $\Phi_{\mathrm{geo\,sum}}$ if the Earth is "fully radiogenic," as described in Section 6.2.

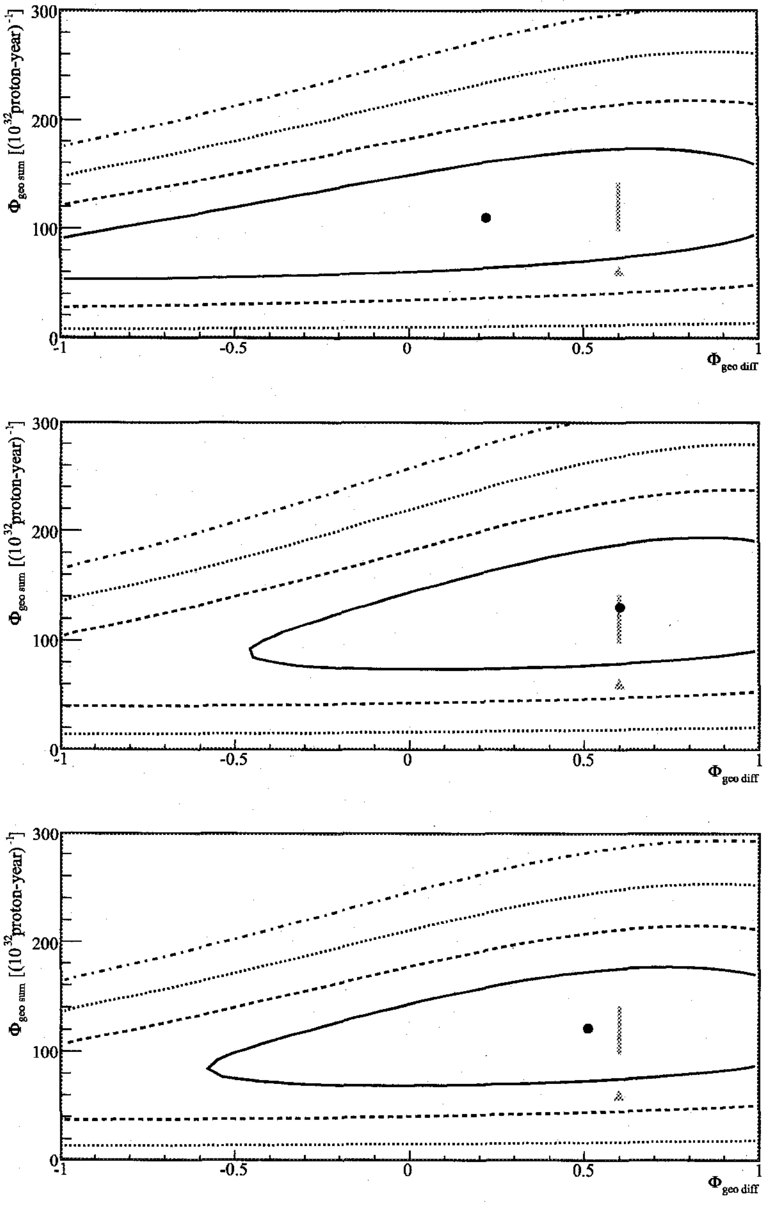

Figure 7.13: $\bar{\nu}_{\rm geo}$ parameter confidence contours for Mode-I (top plot), II (middle plot), and III (bottom plot). The confidence levels are $1\,\sigma$ (solid), $2\,\sigma$ (dashed), $3\,\sigma$ (dotted), and $4\,\sigma$ (dot-dashed). The black circular markers indicate the best-fit values. The gray triangular markers indicate the central predicted value based on the reference Earth model described in Section 1.3.2. The gray line segments represent the range of $\Phi_{\rm geo\,sum}$ if the Earth is "fully radiogenic," as described in Section 6.2.

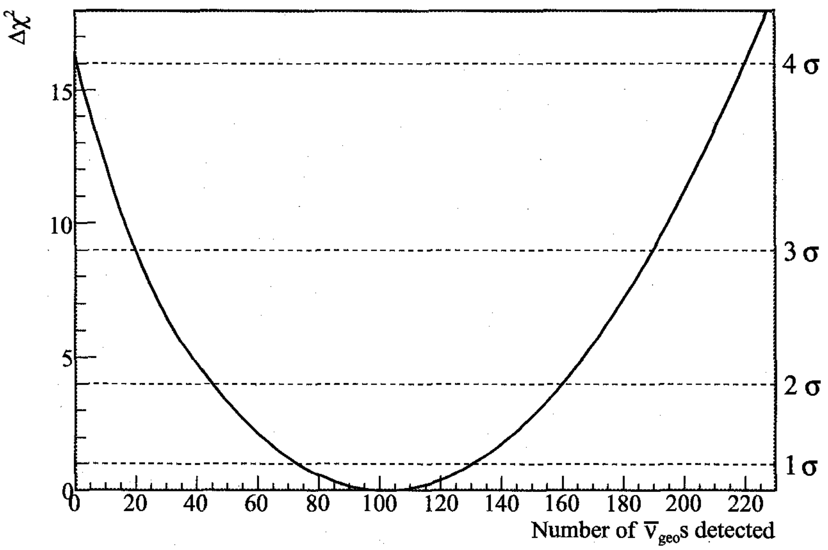

Figure 7.14: One dimensional $\Delta\chi^2$ scan for number of $\bar{\nu}_{\text{geo}}$s detected. The thin dotted horizontal lines indicate the $\Delta\chi^2$ values used to calculate the confidence levels.

allowed maximum value of $\Phi_{\text{geo diff}} = 1$. These best-fit $\Phi_{\text{geo sum}}$ and $\Phi_{\text{geo diff}}$ values correspond to fluxes at the KamLAND site of 5.0 (for Mode-I), 7.8 (for Mode-II), and 6.9 (for Mode-III) $\times 10^6$ $\bar{\nu}$s cm^{-2} s^{-1} from the ^{238}U decay chain and 11 (for Mode-I), 6.4 (for Mode-II), and 7.3 (for Mode-III) $\times 10^6$ $\bar{\nu}$s cm^{-2} s^{-1} from the ^{232}Th decay chain, including $\bar{\nu}_\mu$s and $\bar{\nu}_\tau$s that have oscillated from $\bar{\nu}_e$s as they traverse to reach KamLAND. Figure 7.13 shows the two dimensional confidence contours for $\Phi_{\text{geo sum}}$ verses $\Phi_{\text{geo diff}}$ from Mode-I, II, and III analyses. These results are consistent with "fully radiogenic" Earth model described in Section 6.2, and the central parameter values predicted by the reference Earth model described in Section 1.3.2 are also compatible at the 18.5 %, 11.8 %, and 14.1 % confidence levels for Mode-I, II, and III analyses, respectively.

Instead of fitting $\Phi_{\text{geo sum}}$ and $\Phi_{\text{geo diff}}$, a second analysis in Mode-III fits the absolute number of $\bar{\nu}_{\text{geo}}$s detected to calculate the significance of $\bar{\nu}_{\text{geo}}$ observation. This ignores the correlation with the detection efficiency and $\sin^2 2\theta_{12}$ (see Equation 6.5). This correlation is necessary when determining the central value with error, but not necessary when only testing whether $\bar{\nu}_{\rm geo}$s are observed. Figure 7.14 shows the one dimensional $\Delta\chi^2$ scan for the number of $\bar{\nu}_{\rm geo}$s detected. The observation of $\bar{\nu}_{\rm geo}$s is confirmed at the 99.995 % confidence level.

7.7 Nuclear Reactor at the Center of the Earth

A rather controversial Earth model is proposed, which suggests the existance of a "georeactor," a naturally occurring nuclear reactor, fueled by uranium, at the very center of the Earth's core [73, 74]. This hypothesis conflicts with the widely accepted Earth model that uranium concentration in the iron core is negligible since uranium is chemically incompatible with iron (see Section 1.3.2). However, from a strictly empirical point of view, this hypothesis is difficult to refute using existing geological and geophysical data. If a georeactor existed, it would produce $\bar{\nu}_{\rm e}$s, which could be detected with KamLAND. According to the model [73, 74], the georeactor produces up to approximately 10 TW of thermal power from nuclear fission of ^{235}U and ^{238}U, which comprise 76 % and 24 % of the georeactor fission, respectively. The expected $E_{\rm p}$ spectral shape is the weighted sum of the spectra of $\bar{\nu}_{\rm e}$s from β-decays of fragments following ^{235}U and ^{238}U fission, shown in Figure 1.7, which is then converted into a $E_{\rm vis}$ spectrum. The expected georeactor $\bar{\nu}_{\rm e}$ detection rate, given per target proton per unit time can be expressed as

$$\Phi_{\rm georeactor} = \varepsilon\,\frac{f_{\rm georeactor}}{4\pi R_{\oplus}^2}\int P_{\bar{\nu}_{\rm e}\to\bar{\nu}_{\rm e}}(E_{\bar{\nu}_{\rm e}},\,R_{\oplus})\,\sigma(E_{\bar{\nu}_{\rm e}})\,\frac{dN}{dE_{\bar{\nu}_{\rm e}}}(E_{\bar{\nu}_{\rm e}})\,dE_{\bar{\nu}_{\rm e}}, \tag{7.11}$$

where ε is the detection efficiency, $f_{\rm georeactor}$ denotes the fission rate in the georeactor, $R_{\oplus}$ denotes the radius of the Earth, $P_{\bar{\nu}_{\rm e}\to\bar{\nu}_{\rm e}}(E_{\bar{\nu}_{\rm e}},\,R_{\oplus})$ denotes the $\bar{\nu}_{\rm e}$ survival probability due to neutrino oscillation (see Equation 1.5), σ denotes the inverse β-decay cross-section (see Figure 1.6), and $\frac{dN}{dE_{\bar{\nu}_{\rm e}}}$ denotes the energy spectrum of the produced $\bar{\nu}_{\rm e}$s given in number of $\bar{\nu}_{\rm e}$s per fission per unit energy. Since $R_{\oplus}$ is much larger than $E_{\bar{\nu}_{\rm e}}/\Delta m^2_{21}$, the $\sin^2\left(\frac{\Delta m^2_{21} R_{\oplus}}{E_{\bar{\nu}_{\rm e}}}\right)$ term in the survival probability (see Equation 1.5) results in many oscillations in the $\bar{\nu}_{\rm e}$ energy spectrum. However, an oscillation pattern

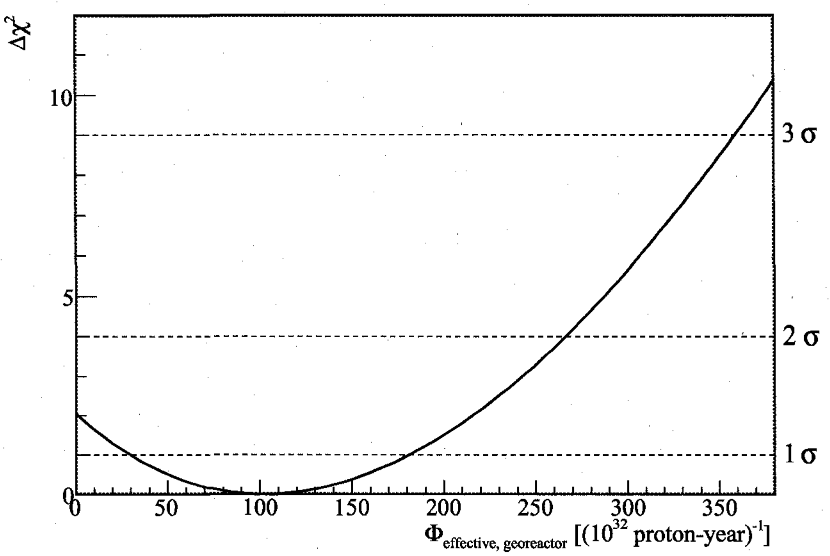

Figure 7.15: One dimensional $\Delta\chi^2$ scan for $\Phi_{\text{effective, georeactor}}$. The thin dotted horizontal lines indicate the $\Delta\chi^2$ values used to calculate the confidence levels.

in the expected E_{p} spectrum is smeared out due to the E_{vis} reconstruction resolution, simply resulting in a overall rate suppression rather than spectral distortion. The suppression factor is given by $1 - 0.5\sin^2 2\theta_{12}$, and Equation 7.11 becomes

$$\begin{aligned} \Phi_{\text{georeactor}} &\approx \varepsilon\,(1 - 0.5\sin^2 2\theta_{12})\,\frac{f_{\text{georeactor}}}{4\pi R_{\oplus}^2}\,I_{\text{U}} \\ &\equiv \varepsilon\,(1 - 0.5\sin^2 2\theta_{12})\,\Phi_{\text{effective, georeactor}}, \end{aligned} \tag{7.12}$$

where

$$I_{\text{U}} \equiv \int \sigma(E_{\bar{\nu}_{\text{e}}})\,\frac{dN}{dE_{\bar{\nu}_{\text{e}}}}(E_{\bar{\nu}_{\text{e}}})\,dE_{\bar{\nu}_{\text{e}}} = 7.04 \times 10^{-43}\,\frac{\bar{\nu}_{\text{e}}\,\text{cm}^2}{\text{fission}}. \tag{7.13}$$

The detection efficiency, E_{d} PDF, and Δt PDF for $\bar{\nu}_{\text{e}}$s from the georeactor are assumed to be the same as those of $\bar{\nu}_{\text{reactor}}$s. The flux is assumed to be constant in time.

$\Phi_{\text{effective, georeactor}}$ is fitted by including the expected PDFs for $\bar{\nu}_{\text{e}}$s from a georeactor in Equation 7.8. The best-fit $\Phi_{\text{effective, georeactor}}$ and its $1\,\sigma$ confidence interval, obtained from the one dimensional $\Delta\chi^2$ scan, shown in Figure 7.15, is 102^{+79}_{-72} $(10^{32}\,\text{p}\cdot\text{yr})^{-1}$. Assuming that 6 $\bar{\nu}_{\text{e}}$s and 200 MeV are produced in each fission and

Table 7.4: Best-fit parameter value comparison for Mode-III analysis with and without georeactor. The errors on the estimated parameter values are given in parentheses.

Parameter	Estimate	With georeactor	Without georeactor
$\Phi_{\text{effective, georeactor}}$ $[(10^{32}\,\text{p}\cdot\text{yr})^{-1}]$	N/A	102	N/A
$\sin^2 2\theta_{12}$	N/A	0.916	$0.901^{+0.028}_{-0.032}$
Δm^2_{21} $[10^{-5}\,\text{eV}^2]$	N/A	7.50	$7.46^{+0.19}_{-0.18}$
$\Phi_{\text{geo sum}}$ $[(10^{32}\,\text{p}\cdot\text{yr})^{-1}]$	N/A	116	122^{+36}_{-35}
$\Phi_{\text{geo diff}}$	N/A	0.31	$0.51^{+0.49}_{-0.64}$
$R_{\text{fast n}}$ $[\text{yr}^{-1}\,\text{MeV}^{-1}]$	N/A	0.2	0.2
$R_{\text{atm}\,\nu}$ $[\text{yr}^{-1}]$	N/A	0	0
a_0	1.061(24)	1.063	1.061
k_b $[\text{mg}\,\text{cm}^{-2}\,\text{MeV}^{-1}]$	9.71(27)	9.74	9.72
k_0	0.84(14)	0.84	0.85
k_C	0.43(11)	0.41	0.42
$\varepsilon_{\text{common}}$	0.875(35)	0.837	0.860
$\varepsilon_{\text{reactor}}$	0.986(34)	0.963	0.983
$N_{\text{random I}}$	202.30(35)	202.31	202.31
$N_{\text{random II}}$	653.41(74)	653.39	653.39
$R_{^{13}\text{C}(\alpha,\text{n})}$ $[10^{-6}\,\text{s}^{-1}]$	1.53(20)	1.54	1.54
$F_{^{13}\text{C}(\alpha,\text{n}),\,\text{C}}$	0.02105(45)	0.02106	0.02106
$F_{^{13}\text{C}(\alpha,\text{n})^{16}\text{O}^*}$	0.09(9)	0.09	0.10
$N_{^9\text{Li}}$	2.98(72)	3.03	3.04
ϕ_1 $[10^{10}\,\text{cm}^{-2}\,\text{s}^{-1}]$	5.94(6)	5.99	6.00
ϕ_7 $[10^{9}\,\text{cm}^{-2}\,\text{s}^{-1}]$	4.9(6)	5.5	5.4
ϕ_8 $[10^{6}\,\text{cm}^{-2}\,\text{s}^{-1}]$	6(1)	5	5

its subsequent decays, and taking $R_{\oplus} = 6400\,\mathrm{km}$, the best-fit $\Phi_{\text{effective, georeactor}}$ corresponds to $f_{\text{georeactor}} = 2.4 \times 10^{23}$ fission per second, or a georeactor power generation of 7.6 TW. However, this result is also consistent with the absence of the georeactor at the 15 % confidence level. Table 7.4 summarizes the best-fit values of all the parameters, none of which changes significantly by the inclusion of the georeactor contribution. The correlation coefficient matrix for this best-fit is given in Table I.4 in Appendix I.

Chapter 8

Conclusions

Based on data acquired with KamLAND from April 2002 to April 2007, corresponding to a 1.8×10^{32} proton-year exposure to $\bar{\nu}_{\mathrm{e}}$s, the neutrino oscillation parameters, $\sin^2 2\theta_{12}$ and Δm^2_{21}, are determined using $\bar{\nu}_{\mathrm{e}}$s originating from nuclear reactors ($\bar{\nu}_{\mathrm{reactor}}$s), and the flux of $\bar{\nu}_{\mathrm{e}}$s originating from the Earth ($\bar{\nu}_{\mathrm{geo}}$s) are measured. The $\bar{\nu}_{\mathrm{e}}$s are detected via inverse β-decay, which produces a positron and a neutron. After selecting candidate prompt-delayed event-pairs and setting up probability distribution functions for the signals and backgrounds, likelihood functions are constructed to extract the signals, making best use of all information available. The analysis is conducted in three modes; Mode-I analysis uses the spectral shapes for the prompt and delayed event energies (E_{p} and E_{d}, respectively), and the time between the prompt and delayed events (Δt), Mode-II analysis additionally uses the spectral shape in absolute time, and Mode-III analysis combines Mode-II analysis with solar ν experimental results assuming CPT-invariance.

Mode-I analysis shows that the E_{p} distribution of the selected $\bar{\nu}_{\mathrm{e}}$ candidates is inconsistent with the spectral shape expected from unoscillated $\bar{\nu}_{\mathrm{e}}$s at 99.98 % confidence level. Rather, the E_{p}, E_{d}, and Δt distributions are more consistent with the spectral shapes expected from a two-flavor neutrino oscillation; the goodness-of-fit p-values of the spectra in E_{p}, E_{d}, and Δt are 15 %, 73 %, and 98 %, respectively, indicating generally good fit. Mode-II analysis yields best-fit neutrino oscillation parameters to KamLAND data of $\sin^2 2\theta_{12} = 0.935^{+0.061}_{-0.065}$ and $\Delta m^2_{21} = 7.44^{+0.19}_{-0.18} \times 10^{-5}\,\mathrm{eV}^2$.

The estimated Δm^2_{21} is slightly lower than the previous result from the KamLAND collaboration, $\Delta m^2_{21} = 7.9^{+0.6}_{-0.5} \times 10^{-5}\mathrm{eV}^2$ [44]. The error on Δm^2_{21} improved significantly due to much larger exposure, extension of the analyzed energy range down to the inverse β-decay threshold, and better overall control of systematics. In Mode-II analysis, the so-called LMA0 and LMA2 parameter regions are now disfavored over LMA1 region at the 99.95 % and 99.9991 % confidence levels, respectively.

Assuming CPT-invariance, Mode-III analysis combines the result obtained with Mode-II analysis with the results from the solar ν experiments, which provides tighter constraint on $\sin^2 2\theta_{12}$, yielding $\sin^2 2\theta_{12} = 0.901^{+0.028}_{-0.032}$ and $\Delta m^2_{21} = 7.46^{+0.19}_{-0.18} \times 10^{-5}\,\mathrm{eV}^2$. This $\sin^2 2\theta_{12}$ is slightly higher than the previous "global" result from the KamLAND collaboration, $\tan^2\theta_{12} = 0.40^{+0.10}_{-0.07}$, corresponding to $\sin^2 2\theta_{12} = 0.82^{+0.07}_{-0.07}$.

Mode-III analysis is the most appropriate to extract measurements of $\bar{\nu}_{\mathrm{geo}}$s. This estimates the sum of ^{238}U and ^{232}Th $\bar{\nu}_{\mathrm{geo}}$ effective detection rates, the $\bar{\nu}_{\mathrm{geo}}$ detection rate that KamLAND would have in the absence of detection inefficiency and neutrino oscillation, $\Phi_{\mathrm{geo\,sum}} = 122^{+36}_{-35}\ (10^{32}\,\mathrm{proton}\cdot\mathrm{year})^{-1}$, and the normalized difference of these $\bar{\nu}_{\mathrm{geo}}$ effective detection rates, $\Phi_{\mathrm{geo\,diff}} = 0.51^{+0.49}_{-0.64}$. The errors of these are currently dominated by statistics due to the large number of background events, including $\bar{\nu}_{\mathrm{reactor}}$s. $\Phi_{\mathrm{geo\,diff}}$ has a large error since KamLAND does not have much sensitivity in distinguishing the E_{p} spectral shapes of ^{238}U and ^{232}Th $\bar{\nu}_{\mathrm{geo}}$s. The Earth model described in Section 1.3.2 predicts $\Phi_{\mathrm{geo\,sum}} = 61\,(10^{32}\,\mathrm{proton}\cdot\mathrm{year})^{-1}$ and $\Phi_{\mathrm{geo\,diff}} = 0.6$, where $\Phi_{\mathrm{geo\,diff}}$ is better predicted since the mass ratio of ^{232}Th to ^{238}U inside the Earth is known better than the absolute concentration of each. Although the estimated $\Phi_{\mathrm{geo\,sum}}$ is about twice as large as the model prediction, the two are still compatible at the 14.1 % confidence level. This result is also compatible with the "fully radiogenic Earth model," which predicts $\Phi_{\mathrm{geo\,sum}}$ in a range of 98 to 142 $(10^{32}\,\mathrm{proton}\cdot\mathrm{year})^{-1}$. Based on the number of $\bar{\nu}_{\mathrm{geo}}$s observed, the detection of $\bar{\nu}_{\mathrm{geo}}$s is confirmed at the 99.995 % confidence level.

A rather controversial Earth model, which predicts the existence of a nuclear reactor, "georeactor," outputting up to ~10 TW of power at the center of the Earth core is also explored in Mode-III analysis. The effective detection rate of $\bar{\nu}_{\mathrm{e}}$ from the georeactor, the detection rate that KamLAND would have in the absence of detection inefficiency and neutrino oscillation, is estimated at $102^{+79}_{-72}\,(10^{32}\,\mathrm{proton}\cdot\mathrm{year})^{-1}$, whose central value corresponds to ~7.6 TW of georeactor power generation. However, this is also consistent with absence of georeactor at the 15 % confidence level.

KamLAND is the first and only detector so far that has provided strong evidence for $\bar{\nu}_{\mathrm{e}}$ oscillation using $\bar{\nu}_{\mathrm{reactor}}$s. The KamLAND data yields neutrino oscillation parameters in the LMA1 region, in agreement with the solar ν experimental results. With its ability to measure the spectral distortion of the oscillated $\bar{\nu}_{\mathrm{e}}$s, the sensitivity in estimating Δm^2_{21} with KamLAND is currently by far the best achieved.

KamLAND is also the first and only detector that has confirmed the observation of $\bar{\nu}_{\mathrm{geo}}$s. The measurement of $\bar{\nu}_{\mathrm{geo}}$s is the only chemical analysis available today to directly explore the Earth interior. This may become a new tool for understanding the radiogenic heat production in the Earth, which drives the Earth dynamics.

Appendix A

Trigger Electronics

This section is based on [27], and modified or added more information as necessary.

The trigger system communicates with the DAQ system, the KamFEE system, the MACRO system, the absolute time acquisition system, and the trigger backup DAQ system. The absolute time acquisition system is described in Appendix C.

As shown in Figure A.1, the trigger board communicates with the DAQ system via commercial VME output register (SIS3601) and latches (SIS3600) manufactured by Struck Innovative Systeme. The output register is used to send information from the DAQ system to the trigger board. The trigger board receives commands such as run start and run stop, and run conditions such as which trigger types to enable and thresholds. The latches are used to send information from the trigger board to the DAQ system; latch 1 and latch 3 are used for the trigger record transfer, and latch 2 is used for other purposes. For example, upon receiving run conditions from the DAQ system, the trigger board sends them back to the DAQ system through latch 2 for confirmation. The trigger record was sent directly to latch 1 before the trigger backup DAQ system was installed. Now the signal is split into two sets, one of which is sent to latch 1 as before, and the other is sent to latch 3 in the backup VME crate. The trigger backup DAQ system uses an independent computer from the main DAQ system, so the backup computer would keep the trigger record even if the main computer crashes. The trigger record can yield valuable information about events: the time differences between events can be accurately determined from the

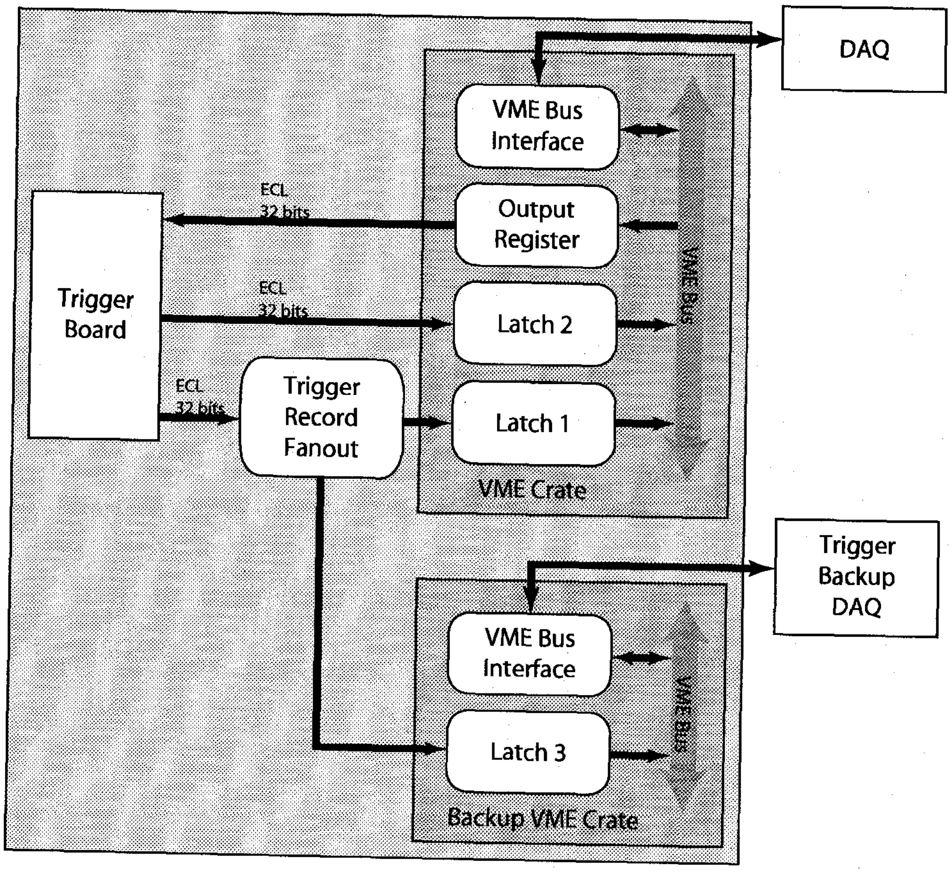

Figure A.1: An overview of the trigger system components that communicate with the DAQ system and the trigger backup DAQ system. The trigger backup system, which consists of the trigger record fanout, a latch and a VME bus interface in the backup VME crate, and the trigger backup DAQ system, was added in January 2006 in case the main DAQ system temporarily failed.

timestamps; high N_{ODtop}, N_{ODupper}, N_{ODlower}, or N_{ODbottom} indicates the presence of a muon; and N_{ID} is closely related to the energy of an event, although this relationship depends on the position of an event, which cannot be reconstructed since the trigger record does not contain individual PMT information.

Figure A.2 shows the communication between the trigger board and the KamFEE system. Each N_{KamFEE} is a 4-bit LVPECL signal, which corresponds to a total of 800 bit input to the trigger board. Based on this input, the trigger board must issue a global acquisition command to the KamFEE boards within ~400 ns. The trigger

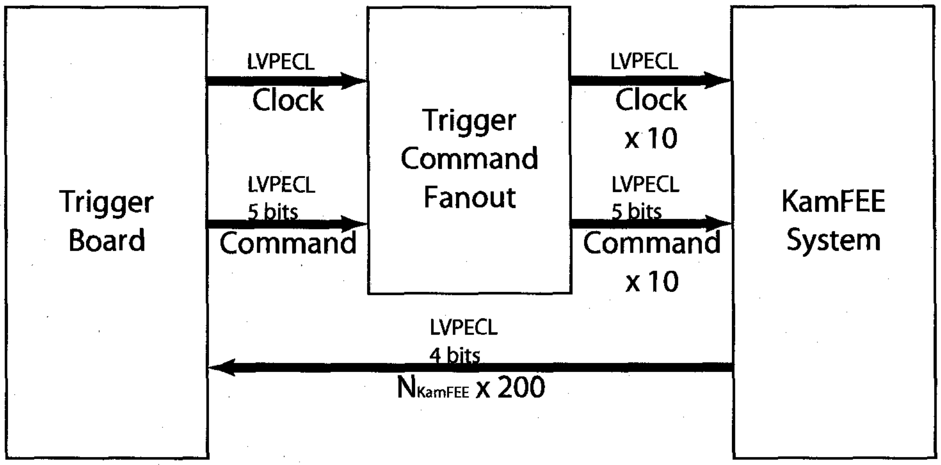

Figure A.2: An overview of the communication between the trigger board and the KamFEE system.

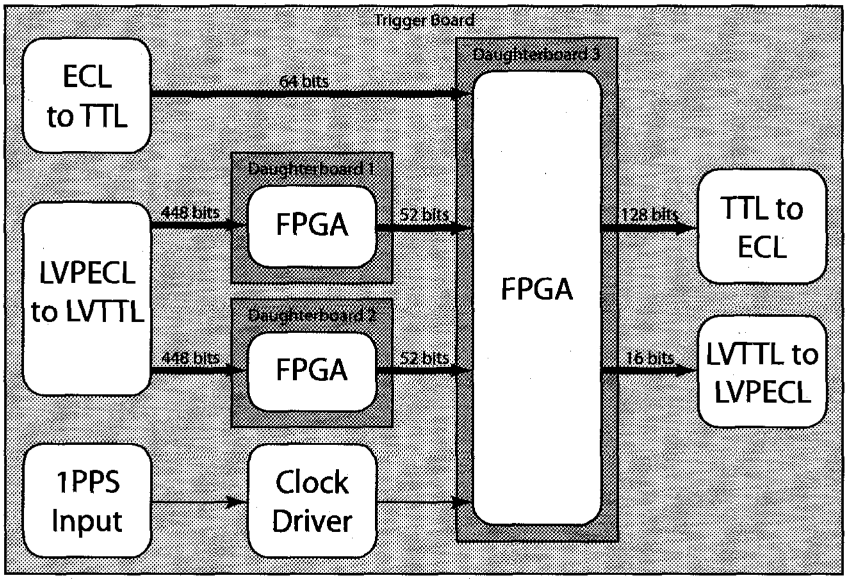

Figure A.3: An overview of the trigger board.

sends the clock and trigger command signals to the trigger command fanout, which splits them into 10 sets and sends them to the ten KamFEE VME crates.

Figure A.3 shows a schematic of the trigger board. The LVPECL signals from the KamFEE boards are converted to LVTTL signals before being sent to the FPGA's (XCV600 by Xilinx). This has two advantages: the converter chips act as a buffer to the expensive FPGA chip, and LVTTL signals require only one input line referenced to ground while LVPECL signals require two input lines. The trigger board receives 800 inputs from the KamFEE boards. However, the largest number of I/O's available was ~500 at the time the trigger board was designed in 2000, so three FPGA's are used. Each FPGA is mounted on a separate daughterboard, which can be removed from the trigger motherboard. Each daughterboard contains all the components necessary to run the FPGA, and all the other components are contained on the motherboard. These three daughterboards are identical except for the code stored on the PROM. This code is transferred to the FPGA on power up. The FPGA's are reprogrammable, allowing for development of new trigger algorithms. To confirm the trigger algorithm versions, the DAQ system prompts the trigger board to send the versions of each FPGA code to latch 2 at the beginning of each run. The FPGA's perform highly parallel calculations. Two input FPGA's perform initial calculations and pass the reduced information to a third FPGA. The third FPGA then combines the information from the first two FPGA's. The third FPGA generates the KamFEE trigger commands, the MACRO electronics stop commands, and the trigger records. A buffer, 511 trigger-record deep, incorporated into the third FPGA allows for a trigger rate of 40 MHz for a brief period. Also, the buffer in latch 1 can contain up to 12800 trigger records. This is important for detecting a galactic supernova, which would produce a burst of events. The continuous possible trigger rate depends on the total data transfer speed, which is limited by the latch 1 to ~40 kHz.

Appendix B

Trigger Types

Triggers are issued for a variety of reasons which can be split into four basic groups: triggers that issue global acquisition commands to the ID KamFEE boards, triggers that issue global acquisition commands to the OD KamFEE boards, triggers that issue stop commands to the MACRO electronics, and other triggers that do not necessarily issue a trigger command. Two ID KamFEE triggers or two OD KamFEE triggers are not issued within 200 ns of each other since two triggers in a short period would record the same waveforms. Most of these triggers can be enabled or disabled. Most of the trigger types available are described in [27]. Only the trigger types newly implemented or modified in February 2004 are listed below.

B.1 ID KamFEE Triggers

- MACRO to ID Trigger: A global acquisition command is issued to the ID KamFEE boards when there is a MACRO Singles Trigger. This trigger is issued 40 μs before the MACRO Singles Trigger. This trigger type is enabled only during the calibration runs.

B.2 MACRO Triggers

- MACRO Calibration Trigger: A short stop command is issued to the MACRO electronics $20\,\mu$s after every fixed number of calibration device input signals. This number can be set by the DAQ.

B.3 Other Triggers

- 1PPS Trigger: A trigger record is produced every time the trigger module receives a 1PPS input. The issuing of a global acquisition command to all the KamFEE boards at the same time can be enabled by the DAQ.
- Supernova Trigger: This is designed to detect the neutrino signal from a supernova. If the trigger board observes eight events with $N_{\mathrm{ID}} \geq 772$ (before February 2004) or $N_{\mathrm{ID}} \geq 1100$ (after February 2004) in $\sim$0.84 s, this is treated as a supernova candidate. After a supernova candidate is observed, the trigger board sets optimal trigger parameters (supernova mode) to collect as many supernova events as possible for 1 min before returning to the initial trigger parameters. Normal trigger parameters would collect most supernova events, but could miss the important proton scattering events. The rarity of observation of supernova explosions makes it important to collect as many supernova events as possible. This trigger is almost always enabled so that supernova events will be collected even if we are operating with sub optimal trigger parameters. When the DAQ receives the supernova trigger, it prevents the shift taker from stopping the run for 1 min.
- Global Calibration Trigger: A global acquisition command is issued to either the ID or OD KamFEE boards 8 clock-ticks (before February 2004) or 15 clock-ticks (after February 2004)[1] after the trigger board receives an input pulse. The pulse is generated by a calibration device, such as a LASER, and must arrive just before the signals from the photons have reached the KamFEE boards.

---

[1] The 8 clock-tick duration was too short to collect all the light, so it was increased to 15 clock-ticks.

- Run Condition Change Trigger: A trigger record is produced whenever run conditions are changed by the DAQ or by the supernova trigger.

Appendix C

Absolute Time Acquisition System

Knowing the absolute time for each event is important to compare results on a common source, such as a supernova, with other experiments. In KamLAND, the absolute time is obtained from a Global Positioning System (GPS) receiver (Model 600-000 manufactured by TrueTime). As shown in Figure C.1, the GPS receiver and its antenna are located outside the mine to receive signals from the GPS satellites, to which the GPS receiver's internal clock locks. When receiving signals from at least 4 GPS satellites, the GPS receiver calculates the absolute time to an accuracy of 100 ns of Universal Time Co-ordinates (UTC). Even when the GPS receiver does not receive signals from any satellite, it continues to calculate the time using its internal clock. The status of the GPS receiver, such as the number of GPS satellites the GPS receiver is tracking, is checked every 60 s by a computer using the serial port from the GPS receiver. This information is only used to monitor the GPS receiver and is not sent to the main DAQ system.

The absolute time, encoded in a serial digital format (IRIG-B), and One Pulse Per Second (1PPS) signals, generated as TTL signals by the GPS receiver, are converted into optical signals and sent to the electronics hut inside the mine through optical fibers. Inside the electronics hut, these signals are converted back to TTL signals. The 1PPS signal is sent to the trigger board, and the encoded time is sent to a GPS VME interface (Model 560-5608 VME-SG2 manufactured by TrueTime), which synchronizes its internal clock to the received time code. The GPS VME interface

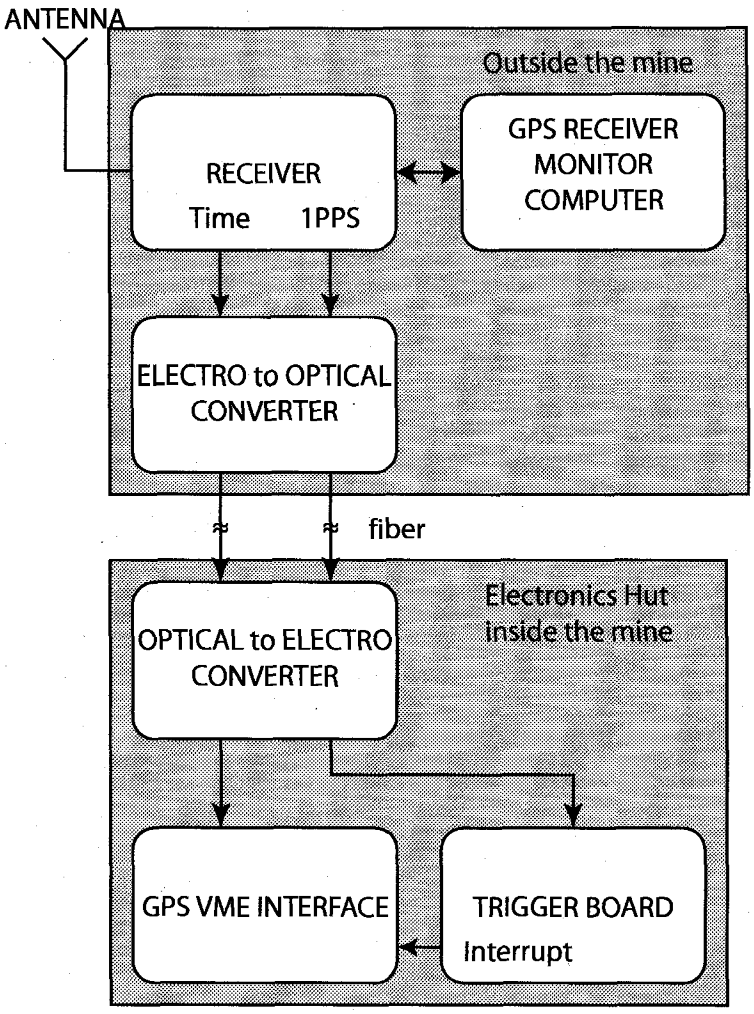

Figure C.1: Schematic of the absolute time acquisition system.

captures the time when it receives an interrupt signal, and stores it until the DAQ system reads the time and clears it. An interrupt is sent to the GPS VME interface when the trigger board issues a GPS trigger, which is always issued two clock ticks after the integer multiples of 32 1PPS signals. Since 1PPS signals are accurate to ~150 ns to UTC second, the absolute time of GPS triggers are also calculated to an accuracy of ~150 ns although the time stored in the GPS VME interface is only accurate to 1 μs. The DAQ system records timestamps and the absolute times from the GPS triggers asynchronously, but the trigger data analyzer later associates each

GPS trigger timestamp with its corresponding absolute time. The absolute time of any event can be calculated with the difference in the timestamps between an event and its nearest 1PPS trigger. The frequency of the trigger board clock drifts slightly depending on various factors such as temperature. However it drifts only about 10 ns per second.

The signal delay time between the GPS receiver and the electronics hut has been measured from the time a pulse takes to make a round trip. Outside the mine, a TTL signal was converted into an optical signal, and sent to the electronics hut through an optical fiber. The signal received in the electronics hut is converted to a TTL signal and then to an optical signal, and sent back to outside of the mine through an optical fiber. The signal is then converted back to a TTL signal outside the mine. Half of the time difference between the initial pulse and the returned pulse was $21.4\,\mu$s, then changed to $12.0\,\mu$s in November 2005, when the GPS receiver was relocated because of a rerouting of the optical fibers.

Appendix D

Event Position Reconstruction Algorithm

The position of an event is first roughly estimated using the distribution of the PEs produced in the PMTs, then fine tuned using the times photons take to travel from the event position to the PMTs in a straight path. Some fraction of photons produced in an event are absorbed at some point along their path and then reemitted in a random direction. These reemitted photons do not yield the event position. Therefore the algorithm mostly uses photons that traveled directly from the event position to PMTs by selecting pulses in the initial peak of arrival time distribution after correcting for the expected flight time. The algorithm follows the steps described below:

1. Only the pulses from Hamamatsu RS7250 PMTs are selected. Pulses with less than 0.2 PEs are discarded to avoid contamination from false pulses from electrical noise. If multiple waveforms from one PMT are recorded, pulses extracted from the waveform with the lowest gain are chosen.

2. If there are less than 4 pulses remaining in the event, the algorithm does not try to fit any further, and exits with a status "Unknown."

3. The initial rough position estimate is made using the distribution of the PEs

produced in the PMTs, and is given by

$$\mathbf{r} = 1.62 \frac{\sum_i PE_i \mathbf{r}_i}{\sum_i PE_i}, \tag{D.1}$$

where i goes over all the remaining pulses, $\mathbf{r}_i$ is the position of the PMT with the ith pulse. If the radius of the estimated position is greater than 8.5 m, the radius is shortened to 8.5 m keeping the direction of $\mathbf{r}$ the same.

4. The times that photons arrive at PMTs are calculated using the pulse times relative to the trigger command, as described in Section 3.1. Because the SPA (see Section 3.1) defines the time of pulse to be when the peak occurs in the waveform, and not the beginning of the pulse, the larger pulse has longer time between the time of pulse and the beginning of the pulse. The time that the photon arrives at the PMT, t_{arrival}, is estimated with

$$t_{\text{arrival}} = t_{\text{relative}} - 0.9 \times PE^{0.65}, \tag{D.2}$$

where t_{relative} is the time of the pulse relative to the trigger command time. The coefficient and exponent in Equation D.2 are empirically tuned using various calibration source runs.

5. Using the estimated position in step 3, δt in Equation 3.3 is calculated for each pulse. The δts are then plotted in a histogram. If the bin which contains the maximum number of entries has less than 7 entries, the bin width is repeatedly doubled until the bin with the maximum number of entries contains at least 7 entries.

6. The δt value of the bin with the maximum number of entries, δt_{max} is obtained and the mean δt of all the pulses that fall within -10 ns and +10 ns of δt_{max}, δt_{mean}, is calculated.

7. The δt_{mean} is then recalculated in multiple iterations using the pulses in the window between -10 ns and +10 ns of the δt_{mean} from the previous iteration.

This process is repeated until the difference between the δt_{mean}s from the current and the previous iterations is less than 0.1 ns, or 100 iterations are performed.

8. Using only the pulses in the peak time window, -10 ns and +5 ns around the δt_{mean} calculated in step 7, the current estimated event position is pushed according to the vector given by

$$\Delta \mathbf{r} = \sum_i \left(\delta t_i - \langle \delta t \rangle\right) \frac{\mathbf{r} - \mathbf{r}_i}{t_{\mathrm{travel},\, i}}, \tag{D.3}$$

   where i goes over all the pulses in the peak time window, $\mathbf{r}$ is the current estimated position, $t_{\mathrm{travel},\, i}$ is the time of travel from the current estimated position to the PMT with the ith pulse, δt_i is the δt of the ith pulse, and $\langle \delta t \rangle$ is the mean δt in the peak time window. The event position, $\langle \delta t \rangle$, and peak time window are recalculated in each of multiple iterations. After the first iteration, the peak time window is defined to be -10 ns and +5 ns around $\langle \delta t \rangle$. The iterations continue until the distance between the current estimated position and the estimated position in the previous iteration is less than 1 mm, or 100 iterations are performed.

9. After step 8, the reconstruction status is assigned based on various factors. There are three variables to assess the quality of the fit: f_{RMS}, $f_{\mathrm{Peak\,pulse\,ratio}}$, and $f_{\mathrm{Peak}\,RMS}$. f_{RMS} is the RMS of the δt distribution, $f_{\mathrm{Peak\,pulse\,ratio}}$ is the fraction of the pulses in the peak time window, and $f_{\mathrm{Peak}\,RMS}$ is the RMS of the δt distribution in the peak time window. Table D.1 summarizes the reconstruction status. An event can have multiple statuses if the reconstruction fails due to multiple factors, as described in Table D.1.

10. If the status assigned in step 9 is "Bad," and none of the other factors failed, then step 8 is repeated using the current estimated position and $\langle \delta t \rangle$. The status is reassigned depending on the result of this step.

11. If the radius of the reconstructed position is greater than 10 m, the position is

Table D.1: Position reconstruction status

Status type	Description
Valid	Successful reconstruction.
Unknown	Number of pulses < 4.
Not valid	Reconstructed radius $> 10\,\mathrm{m}$.
Bad	The fit did not converge.
Bad f_{RMS}	$f_{RMS} < 35$ or $f_{RMS} > 90$.
Bad $f_{\mathrm{Peak\,pulse\,ratio}}$	$f_{\mathrm{Peak\,pulse\,ratio}} < 0.22$ or $f_{\mathrm{Peak\,pulse\,ratio}} > 0.55$.
Bad $f_{\mathrm{Peak}\,RMS}$	$f_{\mathrm{Peak}\,RMS} < 1.7$ or $f_{\mathrm{Peak}\,RMS} > 4$

adjusted. The new position, $\mathbf{r}_{\mathrm{new}}$, is given by

$$\mathbf{r}_{\mathrm{new}} = \frac{10\,\mathrm{m}}{|\mathbf{r}\,[\mathrm{m}]|}\mathbf{r} \tag{D.4}$$

Using $\mathbf{r}_{\mathrm{new}}$ and the $\langle \delta t \rangle$, step 8 is repeated, and the status is reassigned depending on the result of this step.

The ranges for which f_{RMS}, $f_{\mathrm{Peak\,pulse\,ratio}}$, and $f_{\mathrm{Peak}\,RMS}$ are valid are determined using the distributions of these variables for the events which are believed to be point-like events compared with muons or noise events caused by muons. These variables are designed to eliminate muons and noise following muons, such as afterpulses. Figure D.1 shows the distributions of f_{RMS}, $f_{\mathrm{Peak\,pulse\,ratio}}$, and $f_{\mathrm{Peak}\,RMS}$ for events with $N_{\mathrm{Max\,ID}}$ above 200 during normal run 394. The valid ranges, indicated by the vertical dotted lines, reject large fractions of muons or post muon noises while remaining the other events.

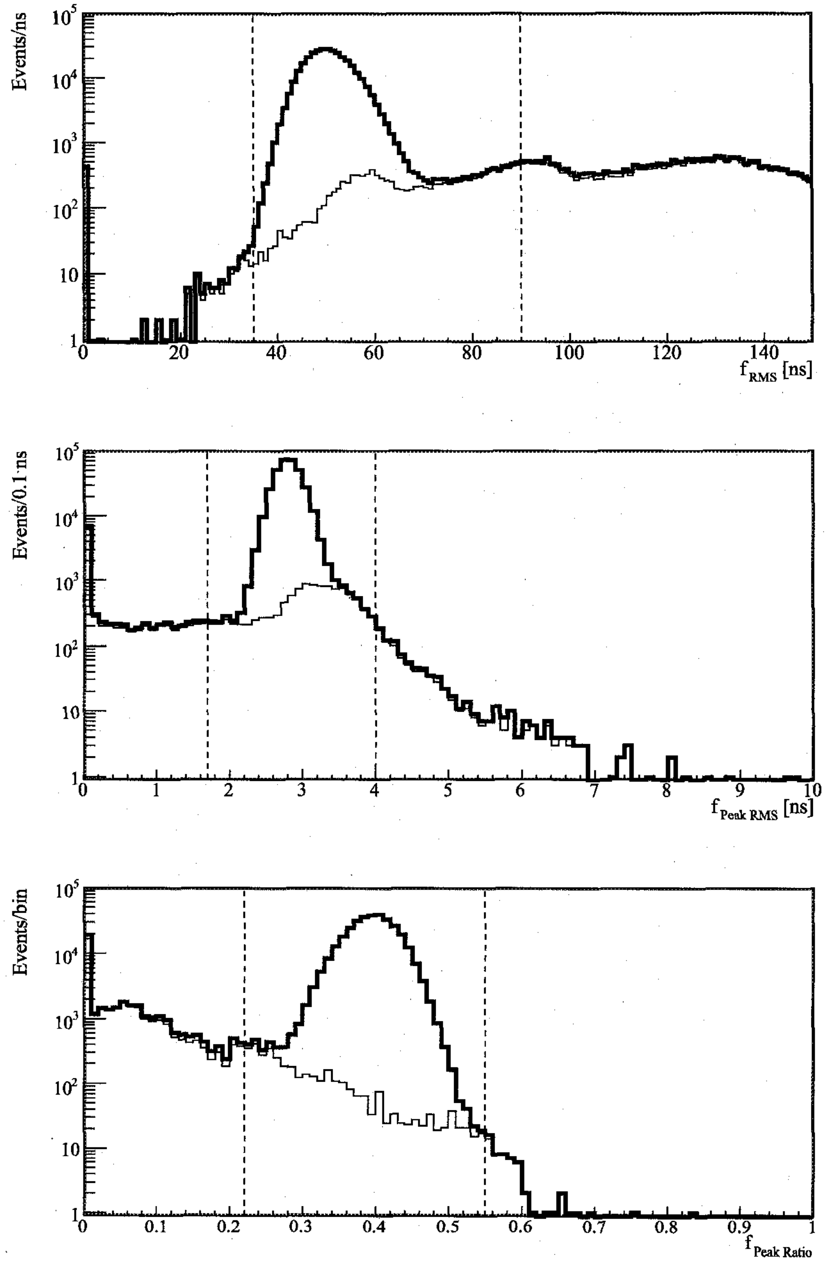

Figure D.1: f_{RMS} (top plot), $f_{\text{Peak pulse ratio}}$ (middle plot), and $f_{\text{Peak}\,RMS}$ (bottom plot) distributions for events from normal run 394. The thick solid lines are for all the events with $N_{\text{Max ID}}$ above 200. The thin solid lines are for events tagged as Muons or Post Muon Noise (see Section 3.6). The dotted lines indicate the valid ranges.

Appendix E

Energy Calibration Points

The measurements used to fit the model of $E_{\text{vis}}/E_{\text{real}}$ (see Section 3.4) are described below. The calibration points are defined to be E_{vis} at the center of detector, and its error includes temporal and spatial uncertainties. Many of the calibration points are estimated using radioactive sources deployed in the LS (see Section 2.4).

E.1 ^{203}Hg E_{vis}

E_{vis} calibration point of ^{203}Hg is estimated by fitting a Gaussian function to the E_{vis} distribution of the γs from the ^{203}Hg source deployed at the center. The time variation of 1.4 % is estimated to be the same as the E_{vis} time variation of ^{214}Po α-decays, described in Section E.7. In addition, a conservative error of 1.8 % due to the position uncertainty is estimated by comparing the E_{vis} means obtained from the ^{203}Hg source deployed at the center and $\pm 3\,\text{m}$[1]. The estimated E_{vis} calibration point of ^{203}Hg is $0.2400 \pm 0.0055\,\text{MeV}$.

E.2 ^{68}Ge E_{vis}

E_{vis} calibration point of ^{68}Ge is estimated by fitting a Gaussian function to the E_{vis} distributions of the γs from the ^{68}Ge source deployed at the center in various runs.

---

[1] Unlike other source calibrations, there is no calibrations at $\pm 1\,\text{m}$ for ^{203}Hg source.

The time variation of 1.4 % is estimated from the difference between the maximum and minimum E_{vis} means from these different runs. In addition, a conservative error of 0.3 % due to the position uncertainty is estimated by comparing the E_{vis} means obtained from the ^{68}Ge source deployed at the center and ±1 m. The estimated E_{vis} calibration point of ^{68}Ge is 0.923 ± 0.013 MeV.

E.3 ^{65}Zn E_{vis}

E_{vis} calibration point of ^{65}Zn is estimated by fitting a Gaussian function to the E_{vis} distributions of γs from the ^{65}Zn source deployed at the center in various runs. The time variation of 0.7 % is estimated from the difference between the maximum and minimum E_{vis} means from these different runs. In addition, a conservative error of 0.26 % due to the position uncertainty is estimated by comparing the E_{vis} means obtained from the ^{65}Zn source deployed at ±1 m. The estimated E_{vis} calibration point of ^{65}Zn is 1.1031 ± 0.0082 MeV.

E.4 ^{1}H(n,γ)^{2}H E_{vis}

E_{vis} calibration point of ^{1}H(n,γ)^{2}H is estimated by fitting a Gaussian function to the E_{vis} distributions of neutron capture events from the ^{241}Am^{9}Be source deployed at the center. The neutron capture events are selected by applying temporal coincidence cuts and position cuts around the source. To reduce background events, the first event is selected if its E_{vis} is greater than 4 MeV. The temporal coincidence cut requires the time between the first and the second events are between 30 μs and 1 ms. The spatial coincidence cut requires the reconstructed positions of both events are within 1.5 m from the deployed source position. The fitted mean E_{vis} of neutron capture events from the ^{241}Am^{9}Be source are corrected by the expected shift of $0.854 \pm 0.29\%$ due to the source capsule shadowing, as described in Section E.4.1. A conservative error of 0.2 % due to the position uncertainty is estimated by comparing the E_{vis} means obtained from the ^{241}Am^{9}Be source deployed at the center and ±1 m. The time variation of 1 % is estimated to be close to the time variations estimated with the

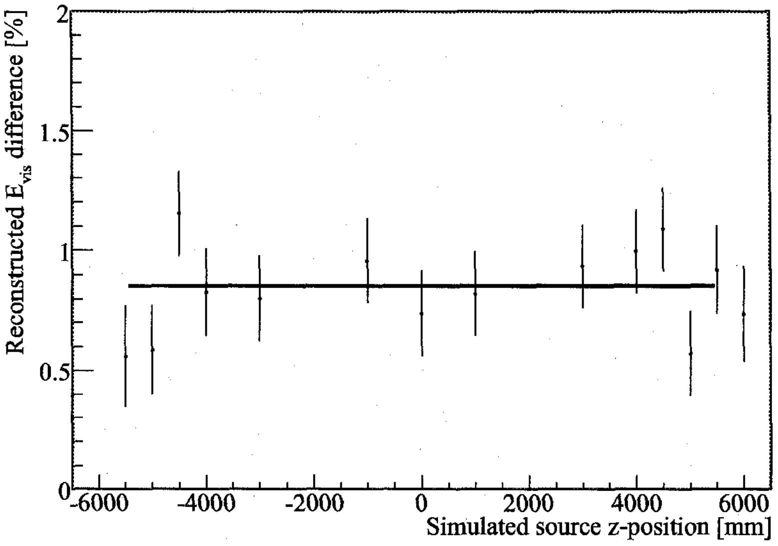

Figure E.1: Reconstructed mean E_{vis} differences for simulated ^{241}Am^{9}Be neutrons with and without ^{241}Am^{9}Be source capsule at various source positions along the z-axis. The thick horizontal line is a flat line fit to these mean E_{vis} fractional differences from -5500 m to 5500 m. The fit yields a shift of 0.854 ± 0.050 %. The $\chi^2/n.d.f.$ of this fit is 13.2/12.

^{68}Ge (see Section E.2) and ^{65}Zn (see Section E.3) sources. The estimated E_{vis} of ^{1}H(n,γ)^{2}H calibration point is 2.333 ± 0.025 MeV.

E.4.1 ^{241}Am^{9}Be Source Shadowing Estimation

The reconstructed E_{vis} of ^{241}Am^{9}Be neutron capture events needs to be corrected to account for the shadowing of the deployment equipments such as the source capsule. The amount of the shadowing is estimated by simulating the ^{241}Am^{9}Be source with and without the deployment equipment at various positions along the z-axis using KLG4sim. The simulated data is then reconstructed using the default event reconstruction algorithms. The percentage difference of reconstructed E_{vis} of these simulated events at various z-positions are fairly constant, as shown in Figure E.1. The shadowing effect is estimated to be 0.854 ± 0.29 % by fitting a constant across the z-positions and taking the maximum variation.

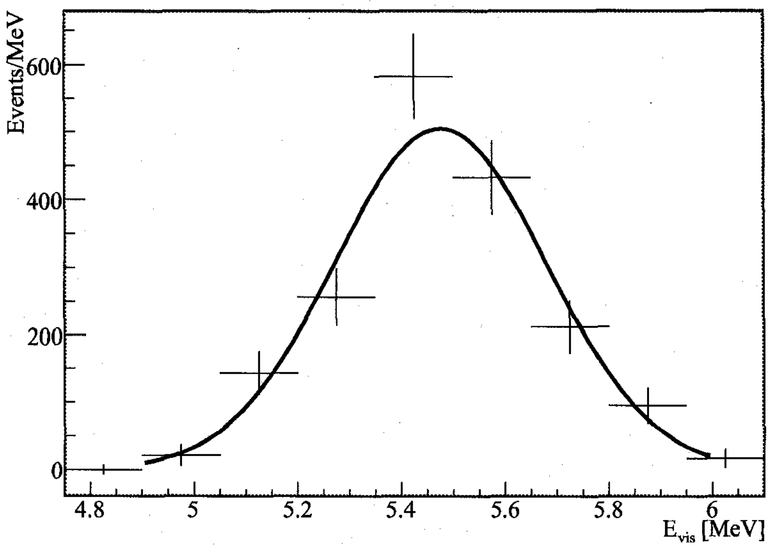

Figure E.2: The background subtracted E_{vis} of spallation neutron capture on ^{12}C. The Gaussian function fit (solid line) yields the mean of 5.476 ± 0.014 MeV. The $\chi^2/n.d.f.$ of this fit is 5.8/4.

E.5 ^{60}Co E_{vis}

Since the reconstructed E_{vis} is calibrated to be the same as the $E_{\text{real}} = 2.50572$ MeV of ^{60}Co, only the position uncertainty is considered. A conservative error of 0.37 % is estimated by comparing the E_{vis} means of γs from the ^{60}Co source deployed at the center and ±1 m. The estimated E_{vis} calibration point of ^{60}Co is 2.5057 ± 0.0093 MeV.

E.6 ^{12}C(n,γ)^{13}C E_{vis}

E_{vis} calibration point of ^{12}C(n,γ)^{13}C is estimated using the spallation neutrons, captured on ^{12}C. The events are selected by temporal coincidence with muons. The neutron capture candidate events are selected between 0.2 ms and 1.2 ms after muons, while background events to be subtracted from the neutron capture candidate events are selected between 1.2 ms and 5.2 ms after muons. The neutron capture events are selected within the reconstructed radius of 4.7 m. Figure E.2 shows the background subtracted $E_{\rm vis}$ distribution and a Gaussian function fit to this distribution. There are two types corrections that need to be applied to the mean from this Gaussian function fit. The first is the $E_{\rm vis}$ reconstruction bias after muons. The fitted mean $E_{\rm vis}$ is shifted down by $0.72 \pm 0.17\,\%$, estimated in Section 3.3.1. The other correction is the $E_{\rm vis}$ reconstruction bias due to the position of the events. Since all the events are selected within 4.7 m, the $E_{\rm vis}$ at the center needs to be estimated. This is done by comparing the reconstructed $E_{\rm vis}$ for spallation neutrons, captured on ^{1}H within 4.7 m radius after correcting for after muon effect (see Section 3.3.1) to the $E_{\rm vis}$ of neutron capture events from the ^{241}Am^{9}Be source deployed at the center after correcting for the ^{241}Am^{9}Be capsule shadowing effect (see Section E.4.1). The $E_{\rm vis}$ shift necessary due to the position variation is $0.54 \pm 0.54\,\%$. The time variation of 1 % is estimated to be close to the time variation estimated with the ^{68}Ge (see Section E.2) and ^{65}Zn (see Section E.3) sources. The estimated $E_{\rm vis}$ calibration point of ^{12}C(n,γ)^{13}C is 5.407 ± 0.063 MeV.

E.7 ^{214}Po α-decay $E_{\rm vis}$

^{214}Po α-decays can be selected using the coincidence with ^{214}Bi β-decays. ^{214}Bi β-decays with an endpoint of 3.272 MeV. Then the daughter nucleus, ^{214}Po, α-decays with Q = 7.833 MeV and half-life of 164.3 μs. The following cuts are applied to select the ^{214}Po α-decay events; the ^{214}Bi β-decay $E_{\rm vis}$ is between 1.5 MeV and 5 MeV, the distance between the ^{214}Bi β-decay and ^{214}Po α-decay events is less than 1 m, and the time between these events is between 0.5 μs and 1 ms. Both events are also required to be within 1 m from the center of the ID. The top plot in Figure E.3 shows distribution of the time difference between the ^{214}Bi β-decay and ^{214}Po α-decay candidates. The fitted half-life of $167.2 \pm 3.4\,\mu$s is consistent with the nominal value of 164.3 μs. The bottom plot in Figure E.3 shows the $E_{\rm vis}$ distribution of ^{214}Po α-decay events. The mean $E_{\rm vis}$ of 0.62006 ± 0.00098 MeV is obtained by fitting a Gaussian function. The $E_{\rm vis}$ error of 0.67 % due to the position uncertainty is taken by comparing the events within 1 m radius to within the spherical shell of between 1 m and 2 m radius. Figure E.4 shows the ~1.4 % time variation of mean $E_{\rm vis}$ of ^{214}Po

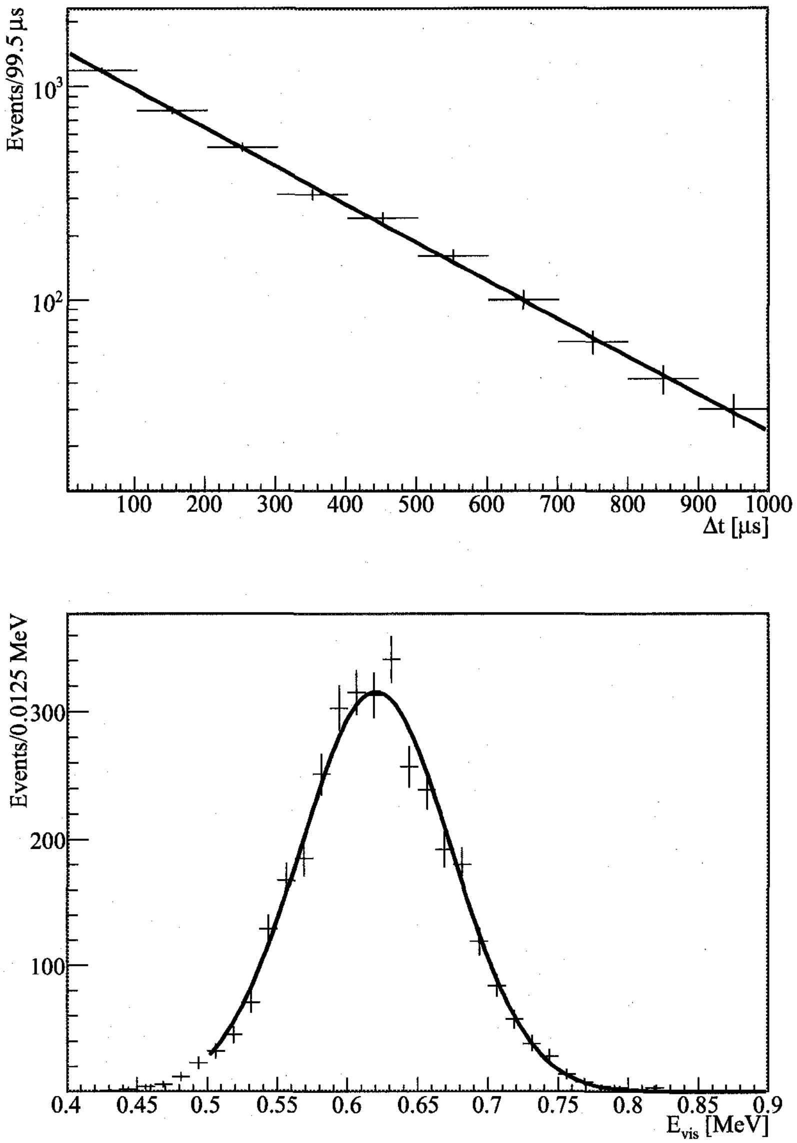

Figure E.3: ^{214}Po α-decay candidates within 1 m from the center of the ID. The top plot shows the time difference between the ^{214}Bi β-decay and ^{214}Po α-decay events. The exponential fit yields the half-life of $167.2 \pm 3.4\,\mu$s with a $\chi^2/n.d.f.$ of 4.7/8. The bottom plot shows the E_{vis} distribution. The Gaussian function fit yields the mean of 0.62006 ± 0.00098 MeV, and sigma of 0.05412 ± 0.00076 MeV with a $\chi^2/n.d.f.$ of 24.0/29

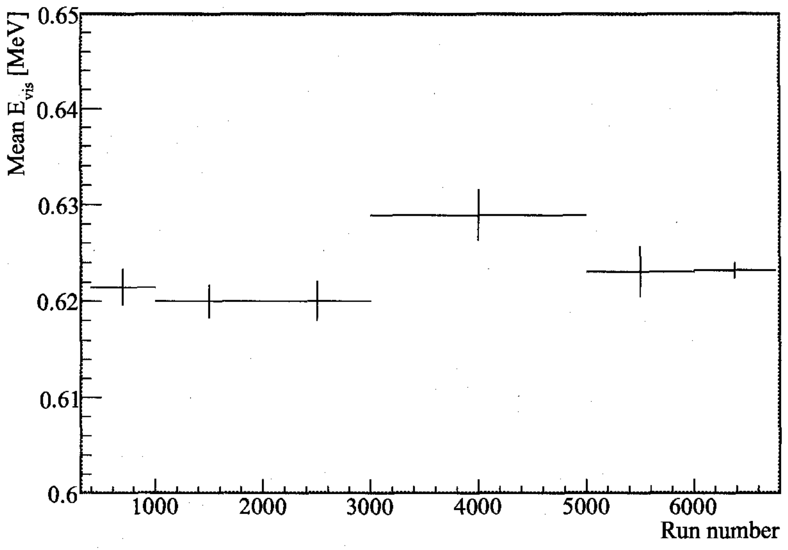

Figure E.4: E_{vis} time variation of ^{214}Po α decay candidates within 3 m from the center of the ID. Approximately 1.4 % variation is seen.

α-decay events within a 3 m radius. The estimated E_{vis} calibration point of ^{214}Po α-decay is 0.6201 ± 0.0097 MeV.

E.8 ^{212}Po α-decay E_{vis}

^{212}Po α-decays can be selected using the coincidence with ^{212}Bi β-decays. ^{212}Bi β-decays with an endpoint of 2.25 MeV. Then the daughter nucleus, ^{212}Po, α-decays with Q = 8.954 MeV and half-life of 0.299 μs. The following cuts are applied to select ^{212}Po α-decay events; the ^{212}Bi β-decay E_{vis} is between 1 MeV and 2.6 MeV, the distance between the ^{212}Bi β-decay and ^{212}Po α-decay events is less than 1 m, and the time between these events is between 0.5 μs and 1 μs. Both events are also required to be within 3 m from the center of the ID. The top plot in Figure E.5 shows distribution of the time difference between the ^{212}Bi β-decay and ^{212}Po α-decay candidates. The fitted half-life of 0.45 ± 0.15 μs is consistent with the nominal value of 0.299 μs. The bottom plot in Figure E.5 shows the E_{vis} distribution of ^{212}Po α-decay events. The

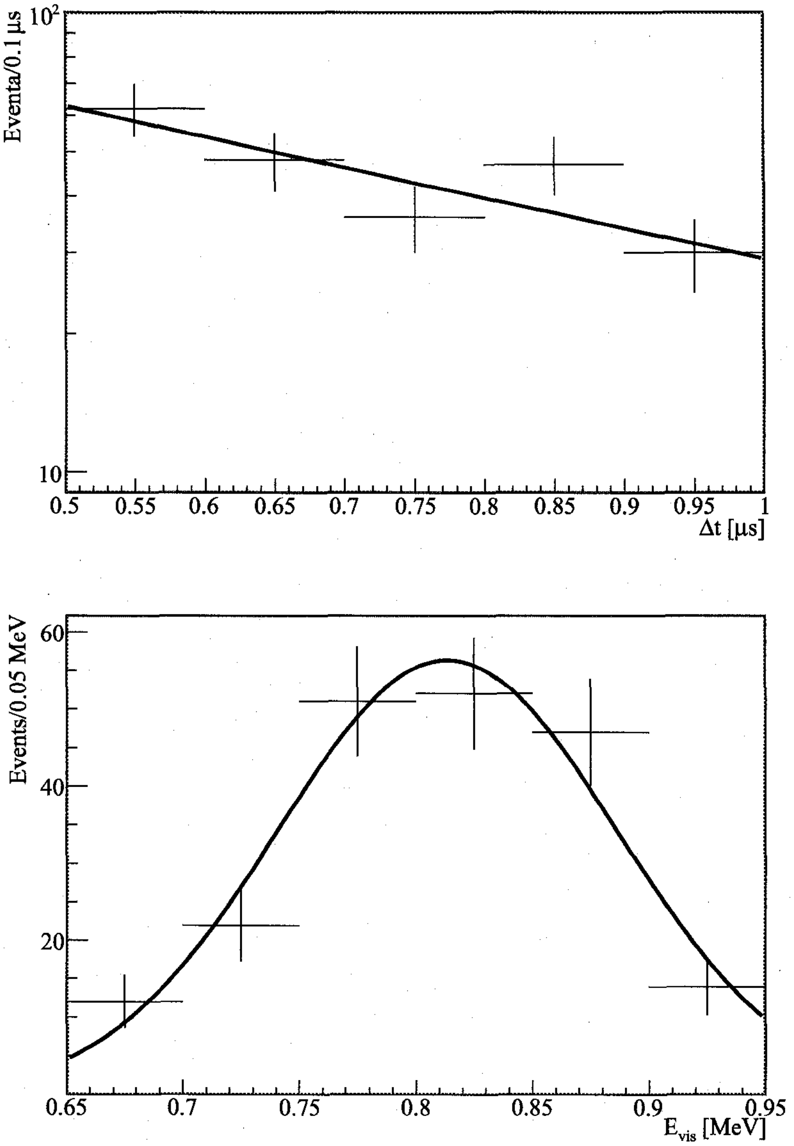

Figure E.5: ^{212}Po α-decay candidates within 3 m from the center of the ID. The top plot shows the time difference between the ^{212}Bi β-decay and ^{212}Po α-decay events. The exponential fit yields the half-life of $0.45 \pm 0.15\,\mu$s with a $\chi^2/n.d.f.$ of 3.9/3. The bottom plot shows the E_{vis} distribution. The Gaussian function fit yields the mean of 0.8136 ± 0.0059 MeV, and sigma of 0.0729 ± 0.0056 MeV with a $\chi^2/n.d.f.$ of 4.2/3.

error due to the position variation is estimated from the percentage difference in the E_{vis} means obtained with the captures of neutrons from the ^{241}Am^{9}Be source deployed at the center and 3 m. The time variation of 1.4 % is chosen to be the same as that of ^{214}Po α-decays. The estimated E_{vis} calibration point of ^{212}Po α-decays is 0.806 ± 0.013 MeV.

Appendix F

Spallation Product Selection Cuts

The cuts to select spallation products, ^{12}B and neutrons, used in Chapter 4 are described in the following sections. See Section 3.6 for the definitions of the various events tags used in these cuts.

F.1 ^{12}B

The ^{12}B β-decay candidates are selected using the following cuts:

- The ^{12}B β-decay candidate event has valid position and E_{vis} reconstruction statuses.
- The ^{12}B β-decay candidate event has E_{vis} above 4 MeV. Although the E_{vis} spectrum of ^{12}B β spans below 4 MeV, background events overwhelm E_{vis} below 4 MeV.
- The ^{12}B β-decay candidate event is not tagged as a Muon.
- The ^{12}B β-decay candidate event follows within 2 to 52 ms of the last muon.
- Events for background subtraction follow within 52 to 202 ms of the last muon.
- The associated muon event is tagged as both OD and ID Muon, which does not follow and is not followed by another event tagged as an ID Muon within

202 ms. This timing restriction is to ensure each of the selected ^{12}B β-decay candidates and background events are associated with only one muon.

F.2 Neutrons

Different sets of cuts are used to select spallation neutron candidate events in the $\tau_{\text{capture spall}}$, the reconstructed E_{vis} distribution, and the reconstructed radial distribution studies. Most of the differences are to optimize the selection of neutron capture events for a specific study[1]. The common cuts to all of these studies are that the associated muon does not follow and is not followed by another event tagged as a ID Muon within 0.1 s, and the neutron capture candidate event has valid position and E_{vis} reconstruction statuses. The differences are described in the following sections.

F.2.1 Neutrons for $\tau_{\text{capture, spall}}$ Estimation

In order to estimate $\tau_{\text{capture, spall}}$, spallation neutrons are selected using the following additional cuts:

- The associated muon is tagged as a LS Muon and has a $N_{\text{Max ID}}$ greater than 1250 to ensure that it is indeed a LS muon, but not tagged as a Shower Muon since large charge deposits from Shower Muons affect the detector performance for a long time afterwards.

- The neutron capture candidate event has a $N_{\text{Max ID}}$ between 400 and 490, and reconstructed E_{vis} between 1.4 MeV and 3.4 MeV to reduce the contamination from ^{12}B β-decays[2].

- The neutron capture candidate event is reconstructed within the fiducial volume of 5.5 m radius to avoid bias in the estimated $\tau_{\text{capture, spall}}$ due to the $\tau_{\text{capture, spall}}$ difference in the LS and buffer oil.

---

[1] Some of the cuts, E_{vis} window for example, happen to differ slightly in each study since the studies are conducted separately although these slight differences would not make noticeable difference in the results.

[2] See Section 4.1 for more details on ^{12}B β-decays.

F.2.2 Neutrons for E_{vis} Estimation

In order to estimate the mean capture E_{vis}, spallation neutrons are selected using the following additional cuts:

- The associated muon is tagged as a LS Muon and has a $N_{\text{Max ID}}$ greater than 1250 to ensure that it is indeed a LS muon, but not tagged as a Shower Muon since large charge deposits from Shower Muons affect the detector performance for a long time afterwards.
- The neutron capture candidate events and background events are taken from 0.8 ms to 1.2 ms, and 1.2 ms to 5.2 ms after the previous muons, respectively. The events that closely follow muons are avoided to reduce possible effects from the E_{vis} bias due to the electronics baseline shift after muons.

F.2.3 Neutrons for Position Distribution Estimation

To obtain reconstructed radial distribution, spallation neutrons are selected using the following additional cuts:

- The associated muon is tagged as both OD and ID Muon.
- The neutron capture candidate and background events follow within 0.8 to 1.2 ms and 1.2 to 5.2 ms of the last muon, respectively. The events that closely follow muons are avoided to reduce possible effects from the E_{vis} bias due to the electronics baseline shift after muons.
- The neutron capture candidate and background events have E_{vis} between 1.5 and 3.5 MeV.
- The neutron capture candidate and background events are not tagged as an OD Muon.
- The $N_{\text{Max ID}}$ of the neutron capture candidate event is greater than 200 (period I) or 180 (period II).

Appendix G

$N_{\mathrm{Max\,ID}}$ Threshold Efficiency Calculation

The details of the estimation of $\varepsilon_{N_{\mathrm{Max\,ID}}}$ are discussed below.

$N_{\mathrm{Max\,ID}}$ depends on both the E_{vis} and position of an event; the larger the radius, the larger the E_{vis} for the same $N_{\mathrm{Max\,ID}}$, as shown in Figure G.1. Therefore $\varepsilon_{N_{\mathrm{Max\,ID}}}(E_{\mathrm{vis}})$ (see Equation 5.3) is estimated for period I and II in each of three concentric regions in the detector: $r < 4.7\,\mathrm{m}$, $4.7\,\mathrm{m} < r < 5.5\,\mathrm{m}$, and $5.5\,\mathrm{m} < r < 6.3\,\mathrm{m}$ as shown in Figure 5.4. The $\varepsilon_{N_{\mathrm{Max\,ID}}}(E_{\mathrm{vis}})$ is obtained using run 3888, which is a special run with a low trigger N_{ID} threshold of 35; since the mean reconstructed E_{vis} of events whose $N_{\mathrm{Max\,ID}}$ is equal to 35 is $\sim$0.1 MeV, the $\varepsilon_{N_{\mathrm{Max\,ID}}}(E_{\mathrm{vis}})$ distribution distortion around the analysis E_{vis} thresholds of 0.9 MeV and 0.8 MeV in periods I and II, respectively, caused by the detector N_{ID} threshold of 35 is negligible. An error function is fitted to only some portion of each $\varepsilon_{N_{\mathrm{Max\,ID}}}(E_{\mathrm{vis}})$ to approximate the shape. The means, $\mu_{N_{\mathrm{Max\,ID}}}$, and sigmas, $\sigma_{N_{\mathrm{Max\,ID}}}$, of the fitted error functions are shown in Table G.1.

The relation between E_{vis} and $N_{\mathrm{Max\,ID}}$, shown in Figure G.1, can change depending on the scintillation level at a given time due to various factors such as the oxygen content and temperature in the LS. This change can affect the values of $\mu_{N_{\mathrm{Max\,ID}}}$ and $\sigma_{N_{\mathrm{Max\,ID}}}$. Their time variations are estimated using the time variations of means and RMS of the E_{vis} of events whose $N_{\mathrm{Max\,ID}}$ is equal to the analysis $N_{\mathrm{Max\,ID}}$ threshold. Table G.2 summarizes such E_{vis} means and RMS from run 3888. Figure G.2 shows

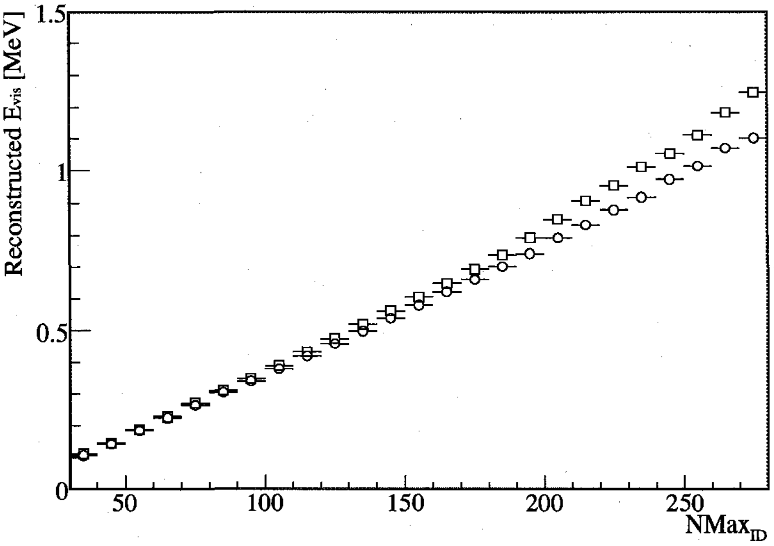

Figure G.1: Correlation between reconstructed E_{vis} and $N_{\mathrm{Max\,ID}}$ from a special low N_{ID} threshold run. The square markers are for events in a spherical shell from radius of 4.5 m to 5.5 m. The circle markers are for events within a 2 m radius sphere.

these values as a function of run number. In period I, the E_{vis} means and RMS's deviate up to ~5.1 % and ~6.2 % from those values from run 3888, respectively. For period II, the E_{vis} means and RMS's vary up to ~1.7 % and ~1.4 % from those values from run 3888, respectively. These time variations as systematic errors are added in quadrature to the errors of $\mu_{N_{\mathrm{Max\,ID}}}$ and $\sigma_{N_{\mathrm{Max\,ID}}}$ from Table G.1.

Using each set of $\mu_{N_{\mathrm{Max\,ID}}}$ and $\sigma_{N_{\mathrm{Max\,ID}}}$ including their time variation systematic errors, $\varepsilon_{N_{\mathrm{Max\,ID}}}$ is calculated from Equation 5.4 for each period, radial region, and event type, as summarized in Table G.3.

For each event type, $\varepsilon_{N_{\mathrm{Max\,ID}}}$ in three radial regions are weight-averaged according to the event fractions estimated in Section 5.4, in each period I and II. Table G.4 summarizes the results. For all of the event types, $\varepsilon_{N_{\mathrm{Max\,ID}}}$ is basically 1 within errors, and these errors are negligible.

Table G.1: The fitted $\mu_{N_{\mathrm{Max\,ID}}}$ and $\sigma_{N_{\mathrm{Max\,ID}}}$ obtained from run 3888 with the low N_{ID} threshold.

$N_{\mathrm{Max\,ID}}$ threshold	r range [m]	$\mu_{N_{\mathrm{Max\,ID}}}$ [MeV]	$\sigma_{N_{\mathrm{Max\,ID}}}$ [MeV]
200	$r < 4.7$	0.7803 ± 0.0016	0.0341 ± 0.0019
	$4.7 < r < 5.5$	0.8140 ± 0.0037	0.0454 ± 0.0035
	$5.5 < r < 6.3$	0.9119 ± 0.0036	0.0880 ± 0.0034
180	$r < 4.7$	0.6854 ± 0.0013	0.0387 ± 0.0015
	$4.7 < r < 5.5$	0.7168 ± 0.0018	0.0458 ± 0.0022
	$5.5 < r < 6.3$	0.7876 ± 0.0029	0.0877 ± 0.0031

Table G.2: The mean and RMS of E_{vis} for events with $N_{\mathrm{Max\,ID}} = 200$ and $N_{\mathrm{Max\,ID}} = 180$ from the special low N_{ID} threshold run 3888.

$N_{\mathrm{Max\,ID}}$	E_{vis} mean [MeV]	E_{vis} RMS [MeV]
200	0.7804	0.0453
180	0.6837	0.0355

Table G.3: $\varepsilon_{N_{\mathrm{Max\,ID}}}$ for various event types in three radial regions. The errors are given in parenthesis.

Event type	r range [mm]	$\varepsilon_{N_{\mathrm{Max\,ID}}}$ period I	$\varepsilon_{N_{\mathrm{Max\,ID}}}$ period II
$\bar{\nu}_{\mathrm{reactor}}$	$r < 4.7$	1.0000000(26)	0.999999983(56)
	$4.7 < r < 5.5$	0.999993(75)	0.9999992(14)
	$5.5 < r < 6.3$	0.9989(11)	0.999845(71)
^{238}U $\bar{\nu}_{\mathrm{geo}}$	$r < 4.7$	1.000000(38)	0.9999998(77)
	$4.7 < r < 5.5$	0.9999(10)	0.999989(18)
	$5.5 < r < 6.3$	0.986(15)	0.9980(92)
^{232}Th $\bar{\nu}_{\mathrm{geo}}$	$r < 4.7$	0.999999(99)	0.9999994(20)
	$4.7 < r < 5.5$	0.9997(26)	0.999972(47)
	$5.5 < r < 6.3$	0.964(0.038)	0.9948(24)
^{13}C(α, n) (p scattering)	$r < 4.7$	1.00000(29)	0.999978(66)
	$4.7 < r < 5.5$	0.9993(62)	0.9992(10)
	$5.5 < r < 6.3$	0.960(40)	0.9912(88)

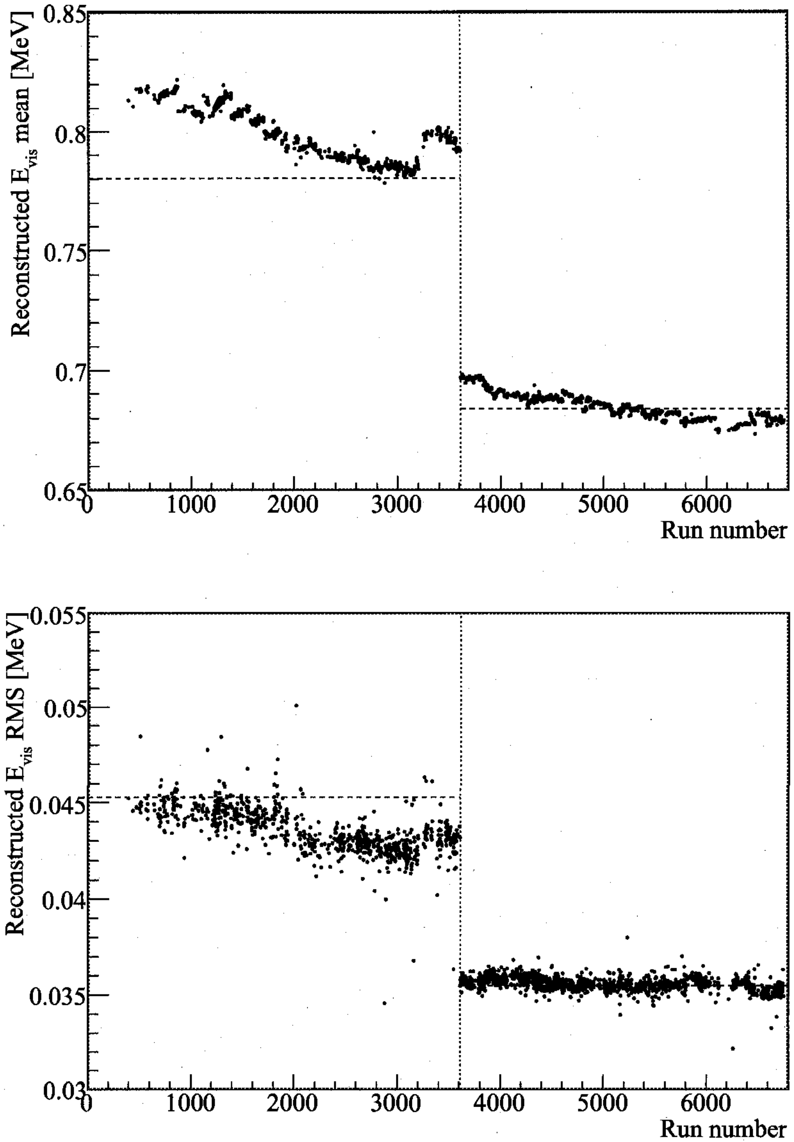

Figure G.2: Means (top plot) and *RMS* (bottom plot) of the reconstructed E_{vis} for all the events with $N_{\mathrm{Max\,ID}}$ equal to the analysis $N_{\mathrm{Max\,ID}}$ threshold. The vertical dotted line separates the two periods with $N_{\mathrm{Max\,ID}}$ threshold of 200 (period I) and 180 (period II). Two horizontal dashed lines before and after run 3611 indicate the mean (top plot) and *RMS* (bottom plot) of E_{vis} at $N_{\mathrm{Max\,ID}}$ equal to the analysis $N_{\mathrm{Max\,ID}}$ threshold, taken from run 3888, the special low threshold run.

Table G.4: $\varepsilon_{N_{\mathrm{Max\,ID}}}$ for various event types. The errors are given in parenthesis.

Event type	$\varepsilon_{N_{\mathrm{Max\,ID}}}$ period I	$\varepsilon_{N_{\mathrm{Max\,ID}}}$ period II
$\bar{\nu}_{\mathrm{reactor}}$	0.999954(54)	0.9999934(30)
^{238}U $\bar{\nu}_{\mathrm{geo}}$	0.99941(70)	0.999914(38)
^{232}Th $\bar{\nu}_{\mathrm{geo}}$	0.9984(18)	0.99978(10)
^{13}C$(\alpha, \mathrm{n})^{16}$O (p scattering)	0.9976(27)	0.99837(51)

Appendix H

Reconstruction Efficiency Calculation

The details on the calculation of $\varepsilon_{\mathrm{recon}}$ are described below.

$\varepsilon_{\mathrm{recon}}$ is estimated as the fraction of events with "reasonable reconstruction," defined in Table H.1, using the $^{60}\mathrm{Co}^{68}\mathrm{Ge}$ and $^{241}\mathrm{Am}^{9}\mathrm{Be}$ sources with known energies and deployed positions, and the events acquired during normal runs. The reconstruction efficiency for the source events, $\varepsilon_{\mathrm{recon,\,source}}$, is calculated by properly subtracting the background events obtained from a normal run without the source, and is given by

$$\varepsilon_{\mathrm{recon,\,source}} = \frac{N_{\mathrm{recon,\,source}} - N_{\mathrm{recon,\,BG}}}{N_{N_{\mathrm{Max\,ID}},\,\mathrm{source}} - N_{N_{\mathrm{Max\,ID}},\,\mathrm{BG}}}, \tag{H.1}$$

where $N_{\mathrm{recon,\,source}}$ and $N_{\mathrm{recon,\,BG}}$ denote the number of events that pass all the cuts in Table H.1 and have valid statuses returned by the reconstruction algorithms in the source and normal runs, respectively. $N_{N_{\mathrm{Max\,ID}},\,\mathrm{source}}$ and $N_{N_{\mathrm{Max\,ID}},\,\mathrm{BG}}$ denote the number of events that pass only the $N_{\mathrm{Max\,ID}}$ cut in the source and normal runs, respectively.

Figure 5.5 shows $\varepsilon_{\mathrm{recon,\,source}}$ at various positions along the vertical central axis of the detector for $^{60}\mathrm{Co}^{68}\mathrm{Ge}$ and $^{241}\mathrm{Am}^{9}\mathrm{Be}$ sources, each of which indicates that $\varepsilon_{\mathrm{recon,\,source}}$ is reasonably constant across various positions. $\varepsilon_{\mathrm{recon,\,source}}$ for $^{60}\mathrm{Co}^{68}\mathrm{Ge}$

Table H.1: Cuts for evaluating $\varepsilon_{\text{recon, source}}$ of "reasonable reconstruction."

Source	$N_{\text{Max ID}}$	E_{vis} [MeV]	Position [m]
^{60}Co^{68}Ge	$180 \leq N_{\text{Max ID}} \leq 600$	$0.5 < E_{\text{vis}} < 3.5$	$\lvert \mathbf{r}_{\text{source}} - \mathbf{r}_{\text{recon}} \rvert < 1.5$
^{241}Am^{9}Be	$600 \leq N_{\text{Max ID}} \leq 1100$	$2 < E_{\text{vis}} < 12$	$\lvert \mathbf{r}_{\text{source}} - \mathbf{r}_{\text{recon}} \rvert < 2.5$

and ^{241}Am^{9}Be are estimated by fitting a constant to the $\varepsilon_{\text{recon, source}}$ at various positions, resulting in 0.99986 ± 0.00020 and 0.99747 ± 0.00012, respectively. The average of these two fitted $\varepsilon_{\text{recon, source}}$s is 0.998665 ± 0.00012.

The error of $\varepsilon_{\text{recon}}$ is estimated by comparing $\varepsilon_{\text{recon, source}}$ with the reconstruction efficiency for events during normal runs, $\varepsilon_{\text{recon, normal}}$, whose true positions and E_{vis} are not known. The $N_{\text{Max ID}}$ of radioactivity during normal runs spans up to $N_{\text{Max ID}}$ of ~450, so $\varepsilon_{\text{recon, normal}}$ is estimated using the events whose $N_{\text{Max ID}}$ is between 200 (period I) or 180 (period II) and 450. Since the exact position or E_{vis} of the radioactive background events are not known, $\varepsilon_{\text{recon, normal}}$, is calculated from

$$\varepsilon_{\text{recon, normal}} = \frac{N_{\text{valid}}}{N_{N_{\text{Max ID}}}}, \tag{H.2}$$

where N_{valid} denotes the number of events that pass the $N_{\text{Max ID}}$ cut and the Cosmogenic Spallation Cuts, defined in Section 5.3.2, and have valid statuses returned by the reconstruction algorithms, and $N_{N_{\text{Max ID}}}$ denotes the number of events that pass the $N_{\text{Max ID}}$ cut and the Cosmogenic Spallation Cuts.

Figure H.1 shows $\varepsilon_{\text{recon, normal}}$ as a function of $N_{\text{Max ID}}$ for all the good runs in periods I and II. The events with low $N_{\text{Max ID}}$ have slightly lower $\varepsilon_{\text{recon, normal}}$ due to lack of photons produced in the LS for low E_{vis} events. Figure 5.6 shows the time variation of $\varepsilon_{\text{recon, normal}}$. The maximum deviation of $\varepsilon_{\text{recon, normal}}$ at various $N_{\text{Max ID}}$ and time from $\varepsilon_{\text{recon, source}}$ is 0.0022, which is taken as the error of $\varepsilon_{\text{recon}}$, resulting in an estimated $\varepsilon_{\text{recon}}$ of 0.9987 ± 0.0022.

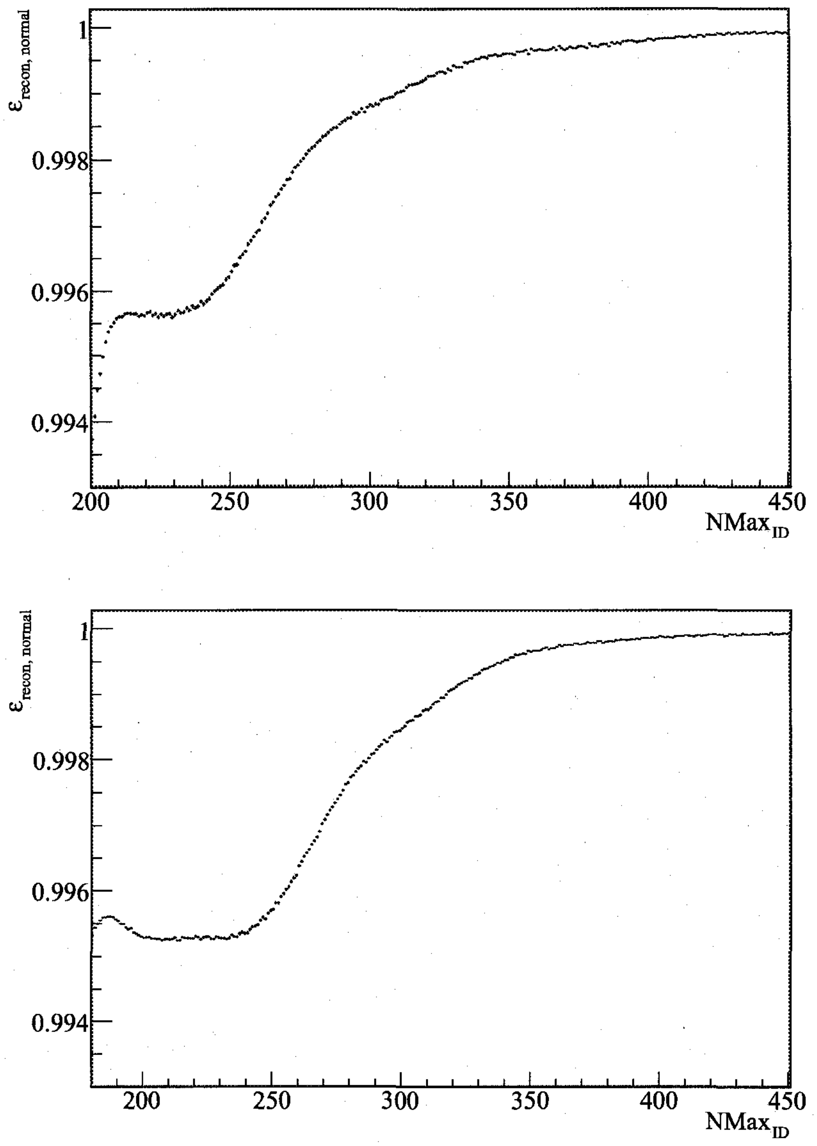

Figure H.1: $\varepsilon_{\text{recon, normal}}$ as a function of $N_{\text{Max ID}}$ from normal runs in period I (top plot) and period II (bottom plot).

Appendix I

Correlation Coefficient Matrices

The correlation coefficient matrices from Mode-I, II, III analyses, and Mode-III analysis with georeactor best-fits are given in the following tables.

Table I.1: Correlation coefficient matrix for Mode-I analysis best-fit.

Parameter	Global	$\sin^2 2\theta_{12}$	Δm^2_{21}	$\Phi_{\text{geo sum}}$	$\Phi_{\text{geo diff}}$	a_0	k_b	k_0	k_C	$N_{\text{random I}}$	$N_{\text{random II}}$	$N_{^9\text{Li}}$	$R_{^{13}\text{C}(\alpha,\text{n})}$	$F_{^{13}\text{C}(\alpha,\text{n}),\text{C}}$	$F_{^{13}\text{C}(\alpha,\text{n})^{16}\text{O}^*}$	$R_{\text{fast n}}$	$R_{\text{atm}\,\nu}$	$\varepsilon_{\text{reactor}}$	$\varepsilon_{\text{common}}$
$\sin^2 2\theta_{12}$	0.79601	1.000	-0.226	0.416	0.329	-0.024	-0.022	0.015	0.034	0.001	0.001	0.013	-0.007	-0.000	0.185	0.097	0.004	0.368	0.431
Δm^2_{21}	0.64157	-0.226	1.000	-0.398	-0.547	0.290	0.244	-0.195	-0.383	-0.001	-0.001	-0.007	0.033	-0.002	-0.145	-0.024	-0.001	0.045	0.054
$\Phi_{\text{geo sum}}$	0.76288	0.416	-0.398	1.000	0.585	-0.102	-0.072	0.078	0.137	-0.001	-0.001	0.008	-0.370	0.002	0.312	0.037	-0.000	0.048	-0.066
$\Phi_{\text{geo diff}}$	0.71428	0.329	-0.547	0.585	1.000	-0.228	-0.180	0.140	0.303	0.001	0.001	0.006	-0.052	0.002	0.112	0.019	0.001	-0.040	-0.048
a_0	0.99002	-0.024	0.290	-0.102	-0.228	1.000	0.865	-0.920	-0.924	-0.000	-0.000	0.008	0.021	-0.000	0.171	0.073	0.001	0.015	0.018
k_b	0.87406	-0.022	0.244	-0.072	-0.180	0.865	1.000	-0.769	-0.791	-0.000	-0.000	0.007	0.016	-0.000	0.147	0.062	0.001	0.013	0.015
k_0	0.96225	0.015	-0.195	0.078	0.140	-0.920	-0.769	1.000	0.745	0.000	0.000	-0.005	-0.019	0.000	-0.112	-0.050	-0.001	-0.013	-0.015
k_C	0.96832	0.034	-0.383	0.137	0.303	-0.924	-0.791	0.745	1.000	0.000	0.000	-0.010	-0.026	0.000	-0.238	-0.096	-0.001	-0.019	-0.023
$N_{\text{random I}}$	0.00411	0.001	-0.001	-0.001	0.001	-0.000	-0.000	0.000	0.000	1.000	0.000	0.000	-0.001	0.000	0.001	0.000	-0.000	0.000	0.000
$N_{\text{random II}}$	0.00461	0.001	-0.001	-0.001	0.001	-0.000	-0.000	0.000	0.000	0.000	1.000	0.000	-0.002	0.000	0.001	0.000	-0.000	0.000	0.000
$N_{^9\text{Li}}$	0.07794	0.013	-0.007	0.008	0.006	0.008	0.007	-0.005	-0.010	0.000	0.000	1.000	-0.000	0.000	0.003	-0.069	-0.002	-0.000	-0.000
$R_{^{13}\text{C}(\alpha,\text{n})}$	0.49886	-0.007	0.033	-0.370	-0.052	0.021	0.016	-0.019	-0.026	-0.001	-0.002	-0.000	1.000	0.002	-0.229	-0.002	-0.001	-0.016	-0.018
$F_{^{13}\text{C}(\alpha,\text{n}),\text{C}}$	0.00448	-0.000	-0.002	0.002	0.002	-0.000	-0.000	0.000	0.000	0.000	0.000	0.000	0.002	1.000	0.000	0.000	-0.000	-0.002	-0.002
$F_{^{13}\text{C}(\alpha,\text{n})^{16}\text{O}^*}$	0.50747	0.185	-0.145	0.312	0.112	0.171	0.147	-0.112	-0.238	0.001	0.001	0.003	-0.229	0.000	1.000	0.034	0.001	0.006	0.006
$R_{\text{fast n}}$	0.21237	0.097	-0.024	0.037	0.019	0.073	0.062	-0.050	-0.096	0.000	0.000	-0.069	-0.002	0.000	0.034	1.000	-0.094	0.005	0.006
$R_{\text{atm}\,\nu}$	0.09716	0.004	-0.001	-0.000	0.001	0.001	0.001	-0.001	-0.001	-0.000	-0.000	-0.002	-0.001	-0.000	0.001	-0.094	1.000	-0.001	-0.001
$\varepsilon_{\text{reactor}}$	0.61682	0.368	0.045	0.048	-0.040	0.015	0.013	-0.013	-0.019	0.000	0.000	-0.000	-0.016	-0.002	0.006	0.005	-0.001	1.000	-0.178
$\varepsilon_{\text{common}}$	0.67985	0.431	0.054	-0.066	-0.048	0.018	0.015	-0.015	-0.023	0.000	0.000	-0.000	-0.018	-0.002	0.006	0.006	-0.001	-0.178	1.000

Table I.2: Correlation coefficient matrix for Mode-II analysis best-fit.

Parameter	Global	$\sin^2 2\theta_{12}$	Δm^2_{21}	$\Phi_{\rm geo\,sum}$	$\Phi_{\rm geo\,diff}$	a_0	k_b	k_0	k_C	$N_{\rm random\,I}$	$N_{\rm random\,II}$	$N_{^9{\rm Li}}$	$R_{^{13}{\rm C}(\alpha,{\rm n})}$	$F_{^{13}{\rm C}(\alpha,{\rm n}),{\rm C}}$	$F_{^{13}{\rm C}(\alpha,{\rm n})^{16}{\rm O}^*}$	$R_{\rm fast\,n}$	$R_{\rm atm\,\nu}$	$\varepsilon_{\rm reactor}$	$\varepsilon_{\rm common}$
$\sin^2 2\theta_{12}$	0.79615	1.000	-0.264	0.562	0.358	-0.044	-0.041	0.017	0.070	0.001	0.000	0.010	-0.058	0.001	0.223	0.123	0.029	0.435	0.369
Δm^2_{21}	0.57942	-0.264	1.000	-0.296	-0.436	0.289	0.245	-0.201	-0.378	-0.000	-0.000	0.008	-0.006	-0.002	-0.070	-0.036	0.001	0.069	-0.145
$\Phi_{\rm geo\,sum}$	0.70666	0.562	-0.296	1.000	0.365	-0.091	-0.055	0.080	0.109	-0.002	-0.001	0.023	-0.332	0.001	0.255	0.095	-0.043	0.052	0.208
$\Phi_{\rm geo\,diff}$	0.57644	0.358	-0.436	0.365	1.000	-0.225	-0.181	0.144	0.291	0.001	0.001	-0.001	0.057	0.001	-0.007	0.037	-0.006	-0.044	0.146
a_0	0.99038	-0.044	0.289	-0.091	-0.225	1.000	0.869	-0.922	-0.926	-0.000	0.000	0.012	0.014	-0.000	0.179	0.075	-0.000	0.010	-0.012
k_b	0.87914	-0.041	0.245	-0.055	-0.181	0.869	1.000	-0.777	-0.793	0.000	-0.000	0.009	0.006	-0.000	0.168	0.055	0.018	-0.001	0.005
k_0	0.96272	0.017	-0.201	0.080	0.144	-0.922	-0.777	1.000	0.753	0.001	-0.000	-0.013	-0.020	0.000	-0.105	-0.058	0.009	-0.016	-0.015
k_C	0.96960	0.070	-0.378	0.109	0.291	-0.926	-0.793	0.753	1.000	-0.000	0.000	-0.012	-0.013	0.000	-0.264	-0.103	-0.006	-0.009	0.042
$N_{\rm random\,I}$	0.00614	0.001	-0.000	-0.002	0.001	-0.000	0.000	0.001	-0.000	1.000	-0.000	0.000	-0.000	0.000	-0.001	0.001	-0.002	0.001	-0.000
$N_{\rm random\,II}$	0.00471	0.000	-0.000	-0.001	0.001	0.000	-0.000	-0.000	0.000	-0.000	1.000	0.001	-0.002	0.000	0.002	0.000	0.001	-0.000	-0.001
$N_{^9{\rm Li}}$	0.05093	0.010	0.008	0.023	-0.001	0.012	0.009	-0.013	-0.012	0.000	0.001	1.000	-0.008	-0.000	-0.004	-0.022	0.022	-0.001	-0.009
$R_{^{13}{\rm C}(\alpha,{\rm n})}$	0.47511	-0.058	-0.006	-0.332	0.057	0.014	0.006	-0.020	-0.013	-0.000	-0.002	-0.008	1.000	0.003	-0.215	-0.002	0.023	-0.008	-0.176
$F_{^{13}{\rm C}(\alpha,{\rm n}),{\rm C}}$	0.00506	0.001	-0.002	0.001	0.001	-0.000	-0.000	0.000	0.000	0.000	0.000	-0.000	0.003	1.000	-0.002	0.001	-0.001	-0.002	-0.000
$F_{^{13}{\rm C}(\alpha,{\rm n})^{16}{\rm O}^*}$	0.50348	0.223	-0.070	0.255	-0.007	0.179	0.168	-0.105	-0.264	-0.001	0.002	-0.004	-0.215	-0.002	1.000	0.068	-0.063	0.019	0.123
$R_{\rm fast\,n}$	0.21698	0.123	-0.036	0.095	0.037	0.075	0.055	-0.058	-0.103	0.001	0.000	-0.022	-0.002	0.001	0.068	1.000	-0.017	-0.013	0.011
$R_{\rm atm\,\nu}$	0.12417	0.029	0.001	-0.043	-0.006	-0.000	0.018	0.009	-0.006	-0.002	0.001	0.022	0.023	-0.001	-0.063	-0.017	1.000	0.046	-0.008
$\varepsilon_{\rm reactor}$	0.59968	0.435	0.069	0.052	-0.044	0.010	-0.001	-0.016	-0.009	0.001	-0.000	-0.001	-0.008	-0.002	0.019	-0.013	0.046	1.000	-0.076
$\varepsilon_{\rm common}$	0.50195	0.369	-0.145	0.208	0.146	-0.012	0.005	-0.015	0.042	-0.000	-0.001	-0.009	-0.176	-0.000	0.123	0.011	-0.008	-0.076	1.000

Table I.3: Correlation coefficient matrix for Mode-III analysis best-fit.

Parameter	Global	$\sin^2 2\theta_{12}$	Δm^2_{21}	$\Phi_{\mathrm{geo\,sum}}$	$\Phi_{\mathrm{geo\,diff}}$	a_0	k_b	k_0	k_C	$N_{\mathrm{random\,I}}$	$N_{\mathrm{random\,II}}$	$N_{^9\mathrm{Li}}$	$R_{^{13}\mathrm{C}(\alpha,\mathrm{n})}$	$F_{^{13}\mathrm{C}(\alpha,\mathrm{n}),\,\mathrm{C}}$	$F_{^{13}\mathrm{C}(\alpha,\mathrm{n})^{16}\mathrm{O}^*}$	$R_{\mathrm{fast\,n}}$	$R_{\mathrm{atm}\,\nu}$	$\varepsilon_{\mathrm{reactor}}$	$\varepsilon_{\mathrm{common}}$	ϕ_1	ϕ_7	ϕ_8
$\sin^2 2\theta_{12}$	0.80934	1.000	-0.095	0.219	0.139	-0.015	-0.024	0.006	0.018	0.002	-0.000	0.009	-0.019	0.001	0.082	0.058	-0.002	0.173	0.216	-0.227	0.238	-0.777
Δm^2_{21}	0.56669	-0.095	1.000	-0.296	-0.442	0.275	0.232	-0.188	-0.365	-0.000	-0.000	-0.003	0.028	-0.002	-0.072	-0.004	0.002	0.092	0.111	0.020	-0.021	0.072
$\Phi_{\mathrm{geo\,sum}}$	0.66611	0.219	-0.296	1.000	0.389	-0.080	-0.050	0.065	0.108	-0.002	-0.002	0.003	-0.403	0.002	0.262	0.006	-0.002	-0.050	-0.222	-0.046	0.048	-0.168
$\Phi_{\mathrm{geo\,diff}}$	0.57303	0.139	-0.442	0.389	1.000	-0.212	-0.169	0.127	0.281	0.001	0.001	-0.009	0.004	0.001	0.006	-0.007	-0.003	-0.113	-0.139	0.032	0.033	-0.104
a_0	0.98999	-0.015	0.275	-0.080	-0.212	1.000	0.867	-0.921	-0.924	-0.000	-0.000	0.009	0.017	-0.000	0.182	0.076	0.006	0.012	0.015	0.003	-0.004	0.012
k_b	0.87516	-0.024	0.232	-0.050	-0.169	0.867	1.000	-0.772	-0.793	0.001	-0.000	0.016	0.011	0.000	0.158	0.062	0.006	0.006	0.009	0.003	-0.003	0.015
k_0	0.96235	0.006	-0.188	0.065	0.127	-0.921	-0.772	1.000	0.749	0.000	0.000	-0.007	-0.018	0.000	-0.117	-0.051	-0.005	-0.013	-0.014	-0.000	0.000	-0.005
k_C	0.96795	0.018	-0.365	0.108	0.281	-0.924	-0.793	0.749	1.000	0.000	-0.000	-0.010	-0.024	0.000	-0.256	-0.101	-0.007	-0.018	-0.021	-0.004	0.004	-0.014
$N_{\mathrm{random\,I}}$	0.00582	0.002	-0.000	-0.002	0.001	-0.000	0.001	0.000	0.000	1.000	0.000	-0.000	-0.001	-0.000	0.001	0.002	-0.000	-0.000	-0.000	-0.000	0.000	-0.002
$N_{\mathrm{random\,II}}$	0.00439	-0.000	-0.000	-0.002	0.001	-0.000	-0.000	0.000	-0.000	0.000	1.000	0.000	-0.002	0.000	0.001	-0.001	0.000	0.000	-0.000	-0.000	0.000	0.000
$N_{^9\mathrm{Li}}$	0.05490	0.009	-0.003	0.003	-0.009	0.009	0.016	-0.007	-0.010	-0.000	0.000	1.000	-0.001	-0.001	-0.008	-0.022	-0.001	-0.007	-0.008	-0.002	0.001	-0.026
$R_{^{13}\mathrm{C}(\alpha,\mathrm{n})}$	0.50063	-0.019	0.028	-0.403	0.004	0.017	0.011	-0.018	-0.024	-0.001	-0.002	-0.001	1.000	0.002	-0.241	0.002	0.001	-0.021	-0.025	0.001	-0.001	0.012
$F_{^{13}\mathrm{C}(\alpha,\mathrm{n}),\,\mathrm{C}}$	0.00564	0.001	-0.002	0.002	0.001	-0.000	0.000	0.000	0.000	-0.000	0.000	-0.001	0.002	1.000	-0.000	0.001	-0.000	-0.002	-0.002	-0.000	0.000	-0.001
$F_{^{13}\mathrm{C}(\alpha,\mathrm{n})^{16}\mathrm{O}^*}$	0.47451	0.082	-0.072	0.262	0.006	0.182	0.158	-0.117	-0.256	0.001	0.001	-0.008	-0.241	-0.000	1.000	0.021	0.002	-0.039	-0.047	-0.017	0.018	-0.001
$R_{\mathrm{fast\,n}}$	0.16458	0.058	-0.004	0.006	-0.007	0.076	0.062	-0.051	-0.101	0.002	-0.001	-0.022	0.002	0.001	0.021	1.000	-0.001	-0.026	-0.033	-0.010	0.011	-0.061
$R_{\mathrm{atm}\,\nu}$	0.00794	-0.002	0.002	-0.002	-0.003	0.006	0.006	-0.005	-0.007	-0.000	0.000	-0.001	0.001	-0.000	0.002	-0.001	1.000	0.000	-0.000	0.003	-0.003	-0.052
$\varepsilon_{\mathrm{reactor}}$	0.54599	0.173	0.092	-0.050	-0.113	0.012	0.006	-0.013	-0.018	-0.000	0.000	-0.007	-0.021	-0.002	-0.039	-0.026	0.000	1.000	-0.370	-0.041	0.043	-0.132
$\varepsilon_{\mathrm{common}}$	0.60546	0.216	0.111	-0.222	-0.139	0.015	0.009	-0.014	-0.021	-0.000	-0.000	-0.008	-0.025	-0.002	-0.047	-0.033	-0.000	-0.370	1.000	-0.049	0.051	-0.165
ϕ_1	0.96746	-0.227	0.020	-0.046	-0.032	0.003	0.003	-0.000	-0.004	-0.000	-0.000	-0.002	0.001	-0.000	-0.017	-0.010	0.003	-0.041	-0.049	1.000	-0.967	0.280
ϕ_7	0.96773	0.238	-0.021	0.048	0.033	-0.004	-0.003	0.000	0.004	0.000	0.000	0.001	-0.001	0.000	0.018	0.011	-0.003	0.043	0.051	-0.967	1.000	-0.293
ϕ_8	0.78509	-0.777	0.072	-0.168	-0.104	0.012	0.015	-0.005	-0.014	-0.002	0.000	-0.026	0.012	-0.001	-0.061	-0.052	0.001	-0.132	-0.165	0.280	-0.293	1.000

Table I.4: Correlation coefficient matrix for Mode-III analysis with georeactor best-fit.

Parameter	Global	$\sin^2 2\theta_{12}$	Δm^2_{21}	$\Phi_{\mathrm{geo\,sum}}$	$\Phi_{\mathrm{geo\,diff}}$	a_0	k_b	k_0	k_C	$N_{\mathrm{random\,I}}$	$N_{\mathrm{random\,II}}$	$N_{^9\mathrm{Li}}$	$R_{^{13}\mathrm{C}(\alpha,\mathrm{n})}$	$F_{^{13}\mathrm{C}(\alpha,\mathrm{n}),\mathrm{C}}$	$F_{^{13}\mathrm{C}(\alpha,\mathrm{n})^{16}\mathrm{O}^*}$	$R_{\mathrm{fast\,n}}$	$\Phi_{\mathrm{georeactor}}$	$R_{\mathrm{atm}\,\nu}$	$\epsilon_{\mathrm{reactor}}$	$\epsilon_{\mathrm{common}}$	ϕ_1	ϕ_7	ϕ_8
$\sin^2 2\theta_{12}$	0.83362	1.000	-0.015	0.144	0.044	0.009	0.006	-0.012	-0.011	-0.001	-0.000	-0.009	-0.029	-0.001	0.009	0.006	0.349	-0.001	-0.016	-0.005	-0.223	0.235	-0.799
Δm^2_{21}	0.58449	-0.015	1.000	-0.317	-0.480	0.275	0.229	-0.187	-0.366	-0.001	0.000	-0.010	0.031	-0.003	-0.099	-0.016	0.153	0.000	0.020	0.024	0.006	-0.006	0.012
$\Phi_{\mathrm{geo\,sum}}$	0.69702	0.144	-0.317	1.000	0.481	-0.084	-0.053	0.066	0.116	-0.001	-0.002	0.001	-0.398	0.003	0.279	0.022	-0.135	-0.001	0.009	-0.129	-0.030	0.032	-0.107
$\Phi_{\mathrm{geo\,diff}}$	0.64489	0.044	-0.480	0.481	1.000	-0.216	-0.166	0.132	0.289	0.001	0.000	0.006	-0.033	0.002	0.062	0.018	-0.225	-0.001	-0.010	-0.017	-0.011	0.011	-0.035
a_0	0.99017	0.009	0.275	-0.084	-0.216	1.000	0.867	-0.920	-0.924	0.000	-0.000	0.006	0.015	-0.000	0.174	0.069	0.049	0.000	-0.008	-0.009	-0.002	0.002	-0.009
k_b	0.87614	0.006	0.229	-0.053	-0.166	0.867	1.000	-0.771	-0.792	0.000	-0.001	0.015	0.010	0.000	0.149	0.061	0.040	-0.000	-0.006	-0.006	-0.002	0.003	-0.005
k_0	0.96242	-0.012	-0.187	0.066	0.132	-0.920	-0.771	1.000	0.747	-0.000	0.001	-0.001	-0.016	-0.000	-0.114	-0.045	-0.034	-0.000	0.001	0.003	0.007	-0.007	0.013
k_C	0.96857	-0.011	-0.366	0.116	0.289	-0.924	-0.792	0.747	1.000	0.000	0.000	-0.007	-0.020	0.000	-0.242	-0.091	-0.067	0.000	0.011	0.013	0.002	-0.002	0.011
$N_{\mathrm{random\,I}}$	0.00429	-0.001	-0.001	-0.001	0.001	0.000	0.000	-0.000	0.000	1.000	0.000	0.001	-0.001	0.000	0.001	0.000	-0.001	0.000	0.000	0.000	-0.000	0.000	0.001
$N_{\mathrm{random\,II}}$	0.00512	-0.000	0.000	-0.002	0.000	-0.000	-0.001	0.001	0.000	0.000	1.000	-0.001	-0.002	0.000	0.001	-0.001	-0.001	-0.000	-0.000	-0.000	0.000	-0.000	-0.001
$N_{^9\mathrm{Li}}$	0.04768	-0.009	-0.010	0.001	0.006	0.006	0.015	-0.001	-0.007	0.001	-0.001	1.000	-0.004	0.001	-0.006	-0.019	-0.016	-0.000	0.001	-0.001	0.002	-0.000	0.014
$R_{^{13}\mathrm{C}(\alpha,\mathrm{n})}$	0.49349	-0.029	0.031	-0.398	-0.033	0.015	0.010	-0.016	-0.020	-0.001	-0.002	-0.004	1.000	0.001	-0.222	-0.010	-0.008	0.000	-0.017	-0.014	0.002	-0.002	0.015
$F_{^{13}\mathrm{C}(\alpha,\mathrm{n}),\mathrm{C}}$	0.00534	-0.001	-0.003	0.003	0.002	-0.000	0.000	-0.000	0.000	0.000	0.000	0.001	0.001	1.000	0.000	0.001	-0.002	0.000	-0.000	-0.001	0.000	0.000	0.001
$F_{^{13}\mathrm{C}(\alpha,\mathrm{n})^{16}\mathrm{O}^*}$	0.49206	0.009	-0.099	0.279	0.062	0.174	0.149	-0.114	-0.242	0.001	0.001	-0.006	-0.222	0.000	1.000	0.035	-0.156	-0.000	0.023	0.029	-0.005	0.005	-0.006
$R_{\mathrm{fast\,n}}$	0.16774	0.006	-0.016	0.022	0.018	0.069	0.061	-0.045	-0.091	0.000	-0.001	-0.019	-0.010	0.001	0.035	1.000	-0.086	-0.000	0.014	0.024	0.001	0.000	0.003
$\Phi_{\mathrm{georeactor}}$	0.84561	0.349	0.153	-0.135	-0.225	0.049	0.040	-0.034	-0.067	-0.001	-0.001	-0.016	-0.008	-0.002	-0.156	-0.086	1.000	-0.000	-0.430	-0.512	-0.071	0.075	-0.277
$R_{\mathrm{atm}\,\nu}$	0.00197	-0.001	0.000	-0.001	-0.001	0.000	-0.000	-0.000	0.000	0.000	-0.000	-0.000	0.000	0.000	-0.000	-0.000	-0.000	1.000	-0.000	0.001	0.000	0.000	0.001
$\epsilon_{\mathrm{reactor}}$	0.66751	-0.016	0.020	0.009	-0.010	-0.008	-0.006	0.001	0.011	0.000	-0.000	0.001	-0.017	-0.000	0.023	0.014	-0.430	-0.000	1.000	-0.089	-0.002	0.002	0.007
$\epsilon_{\mathrm{common}}$	0.74148	-0.005	0.024	-0.129	-0.017	-0.009	-0.006	0.003	0.013	0.000	-0.000	-0.001	-0.014	-0.001	0.029	0.024	-0.512	0.001	-0.089	1.000	-0.002	0.002	0.003
ϕ_1	0.96822	-0.223	0.006	-0.030	-0.011	-0.002	-0.002	0.007	0.002	-0.000	0.000	0.002	0.002	0.000	-0.005	0.001	-0.071	0.000	-0.002	-0.002	1.000	-0.968	0.283
ϕ_7	0.96847	0.235	-0.006	0.032	0.011	0.002	0.003	-0.007	-0.002	0.000	-0.000	-0.000	-0.002	0.000	0.005	0.000	0.075	0.000	0.002	0.002	-0.968	1.000	-0.295
ϕ_8	0.80661	-0.799	0.012	-0.107	-0.035	-0.009	-0.005	0.013	0.011	0.001	-0.001	0.014	0.015	0.001	-0.006	0.003	-0.277	0.001	0.007	0.003	0.283	-0.295	1.000

Bibliography

[1] W. Pauli, Letter to the physical society of Tubingen, Unpublished., 1930.

[2] L. M. Brown, Phys. Today **31N9** (1978).

[3] E. Fermi, Z. Phys. **88**, 161 (1934).

[4] F. Reines and C. L. Cowan, Phys. Rev. **92**, 830 (1953).

[5] C. L. Cowan, F. Reines, F. B. Harrison, H. W. Kruse, and A. D. McGuire, Science **124**, 103 (1956).

[6] J. Davis, Raymond, D. S. Harmer, and K. C. Hoffman, Phys. Rev. Lett. **20**, 1205 (1968).

[7] G. Danby *et al.*, Phys. Rev. Lett. **9**, 36 (1962).

[8] M. L. Perl *et al.*, Phys. Rev. Lett. **35**, 1489 (1975).

[9] DONUT, K. Kodama *et al.*, Phys. Lett. **B504**, 218 (2001), hep-ex/0012035.

[10] J. N. Bahcall, N. A. Bahcall, and G. Shaviv, Phys. Rev. Lett. **20**, 1209 (1968).

[11] D. N. Abdurashitov *et al.*, Phys. Lett. **B328**, 234 (1994).

[12] GALLEX, W. Hampel *et al.*, Phys. Lett. **B447**, 127 (1999).

[13] K. S. Hirata *et al.*, Phys. Rev. Lett. **65**, 1297 (1990).

[14] Y. Fukuda *et al.*, Phys. Rev. Lett. **81**, 1158 (1998).

[15] R. Becker-Szendy *et al.*, Phys. Rev. D **46**, 3720 (1992).

[16] Kamiokande-II, K. S. Hirata *et al.*, Phys. Lett. **B280**, 146 (1992).

[17] Z. Maki, M. Nakagawa, and S. Sakata, Prog. Theor. Phys. **28**, 870 (1962).

[18] Q. R. Ahmad *et al.*, Phys. Rev. Lett. **89**, 011301 (2002).

[19] SNO, S. N. Ahmed *et al.*, Phys. Rev. Lett. **92**, 181301 (2004), nucl-ex/0309004.

[20] Super-Kamiokande, Y. Ashie *et al.*, Phys. Rev. Lett. **93**, 101801 (2004), hep-ex/0404034.

[21] CHOOZ, M. Apollonio *et al.*, Phys. Lett. **B466**, 415 (1999), hep-ex/9907037.

[22] R. D. McKeown and P. Vogel, Phys. Rept. **394**, 315 (2004), hep-ph/0402025.

[23] K. Schreckenbach, G. Colvin, W. Gelletly, and F. Von Feilitzsch, Phys. Lett. **B160**, 325 (1985).

[24] P. Vogel, G. K. Schenter, F. M. Mann, and R. E. Schenter, Phys. Rev. C **24**, 1543 (1981).

[25] A. A. Hahn *et al.*, Phys. Lett. **B218**, 365 (1989).

[26] C. Bemporad, G. Gratta, and P. Vogel, Rev. Mod. Phys. **74**, 297 (2002).

[27] N. R. Tolich, *Experimental study of terrestrial electron anti-neutrinos with KamLAND*, PhD thesis, Stanford University, 2005, UMI-31-62346.

[28] S. Enomoto, *Neutrino geophysics and observation of geo-neutrinos at KamLAND*, PhD thesis, Tohoku University, 2005.

[29] F. Mantovani, L. Carmignani, G. Fiorentini, and M. Lissia, Phys. Rev. **D69**, 013001 (2004), hep-ph/0309013.

[30] A. M. Dziewonski and D. L. Anderson, Phys. Earth Planet. Interiors **25**, 297 (1981).

[31] A. A. Kremenetsky and L. N. Ovchinnikov, Precambrian Res. **33**, 11 (1986).

[32] E. Anders and N. Grevesse, Geochim. Cosmochim. Acta **53**, 197 (1989).

[33] W. F. McDonough and S. s. Sun, Chem. Geol. **120**, 223 (1995).

[34] A. Rocholl and K. P. Jochum, Earth Planet. Sci. Lett. **117**, 265 (1993).

[35] H. N. Pollack, S. J. Hurter, and J. R. Johnson, Rev. Geophys. **31**, 267 (1993).

[36] A. M. Hofmeister and R. E. Criss, Tectonophysics **395**, 159 (2005).

[37] F. M. Richter, Earth Planet. Sci. Lett. **68**, 471 (1984).

[38] M. J. Jackson and H. N. Pollack, J. Geophys. Res. **89**, 10103 (1984).

[39] T. Spohn and G. Schubert, J. Geophys. Res. **87**, 4682 (1982).

[40] O. E. Mogensen and F. M. Jacobsen, Chemical Physics **73**, 223 (1982).

[41] P. Vogel and J. F. Beacom, Phys. Rev. **D60**, 053003 (1999), hep-ph/9903554.

[42] A. Kurylov, M. J. Ramsey-Musolf, and P. Vogel, Phys. Rev. **C67**, 035502 (2003), hep-ph/0211306.

[43] KamLAND, K. Eguchi *et al.*, Phys. Rev. Lett. **90**, 021802 (2003), hep-ex/0212021.

[44] KamLAND, T. Araki *et al.*, Phys. Rev. Lett. **94**, 081801 (2005), hep-ex/0406035.

[45] T. Araki *et al.*, Nature **436**, 499 (2005).

[46] J. B. Benziger *et al.*, Nucl. Instrum. Meth. **A417**, 278 (1998).

[47] F. Suekane *et al.*, (2004), physics/0404071.

[48] A. D. Vijaya and A. Kumar, Nucl. Instrum. Meth. **111**, 435 (1973).

[49] W. H. Press, B. P. Flannery, S. A. Teukolsky, and W. T. Vetterling, *Numerical Recipes in C: The Art of Scientific Computing* (Cambridge University Press, Cambridge, 1992).

[50] D. Dwyer, *Precision Measurement of Neutrino Oscillation Parameters with KamLAND*, PhD thesis, University of California, Berkeley, 2007.

[51] B. K. Fujikawa, Quenching and Cerenkov corrections to the KamLAND energy scale, KamLAND collaboration internal document. Unpublished., 2003.

[52] J. B. Birks, *The theory and practice of scintillation counting* Vol. 27, International series of monographs on electronics and instrumentation (Macmillian, New York, 1964).

[53] J. D. Jackson, *Classical Electrodynamics* (Wiley, New York, 1990).

[54] T. Hagner *et al.*, Astropart. Phys. **14**, 33 (2000).

[55] D. R. Tilley *et al.*, Nucl. Phys. A **745**, 155 (2004).

[56] T. R. England and B. F. Rider, 1994, LA-UP-94-3106, ENDF-349.

[57] http://wwwndc.tokai-sc.jaea.go.jp/ftpnd/jendl/jendl-an-2003.html.

[58] http://www.srim.org/.

[59] D. West and A. C. Sherwood, Ann. Nucl. Energy **9**, 551 (1982).

[60] D. A. Dwyer and R. McKeown, Calculation of atmospheric neutrino background in Kamland, KamLAND collaboration internal document. Unpublished., 2007.

[61] L. A. Ahrens *et al.*, Phys. Rev. **D35**, 785 (1987).

[62] M. Honda, T. Kajita, K. Kasahara, S. Midorikawa, and T. Sanuki, Phys. Rev. **D75**, 043006 (2007), astro-ph/0611418.

[63] J. N. Bahcall, A. M. Serenelli, and S. Basu, Astrophys. J. **621**, L85 (2005), astro-ph/0412440.

[64] SNO, B. Aharmim *et al.*, Phys. Rev. **C72**, 055502 (2005), nucl-ex/0502021.

[65] Super-Kamkiokande, J. Hosaka *et al.*, Phys. Rev. **D73**, 112001 (2006), hep-ex/0508053.

[66] B. T. Cleveland *et al.*, Astrophys. J. **496**, 505 (1998).

[67] SAGE, V. N. Gavrin, Nucl. Phys. Proc. Suppl. **138**, 87 (2005).

[68] GNO, M. Altmann *et al.*, Phys. Lett. **B616**, 174 (2005), hep-ex/0504037.

[69] R. G. H. Robertson, Prog. Part. Nucl. Phys. **57**, 90 (2006), nucl-ex/0602005.

[70] J. N. Bahcall and M. H. Pinsonneault, Phys. Rev. Lett. **92**, 121301 (2004), astro-ph/0402114.

[71] J. N. Bahcall and M. H. Pinsonneault, Rev. Mod. Phys. **67**, 781 (1995), hep-ph/9505425.

[72] A. Stuart *et al.*, *Kendall's Advanced Theory of Statistics* Vol. 2A (Oxford University Press, New York, 1999).

[73] J. M. Herndon, Proc. Nat. Acad. Sci. **100**, 3047 (2003).

[74] J. M. Herndon and D. A. Edgerley, (2005), hep-ph/0501216.